Exploring Quartz Luminescence: Application in Provenance Analysis and Sediment Transport

A thesis submitted in partial fulfilment of

the requirements for the degree of

Doctor of Philosophy

by

Santunu Kumar Panda

(Roll No. 19330015)

Under the supervision of

Dr. Naveen Chauhan

Associate Professor

Atomic, Molecular, and Optical Physics Division,

Physical Research Laboratory, Ahmedabad, India

DISCIPLINE OF PHYSICS

INDIAN INSTITUTE OF TECHNOLOGY GANDHINAGAR

2025

Department of Physics

Indian Institute of Technology, Gandhinagar

Gujarat-382355

CERTIFICATE

It is certified that the work contained in the thesis titled "**Exploring Quartz Luminescence: Application in Provenance Analysis and Sediment Transport**" by **Mr. Santunu Kumar Panda** (Roll no: 19330015) has been carried out under my supervision and that this work has not been submitted elsewhere for a degree.

Dr. Naveen Chauhan
(Thesis Supervisor)
Associate Professor,
Atomic Molecular and Optical Physics Division,
Physical Research Laboratory,
Ahmedabad 380009,
India.

Date:

Declaration

I declare that this thesis report represents my own ideas in my own words, and I have included others' ideas with appropriate citations from original sources. I also declare that I have followed all principles of academic honesty and integrity and have not misrepresented, fabricated or falsified any idea/fact/source/data in my submission. I understand that any violation of the above can cause disciplinary action by the Institute and can also evoke penal action from the sources which have thus not been properly cited or from whom proper permission has not been taken when needed.

Santunu Kumar Panda

Date:

(Roll No.: 19330015)

Dedicated to
my Family, Teachers, and Friends

It is not the perfect lattice; it is the defects in lattice that make the crystal luminous. Defects are part of life.

Acknowledgements

My PhD is a transformative journey from who I was in 2019 to who I have become in 2024. It has been shaped and enriched by the support, guidance, and kindness of many individuals who have left a lasting impact on my life and thought process. This journey has taught me that life's hardships often deepen our sense of kindness.

First and foremost, I am profoundly grateful to my family: my Baba (father), my Bou (mother), and my two wonderful sisters (Anee and Khushi). From my father, I learned the value of hard work and resilience. Their unwavering love, encouragement, and wisdom sustained me through the most challenging times.

I extend my heartfelt thanks to Prof. Singhvi for his invaluable mentorship, his insights into the scientific process, and his encouragement to question deeply. His guidance has been instrumental in shaping my scientific thinking. I am also grateful to Anita Madam, whose delicious meals and life advice made me feel at home despite being 2000 kilometres away from my own family. The lab itself became a place of inspiration, with its well-cared-for instruments reminding me of the meticulous work of Prof. Singhvi and his team. Their legacy lives on in the equipment and space they created.

I am grateful to my supervisor, Dr. Naveen Chauhan, for entrusting me with a significant research topic and providing the freedom and support I needed. My sincere thanks to Prof. R.P. Singh for his belief that "every person is unique," which motivated me throughout. I also thank my DSC members, Dr. M.K. Shrivastava, Dr. Vineet Goswami, and Dr. B. Sivaraman, for their valuable guidance. Special thanks to the Director of PRL, Prof. Anil Bharadwaj and Prof. Bijoy Sahoo for their trust and support.

I would like to acknowledge the contributions of my lab mates and colleagues. Special thanks to Dr Rahul Kaushal, Dr Saptarshi, Dr Sukumar Parida, and Dr Kartika Goswami for their support. To my lab mates, Dr. Monika and Malika, thank you for your insightful discussions. Thanks to Dr Suchinder Sharma and Ankit for collaboration. A heartfelt thanks to Dr. Raja, whose humour, camaraderie, and elder-brotherly presence brightened many challenging days and made this journey truly memorable.

Thanks to batchmate and hostellers Swagatika, Birendra, Kimi, Saumya, Vardaan, Vineet, Bharathi, Yogesh, Meghna, Arijit, Narayan, Guru, Wafikul, Arup, Trinesh, Rahul, Akash, Sahil and Ishwarya and all the hoteliers whom I missed in the list for their presence thanks so much for making the journey beautiful.

A note of gratitude to Shaina for friendship and emotional support during submission phase. I also cherish the memories of my beloved pets, especially Chiau Chiau (a baby jungle pedler) and my fishes, whose companionship brought me joy.

I thank the staff and departments at PRL—Library (Nistha maam, Pragnya ji, Alam ji, Ayush), Workshop (Baghela ji, Bipul bhai, Rohit), CMD, Purchase (Nandini maam, Mantu), and Stores—for their assistance and friendly support throughout this journey and CISF for protective environment. I also wish to acknowledge modern technology for its support in

various stages of this work. I want to thank IITGN for using instruments and updated of new technologies.

Finally, my heartfelt thanks to the philosophers and deep thinkers whose wisdom broadened my perspectives and guided my personal growth. This journey has taught me that transformation comes from within. Embracing the hardest moments allowed me to discover the best version of myself. I want to thank to me for being best friend with me.

Thank you to everyone who made this journey possible.

Abstract

The thesis investigates the potential of quartz luminescence as a tool for sediment tracing in natural systems. Over the last five decades, the luminescence properties of natural minerals have been extensively utilised as a dating method for Quaternary research. Among these minerals, quartz is the most widely used due to its well-characterised luminescence properties, no fading, abundance, and resilience to weathering. Quartz's luminescence properties are determined by structural defects, which are influenced by magma composition and thermodynamic conditions during crystallisation. The presence of variable concentrations and types of impurities results in unique luminescence characteristics in quartz, making it suitable for provenance studies.

Luminescence is emitted when pre-irradiated quartz is stimulated by heat or light. At a linear heating rate, this produces thermoluminescence (TL), characterised by a glow curve with multiple peaks, each corresponding to trap groups with distinct trap depth and frequency factors. When stimulated with constant or linearly ramped optical power, the resulting luminescence is referred to as continuous wave optically stimulated luminescence (CW-OSL), which appears as a decay signal, or linearly modulated optically stimulated luminescence (LM-OSL), which exhibits multiple peaks. These OSL signals contain traps with distinct photoionisation cross-sections (PICS). By separating the TL peaks or OSL components, specific trap groups with unique physical characteristics can be identified associated with different luminescence parameters. These features make luminescence a robust multiproxy system for provenance studies.

Past studies have shown that a grain's luminescence properties are influenced by the natural conditions it encounters during transport, recording its journey from mineral crystallisation to the time of measurement. However, several gaps limit the full potential of luminescence in provenance research and earth surface process studies. Some of these include:

1. Transportation Processes:

Limited understanding of the mechanisms behind luminescence property changes during sediment transport. To simulate natural transportation processes, quartz samples with dull, medium, and high luminescence sensitivities were subjected to laboratory treatments, including annealing, high-dose irradiation, prolonged solar exposure, and UV exposure. The effects of these treatments were evaluated by systematically recording changes in luminescence parameters, which are linked to modifications in the traps or defects within the crystal structure.

Annealing significantly enhances 110 °C TLS, increasing 80-fold in dull samples and 3–6-fold in bright samples, while irradiation increases TLS by 7-fold in dull samples and 2–3-fold in bright samples. UV and sunlight exposure reduces TLS, with the bright sample showing a maximum reduction of 0.55 of its natural value. Similar trends are observed for BSLS. LM-

BSL signals show two components: annealing activates new defects in dull samples, while irradiation activates two new defects in all samples. Sunlight and UV exposure do not alter these components but consistently reduce TL peaks.

Annealing reduces broad TL peaks around 300 °C, while irradiation decreases peaks in dull and medium samples but increases them in bright samples in the 200–300 °C range. Sunlight and UV exposure consistently reduce TL peaks. Light-sensitive and light-insensitive components behave differently under treatments, with annealing and UV reducing the light-insensitive part, while irradiation slightly enhances the 200–300 °C range in bright samples.

These findings highlight how luminescence parameters change along transport pathways, with signals like BSLS and 110 °C TLS reflecting natural factors. Unique behaviours of other components record distinct environmental conditions, offering insights into past influences. These results underscore the potential of luminescence as a multiproxy system for tracing sediment origins and reconstructing past environmental influences.

2. Defect Dynamics:

Although it is known that defects in the quartz lattice influence luminescence and there are structural changes in quartz lattice during its antiquity, yet the mechanisms linking luminescence changes to structural modifications are poorly understood.

In high-temperature annealing, the quartz at 220 °C, 400 °C, and 550 °C enhances TLS and BSLS, but sensitivity decreases beyond natural levels at 700 °C–900 °C due to structural changes during the alpha-to-beta quartz phase transition at 573 °C. Sensitivity partially recovers after repeated heating at 450 °C but not for samples annealed at 900 °C, indicating permanent lattice damage. These findings highlight the role of structural rearrangements in luminescence behaviour.

Thermogravimetric Analysis (TGA) revealed noticeable mass loss in dull and medium quartz samples, while bright quartz exhibited minimal mass loss. This suggests that structural water-related defects, such as silanol groups, may be converted to water vapour during heating (Bambauer et al., 1969). The DSC analysis reveals three distinct thermal regions: up to 200 °C, 200–420 °C, and beyond 600 °C, suggesting chemical reactions or phase changes in the quartz samples highlight changes in crystal properties around 200 °C, 420 °C, and 620 °C. These thermal regions align with the luminescence changes observed during heating, highlighting the critical role of structural changes in determining sensitivity.

In the FTIR analysis, it is observed that dull quartz exhibits significantly higher absorbance in the O-H vibrational range, whereas bright quartz shows comparatively lower absorbance. These results are consistent with the findings of S. K. Sharma et al. (2017) and suggest the potential role of O-H groups acting as luminescence quenchers. This observation is further supported by TGA results, which indicate a mass loss likely corresponding to the release of water associated with these O-H groups. The crystallinity index study reveals dull quartz has higher crystallinity and lower luminescence, while bright quartz shows the opposite. This suggests either transportation-induced amorphisation or increased impurities reduce crystallinity and enhance luminescence.

Understanding these factors provides valuable insights into the mechanisms underlying luminescence behaviour, with implications for luminescence changes in natural environments and the processes driving these variations. Overall, the chapter provides insights into the interplay of thermal processes, water content, and crystal structure in determining quartz's luminescence behaviour.

3. Application in earth surface process:

There is a lack of comprehensive studies quantifying sediment budgeting and evaluating the applicability of luminescence in complex environmental settings, such as hillslope processes. Additionally, the relationship between grain morphology (e.g., roundness and sphericity) and luminescence sensitivity remains poorly understood. Furthermore, limited research has been conducted on using luminescence for provenance analysis in the Indian context, particularly within its diverse and complex geological environments.

Sediment budgeting at confluences was successfully achieved using multiple luminescence parameter measurements (205 °C TL, annealed 90 °C TL, annealed 135 °C TL, and BSLS). For artificially mixed samples, the measured contributions closely matched applied proportions, validating the approach for natural systems. At the Nubra-Shyok confluence, present-day contributions from the Nubra River were estimated at 19% to 24%. In the Beas River system, a tributary contributed 24% to 36% of sediment load. A three-body mixing model effectively quantified additional hill slope contributions in the Wakal River system, with unknown luminescence parameters indicating a maximum input of approximately 54%.

The study also focuses on two fluvial systems: the Sabarmati River, characterised by its seasonal flow and semi-arid setting, and a section of the Yamuna River. It provides insights into fluvial sediment transport across a broad floodplain, assessing the influence of transport distance and exploring the impact of aeolian input on the luminescence properties of quartz in semi-arid river environments. These results of the Sabarmati River showed a broad co-variation between 110 °C TLS (thermoluminescence sensitivity) and BSLS (blue light stimulated luminesce sensitivity). Rock samples exhibit TLS values ranging from 1.6 to 6.2 units, weathered rock samples range from 5.9 to 15.6 units, and sediment samples show significantly higher TLS values ranging from 66 to 325 units. OSL analysis suggests a 3.8-fold sensitisation over the 18 Gy of equivalent dose difference, implying the effect of pedoturbation on quartz's luminescence sensitivity. Recycling experiments involving dose and bleaching cycles suggest that sediment 110 °C TLS evolved from rock 110 °C TLS over a timescale of more than a million years. The analysis concludes that transport distance alone does not influence luminescence sensitivity (110 °C TLS and BSLS) in the Sabarmati River. Instead, aeolian

input, hillslope contributions, and confluence effects significantly impact luminescence sensitivity. Conversely, the Yamuna River along the floodplain shows no increasing trend in luminescence sensitivity across a transport distance of 200 km, likely due to the rapid transport of quartz grains in this system.

This thesis also tried to find the relation between grain shape and luminescence. Although initial hypotheses suggested that sphericity and roundness could influence luminescence sensitivity, no clear trends were observed, implying that intrinsic mineral properties may be more significant. Overall, luminescence sensitivity proves to be a valuable tool for provenance studies, provided that interpretations consider environmental and geological complexities, offering a solid foundation for future research in dynamic sedimentary systems.

In conclusion, this thesis explores the fundamental question of how natural processes influence the luminescence properties of quartz grains. It also examines the relationship between luminescence sensitivity and the crystal domains of quartz. Additionally, the study evaluates the applicability of quartz luminescence in natural environments, with an emphasis on variations in luminescence sensitivity within fluvial systems, its role in sediment budgeting in river confluences.

Keywords: Luminescence; TL; OSL; quartz; structural defects; O-H defects; annealing; irradiation; sun exposure; UV exposure crystallinity; provenance; luminescence sensitivity (LS); sediment budgeting; sediment transport; Sabarmati River; Yamuna River: Beas River; Nubra River; Shyok River; grain morphology; fluvial processes; earth surface process.

Table of contents

List of figures

Chapter 1: Introduction

Chapter 2: Technical information and methodology

Chapter 3: Natural factors affecting the sensitivity of quartz

Chapter 4: Exploring luminescence variations in quartz and their relation to structural defects

Chapter 5: Luminescence: a proxy for earth surface studies

List of Tables

Chapter 1: Introduction

Chapter 2: Technical information and methodology

Chapter 3: Natural factors affecting the sensitivity of quartz

Chapter 4: Exploring luminescence variations in quartz and their relation to structural defects

Chapter 5: Luminescence: a proxy for earth surface studies

Abbreviations

Abbreviation	**Full Form**
ATR	Attenuated Transmitted Reflectance
BSL	Blue Stimulated Luminescence
BSLS	Blue Stimulated Luminescence Sensitivity
CB	Conduction Band
CH	Cut heat
CW-BSL	Continuous Wave Blue Stimulated Luminescence
CW-OSL	Continuous Wave Optically Stimulated Luminescence
DSC	Differential Scanning Calorimetry
ESR	Electron Spin Resonance
FTIR	Fourier Transform Infrared Spectroscopy
Gy	Gray, SI unit of radiation dose (1 Gy is 1 Joule received per 1 kg of material)
IRSL	Infrared Stimulated Luminescence
LED	Light Emitting Diode
LM-BSL	Linearly Modulated Blue Stimulated Luminescence
LM-OSL	Linearly Modulated Optically Stimulated Luminescence
LS	Luminescence Sensitivity
NBOHC	Non-Bridging Oxygen Hole Center
OSL	Optically Stimulated Luminescence
OTOR	One Trap One Recombination
PH	Pre heat
PMT	Photo Multiplier Tube
POR	Peroxy Radicals
SG	Single Grain
SS	Stainless Steel
TGA	Thermo Gravimetric Analysis
TL	Thermoluminescence
TLS	Thermoluminescence Sensitivity
UV	Ultraviolet
VB	Valence Band
XAS	X-ray Absorption Spectroscopy

Chapter 1

1. Introduction

1.1 Background

The Earth's surface is in a constant state of transformation due to sediment transport and deposition. Quantifying these processes in dynamic fluvial systems is essential for understanding the movement of eroded materials from their sources to depositional sinks. Such insights are crucial for studying landscape evolution (Tucker & Hancock, 2010), river morphology and dynamics (van Rijn, 1993), and the long-term sustainability of reservoirs (Syvitski et al., 2005; Papanicolaou et al., 2008). Commonly used proxies, such as grain size distribution, mineralogical, heavy mineral compositions, and isotope systematics, aid in reconstructing source lithologies, sediment production rates, and transport pathways (Basu et al., 1990; Morton, 1985; Weltje & von Eynatten, 2004). These inferences are then interpreted in the context of tectonic and climatic forcings. A promising addition to sediment tracing and fingerprinting techniques is luminescence, a method based on trapped charge phenomena, with particular emphasis on quartz. Quartz luminescence is especially advantageous because it is applicable to fine and very fine sand, which are often dominant in sedimentary environments and has low susceptibility to weathering and high preservation potential. quartz luminescence has the benefit of low weathering rates and high preservation potential over long timescales. Quartz luminescence stands out due to its high analytical sensitivity, cost-effectiveness, and non-destructive nature, making it easy and inexpensive to quantify. Additionally, as quartz luminescence acts as a multiproxy system, it enables cross-checking for reliability and effectively records transport information. A detailed discussion of the theoretical aspects of the multiproxy system will be presented in Chapter 2.

Luminescence techniques have been extensively used for dating Quaternary sediments over the past five decades. These studies have revealed significant variations in quartz luminescence properties across different locations. This raised the question of whether luminescence could serve as a fingerprinting tool for sediment sources. In the last two decades, researchers have applied luminescence to natural systems, comparing it with other proxies, and have established its potential as a provenance tool. Quartz luminescence properties, such as sensitivity, characteristic dose, and LM-OSL components, have also been used to infer sediment pathways and transport processes (Gray et al., 2019; Jeong & Choi, 2012; Sawakuchi et al., 2020; Tsukamoto et al., 2010).

Quartz luminescence properties are influenced by thermodynamic conditions and fluid composition during rock formation (Sawakuchi et al., 2010). Physical and chemical weathering (Cao et al., 2022; Tanski et al., 2024) of parent rocks, followed by erosion and deposition cycles, further modifies their luminescence properties. Preliminary findings suggest that fluvial quartz grains exhibit significantly higher TL and OSL sensitivity than source rocks (Guralnik et al., 2015) and that OSL sensitivity increases as sand grains are transported farther (Pietsch et al., 2008). Experimental studies have shown that processes like irradiation and heating impact the luminescence sensitivity of quartz (Li, 2002). Notable research by Lü and Sun (2011) has highlighted the influence of grain size on luminescence sensitivity, while Chauhan and Singhvi (2019) observed heterogeneity in luminescence characteristics within individual grains during measurement. Limited studies have investigated the potential of thermoluminescence (TL), particularly high-temperature TL peaks, and optically stimulated luminescence (OSL) sensitivity, especially its components, as tools for inferring sediment provenance and transport history. Additionally, there is a lack of understanding regarding the reasons behind their changes in natural settings.

This thesis explores the application of quartz luminescence in natural systems for sediment tracing, with a focus on its potential in provenance research and earth surface processes. It investigates the fundamental question of **how natural processes influence the luminescence properties of quartz grains**. The study also investigates the **correlation between luminescence sensitivity and structural defects within quartz**. Additionally, the study evaluates the **applicability of quartz luminescence across diverse geological settings**, focusing on variations in luminescence sensitivity within fluvial systems, such as the Sabarmati and Yamuna Rivers. The multiproxy system enhances reliability by enabling cross-verification for sediment budgeting in natural river confluences, such as the Nubra-Shyok and Beas River confluences. Furthermore, the relationship between quartz luminescence and grain morphology is explored. The primary objective is to advance this technique and broaden its applications, offering new insights into the earth's surface processes.

1.2 Luminescence

Luminescence is the emission of light by a material that has absorbed energy, typically from irradiation and is distinct from incandescence. The type of energy that stimulates the emission determines the specific form of luminescence. For example, photoluminescence occurs when the material is excited by optical or ultraviolet light, radioluminescence is triggered by nuclear radiation (e.g., gamma rays, beta particles, X-rays), and cathodoluminescence results from excitation by an electron beam. Beyond radiation-induced luminescence, other forms include chemiluminescence (generated by chemical reactions), triboluminescence (from mechanical energy), electroluminescence (from electrical energy), bioluminescence (from biochemical reactions), and sonoluminescence (induced by sound waves) (McKeever, 1985).

Light emission occurs at a characteristic time (τ_c) following the absorption of radiation, and this parameter is used to classify the type of luminescence process. Fluorescence is defined by $\tau_c < 10^{-8}$ s, whereas phosphorescence is characterised by $\tau_c > 10^{-8}$ s (Garlick, 1949). Phosphorescence can be further categorised into short-period and long-period luminescence. The present thesis focuses on thermoluminescence, which is a form of long-period phosphorescence ($\tau_c > 10^{-8}$ s).

1.2.1 Luminescence Mechanism in insulators: Energy band mode

Luminescence in insulator material can be explained using the band theory of solids (Fig. 1. 1). The energy levels of the valence band are filled at room temperature, while those in the conduction band are empty. Natural minerals like quartz exhibit a band gap of approximately 9.5 eV (Güler et al., 2020; Vella et al., 2011). In the ideal crystals, no energy states are allowed in the forbidden gap.

However, during natural crystallisation from magma, impurities are incorporated into the host lattice. The incorporation of these impurities depends on factors such as their concentration, charge, ionic radii, and the thermal and chemical environment during crystallisation. These impurities disrupt the periodicity of the crystal lattice, leading to the formation of discrete energy levels within the forbidden band. These energy levels act as "traps" that can capture electrons or holes. Electron traps typically exist above the Fermi level, while hole traps lie below it, both playing a critical role in the luminescence properties of quartz.

Excitation of electron-hole (e-h) pairs in a crystal requires radiation with energy exceeding the material's band gap. Ionising radiation transfers energy to ionisations until the initial energy is fully dissipated. Charged particles deposit energy primarily via coulomb interactions with the medium. The energy deposition mechanisms differ based on particle type. Due to their higher mass, alpha particles follow straight trajectories within a crystal with a short range of approximately 0.005 mm/MeV. In contrast, beta particles, being much lighter, have longer ranges of about 1 mm/MeV. High-energy photons interact with the medium primarily through the photoelectric effect, Compton scattering, and pair production (Levy, 1974), generating charged particles that contribute to further energy deposition. The total irradiation received by a material is referred to as the dose. The dose is defined as the amount of energy deposited in a material by ionising radiation, measured in Gray (Gy), where 1 Gray corresponds to 1 joule of energy absorbed per kilogram of material.

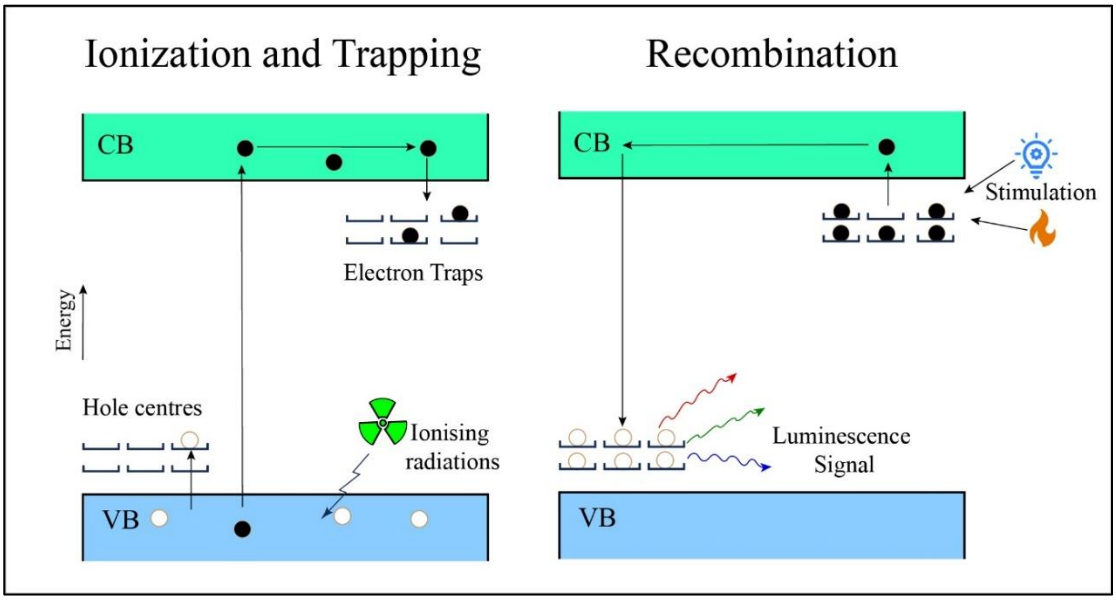

Fig. 1. 1: (left)Mechanism of luminescence ionisation and trapping of electrons and holes at localised energy state, (right) release of luminescence signal after external stimulation like heat and light (CB - Conduction Band & VB - Valence Band).

The excited electrons and holes, generated by ionising radiation, become trapped at defect or trap centres within the crystal lattice. The lifetime of these trapped charges depends on the local charge environment, specifically the binding energy at the trapping site, referred to as the trap depth (E). The lifetime can be expressed as in Equation 1.1.

$$\tau = s^{-1} \exp(E/kT) \tag{1.1}$$

Where s is the frequency factor (of the order 10^9 to10^{16} sec^{-1}) (Aitken, 1985), E is the trap depth, k is the Boltzmann constant, and T is ambient temperature. For quartz, the trap depth generally ranges from 0.5-2.0 eV.

When a pre-irradiated insulating crystal is stimulated by heat or light, the trapped charges are released, resulting in the emission of radiation. This phenomenon is called thermoluminescence (TL) when stimulated by heat and optically stimulated luminescence (OSL) when stimulated by light.

1.2.2 Thermoluminescence (TL)

When a pre-irradiated crystal is stimulated with heat, the light that is emitted is called thermoluminescence. If the temperature increases linearly over time, the luminescence intensity plotted against temperature produces a TL glow curve (Fig. 1. 2). The peaks in a TL glow curve represent trap depths, with lower trap depths corresponding to lower temperature peaks. Quartz exhibits fundamental TL peaks at ~ 85, 110, 190, 230, 240, 310, 325, and 375 °C (Aitken, 1985).

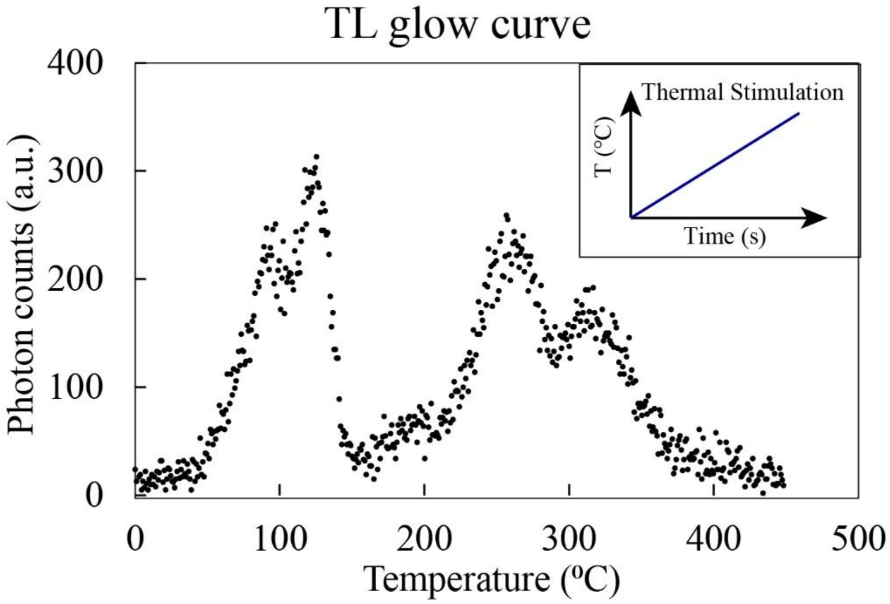

Fig. 1. 2: TL glow curve, with thermal stimulation curve shown as an inset.

1.2.3 Optically Stimulated Luminescence (OSL)

OSL occurs when a pre-irradiated crystal is stimulated by light, resulting in the release of trapped electrons and the emission of luminescence. If the crystal is stimulated using constant-intensity light, the resulting luminescence is termed continuous wave OSL (CWOSL), which produces a decay curve (Fig. 1. 3). The OSL signal typically comprises multiple components, categorised as ultra-fast, fast, medium, slow1, slow2, and slow3 decay curves. These components are distinguished based on the photoionisation cross-sections (PICS) of the associated electron traps and the stimulation wavelength used (Bailey et al., 1997; Choi et al., 2006; Jain et al., 2003; Singarayer and Bailey, 2003). The fast components arise from traps that exhibit high sensitivity to the stimulation wavelength, whereas slow components correspond to traps with progressively lower sensitivity.

Alternatively, when the light intensity increases linearly during stimulation, the resulting luminescence is known as linearly modulated OSL (LMOSL), which produces a peak-shaped curve (Fig. 1. 4) (Bulur et al., 2000). Each LMOSL peak corresponds to a specific group of electron traps, characterised by a unique photoionisation cross-section (PICS).

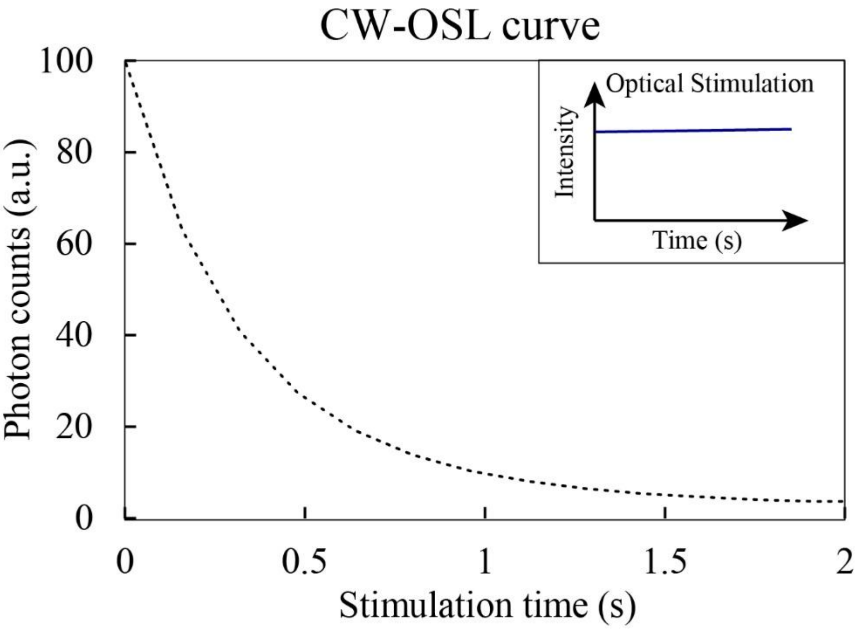

Fig. 1. 3: CW-OSL curve, with optical stimulation curve shown as an inset.

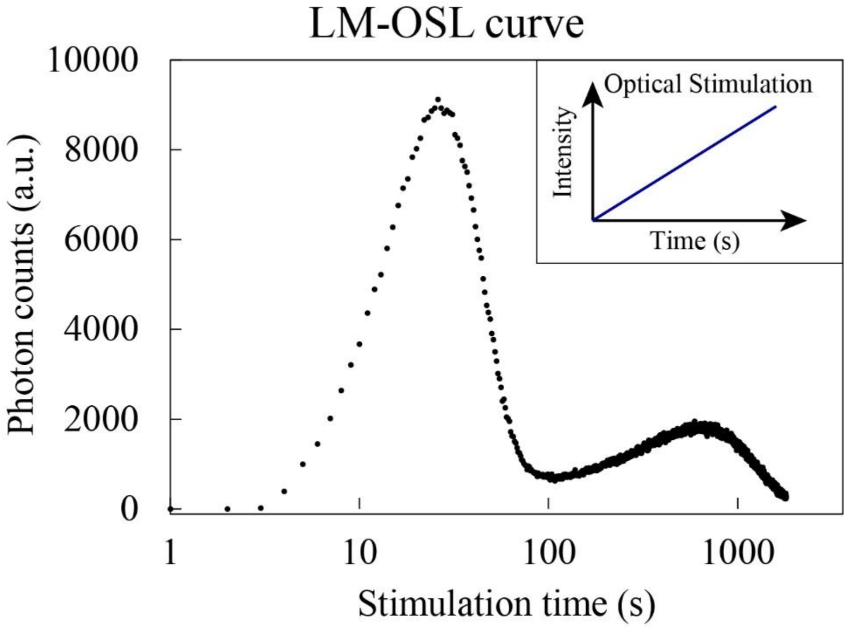

Fig. 1. 4: LM-OSL curve, with optical stimulation curve shown as an inset.

The separation of TL peaks and the components of CWOSL and LMOSL enables the characterisation of distinct trap groups (or impurities) within quartz, referred to as **luminescence parameters**. The presence of multiple luminescence parameters makes quartz luminescence a valuable multiproxy system for provenance studies. Detailed methods for trap separation of TL and OSL and their associated mathematical models are presented in Chapter 2.

1.3 Structure and defects in quartz crystals

Quartz is the second most abundant and widespread mineral on the earth's surface. It is a common mineral found in various igneous (both plutonic and volcanic), metamorphic, and sedimentary rocks. Silica (SiO_2) constitutes approximately 12.6 weight% of the earth's crust as crystalline and amorphous phases. Quartz is composed exclusively of $[SiO_4]^{4-}$ tetrahedra, with all oxygens joined together in a three-dimensional network. Thus, the formula is SiO_2; the atoms are arranged in a trigonal symmetry. Quartz exists in two primary structural forms, known as alpha (α) quartz and beta (β) quartz, which differ based on the temperature of stability and show varied symmetry and physical properties (Götze & Zimmerle, 2000) detailed in Table 1. 1.

Table 1. 1: Physical properties of alpha and beta quartz

Physical properties	**Alpha quartz (Low quartz)**	**Beta quartz (High quartz)**
Stability	below 573 °C	Above 573 °C
Crystal structure	Trigonal-trapezohedral	Hexagonal-trapezohedral
Lattice parameters	a_0=4.91 Å, c_0=5.41 Å	a_0=5.00 Å, c_0=5.46 Å
Bond lengths	Si-O = 1.61 Å, O-O = 2.65 Å, Si-Si = 3.04 Å	Si-O = 1.60 Å, O-O = 2.65 Å, Si-Si = 3.03 Å
Bond angle	Si-O-Si = 144°	Si-O-Si = 153°
Lattice energy	12,967–15,043 kJ/mol	13,596 kJ/mol
Hardness (Mohs scale)	7	7
Specific gravity	2.65 g/cm³	2.51 g/cm³

The transition from alpha to beta quartz is reversible and is accompanied by slight changes in bond angles and distances, impacting the physical properties of the crystal. This transition is important for understanding quartz's behaviour under varying temperature conditions, which also influences its luminescent properties.

Ideal crystals practically do not exist. The thermodynamic condition influences the type and concentration of lattice defects during the mineralisation. Lattice defects in quartz are categorised by structural characteristics, including point defects, linear defects, planar defects, and volume defects. Quartz often incorporates point defects that involve foreign ions occupying lattice sites or interstitial positions, displaced atoms, or vacancies associated with silicon or oxygen atoms. Intrinsic point defects are present in any ideal crystal above zero Kelvin, and their concentration can be estimated from the equation.

$$c_D = \exp\left(-\frac{\Delta G_D}{kT}\right) \qquad 1$$

C_D represents the defect concentration, ΔG_D is the Gibbs free energy of defect formation, T is the absolute temperature, and k is the Boltzmann constant (cf. Bohm, 1995).

The structural positions and orientations of these defect centres are governed by their interactions with the surrounding lattice, which affect electron–hole dynamics and lead to the wide range of colours observed in both natural and synthetic quartz. These defects can be intrinsic or impurity-related, as illustrated in Fig. 1. 5. They are commonly characterised using EPR spectroscopy, together with complementary methods such as luminescence spectroscopy, UV–Vis–IR absorption spectroscopy, synchrotron-based X-ray absorption spectroscopy (XAS), Mössbauer spectroscopy, and trace element analysis.

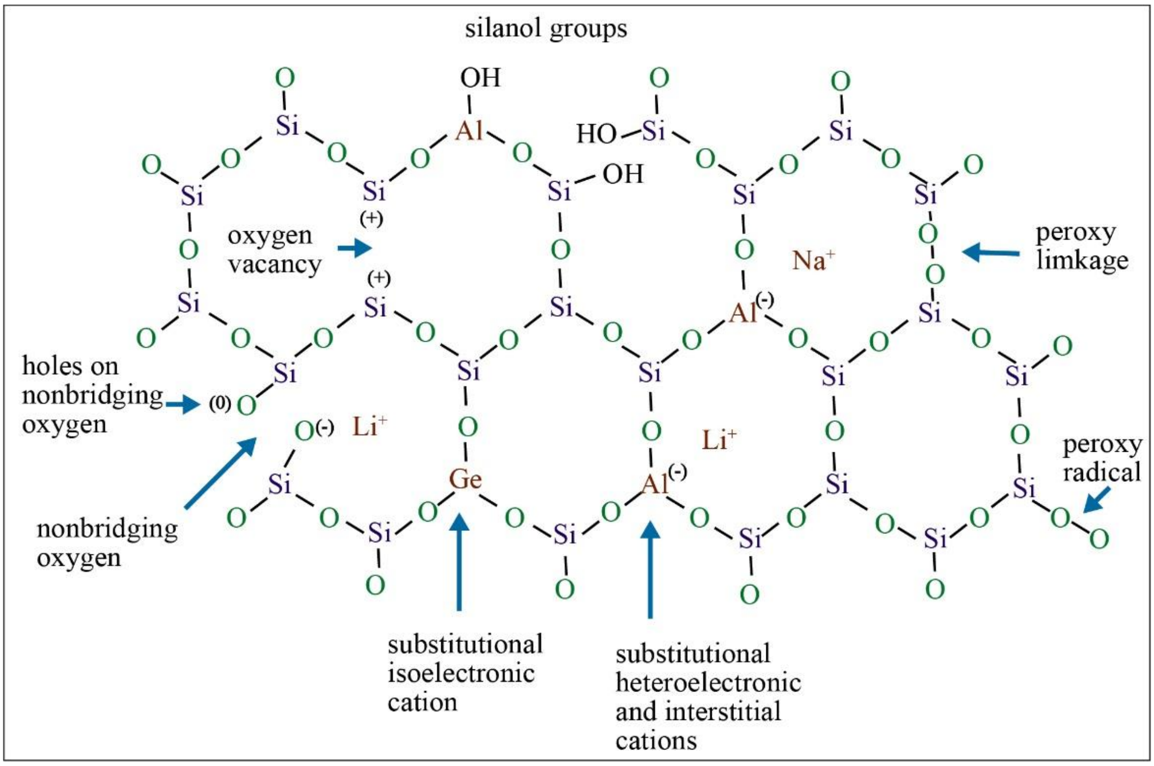

Fig. 1. 5: Schematic quartz structure showing the most common intrinsic and extrinsic lattice defects. (Redrawn after Götze et al. (2001))

Oxygen excess centres, such as Non-Bridging Oxygen Hole Centres (NBOHC) and Peroxy Radicals (POR), have been identified in neutron-irradiated quartz (Skuja, 2000). NBOHC features a dangling bond with an unpaired electron in an oxygen orbital unlinked to silicon. POR is a paramagnetic defect where the unpaired spin is shared between two oxygen atoms bonded to a single silicon atom. Silicon vacancies are less well-characterised but can host hydrogen ions, forming complexes like H_3O_4 and H_4O_4, linking these vacancies to hydrogen-related defects such as hydrogarnet (Paterson, 1986).

These defects result from electron trapping within the tetrahedral SiO_4 framework and significantly influence quartz's optical properties, including UV absorption bands (207–218 nm). Such intrinsic defects are especially prominent in irradiated quartz samples (Marfunin, 1979).

1.3.1 Impurity-related defects

Substitution of silicon atoms in the lattice is rare because of the small ion radius of Si^{4+} (0.42 A) and the high valence. So far, Al^{3+} (0.51 A), Ga^{3+} (0.62 A), Fe^{3+} (0.64 A), Ge^{4+} (0.53 A), Ti^{4+} (0.64 A), and P^{5+} (0.35 A) have been detected as substitutes (Krbetschek et al., 1997). The defects Al^{3+} is by far the most common and typically the most abundant. Where Al placed as $[AlO_4]^0$ and its precursor state $[AlO_4/M^+]^0$ with an adjacent charge compensating cation (M^+=H^+, Li^+, Na^+) at an interstitial position in the c-axis channel (Götze et al., 2021). These defects Ti and Fe have a higher concentration in high temperature early formed quartz, whereas P, Ge, Al and Li are more likely to be found in low temperatures in evolved melts and pegmatite. These impurities are the base of the luminescence production of the crystal, and their variations make the luminescence signal of quartz unique.

1.3.2 Luminescence spectral emissions and probable defects

Specific emission bands in quartz luminescence are linked to recombination processes at hole centres. Various techniques, including cathodoluminescence (CL), radioluminescence (RL), photoluminescence (PL), and thermoluminescence (TL), are used to correlate the spectral emissions observed in quartz with specific wavelength ranges and associated defects within the crystal lattice. According to Krbetschek et al. (1997), the primary spectral ranges and their probable defect centres are as follows:

- 330–390 nm: Associated with {$(H_3O_4)^0$, E', $[AlO_4/M^+]$, $[TiO_4/Li^+]$}.
- 420–580 nm: Linked to {STE, $[AlO_4]^0$, $[GeO_4/M^+]^0$}.
- 620–700 nm: Attributed to {NBOHC, E', Peroxy linkage, Fe^{3+}}.

-

1.4 Provenance

Provenance comes from the French word *provenir*, which means "to come from," provenance is the history of ownership of a valued object, such as a work of art. In Earth sciences, provenance refers to identifying the source of sediments to monitor crustal evolution. The primary goal of provenance studies is to reconstruct tectonic, paleo-geographic, and paleo-climatic histories, contributing to the broader understanding of the earth's lithospheric evolution. Reconstruction of the lithospheric history of the earth includes-

- The source of the particles that make up the rocks,
- The erosion and transport mechanisms that moved the particles from source areas to depositional sites,
- The depositional setting and depositional processes responsible for the sedimentation of the particles (the depositional environment) and
- The physical and chemical conditions of the burial environment and diagenetic changes that occur in siliciclastic sediment during burial and uplift.

Provenance studies reveal information about sediment sources, rates and directions of sediment transport, residence times, and depositional areas. It addresses some essential questions, such as how a landscape produces sediments and how geomorphic processes modulate the sediment fluxes. It has implications for reservoir design (Tobin & Schwarzer, 2013), erosion management (Jain et al., 2022), and archaeological reconstruction (Harbottle, 1988; Jung et al., 2015; Pollard & Liu, 2023). These studies are helpful in predicting natural or human-induced landscape evolution, as well as paleoclimatic and tectonic changes from the stratigraphic records. Rivers, as primary sediment transport systems, play a critical role in moving sediments, nutrients, and pollutants from higher elevations to the basin outlets via channels and are thus useful for provenance studies.

1.4.1 Proxies of provenance studies

Provenance studies utilise a wide range of proxies to uncover the origin and evolution of sedimentary materials. These proxies provide crucial insights by linking sediments to their source rocks while accounting for the effects of transport, weathering, and depositional processes. Key approaches include petrographic analysis, geochemical methods, single-grain studies, and textural characterisation, which facilitate the detailed reconstruction of sediment provenance and evolutionary pathways (Weltje & von Eynatten, 2004).

Proxies for provenance studies include chemical analysis of bulk mineralogy, bulk chemistry, and isotopic ratios (Garver et al., 1996; Bock et al., 2000) and heavy mineral assemblages (Morton et al., 2012). Radiometric dating of single detrital minerals (von Eynatten and Wijbrans, 2003) and bulk sediment Nd and Sr isotope analyses (Goldstein et al., 1984) provide valuable insights into sediment sources. Concentrations of zircon, tourmaline, and rutile (ZTR-index; Hubert, 1962) are also widely used as provenance indicators. Advanced microscopic techniques, including SEM and CL analysis of quartz grains (Seyedolali et al., 1997; Dunkl et al., 2001), further enhance provenance studies by providing detailed information about sedimentary processes and sources.

Quartz, an abundant component of sedimentary systems, plays a crucial role in provenance studies. Various properties and parameters are routinely analysed to reconstruct its provenance, including colour, shape, internal structure, types of inclusions, geochemical characteristics, and cathodoluminescence. Internal crystallographic features, such as the type and size of primary grain intergrowths and undulatory extinction patterns, are recognised as reliable indicators of quartz provenance. Recently, luminescence techniques have gained prominence as a promising proxy, providing a novel and efficient approach for sediment provenance analysis. It is cost-effective, has high analytical sensitivity, and is a non-destructive tool for provenance studies.

1.5 Quartz luminescence and provenance

Quartz is an abundant mineral and highly resistant to weathering, allowing it to remain intact during its journey from source to sink. Quartz can record exposure to ionising radiation as a latent signal within its crystal lattice. Thermoluminescence (TL) and optically stimulated luminescence (OSL) detect these signals by measuring emitted photons by recombination of trapped electrons at trapped holes in the lattice defects.

Several studies have shown that the luminescence properties of quartz vary depending on impurities within its crystal structure. These properties are influenced by geological factors such as:

- Fluid composition of the magma – Variations in fluid composition result in different types of point defects in the crystal lattice (Götze, 2009).
- Crystallisation thermodynamic condition –Crystallisation temperatures and cooling rate influence the incorporation of impurities (Götze et al., 2021; Rink et al., 1993; Wark & Watson, 2006).
- Erosion and deposition events – Sedimentary processes, including irradiation, bleaching, and heating during erosion and deposition cycles, alter quartz crystal sensitivity (Pietsch et al., 2008).

Hashimoto et al. (1986a, 1986b, 1989), Rink et al. (1993), and Kuhn et al. (2000) reported distinct thermoluminescence (TL) emission bands among quartz samples from different provenances, revealing source-dependent spectral diversity. Variations in linearly modulated OSL (LM-OSL) spectra were later shown to effectively discriminate quartz types, providing a reliable basis for fingerprinting (Tsukamoto et al., 2010). Götte and Ramseyer (2012) demonstrated that the elemental composition of quartz varies with its formation environment: aluminium, lithium, and hydrogen dominate in authigenic, hydrothermal, and metamorphic quartz, whereas magmatic quartz is typically enriched in titanium, with trace amounts of germanium, iron, boron, and sodium. Subsequent investigations have explored the luminescence characteristics of quartz across different geological settings.

Sawakuchi et al. (2010) found that quartz from high-temperature source rocks exhibits higher inherent OSL sensitivity, which can be further enhanced through sedimentary processes such as burial, erosion, and sunlight exposure. Lü and Sun (2011) used the 110 °C TL peak and OSL sensitivity as provenance indicators in Chinese deserts, demonstrating their dependence on grain size. Jeong and Choi (2012) observed that weathered bedrock retains slow OSL components with minimal sensitisation, whereas fluvial transport enhances the fast component; thermal metamorphism and recrystallisation, in contrast, reduce overall sensitivity. Sawakuchi et al. (2012) employed OSL sensitivity as a proxy to reconstruct storm activity along the southern Brazilian coast, identifying a positive correlation with heavy-mineral concentrations in sediments. Shimada et al. (2013) combined Thermoluminescence Colour Imaging (TLCI) and Electron Spin Resonance (ESR) to distinguish quartz from different sources, showing that volcanic quartz emits red TL, while granitic and sedimentary quartz emit blue. Zular et al. (2015) demonstrated that both TL and OSL sensitivities serve as robust provenance proxies, with the 110 °C TL sensitivity being more reliable because of its stronger correlation with grain size and heavy-mineral content. Sawakuchi et al. (2018) further showed that quartz OSL sensitivity inversely correlates with denudation rates, making it a valuable proxy for erosion intensity, source-area stability, and sediment dynamics. Nelson et al. (2022) highlighted that OSL effectively distinguishes transported sediments from in situ weathered bedrock, even in highly weathered conditions, underscoring its value in tracking quartz sensitisation within the critical zone. Goswami et al. (2023) showed that luminescence properties can quantify sediment provenance by distinguishing signals from different sources, using a two-component mixing model validated with natural and controlled samples. More recently, Tanski et al. (2025) demonstrated that quartz luminescence sensitivity increases with longer residence time in the critical zone. They found that modern alluvium exhibits higher OSL sensitivity than Late Pleistocene deposits, attributed to enhanced chemical weathering and prolonged near-surface exposure. Collectively, these studies establish luminescence as a versatile and reliable multiproxy approach for provenance and environmental reconstruction.

Since variations in quartz luminescence provide valuable insights into geological processes, understanding its natural variability is crucial for the accurate interpretation of sediment histories. Numerous studies have demonstrated that heating (Aitken and Smith, 1988; Bøtter-Jensen et al., 1995; Rhodes and Bailey, 1997; Rhodes, 2000; Wintle and Murray, 2000; Bailey, 2001), bleaching (Wintle, 1985; Bowall et al., 1987; McKeever, 1991; Li and Wintle, 1991, 1992; Morris and McKeever, 1993; Stokes, 1994; Zhou and Wintle, 1994), and irradiation (Zimmerman, 1971; Durrani et al., 1977; Stoneham and Stokes, 1991; Bailiff, 1994; Chawla et al., 1998; Benny et al., 2000) can significantly modify the luminescence sensitivity of quartz. Furthermore, several laboratory investigations have explored how such experimental treatments affect quartz luminescence behaviour. In particular, studies focusing on the bleaching–erosion cycle have revealed a progressive sensitisation process, wherein repeated bleaching and erosion enhance quartz sensitivity by approximately 2–6 times before reaching a stable saturation level (Moska, 2006; Pietsch et al., 2008; Cao et al., 2022; Soares et al., 2023; Moayed et al., 2023).

As observed, luminescence in quartz records the mineral's journey from its crystallisation to the time of measurement. However, several knowledge gaps still limit its full potential for provenance and Earth surface process studies:

Transportation processes: The mechanisms governing sensitivity changes during sediment transport remain poorly understood. Limited research exists on how irradiation, annealing, and ultraviolet exposure influence luminescence properties, making it challenging to apply luminescence effectively to landscape evolution studies.

Defect dynamics: Although it is known that defects in the quartz lattice influence luminescence and there are structural changes in quartz lattice during its antiquity, yet the mechanisms linking luminescence changes to structural modifications are poorly understood.

Applicability in natural systems: There is a lack of comprehensive studies quantifying sediment budgeting and evaluating the applicability of luminescence in complex environmental settings, such as hillslope processes. Additionally, the relationship between grain morphology (e.g., roundness and sphericity) and luminescence sensitivity remains poorly understood. Furthermore, limited research has been conducted on using luminescence for provenance analysis in the Indian context, particularly within its diverse and complex geological environments.

The objectives of this thesis are designed to address these gaps by advancing the understanding of luminescence properties, exploring their relationship with crystal structure, and enhancing their applications in geological and provenance studies.

1.6 Objectives

The primary aim of this thesis is to develop a physics-based understanding of quartz luminescence sensitivity and evaluate its application as a sediment tracer in fluvial systems. By addressing existing methodological and conceptual gaps, this research seeks to enhance the reliability of luminescence as a tool in sedimentary and geomorphological studies.

To fulfil this aim, the thesis is structured around three specific objectives, each targeting a distinct aspect of quartz luminescence to advance both fundamental knowledge and practical applications:

1. ***Investigate natural factors affecting the luminescence characteristics of quartz during its antiquity in nature.***

Sediments in natural environments are subjected to cycles of transport, burial, and erosion, during which quartz grains experience exposure to ionising radiation, sunlight, and heating. These factors are hypothesised to enhance luminescence sensitivity over time. This objective involves replicating such conditions in controlled laboratory settings to evaluate their effects on luminescence characteristics. The goal is to establish a connection between environmental exposure and changes in luminescence behaviour along the sediment's journey from source to sink.

2. *Role of structural defects of quartz crystal in its luminescence properties*

This objective focuses on the internal structure of quartz, particularly the influence of lattice defects, impurities, and water content on its luminescence response. Earlier studies have suggested a strong link between water diffusion and sensitivity development. In this work, high-temperature experiments are used to introduce water into the quartz lattice, followed by thermal and spectroscopic analyses. These investigations aim to track structural changes and correlate them with luminescence sensitivity across different quartz samples.

3. *Implications for provenance Studies*

This part of the thesis demonstrates how luminescence sensitivity can be used as a sediment tracer in natural systems. Case studies from the Sabarmati and Yamuna River basins are examined to determine sediment source contributions, transport dynamics, and the influence of hillslope and aeolian inputs. Additional analysis explores sediment budgeting and the relationship between grain morphology and luminescence sensitivity. These findings highlight the practical utility of quartz luminescence in understanding sedimentary processes and reconstructing provenance.

The thesis progresses from foundational laboratory investigations aimed at understanding the luminescence behaviour of quartz to applied case studies, thereby offering a comprehensive evaluation of quartz luminescence as a tool for studying Earth surface processes.

1.7 Thesis outline

Following the introductory Chapter 1, which outlines the motivation, background, and objectives of the study, the subsequent chapters are structured as follows:

Chapter 2: Instrumentation and experimental methods

This chapter details the laboratory procedures for sample collection and preparation for luminescence measurements. It describes the instrumentation techniques used for luminescence analysis and the measurement of luminescence parameters, including TL, CW-OSL, and LM-OSL. The focus is on analysing TL peaks to extract information about trap depth (τ) and electron population (n) associated with different types of traps. Additionally, CW blue light-stimulated luminescence (CW-BSL) and LM blue light-stimulated luminescence (LM-BSL) are employed to determine the photoionisation cross-section (σ) and the corresponding electron population (n), exploring their relationships with trapping and recombination centres. Finally, the chapter addresses thermal analysis techniques and infrared spectroscopic methods.

Chapter 3: Natural factors affecting the quartz luminescence

This study aims to identify luminescence parameters relevant to provenance studies and to infer the natural conditions experienced by quartz crystals. Quartz luminescence has recently been proposed as a sediment tracer. Research has shown that sediment sensitisation occurs during its transport and is influenced by sedimentary history and the source lithology of quartz (Fitzsimmons, 2011). In some cases, repeated deposition and reworking enhance the luminescence sensitivity of quartz (Pietsch et al., 2008). To simulate natural transportation processes, quartz samples with dull, medium, and high luminescence sensitivities were subjected to laboratory treatments, including annealing, high-dose irradiation, prolonged solar exposure, and UV exposure. The effects of these treatments were evaluated by systematically recording changes in luminescence parameters, which are linked to modifications in the traps or defects within the crystal structure.

Potential natural processes and their effect on luminescence properties of quartz (Panda, S. K., Chauhan, N.) (In preparation).

Chapter 4: Exploring luminescence variations in quartz and their relation to structural defects

This chapter investigates the factors influencing the luminescence sensitivity of quartz crystals, with particular emphasis on the effects of annealing, water diffusion, and structural modifications. Luminescence in quartz is governed by crystal defects, which are in turn influenced by the composition of the parent magma and the thermodynamic conditions prevailing during the formation of the source rock (Preusser et al., 2009). Quartz typically forms under hydrothermal conditions, where the presence of O-H bonds constitutes a prominent type of defect. Chemical analyses of natural quartz samples from various geological settings have demonstrated a negative correlation between water content within the crystal lattice and optically stimulated luminescence (OSL) sensitivity, underscoring the significant role of water in modulating luminescence properties (S. K. Sharma et al., 2017). To gain deeper insight into this phenomenon, high-pressure and high-temperature (HPHT) experiments aimed at quantifying water diffusion were initially attempted. However, due to challenges at high pressure conditions, high-temperature annealing experiments were conducted, where quartz samples were annealed between 220 °C and 900 °C and subsequently cooled both in the presence and absence of water to examine the thermal and hydration effects on luminescence sensitivity. Given the strong influence of heating temperature on luminescence behaviour, Thermogravimetric Analysis (TGA) and Differential Scanning Calorimetry (DSC) were employed to monitor mass loss and heat exchange during the high temperature. Additionally, Fourier-transform infrared spectroscopy (FTIR) was used to detect characteristic O-H vibrational modes, enabling quantification of hydroxyl defects. Overall, the chapter provides key insights into the interplay between thermal history, water incorporation, and crystal structure in governing the luminescence response of quartz, with implications for understanding natural variations in luminescence sensitivity.

Chapter 5: Luminescence: a proxy for earth surface studies

This chapter focuses on understanding sediment provenance and transport processes through the analysis of luminescence sensitivity. It presents a quantitative approach using luminescence parameters for sediment budgeting at natural river confluences. To select suitable luminescence parameters, artificially mixed sediment samples were tested and subsequently applied to natural settings, including the Nubra–Shyok River confluence and a small tributary joining the Beas River.

A detailed investigation was conducted on luminescence changes during sediment transport in fluvial systems, with a particular emphasis on the Sabarmati River, characterised by its seasonal flow and semi-arid environment. Additionally, the luminescence properties of aeolian sands in the vicinity of the Sabarmati Basin were measured to evaluate their potential mixing with fluvial sediments. The study highlights the significant roles of aeolian input, hillslope contributions, and confluence dynamics in altering luminescence sensitivity. The second part of the study addresses the Yamuna River, offering insights into sediment transport across a broad alluvial floodplain. It assesses how increasing transport distance influences the luminescence sensitivity of quartz grains.

Furthermore, as observed in earlier studies, sands transported over long distances tend to exhibit both changes in grain morphology and enhanced luminescence sensitivity. So, the influence of grain shape (roundness and sphericity) on single-grain luminescence sensitivity is examined.

Overall, luminescence sensitivity emerges as a valuable proxy for provenance analysis, provided that interpretations account for the environmental and geological complexities. This work lays a robust foundation for future research in dynamic sedimentary systems. The research presented in this chapter forms the basis for the manuscript cited below.

1. *Kartika Goswami, Santunu Kumar Panda, Linto Alappat, Naveen Chauhan, (2023) Luminescence for sedimentary provenance quantification in river basins: A methodological advancement. 'Quaternary Geochronology', Volume 79, 101488, (https://doi.org/10.1016/j.quageo.2023.101488)*
2. *Documenting Variations in Luminescence Sensitivity of Quartz in a River Basin at the Desert Margin: The Case of River Sabarmati. (Panda, S. K., Kaushal, R.K., Parida, S., Chauhan, N., Singhvi, A.K.) (Submitted in 'Earth Surface Processes and Landforms', Manuscript number: ESP-24-0319)) (Under review).*

Chapter 6: Summary and future outlook

This chapter summarises the results from all the chapters discussed earlier and provides suggestions for future studies.

Chapter 2

2. Instrumentation and experimental methods

2.1 Introduction

This chapter details the procedures for sample collection and laboratory preparation of quartz samples for luminescence measurements. It describes the instrumentation techniques used for luminescence analysis and the measurement of luminescence parameters, including thermoluminescence (TL), continuous wave optically stimulated luminescence (CW-OSL), and linearly modulated optically stimulated luminescence (LM-OSL), which together function as a multiproxy system. The analysis focuses on extracting information from TL peaks, such as trap depth (τ) and electron population (n) associated with different types of traps. Furthermore, CW blue light-stimulated luminescence (CW-BSL) and LM blue light-stimulated luminescence (LM-BSL) are used to determine the photoionisation cross-section (PICS) (σ) and the corresponding electron population (n), exploring their relationships with trapping and recombination centres. The chapter also addresses thermal analysis techniques and infrared spectroscopic methods to gain insights into quartz's crystal domain and structural properties.

2.2 Sample collection and preparation

In this thesis, various sediment, and rock samples from different origins across India, including the Sabarmati River, Yamuna River, Nubra River, and Beas River, have been studied. Detailed descriptions of the samples used are provided in individual chapters. For luminescence dating, samples were collected in light-tight pipes (Chandel et al., 2006) to prevent any bleaching of the natural dose under light conditions. However, natural dose preservation is not critical for provenance studies, as the samples are typically in a bleached state during collection. This is because the focus is primarily on sediments in transport conditions, particularly those within the active river channels. Sediment samples were collected underwater. In areas where the channel was dry, sampling was carried out after removing the top 5-10 cm layer. On-site sieving of sediments for < 1000 µm fraction range was carried out, and this fraction was sealed in opaque black bags.

The samples were processed under subdued red light using LED arrays emitting at >630 nm (Fig. 2. 1) to prevent the probable effect on the luminescence properties of quartz. Quartz separation followed the procedures outlined by Ichikawa (1965), and Fleming (1979). The chemical pretreatment involved sequential treatment with 10% HCl for 30 minutes to dissolve carbonates and 30% H_2O_2 for one day to remove organic matter. Following these treatments, samples were dried at 45 °C in the oven and then sieved to isolate the desired grain fraction. For this thesis, the 90–150 µm fraction was chosen due to its sufficient availability across the samples. The sieved grains underwent an etching process using 10% HF for 10 minutes to remove iron coatings. Afterwards, the grains were treated for 30 minutes with 12N HCl to remove fluorides. Quartz and feldspar were separated using a Frantz magnetic (Fig. 2. 2) separator at a magnetic field strength of ~15 k Gauss (Porat et al., 2006). The extracted quartz grains were then etched for 80 minutes with 40% HF to remove the α-skin (Aitken, 1985) and treated for another 30 minutes with 12N HCl to remove any remaining fluorides. The collected sediment sample and extracted final quartz are shown in Fig. 2. 3a and b, respectively.

Rock samples were crushed in a mortar, and quartz grains were separated following the procedure as above.

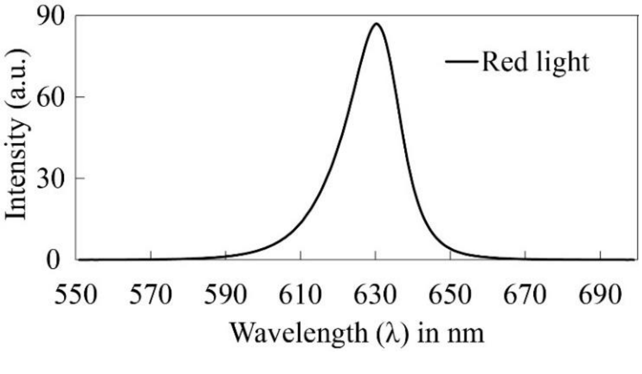

Fig. 2. 1: Spectral emission of red light used for sample preparation.

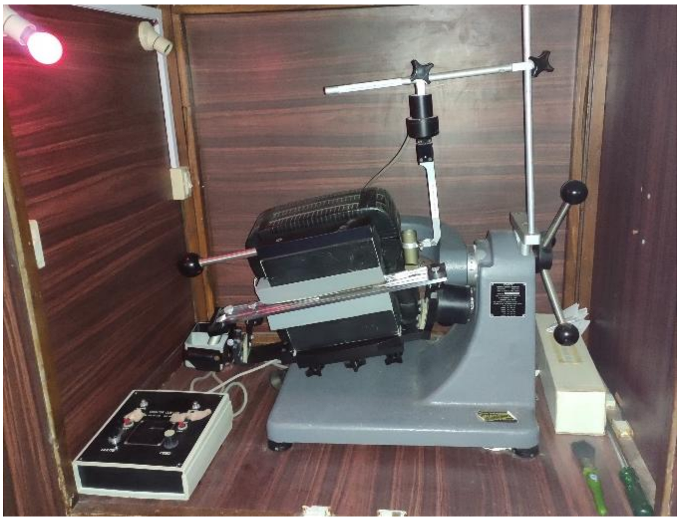

Fig. 2. 2: Magnetic separator.

Fig. 2. 3: Sediment sample collected (a) and the extracted quartz (b).

For luminescence measurements, a 5 mm diameter monolayer of extracted quartz was mounted on stainless steel (SS) discs using Silkospray™ for luminescence measurements (Fig. 2. 4a, b). For single grain measurements, samples were placed in rhodium-plated aluminium discs containing a 10×10 array of 100 holes with 300 µm diameter and 600 µm spacing between hole centres (Fig. 2. 4c). The samples are tested for possible contamination by feldspar luminescence using infrared-stimulated luminescence (IRSL; Hütt et al., 1988; Smith et al., 1990). If a measurable IRSL signal is observed with signal-to-noise ratio (SNR) more than 3, the sample is re-treated with 40% HF for an additional 10 minutes and subjected to further magnetic separation. All final quartz extracts are tested for IRSL contamination. A SNR of up to 3 is used as the maximum acceptable limit. The final quartz samples have the IRSL signal more than 50 times weaker than the quartz OSL signal.

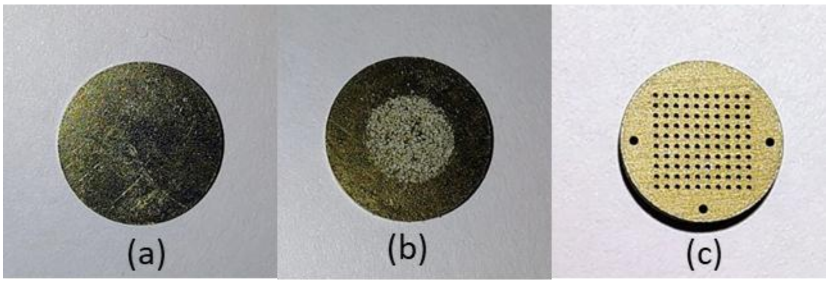

Fig. 2. 4: Stainless steel (SS) disc (a) and SS disc with sample mounted (b) and single grain disc (c).

2.3 Luminescence measurement: Instrumentation

Luminescence measurements in this study were conducted using the Risø TL/OSL reader (Fig. 2. 5) (Bøtter-Jensen et al., 2000). The Risø single grain instrument was also utilised for single-grain luminescence measurements. The system comprises a computer, a controller, and a reader. The controller serves as the interface between the computer and the reader, ensuring communication and control (Fig. 2. 5).

Fig. 2. 5: Riso TL/OSL instrument.

The reader comprises of the following units:

1. Irradiation unit
2. Stimulation unit
3. Detection unit

Fig. 2. 6a shows the schematic diagram of the TL/OSL reader, while Fig. 2. 6b provides a detailed view of the stimulation and detection units.

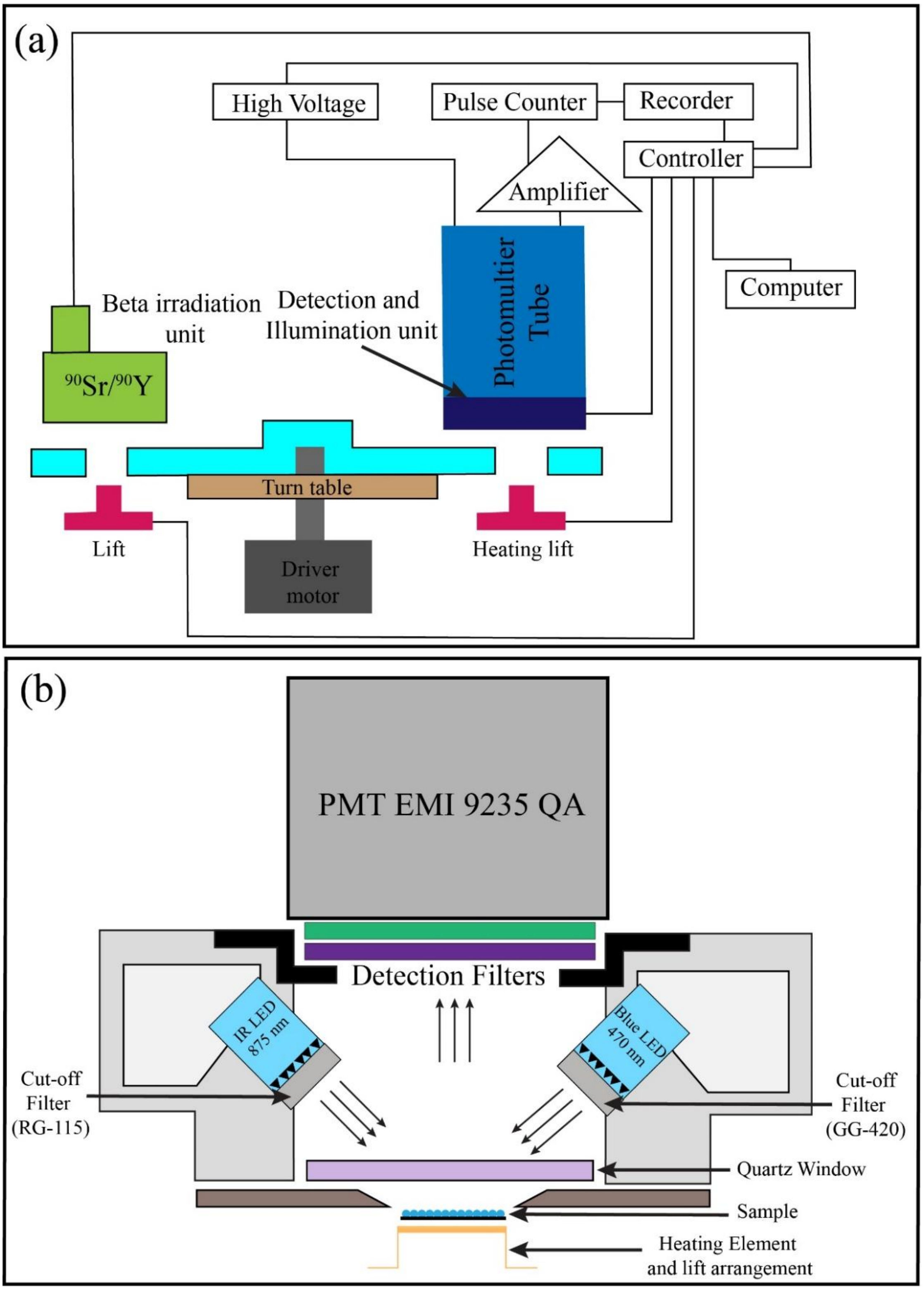

Fig. 2. 6: (a) Schematic diagram of TL OSL reader and (b) stimulation and detection unit (after Bøtter -Jensen et al., 2003b).

2.3.1 Irradiation unit

The extracted quartz samples were irradiated using a calibrated ^{90}Sr/^{90}Y beta source (Bøtter-Jensen et al., 2000). The beta energy involves two stages: ^{90}Sr decays to ^{90}Y, emitting beta particles with a maximum energy of 0.546 MeV and a half-life of 28.78 years, followed by ^{90}Y decaying to ^{90}Zr, emitting beta particles with a maximum energy of 2.28 MeV and a half-life of 64.1 hours.

In the Riso TL/OSL reader, the irradiation source is ~7 mm away from the sample position, and a 0.125 mm beryllium window is located between the irradiator and the measurement chamber to act as a vacuum interface for the measurement chamber. The dose rate is calibrated using coarse-grain quartz provided by Risø National Laboratory, Denmark, to ensure accuracy. Given the 28.78-year half-life of ^{90}Sr, dose rate corrections using the radioactive decay equation and periodic recalibration (approximately every year) are necessary.

2.3.2 Stimulation unit

Thermal Stimulation

The thermal stimulation unit employs a high-resistivity kanthal heating material configured as a low-mass heater strip to provide efficient and uniform heat transfer to the sample. Temperature is precisely controlled using a type K (Chromel-Alumel) thermocouple, spot-welded beneath the heater strip for real-time feedback.

Temperature is controlled using a type K thermocouple, which is spot-welded beneath the heater strip to provide real-time feedback for precise temperature control. The system is continuously purged with nitrogen gas to prevent oxidation of the heater plate at elevated temperatures and to ensure uniform sample heating through convection.

In Risø TL/OSL, reader samples can be heated up to 700 °C, with linear heating rates ranging from 0.1 °C/s to 10 °C/s. The reader offers a precision of ±4 °C and a heating rate reproducibility of better than 1%.

Optical Stimulation

The optical stimulation system incorporates blue LEDs (470 ± 20 nm) and infrared (IR) LEDs (850 nm) for sample excitation. An array of 28 blue LEDs, arranged in four clusters of seven each, delivers a maximum power of 80 mW/cm² at the sample position (~20 mm distance) (Bøtter-Jensen et al., 2003; Guide to the Risø TL/OSL reader- user manual). To minimise scattered light, long-pass green filters (Schott GG-420) are placed in front of the blue LEDs, cutting off wavelengths below ~420 nm (Fig. 2. 7). For IR stimulation, three clusters of IR

LEDs equipped with RG-780 cut-off filters are used, providing a maximum power of ~145 mW/cm² at the sample position (Fig. 2. 7).

In single grain measurement, a 10-mW solid-state Nd: YVO4 green laser emitting at 532 nm is used. The laser is focused to a spot size of <20 µm, delivering a maximum energy fluence rate of ~50 W/cm² (Guide to 'The Risø Single Grain Laser OSL system' user manual). A 140-mW solid-state IR laser diode operating at 830 nm is used, with a maximum energy fluence rate of 500 W/cm² (Bøtter-Jensen et al., 2003). The laser spot is steered by orthogonal mirrors attached to high-precision motors, ensuring precise stimulation of individual grains.

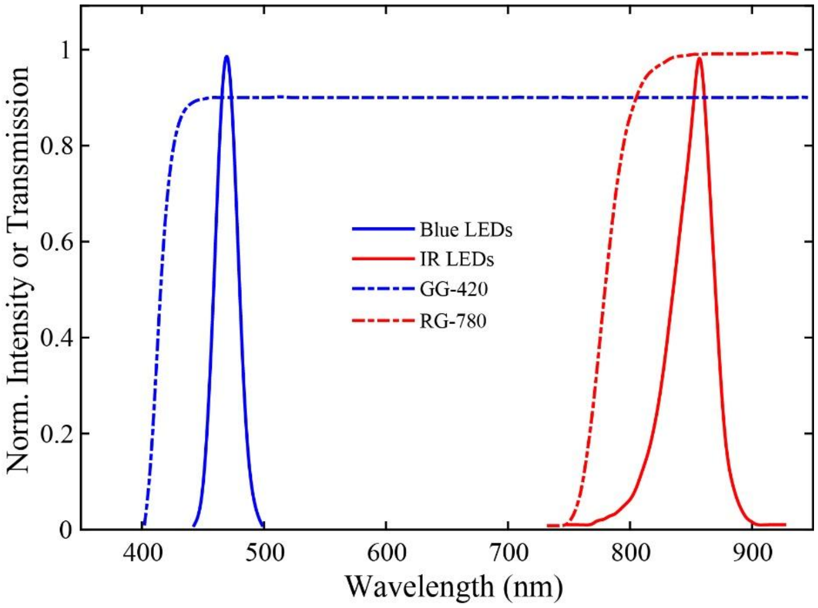

Fig. 2. 7: The emission spectra of the blue and IR LEDs, including transmission curves for GG-420 (blue LEDs) and RG-780 (IR LEDs) long-pass filters (redrawn from the Risø manual).

2.3.3 Detection unit

The detection system uses a bi-alkali type Photomultiplier Tube (PMT), EMI 9235QA, optimised for detecting UV and blue light emissions (Bøtter-Jensen, 1997). The PMT's maximum detection efficiency occurs at ~380 nm, making it suitable for signals emitted by quartz. Its broad detection range (200–600 nm) allows it to cover most luminescence signals (Fig. 2. 8). The PMT is critical for detecting low light signals emitted during sample stimulation. Based on the photoelectric effect, the PMT amplifies weak signals through a cascade process:

- Light photons are absorbed by the photocathode, releasing photoelectrons.
- These electrons are accelerated towards the first dynode using a high voltage (~hundreds of volts).
- At each dynode, the electrons trigger the release of multiple secondary electrons, creating a cascading amplification effect.

- The amplified charge is collected at the anode, generating a measurable voltage pulse. This process occurs within ~10^{-9} seconds and achieves a gain of up to 10^6 times the initial signal.

The amplified signal is processed by a pulse counter, converting it into discrete counts that represent the luminescence intensity. The system's controller ensures precise synchronisation, while data is recorded and analysed using a connected computer (Fig. 2. 6(a)).

A quartz window is placed between the detection unit and the measurement chamber to protect the PMT. This window prevents contamination from evaporated silicon oil. The window is not present in single-grain systems.

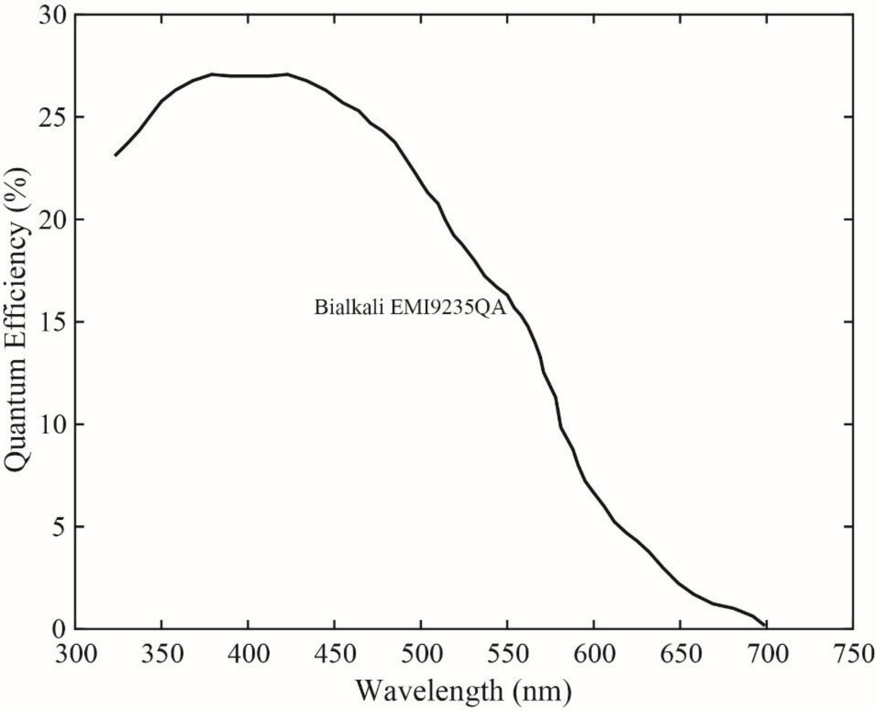

Fig. 2. 8: PMT detection efficiency (Bialkali - EMI 9235QA) (Redrawn after Bøtter-Jensen (1997)).

Filters:

Filters play a vital role in ensuring that only the required spectral signal is transmitted to the PMT while blocking unwanted blackbody radiation and stimulation light. The Risø TL/OSL reader is equipped with the following filters (Fig. 2. 9):

- Hoya U-340 (5 mm and 2.4 mm thick, Φ = 25 mm): Transmits wavelengths between 240–400 nm, with a peak at 340 nm.
- Schott BG39 (2 mm thick, Φ = 25 mm): Transmits 250–3200 nm.
- BG3 (3 mm thick, Φ = 25 mm): Transmits 250–520 nm and >680 nm.

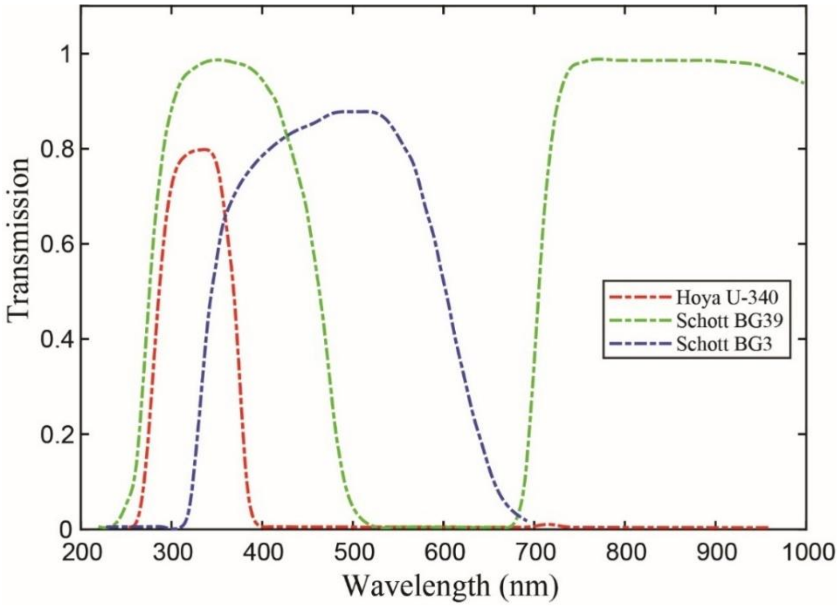

Fig. 2. 9: Transmission characteristics of U-340, BG39 and BG3 (supplied with the Riso TL/OSL Reader).

2.4 Luminescence parameters and its analysis

Luminescence signals originate from various traps in the quartz lattice, which can be categorised based on their characteristics and separated using different types of stimulation. Under thermal stimulation, the TL glow curve appears as a series of peaks, where each peak represents a luminescence parameter with unique trap depth and escape frequency. Isolating the contributions of individual traps is typically achieved through analytical methods (e.g., initial rise method, isothermal decay method, and peak shift method) or computational approaches. In this study, computational methods are prioritised, as analytical approaches often require multiple treatments of quartz, which can alter luminescence sensitivity during the measurement process.

Similarly, under constant-intensity optical stimulation, the luminescence (CW-OSL) appears as a decay curve, which can be separated into components of exponential decay. Each decay component reflects a specific photoionisation cross-section (PICS) and serves as a luminescence parameter. In contrast, under the linearly ramped intensity of optical stimulation, the luminescence (LM-OSL) appears as a series of peaks, with each peak acting as a luminescence parameter, providing insights into unique PICS values. These methods enable a detailed investigation of trap properties and their contributions to luminescence signals. Each luminescence parameter, representing a unique trap group type, will be utilised independently in geological applications based on its specific properties, enabling luminescence to function as a robust multiproxy system.

2.4.1 Thermoluminescence (TL)

Thermoluminescence (TL) occurs when a portion of the energy absorbed by a sample during irradiation is stored and later released as light upon stimulation by heat. The fundamental model assumes that irradiation generates free electrons and holes, some of which become trapped in localised energy levels within the forbidden energy band. During heating, these trapped electrons gain sufficient energy to be thermally released into the conduction band and subsequently recombine with trapped holes. If this recombination process is radiative, it leads to the emission of photon radiation. Under linear heating, trapped electrons evict from shallow traps to deeper traps, producing a glow curve with multiple peaks. Each peak corresponds to specific trap groups characterised by their trap depth (E), frequency factor (s) and kinetic order (b). Various models for the TL glow curve are formulated based on the kinetics of charge-carrier transfer between traps.

Randal and Wilkin (1945) proposed a mathematical model for TL assuming negligible retrapping.

The probability (P) per unit of time that a trapped electron will escape from the trap is given by the Arrhenius equation (equation 2.1), considering that the trapped electrons have a Maxwellian distribution of thermal energies.

$$P = s \exp\left(-\frac{E}{kT}\right) \tag{2.1}$$

Here, s, E, k, and T are the frequency factor, trap depth, Boltzmann constant and temperature. If n is the number of trapped electrons at time t, the time rate of change of n is

$$I(t) = -\frac{dn}{dt} = -Pn = -ns \exp\left(-\frac{E}{kT}\right) \tag{2.2}$$

Assuming that the sample is warmed up at a linear rate of heating,

$$\frac{dT}{dt} = \beta \tag{2.3}$$

Substituting (2.3) into (2.2) and integrating:

$$n = n_0 \exp\left[\frac{s}{\beta}\int_{T_0}^{T} e^{-\frac{E}{kT'}}\, dT'\right] \tag{2.4}$$

Where n_0 is the number of trapped electrons at temperature T_0. The TL intensity I(T) is given as:

$$I(t) = n_0 s \exp\left(\frac{E}{kT}\right) \exp\left[-\frac{s}{\beta}\int_{T_0}^{T} e^{-\frac{E}{kT'}}\, dT'\right] \tag{2.5}$$

This expression represents the first-order kinetic glow curve, assuming negligible retrapping of electrons.

Then, Garlic and Gibson (1997) model considered a high probability of retrapping. Considering the crystal containing a total number of electron traps N of which n is filled by electrons at any instant retrapping combined with the assumption n < N. The probability that an escaping electron will recombine with an empty luminescence centre and not be retrapped is given by n/N, and the luminescence process will be given by

$$I(t) = -\frac{dn}{dt} = -Pn = -\frac{n^2}{N} s \exp\left(-\frac{E}{kT}\right) \tag{2.6}$$

The solution of equation 2.6 for constant heating rate β is

$$I(T) = \frac{n_0^2 S}{N} \exp\left(-\frac{E}{kT}\right)\left[1 + \frac{n_0 S}{\beta N}\int_{T_0}^{T} \exp\left(-\frac{E}{kT'}\right) dT'\right]^{-2} \tag{2.7}$$

The equation 2.7 for the glow curve is called second-order kinetics, assuming high retrapping.

May and Partridge (1964) proposed the expression where the simplifying assumptions do not hold. The TL peak will fit neither the first- nor the second-order kinetics. The TL intensity (I) is represented as

$$I(t) = -\frac{dn}{dt} = n^b s' \exp\left(-\frac{E}{kT}\right) \tag{2.8}$$

Where s' is s/N

The solution of equation 2.8 for constant heating rate β is

$$I(T) = s'' n_0 \exp\left(-\frac{E}{kT}\right)\left[1 + \frac{s''(b-1)}{\beta}\int_{T_0}^{T} \exp\left(-\frac{E}{kT'}\right) dT'\right]^{-\frac{b}{b-1}} \tag{2.9}$$

Equation 2.9 represents the glow curve for general order kinetics, and equations 2.5 and 2.7 are its special case.

The "kinetics order" b is an empirically determined parameter that is not necessarily 1 or 2. It is usually assumed that $1 < b < 2$, but TL peaks with b values outside this range were also found (Kirsh, 1992).

The use of the general order model, namely the analysis of TL peaks by looking for the best fit to (I_o), is quite convenient and, as already mentioned, gives a good estimation of E and S.

TL peak analysis

The computerised glow curve deconvolution (CGCD) analysis has been widely applied since 1980 to resolve composite TL glow curves into individual peak components, which enables estimating the trap groups' physical properties such as activation energy, trap depth and frequency factor.

In CGCD, the general order TL equation (equation 2.9) where $I = I(n_0, E, s, T)$ is transformed to $I = I(I_m, E, T_m, T)$ (equation 2.10) by PMC (Podgorsak-Moran-Cameron) approximation, refer to (Furetta, 2003). By considering the general-order kinetics with the kinetic order parameter b, the equation for the TL glow peak is derived. Its empirical form is described by Kitis et al. (1998).

$$I(T) = I_m b^{\frac{b}{b-1}} \exp\left(\frac{E}{kT}\frac{T-T_m}{T_m}\right)\left[(b-1)\left(1-\frac{2kT}{E}\right)\frac{T^2}{T_m^2}\exp\left(\frac{E}{kT}\frac{T-T_m}{T_m}\right)+1 + \frac{2kT_m(b-1)}{E}\right]^{-\frac{b}{b-1}} \tag{2.10}$$

The parameters are defined in Table 2. 1.

Table 2. 1: Parameters used in the equation 2.10.

Parameter	**Description**	**Unit**
n_0	The initial concentration of trapped electrons	cm^{-3}
E	Activation energy	eV
s	Frequency factor	s^{-1}
T	Absolute temperature	K
I_m	Maximum peak intensity of the glow curve	-
T_m	Temperature corresponding to maximum intensity	K

A tgcd program by Peng et al. (2016) is used for deconvolution of thermoluminescence peaks. Fig. 2. 10 represents the deconvolution of peaks using the CGCD technique.

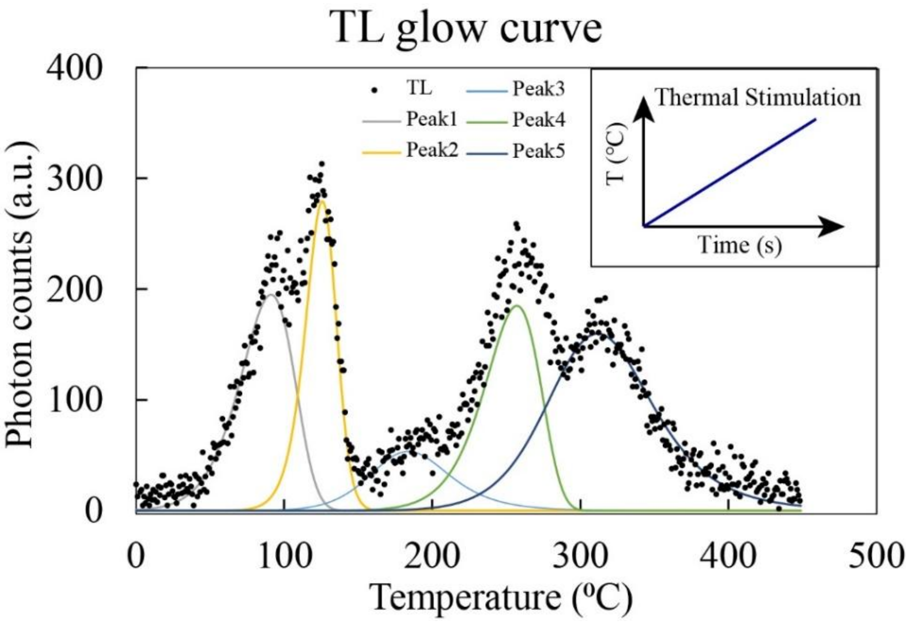

Fig. 2. 10: TL glow curve showing deconvoluted peaks, with thermal stimulation curve shown as an inset.

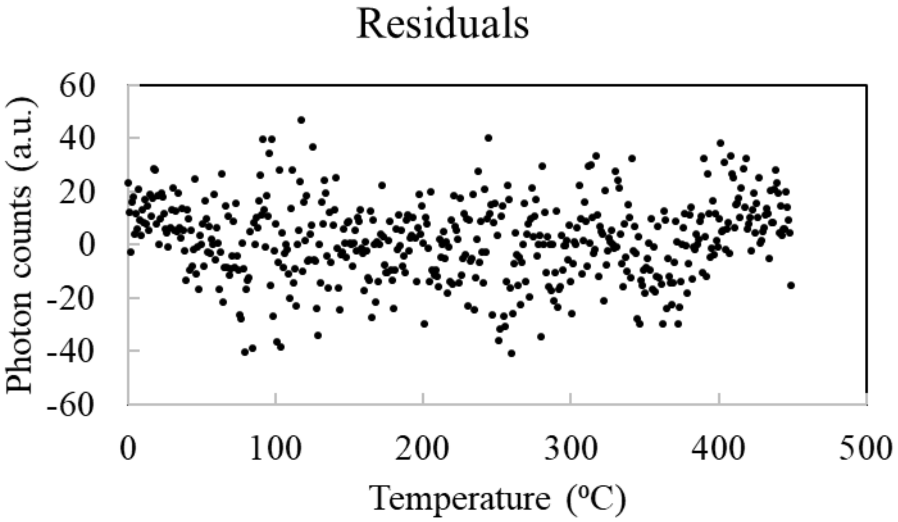

Fig. 2. 11: Residual plot of TL glow curve deconvolution.

To assess the quality of the analytical model fit and optimise peak deconvolution, the following statistical measures were used:

- SSR (Squared Sum of Residuals): Quantifies the deviation between observed and fitted data.
- RCS (Reduced Chi-Square): Indicates the model's goodness-of-fit.

- R^2: Represents the squared Pearson correlation between observed and fitted signals.
- FOM (Figure of Merit): Evaluated using the method of Balian and Eddy (1977).

Residual plots (Fig. 2. 11), the difference between fitted and observed TL glow curves, were also examined to ensure accurate deconvolution.

The analysis of TL glow curves provides crucial insights into trap characteristics such as activation energy, trap depth, and frequency factor. Computerised glow curve deconvolution (CGCD) enables accurate resolution of TL peaks, supported by statistical measures like SSR, RCS, R^2, and FOM to ensure reliable fits.

2.4.2 Continuous wave optically stimulated luminescence (CW-OSL)

Complementing TL glow curve analysis, continuous wave optically stimulated luminescence (CW-OSL) provides complementary insights into trap dynamics. Stimulation of pre-irradiated crystals with a constant power light source produces a decay luminescence curve, as described by Huntley et al. (1985). It has been observed that the decrease in OSL emission of quartz under constant stimulation does not follow a simple exponential decay, as would be expected from a single-trap system governed by first-order kinetics. Instead, the OSL decay could be well approximated by the sum of three exponential components, termed fast, medium, and slow (long-term) components, based on the physically distinct traps with different rates of charge loss (Bailey et al., 1997; Huntley et al., 1996; Smith and Rhodes., 1994).

The transfer of charge between energy levels during irradiation and optical stimulation in a dosimeter is governed by complex, non-linear rate equations, which are often challenging to solve analytically. To derive analytical expressions for the OSL intensity over time and its dependence on absorbed dose, these equations must be simplified. The simplest model for such analysis is the One trap one recombination centre (OTOR) model, which assumes the presence of a single type of electron trap and a single type of hole trap. In this model, trapped holes act as recombination centres where electrons recombine with holes, resulting in luminescence emission.

Charge neutrality for this system can be expressed as:

$$n_c + n = m_v + m \tag{2.11}$$

Where n_c and n are the concentrations of electrons in the conduction band and the traps, respectively, and m_v and m are the concentrations of holes in the valence band and hole traps (recombination centres), respectively.

By introducing a quasi-stationary population of free electrons in the conduction band, it is assumed that the number of electrons in the conduction band (n_c) is always negligible compared with the number of trapped electrons. Under thermal equilibrium at the end of the irradiation period, both n_c and m_v are zero.

$$\frac{dm}{dt} = \frac{dn}{dt} \ll \frac{dn_c}{dt} \tag{2.12}$$

For the first-order kinetic model (Randall and Wilkins, 1945), it is assumed that the probability of recombination is significantly higher than the probability of retrapping. Consequently, the instantaneous luminescence intensity, I(t), is proportional to the rate of release of electrons:

$$I(t) = -\frac{dn}{dt} = Pn \tag{2.13}$$

Here, n is the concentration of the trapped electron, and P represents the probability of electron escape from the trap (decay constant, in s^{-1}).

In continuous wave stimulation, the release rate of the electrons from the traps is linearly dependent on the stimulation intensity. It is determined by the incident photon flux Φ and the photo ionisation cross-section σ according to the relation:

$$P = \sigma(\lambda) \times \Phi \tag{2.14}$$

The expression for intensity of CWOSL is:

$$I_{CW}(t) = -\frac{dn}{dt} = Pn \tag{2.15}$$

The concentration of trapped charge through trapped time can be determined using:

$$\int_{n_0}^{n} \frac{dn}{n} = \int_{0}^{t} -P\,dt \tag{2.16}$$

Which integrates to:

$$n = n_0\,exp(-Pt) \tag{2.17}$$

Multiplying 'P' on both sides

$$Pn = Pn_0\,exp(-Pt) \tag{2.18}$$

Thus, the CW-OSL intensity can be expressed as:

$$I_{CW} = I_0\,exp(-Pt) \tag{2.19}$$

The CW-OSL signal depends on the photoionisation cross-section (PICS) of the traps and the stimulation intensity. The decay curve is a cumulative result of various electron traps with different PICS values. Traps with higher PICS decay more quickly, producing the fast component, while those with lower PICS decay more slowly, contributing to the slow component. The simplified OSL signal model assumes no interaction between traps and considers three optically sensitive traps with charge concentrations n_1, n_2, and n_3 and with detrapping probability/ decay constants P_1, P_2, and P_3. The total CW-OSL intensity is given by.

$$I_{OSL} = n_1 P_1 e^{-tP_1}(fast) + n_2 P_2 e^{-tP_2}(medium) + n_3 P_3 e^{-tP_3}(slow) \tag{2.20}$$

Deconvolution of the OSL signal allows for the identification of individual components and provides insights into how natural environmental conditions influence these components.

CW-OSL component analysis

Component analysis of CW-OSL signals involves fitting the decay curve using weighted least-squares estimates. The fit_CWCurve() function (Kreutzer, 2023) in the R Luminescence package is commonly used for this purpose. This function employs the Levenberg-Marquardt algorithm to fit CW-OSL decay curves and estimate component parameters. The analysis also provides 1-sigma error estimates for the components. Fig. 2. 12 provides deconvolution of CW-OSL having three components denoted as C1, C2, and C3, respectively.

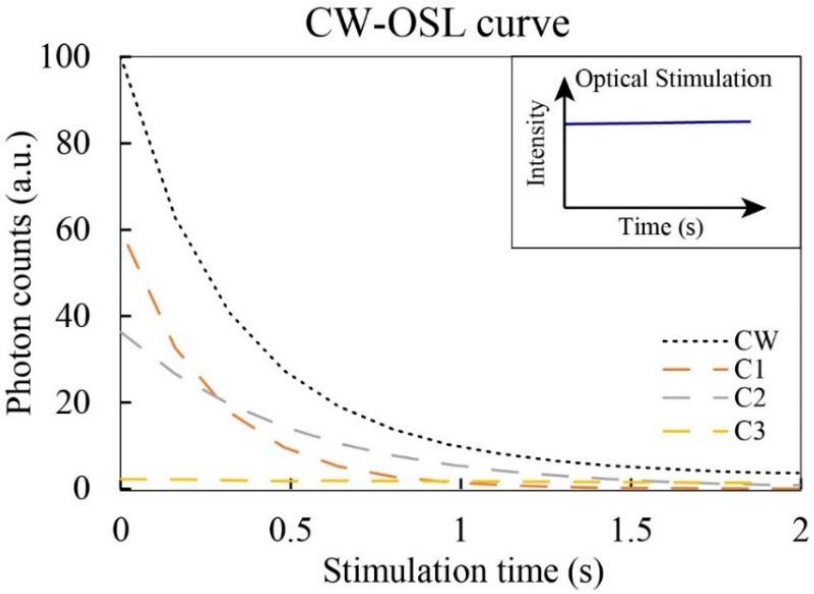

Fig. 2. 12: CW-OSL curve showing deconvoluted decay curves, with optical stimulation curve shown as an inset.

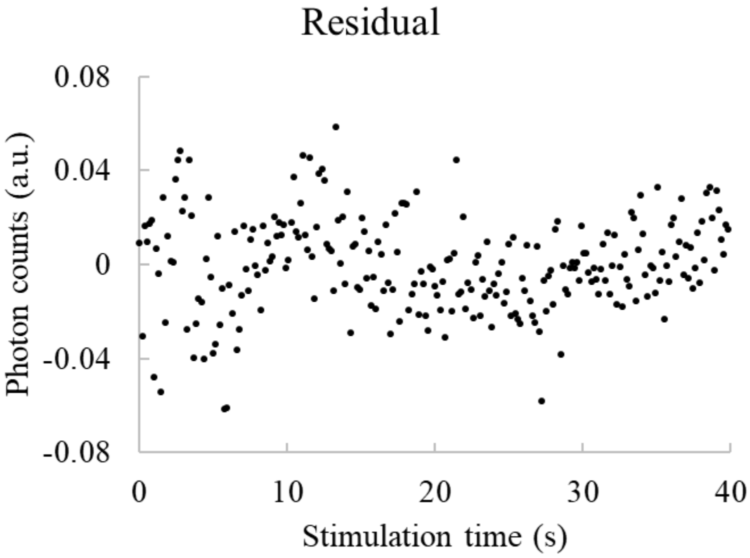

Fig. 2. 13: Residual plot of CW-OSL deconvolution.

The goodness of fit for LM-OSL curves is evaluated using the pseudo-R^2 value (Lave., 1970), defined as:

$$pseudo - R^2 = 1 - \frac{RSS}{TSS} \tag{2.21}$$

RSS is the residual sum of squares, and TSS is the total sum. 1-sigma error values represent the uncertainties in the components. The residual plot (Fig. 2. 13) is also observed for optimal fitting.

The **photoionisation cross-section (PICS)** is calculated based on an optical power of 70%. For luminescence stimulation, the light energy must exceed the trap depth of the trapped electrons. Traps with higher PICS decay more rapidly, forming the fast component, while those with lower PICS decay more slowly, forming the slow component. By analysing these components, one can understand the kinetic behaviour of the system and the relative contributions of different trap groups.

2.4.3 Linearly modulated optically stimulated luminescence (LM-OSL)

Where the stimulation intensity remains constant, LM-OSL involves ramping the intensity of optical stimulation, a method proposed by Bulur (1996). This approach produces luminescence signals in the form of distinct peak-shaped curves (Fig. 2. 14), unlike the monotonically decaying CW-OSL signal. Bulur et al. (2000) observed multiple overlapping peaks in LM-OSL signals from quartz stimulated at 470 nm. The distinct fast and slow component peaks were identifiable, confirming the multi-trap hypothesis proposed by Bailey et al. (1997). Traps with peaks at shorter times have larger photoionisation cross-sections (PICS) and are easier to bleach, while traps with peaks at longer times have smaller PICS and are more resistant to bleaching.

However, despite excellent data-to-theory fits, Kuhns et al. (2000) found discrepancies between the photoionisation cross-sections derived from LM-OSL and the decay constants obtained from CW-OSL. Nevertheless, LM-OSL provides greater clarity in understanding the structure of the luminescence signal, including the number of components and their kinetics.

In the linear ramping of stimulation intensity, the detrapping probability P varies with time as:

$$P = \sigma(\lambda) \times \Phi \times \frac{t}{T} \tag{2.22}$$

T is the total optical stimulation time, Φ is the photon flux, and σ(λ) is the photoionisation cross-section (PICS). The PICS depends on the stimulation wavelength (λ). For simplicity, define:

$$\gamma = \sigma(\lambda) \times \Phi \tag{2.23}$$

The concentration of trapped electrons as a function of time is derived as:

$$\int_{n_0}^{n} \frac{dn}{n} = \int_{0}^{t} -\gamma \frac{t}{T}\, dt \tag{2.24}$$

Integrating gives:

$$ln(n) = -\frac{\gamma t^2}{2T} + C \tag{2.25}$$

Taking the initial condition ($t = 0$, $n = n_0$):

$$n = n_0\, e^{-\frac{\gamma t^2}{2T}} \tag{2.26}$$

Multiplying 'P' on both sides of the equation 2.26, the LM-OSL intensity for a particular peak is

$$I_{LM}(t) = Pn = n_0 \gamma \frac{t}{T}\, e^{-\frac{\gamma t^2}{2T}} \tag{2.27}$$

For a system with multiple optically sensitive traps, the LM-OSL signal can be expressed as a summation of individual components with initial proportional trapped charge concentrations n_1, n_2, and n_3 and detrapping probabilities P_1, P_2, and P_3 ($P_n = \gamma_n \times t/T$):

$$\mathrm{I_{LM}}(t) = n_1\gamma_1 \frac{t}{T} e^{-\frac{\gamma_1 t^2}{2T}} (fast) + n_2\gamma_2 \frac{t}{T} e^{-\frac{\gamma_2 t^2}{2T}} (medium) + n_3\gamma_3 \frac{t}{T} e^{-\frac{\gamma_3 t^2}{2T}} (Slow) + \cdots \tag{2.28}$$

LM-OSL peak analysis

The analysis and separation of these complex curves into their constituent components can be achieved using computerised curve deconvolution analysis (CCDA). The expression of I (n, γ, t) of equation 2.28 is transformed into experimental variables I (I_m, t_m, t) (Bulur, 1996; Kitis & Pagonis, 2008). The shape of an LM-OSL peak is characterised by the maximum peak intensity I_m, the corresponding time t_m.

$$I(t) = \left(\exp(0.5) \cdot \frac{I_{m_1} \cdot \mathrm{t}}{t_{m_1}}\right) \cdot \exp\left(-\frac{t^2}{2t_{m_1}^2}\right) (fast) + \left(\exp(0.5) \cdot \frac{I_{m_2} \cdot \mathrm{t}}{t_{m_2}}\right) \cdot \exp\left(-\frac{t^2}{2t_{m_2}^2}\right) (medium) + \cdots \tag{2.29}$$

The fit_LMCurve () (Kreutzer, 2024) is a function used for non-linear least squares fitting of LM-OSL curves as part of the R package luminescence. Fig. 2. 14 provides deconvolution of LM-OSL having three components denoted as C1, C2, and C3, respectively.

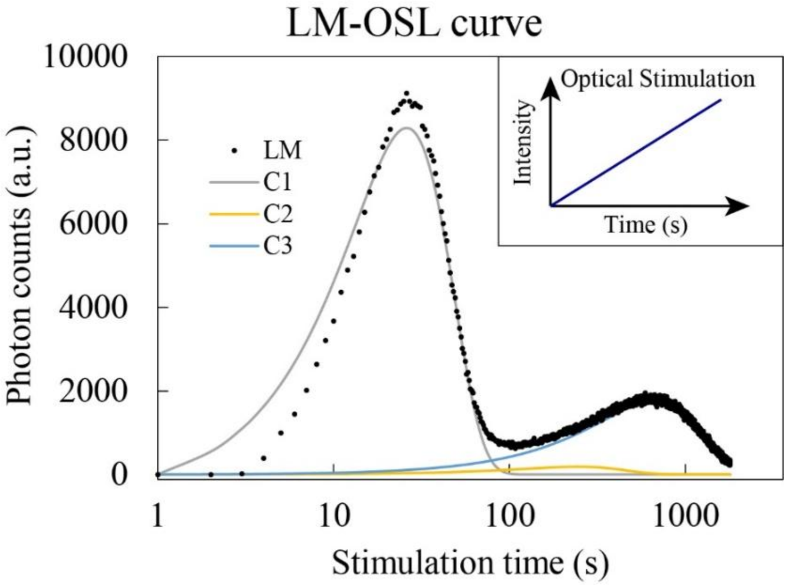

Fig. 2. 14: LM-OSL curve showing deconvoluted peaks, with optical stimulation curve shown as an inset.

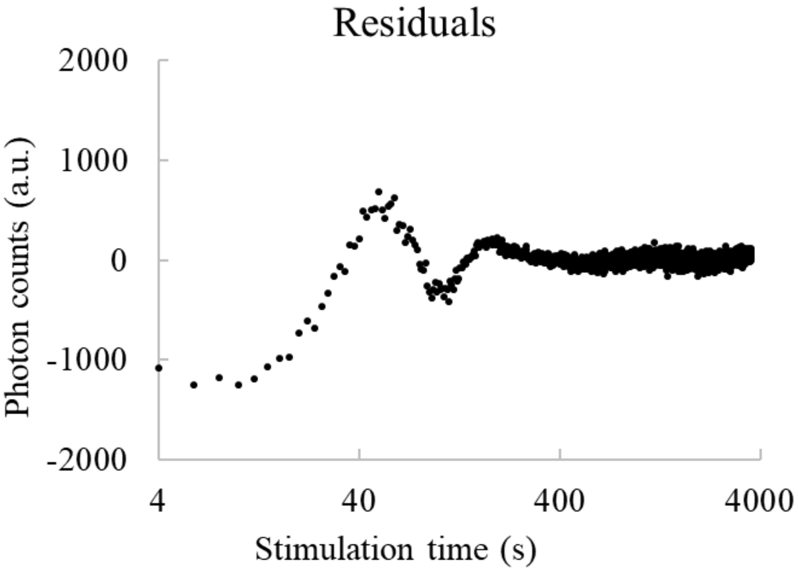

Fig. 2. 15: Residual plot of LM-OSL deconvoluted.

The goodness of fit for LM-OSL curves is evaluated using the pseudo-R^2 using equation 2.21. 1-sigma error values represent the uncertainties in the components. The residual plot (Fig. 2. 15) is also observed for optimal fitting.

From the above fitting equation:

$$\gamma_i = \frac{T}{\left(t_{m_i}\right)^2} \tag{2.30}$$

Here the T is the total optical stimulation time (3600 seconds) and t_{m_i} is the time to peak intensity of the ith LM-OSL component.

From equation 2.23, the photoionisation cross-section is calculated as:

$$\sigma(\lambda)_i = \frac{\gamma_i}{\Phi} \tag{2.31}$$

The optical stimulation was applied using 470 ± 30 nm light at 0–80% power. At the maximum power setting of 64 mW/cm^2, the photon flux Φ is calculated as $(1.51\pm0.10)\times10^{17}$ photons×cm^{-2}×s^{-1}. This value is used to estimate photoionisation cross-sections (PICS) as described above. The uncertainty in stimulation wavelength propagates into the estimation of Φ, resulting in a relative uncertainty in PICS of approximately 7%, as expressed in equation 2.32:

$$\frac{\Delta\sigma}{\sigma} = \frac{\Delta\Phi}{\Phi} = 0.07 \tag{2.32}$$

The stimulation energy must exceed the trap depth for detrapping to occur. Traps with higher PICS values produce fast components, decaying earlier, while those with lower PICS generate slow components, decaying later. Unlike CW-OSL, LM-OSL offers a more refined understanding of PICS by separating trap groups into distinct peak forms.

2.4.4 Luminescence sensitivity (LS)

Quantification of quartz luminescence for comparison between samples in provenance studies, the intensity of various luminescence parameters is normalised by the weight and dose of the sample (Equation 2.30), commonly referred to as OSL and TL sensitivity.

$$Luminescence\ Sensitivity\ (LS) = \frac{Luminescence\ Intensity}{Dose * Weight} \qquad (2.33)$$

The detailed investigation of luminescence parameters highlights the intricate relationship between trap dynamics and the resulting luminescence signals. In nature, these trap groups are affected differently by the conditions they encounter, forming a robust system for capturing the journey of sediment grains. These parameters were further studied under laboratory simulations of natural conditions, as detailed in Chapter 3. Additionally, they are applied as a multiproxy system for sediment budgeting in Chapter 5 and utilised to understand fluvial processes.

Calculation of 110 °C TL and BSL intensity:

For the measurement of 110 °C thermoluminescence (TL) intensity, a linear heating rate of 2 °C/s was applied up to 220 °C. Under these conditions, the 110 °C TL peak—known to be heating rate dependent—typically appears around 90 °C. Photon counts were integrated from 60 °C to 110 °C to quantify TL intensity. In cases where the peak position shifted, the integration window was adjusted to ±25 °C around the peak maximum.

Blue stimulated luminescence (BSL) measurements were carried out using blue LEDs (power: 56 mW/cm^2) at 125 °C for 40 seconds. The first channel (0.16 seconds) was excluded to avoid contributions from ultrafast components (Jain et al., 2003). Photon counts recorded between 0.16 and 0.8 seconds (channels 2–6) were used as the signal, while the average counts from the final 8 seconds (channels 201–250) were used as the background (Fig. 2. 16).

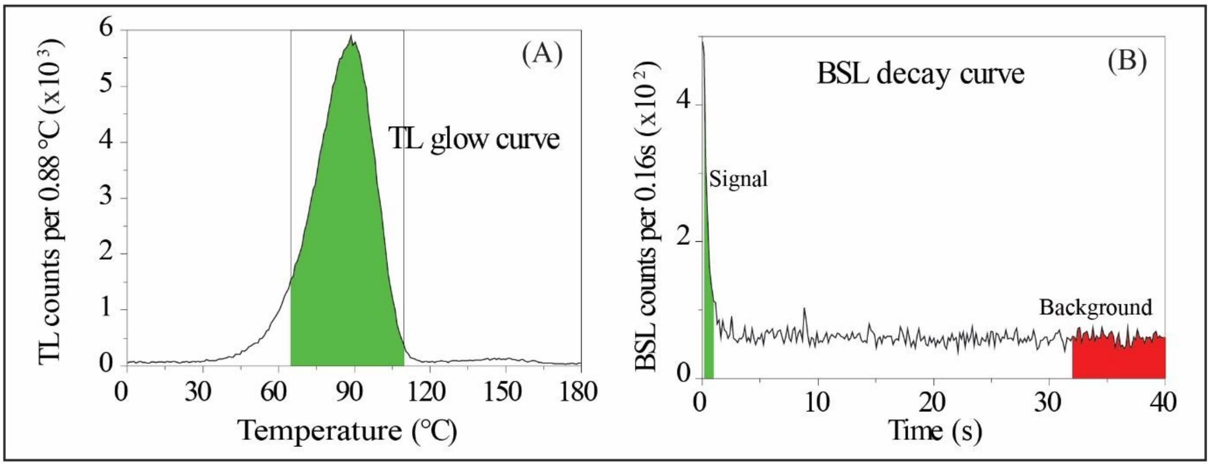

Fig. 2. 16: (A) TL glow curve of a sample and the shaded region is used for measurement for TL 110⁰C intensity (B) BSL decay curve with signal and background as the shaded region.

2.5 Thermal and chemical analysis

The luminescence parameters, i.e., trap groups of unique characteristics, are closely tied to the structural defects of the quartz lattice. To comprehensively understand luminescence properties, it is essential to investigate the crystal domain. As previously noted, structural defects in quartz significantly influence its luminescence spectra (Götze et al., 2021; Preusser et al., 2009). In chemical analysis, Fourier-transform infrared (FTIR) spectroscopy, which probes the fundamental vibrational modes of molecules within the crystal, can be employed to identify specific defects present in the structure. Furthermore, thermal analysis plays a vital role, as variations in quartz luminescence have been observed during annealing (Poolton et al., 2000). In this context, thermogravimetric analysis (TGA) and differential scanning calorimetry (DSC) are utilised to study structural and thermal changes in the crystal during heating.

2.5.1 Fourier transform infrared spectroscopy (FTIR)

Fourier-transform infrared (FTIR) spectroscopy is a pivotal analytical technique for identifying and characterising materials from their infrared absorption spectra. Spectra were acquired with a Nicolet Summit LITE spectrometer (Thermo Fisher Scientific) fitted with a KBr beamsplitter and a $LiTaO_3$ (lithium tantalate) pyroelectric detector operating in mid-infrared transmission mode.

The instrument's infrared source is modulated by a Michelson interferometer: a beamsplitter divides the broadband beam into two orthogonal paths, one reflected by a fixed mirror and the other by a moving mirror. Recombination of the two beams generates an interferogram that encodes intensity information for all IR frequencies simultaneously. After interacting with the sample, the modified interferogram is recorded by the $LiTaO_3$ detector and digitised (24-bit resolution).

Acquisition parameters were 16 sample scans and 16 background scans, 4 cm^{-1} spectral resolution, and a spectral window of 4000–400 cm^{-1}. The raw time-domain interferograms were Fourier-transformed (apodisation: Norton-Beer Strong; phase-correction: Mertz) to yield %-transmittance spectra. These spectra constitute molecular fingerprints that enable qualitative band assignment and subsequent quantitative analyses.

2.5.2 Thermogravimetric analysis (TGA) and differential scanning calorimetry (DSC)

Simultaneous thermal analysis (STA), combining thermogravimetric analysis (TGA) and differential scanning calorimetry (DSC), was conducted using the Hitachi NEXTA STA200. This instrument integrates TGA and DSC capabilities, enabling simultaneous detection of mass changes and thermal transitions during a single measurement cycle. It features a horizontal differential balance for enhanced sensitivity and baseline stability, with operational capability from ambient to 1100 °C. The instrument ensures high precision in detecting minute mass variations, with a thermogravimetric (TG) baseline drift of less than 10 µg. Standard DSC functionality facilitates accurate measurement of heat flow associated with thermal events, and an optional specific heat capacity measurement feature allows for comprehensive thermal characterisation. It boasts a temperature precision of ±0.07 °C and a temperature accuracy of ±0.2 °C, ensuring dependable and reproducible measurements across its operational range. Advanced balance control technology, combined with a horizontal digital dual-beam system, achieves microgram-level baseline stability and reproducibility. The instrument supports constant heating rates. It helps in studying thermally induced phenomena in materials.

In this study, the NEXTA STA200 was utilised to investigate the thermal and structural changes in quartz samples during heating and annealing processes, providing precise and reliable data critical for understanding material behaviour under varying thermal conditions. The STA experiment was performed on sample of ~5 mg using a platinum pan in a nitrogen atmosphere (100 ml/min), with a temperature ramp from 30 to 900 °C at 10 °C/min in a single-ramp programme, followed by automatic air cooling. This single-ramp STA measurement provided concurrent mass-loss (TG) and heat-flow (DSC) data, enabling detailed assessment of thermal and structural changes in the quartz sample.

Chapter 3

3. Natural factors affecting the quartz luminescence

3.1 Introduction

The luminescence of quartz sand grains preserves information about the formation of minerals and their transportation process after the formation. This chapter focuses specifically on the transportation process, which is captured by the change in the structural defect and manifests as variations in the luminescence characteristics of the sand grains. Analysing luminescence reveals insights into the environmental conditions resulting in changes in natural quartz crystals. A key question remains unclear: why and how does quartz's luminescence sensitivity change over time in natural settings? It is often observed that the luminescence signal of quartz significantly sensitises along its journey (Fig. 3. 1), suggesting changes in defect centres during this journey. A fundamental understanding of the process could enhance its utility for understanding sediment dynamics in the earth's surface processes.

The journey of quartz sand grains starts after detaching from their source rock through the weathering process. Quartz minerals are subject to diverse environmental conditions during their transportation, varying from a few years to a million years, depending on the geological settings. Based on established research, luminescence sensitisation of quartz sediment occurs throughout its journey and depends on the sedimentary history and the type of quartz originating from specific lithology (Fitzsimmons, 2011). Repeated deposition and reworking sometimes sensitises the quartz luminescence signal (Pietsch et al., 2008). It is observed that the geological pathway of transport affects quartz luminescence, such as aeolian transport records a higher sensitisation and lacustrine and periglacial sediment lower sensitisation (Fitzsimmons et al., 2010).

There are three crucial potential natural factors experienced by quartz during transit that can have a considerable effect on its luminescence characteristics. These **factors (F)** are (1) variations in temperatures, (2) damage by ionising radiation from natural isotopes of U, Th and K present in the surrounding matrix, and (3) light exposure (Fig. 3. 1). Therefore, a detailed and explicit separate study of these factors on luminescence characteristics is essential. In this chapter, the experiments are typically done by observing changes in luminescence parameters (detailed in Chapter 2), such as peaks of thermoluminescence (TL) and components of optically stimulated luminescence (OSL) signals, by mimicking the above potential natural factors on laboratory condition. The luminescence parameters represent the responses of distinct trap groups, characterised by properties such as trap depth, escape frequency, and photoionisation cross-section (PICS). The effect of factors on these luminescence parameters is studied to establish a connection between defect dynamics in crystal and sediment dynamics in natural systems.

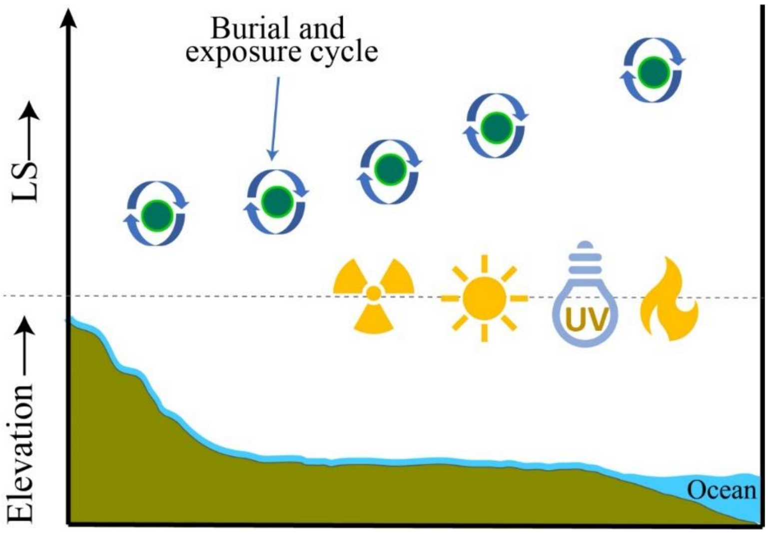

Fig. 3. 1: Sediments travelling from source to sink undergo several deposition cycles that sensitise their luminescence signal and natural factors such as irradiation, light exposure (sunlight), and thermal environment.

This change in luminescence characteristics can be explored using luminescence parameters. By investigating the causes of sensitivity change in a geological environment, key information about the physical conditions experienced by quartz crystals can be inferred.

3.2 Samples

A variety of samples were selected for this study, representing a range of luminescence sensitivities and geological provenances, as summarised in Table 3. 1. Quartz luminescence generally increases along the sedimentary pathway—from freshly liberated quartz grains in bedrock to well-reworked sedimentary quartz. Thus, selecting samples with different luminescence sensitivities reflects their varied transport and exposure histories.

To investigate the effects of laboratory-induced treatments across a spectrum of natural luminescence behaviours, samples were grouped into three distinct categories based on their blue-light stimulated luminescence sensitivity (BSLS): dull, medium, and bright. The method for calculating 110 °C TL and BSL intensity is described in Section 2.4.4.

This classification is grounded in both empirical observations and geological context:

- Dull samples (BSLS ≈ 100 photon counts / (Gy × mg)) are typically derived from rock or weathered bedrock and display low sensitivity.
- Medium samples (500–2000 photon counts / (Gy × mg)) are generally freshly eroded fluvial sediments with intermediate sensitivity.
- Bright samples (>8000 photon counts / (Gy × mg)) are older, well-transported sediments that have likely experienced multiple episodes of transport, erosion, and re-deposition—processes known to enhance luminescence sensitivity.

The thresholds for each category were chosen to ensure clear separation between these distinct geological groups, based on the BSLS values observed across the full dataset. Table 3. 1 presents the sample details, including location, type, BSLS values, and luminescence classification.

Table 3. 1: Details of samples used in the study and their location, sample type, BSLS, and luminescence category.

Sample name	**Location**	**Sample type**	**BSLS (Photon counts / (Gy × mg))**	**Luminescence category**
HELN-2	Himalaya	Quartzite rock	7 ± 1	Dull
SR-1A	Sabarmati River	Weathered quartzite rock	123 ± 30	Dull
SR-25	Sabarmati River	Fluvial sediment	760 ± 82	Medium
MHD	Sabarmati River	Fluvial sediment	10295 ± 953	Bright
PASMI-8	Sahara Desert	Aeolian sediment	10324 ± 1293	Bright

3.3 Measurement protocol and technique

In the luminescence experiment, the protocol is designed to achieve the objective while minimising any impact on the luminescence characteristics of the quartz during measurement. Stimulation is performed using blue LED, and a detection filter U-340 is used to target particular luminescence centres (refer to Chapter 2 for details). The protocol for TL (thermoluminescence), CW-BSL (continuous wave blue-stimulated luminescence), and LM-BSL (linearly modulated blue-stimulated luminescence) measurements covering both **natural conditions and laboratory-treated factors (e.g., annealing, irradiation, or light exposure)** effects on the samples, is elaborated in the following section. The word BSL is used for blue light stimulation. The luminescence signals are weight and dose normalised and averaged.

3.3.1 Resetting of natural signal

The presence of natural irradiation dose, stored as trapped electrons in the quartz lattice, complicates sensitivity analysis due to the lack of prior irradiation information and variation from sample to sample. Even if the surface samples are exposed to sunlight, they have a TL signal above 200 ºC, which might not be fully bleached. Without bleaching, the signal corresponding to a specific irradiation dose may be unreliable. To overcome this, pre-existing trapped electrons and holes are eliminated by light exposure, effectively resetting the luminescence signal. This process ensures that all samples exhibit background-level luminescence before the subsequent known irradiation step.

To investigate this effect, the samples are given a known dose (~20 Gy) without bleaching natural luminescence signal and a full TL glow curve up to 450 ºC is recorded with background subtraction (TL1) (Fig. 3. 2). Similarly, another TL glow curve is also recorded without any artificial dose (TL2), as detailed in

Table 3. 2. The difference (TL1 - TL2) isolates the TL glow peak, corresponding to 20 Gy beta irradiation doses. Figure 3.2 illustrates an undesirable TL signal (TL1-TL2) due to the presence of natural TL signals. Laboratory irradiation faces competition for traps, leading to reduced trapping efficiency. This occurs because the natural dose is often much higher, resulting in negligible luminescence from the test dose. This comparison suggests that the natural signal biases the system, which compromises accuracy. Therefore, removing the natural signal through bleaching is essential to maintain an unbiased system and ensure accurate luminescence measurements.

Table 3. 2: Protocol for measurement of TL glow curve without bleaching natural signal.

Steps	**TL1**	**TL2**
1	Natural	Natural
2	No bleach	No bleach
3	Beta dose (~20 Gy)	Beta dose (0 Gy)
4	TL at 450 °C, background subtracted	TL at 450 °C, background subtracted

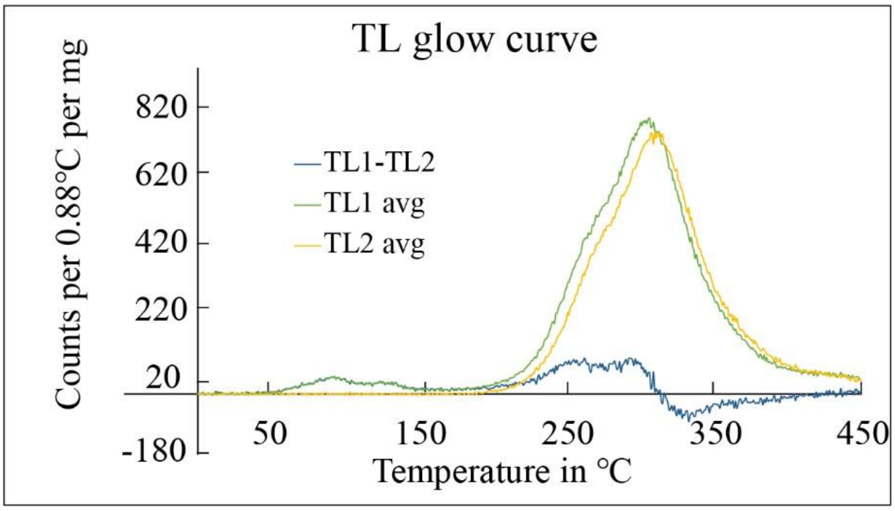

Fig. 3. 2: Natural TL glow curve (TL1), Natural +(20 Gy) TL glow curve (TL2), and TL glow curve corresponding to 20 Gy (TL1-TL2). (Without any bleaching of natural signal)

For the bleaching of natural luminescence, the quartz samples were exposed to blue LED for 10 minutes at 125 °C, and their change in the luminescence sensitivity of the sample was recorded, following the protocol outlined in Table 3. 3. The sample was first bleached for 40 seconds to remove any TL and BSL signals. A beta dose of ~20 Gy was then applied, followed by preheating at 220 °C. During this preheating step, the 110 °C TL signal was measured, and the corresponding thermoluminescence sensitivity (110 °C TLS) was calculated. Then, a 40-second BSL measurement was used to evaluate the BSLS. To examine the effect of prolonged optical stimulation, the sample was subjected to a 10-minute bleaching step at 125 °C. The 110 °C TLS and BSLS signals were recorded during steps 7–9. All BSL measurements were conducted at 125 °C to minimise the retrapping of detrapped electrons. The method for calculating 110 °C TL and BSL intensity is described in section 2.4.4. This protocol allowed for the evaluation of luminescence sensitivity changes in response to bleaching.

Table 3. 3: Protocol for measurement of the effect of prolonged bleaching on 110 ºC TLS and BSLS of the sample.

Steps	**Protocol**	**Remark**
1	Natural	Natural sample
2	BSL 125 ºC (40 s)	Bleaching
3	Beta dose (~20 Gy)	Irradiation
4	Preheat 220 ºC	Record of 110 ºC TLS
5	BSL 125 ºC (40 s)	BSLS
6	BSL 125 ºC (10 min)	Effect of 10 min bleaching
7	Beta dose (~20 Gy)	Irradiation after bleaching
8	Preheat 220 ºC	110 °C TLS (10 min bleach)
9	BSL 125 ºC (40 s)	BSLS (10 min bleach)

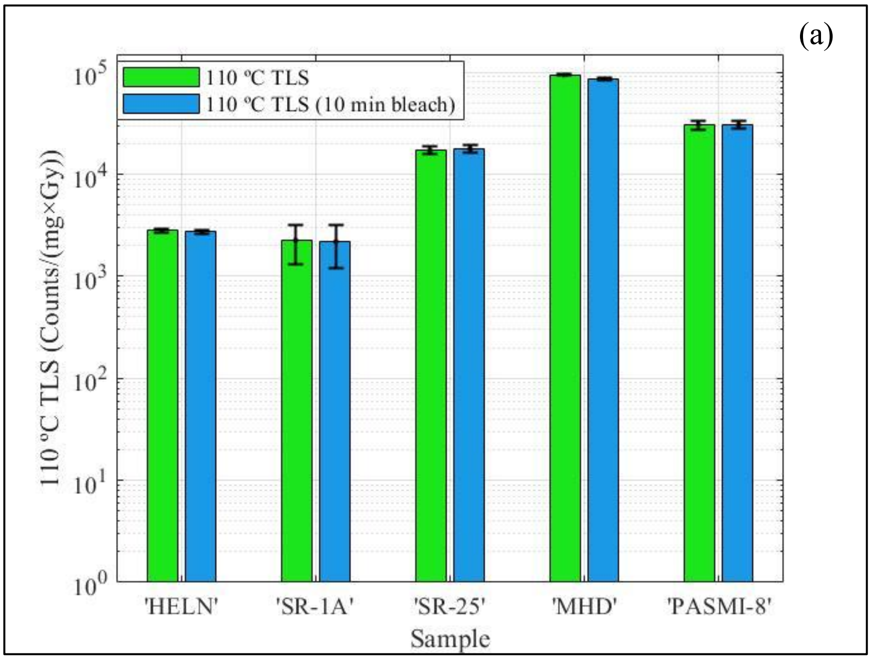

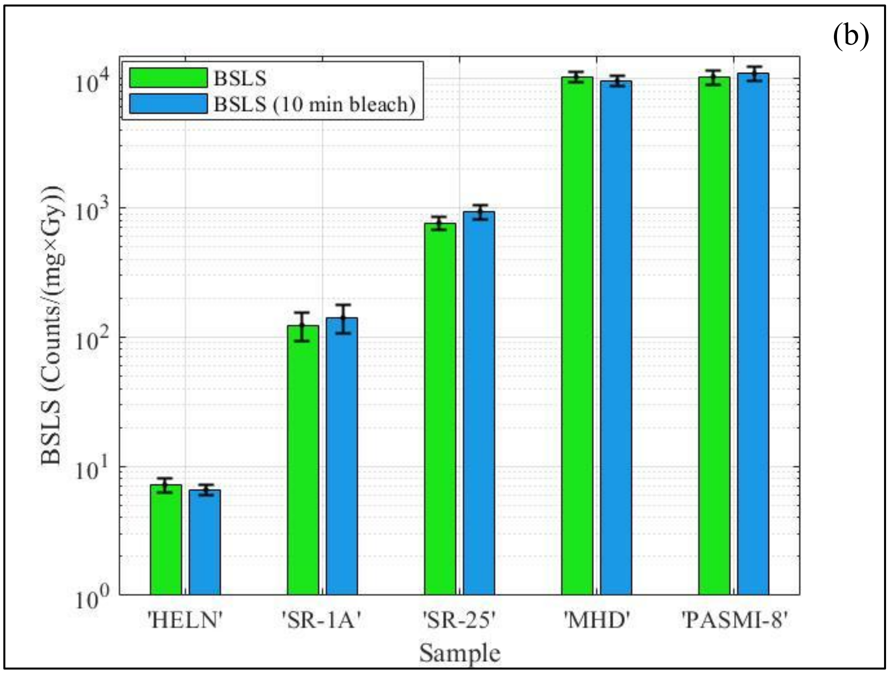

Fig. 3. 3: Effect of prolonged optical stimulation on (a) 110 ºC TLS and (b) BSLS signals.

Fig. 3. 3a and b illustrate no significant change in the 110 ºC TLS and BSLS signals due to the 10-minute bleaching step across all samples. This confirms the suitability of the 10-minute bleaching step, which is therefore adopted for subsequent measurements at 125 ºC.

3.3.2 Protocol for evaluating the effect of laboratory-treated factors on TL

The TL glow curve of natural quartz, ranging from room temperature (RT) to 450 °C, is recorded and analysed to evaluate variations in sensitivity due to different laboratory-treated factors across different samples. The lower TL peak at 110 °C has a lifetime of 0.13 x 10^{-3} years, while the higher temperature peaks at 375 °C exhibit lifetimes extending ≥ 10^8 years (Aitkin, 1985). The 110 °C TL peak is widely used in provenance studies (Liu et al., 2022; Zular et al., 2015). This study focuses on assessing the effects of various treatment factors on the 110 °C TL peak and also examines higher-temperature peaks, which have been less frequently studied and are rarely applied in provenance analysis (Goswami et al., 2023).

Generally, traps corresponding to the TL glow curve consist of light-sensitive and light-insensitive parts. The light-sensitive parts, particularly the 325 °C and 375 °C TL peaks, are believed to be associated with the BSL signal (Franklin et al., 1995; Spooner, 1994). Franklin (1997) further classified these peaks based on their optical interaction, identifying the 375 °C peak as the low bleaching peak (SBP) and the 325 °C peak as the rapid bleaching peak (RBP). This study focuses on three signals: the light-sensitive part, which is bleachable under optical stimulation; the light-insensitive part, which remains unbleached during optical stimulation; and the full TL glow curve. Their changes due to the factors are also explored.

The protocol for TL measurements is outlined in Table 3. 4, where 'F' represents the natural factor, which can include annealing, irradiation, or light exposure. The samples are divided into four parts to measure TLN1, TLN2, TLF1, and TLF2. In step 1, the TLF1 and TLF2 parts are treated with the laboratory-treated factors. In Step 2, all parts are bleached with blue light at 125 °C for 10 minutes to remove natural luminescence signals. Step 3 involves irradiating the samples with beta radiation (~20 Gy) to introduce a known dose of trapped electrons. In Step 4, TLN2 and TLF2 parts are further bleached using 125 °C BSL for 80 seconds to remove light-sensitive trapped electrons. In Step 5, all samples are preheated at 220 °C for each measurement to isolate the lower TL peak, which is several orders of magnitude stronger than the higher TL glow curves (220–450 °C). The preheat signals corresponding to TLN1 and TLF1 are used to evaluate the 110 °C TL sensitivity. In step 6, the full glow curve is recorded in this step with background subtraction to account for potential black body contributions from the higher TL glow curve. For comparison purposes, 3–6 glow curves were averaged for each sample, representing the collective luminescence response of approximately 6,000–10,000 grains. However, around the TL peak regions, the raw photon counts typically exceed 3,000, and the associated counting uncertainty (√N) is less than 1% of the signal. Given this low relative error, the impact on the overall shape of the glow curve is negligible.

Thermoluminescence signals for natural sample:

- TLN1: Full TL glow curve up to 450 °C after preheating.
- TLN2: Light-insensitive part of the TL glow curve up to 450 °C after preheating.
- TLN1-TLN2: Light-sensitive part of the TL glow curve up to 450 °C after preheating.

Similarly, for samples treated with factors:

- TLF1: Full TL glow curve up to 450 °C after preheating following laboratory-treated factors.
- TLF2: Light-insensitive part of the TL glow curve up to 450 °C after preheating following laboratory-treated factors.
- TLF1-TLF2: Light-sensitive part of the TL glow curve up to 450 °C after preheating following laboratory-treated factors.

Full TL glow curve = Light-insensitive TL + Light-sensitive TL

The TL signals are then compared to evaluate changes in luminescence characteristics due to the controlled laboratory-treated factors. The thermoluminescence glow curve are denoted using TLF labels, such as **TLAN** for annealing, **TLIR** for irradiation, **TLS** for sunlight exposure, and **TLU** for UV exposure, as discussed in later sections.

Table 3. 4: Protocol for TL measurement.

Step no	Protocol	TLN1	TLN2	TLF1	TLF2
	Natural	Natural	Natural	Natural	Natural
1	Laboratory-treated factors (e.g., irradiation, annealing, light exposure)			Factor	Factor
2	Bleach for 10 minutes at 125 °C	BSL at 125 ºC (10 min)	BSL at 125 ºC (10 min)	BSL at 125 ºC (10 min)	BSL at 125 ºC (10 min)
3	Beta irradiation	Beta (~20Gy)	Beta (~20Gy)	Beta (~20Gy)	Beta (~20Gy)
4	Bleaching of Light-sensitive trapped electrons		BSL at 125 ºC (80 s)		BSL at 125 ºC (80 s)
5	Preheat at 220 °C for 10 seconds	PH 220 °C (10 s)	PH 220 °C (10 s)	PH 220 °C (10 s)	PH 220 °C (10 s)
6	Record TL signal (up to 450 °C)	TL 450 °C, background subtracted	TL 450 °C, background subtracted	TL 450 °C, background subtracted	TL 450 °C, background subtracted

3.3.3 Protocol for evaluating the effect of laboratory-treated factors on CW-BSL

Continuous wave blue stimulated luminescence (CW-BSL), like the 110 °C TL signal, is widely used in provenance studies (Gray et al., 2019; Sawakuchi et al., 2020; Souza et al., 2023; Zular et al., 2015). The protocol outlined in Table 3. 5 is used to measure the blue-stimulated luminescence (BSL) signals of natural quartz samples and factor-treated quartz to evaluate the effects of the factors on the quartz CW-BSL. The sample is divided into two parts for CWN and CWF measurement.

In Step 1, the CWF samples are treated with factors such as irradiation, annealing, or light exposure to investigate their effects. In Step 2, CWN and CWF samples are bleached for 10 minutes at 125 °C to remove residual natural luminescence signals. In Step 3, the samples are irradiated with a known beta dose (~20 Gy). In Step 4, the samples are preheated at 220 °C for 10 seconds to eliminate unstable traps on a laboratory timescale. Finally, in Step 5, CW-OSL signals are measured at 125 °C for both CWN (natural) and CWF (factor-treated) samples. The BSL measurement at 125 °C minimises retrapping during optical stimulation. CWN and CEF are normalised in weight and dose to find the corresponding BSLS.

- CWN: Blue light-stimulated luminescence of the natural sample for a specified dose.
- CWF: Blue light-stimulated luminescence of the sample treated with laboratory factors for a specified dose.

Table 3. 5: Protocol for CW-BSL measurement.

Steps	**Protocol**	**CWN**	**CWF**
	Natural	Natural	Natural
1	Laboratory-treated factors (e.g., irradiation, annealing, light exposure)		Factor
2	Bleach for 10 minutes at 125 °C	bleach 10 min (125 ºC)	bleach 10 min (125 ºC)
3	Beta irradiation	Beta (~20Gy)	Beta (~20Gy)
4	Preheat at 220 °C for 10 seconds	PH 220 °C (10 s)	PH 220 °C (10 s)
5	Signal measurement	CW-BSL 125°C	CW-BSL 125°C

3.3.4 Protocol for evaluating the effect of laboratory-treated factors on LM-BSL

Linear modulated blue-stimulated luminescence (LM-BSL) measurements were performed by gradually increasing the stimulation light intensity from zero to maximum power over 3600s (as described in detail in Chapter 2). The samples were divided into four categories: LMN1, LMN2, LMF1 and LMF2. The LMN1 and LMN2 are used for the measurement of natural LM-BSL signals. Before their LM-BSL signals were recorded, LMF1 and LMF2 underwent specific laboratory-treated factors, such as annealing, irradiation, or light exposure. After these treatments, the LM-BSL signals were denoted as LMF, representing the factor-treated samples.

Table 3. 6 outlines the protocol for LM-BSL measurement. In Step 1, The LMF1 and L MF2 parts were treated with specific factors such as annealing, irradiation, or light exposure to

investigate their effects on luminescence characteristics. In Step 2, all samples are bleached with blue light for 10 minutes at 125 °C to remove residual natural luminescence signals. In Step 3, a known beta dose (~20 Gy) is applied to the LMN1 and LMF1 samples, while the LMN2 and LMF2 samples are not irradiated as they are used for background subtraction. In Step 4, the samples are preheated at 220 °C for 10 seconds to eliminate unstable traps and stabilise the luminescence signal. Finally, in Step 5, LM-BSL signals are recorded at 125 °C for all samples, with background subtraction applied to isolate the desired luminescence signal. The LM-BSL measurements are conducted at 125 °C to minimise the retrapping of electrons during optical stimulation.

LM-BSL signals and definitions

- LMN1: LM-BSL peak for 20 Gy.
- LMN2: LM-BSL peak for 0 Gy (acts as background).
- LM (Natural) = LMN1 - LMN2: LM-BSL peak for 20 Gy after subtracting the background.

For treated samples:

- LMF1: LM-BSL peak for 20 Gy + residual natural dose after laboratory-treated factors.
- LMF2: LM-BSL peak for 0 Gy + residual natural dose after laboratory-treated factors.
- LM (Factor) = LMF1 - LMF2: LM-BSL peak for 20 Gy after subtracting the background for samples treated under laboratory-controlled factors.

The difference between LMN1 and LMN2 provides the LM-BSL peak for the natural sample (20 Gy dose), while the difference between LMF1 and LMF2 gives the LM-OSL peak for the factor-treated sample (20 Gy dose). These signals are then compared to assess how the laboratory-treated factors influence luminescence characteristics, particularly with respect to trap dynamics and luminescence sensitivity.

Table 3. 6: Protocol for LM-BSL measurement.

Steps	**Protocol**	**LMN1**	**LMN2**	**LMF1**	**LMF2**
	Natural	Natural	Natural	Natural	Natural
1	Laboratory-treated factors (e.g., irradiation, annealing, light exposure)			Factor	Factor
2	Bleach for 10 minutes at 125 °C	bleach 10 min (125 ºC)	bleach 10 min (125 ºC)	bleach 10 min (125 ºC)	bleach 10 min (125 ºC)
3	Beta irradiation	Beta (~20Gy)	Beta (0Gy)	Beta (~20Gy)	Beta (0Gy)
4	Preheat at 220 °C for 10 seconds	PH 220 °C (10 s)	PH 220 °C (10 s)	PH 220 °C (10 s)	PH 220 °C (10 s)
5	Signal measurement	LM-BSL (125 °C), background subtracted	LM-BSL (125 °C), background subtracted	LM-BSL (125 °C), background subtracted	LM-BSL (125 °C), background subtracted

3.4 Effect of annealing on luminescence characteristics of quartz

Earth’s surface temperatures vary widely due to both natural and human-induced events. Naturally, recorded temperatures range from a high of 56.7 °C to a low of −89.2 °C (World Temperature Records - Current Results, n.d.-b). Over geological timescales, global mean surface temperatures have oscillated between 11 °C and 36 °C (Judd et al., 2024). Localised heating events can produce much higher values: lava flows may raise surface temperatures to 1,200 °C (Pinkerton et al., 2002), while lightning strikes can generate temperatures near 30,000 °C, though over very limited areas (NOAA’s National Weather Service, n.d.). Meteorite impacts also produce intense heat at the point of contact, often exceeding several thousand degrees Celsius (Timms et al., 2017). Human activities contribute as well. Industrial accidents, military detonations, and weapons testing can cause extreme surface heating. Coal seam fires, for instance, can elevate ground temperatures from 60 °C to several hundred degrees Celsius (Kuenzer et al., 2013). Forest fires—triggered by lightning or human activity—are among the most widespread heating events, with surface temperatures reaching up to 1,100 °C, often resulting in substantial changes to surface materials (Agbeshie et al., 2022; Chicco et al., 2023; Wotton et al., 2011). This comprehensive view highlights the vast range of temperatures experienced by the Earth's surface due to both natural events and human activities.

Numerous studies have explored the effects of heating on the luminescence characteristics of quartz. High-temperature treatments impact quartz sensitivity significantly (Li, 2002). Wintle and Murray (1999, 2000) state that the thermal sensitisation of Australian quartz could be achieved by long storage at relatively high environmental temperatures. Han et al. (2000) investigated the annealing effects on the TL sensitivity of granite quartz, noting changes in sensitivity between 150 °C and 375 °C. They reported that TL sensitivity increases below 250 °C and continues to rise for peaks above 250 °C. Similarly, Poolton et al. (2000) studied high-temperature annealing effects on natural quartz, finding that both OSL and TL sensitivity were greatly enhanced, likely due to increased recombination centres.

Quartz sediment grains exposed to natural environments over kiloyears can undergo thermal sensitisation from small-scale fire events within a short period. This study aims to determine the impact of annealing on luminescence characteristics of quartz. This study investigates the effect of annealing on the luminescence characteristics of quartz. Quartz samples were annealed at 450 °C for 10 minutes with a heating rate of 2 °C/s to assess changes in their luminescence characteristics.

3.4.1 Effect of annealing on 110 ºC TLS

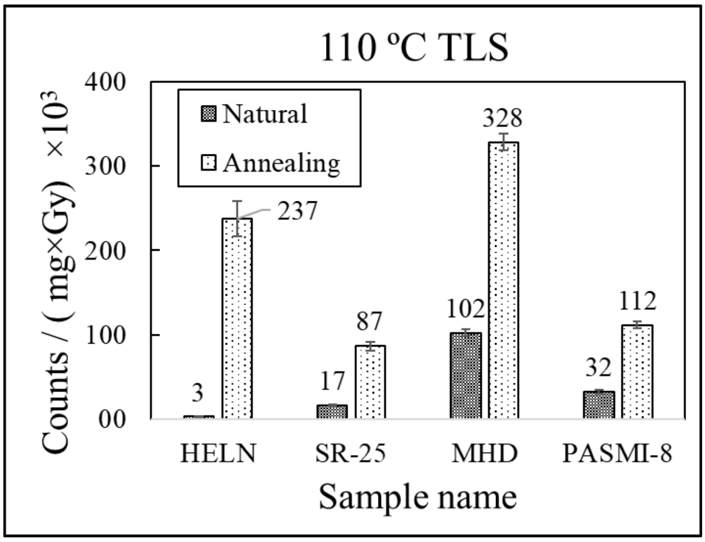

Fig. 3. 4: 110 ºC TLS for quartz samples HELN, SR-25, MHD, and PASMI-8 under natural conditions and after annealing at 450 °C for 10 minutes.

Fig. 3. 4 presents the 110 °C TLS for four quartz samples—HELN, SR-25, MHD, and PASMI-8—under natural conditions and after annealing. The results are summarised as follows:

HELN (Dull sample):

Under natural conditions, the 110 ºC TLS is minimal, with a value of 3×10^3 counts/(mg×Gy). After annealing, there is a significant increase, with the 110 ºC TLS reaching 237×10^3 counts/(mg×Gy), indicating an 80-fold sensitisation effect.

SR-25 (Medium sample):

The 110 ºC TLS under natural conditions is 17×10^3 counts/(mg×Gy). After annealing, the 110 ºC TLS increases to 87×10^3 counts/(mg×Gy), showing a 5-6-fold enhancement.

MHD (Bright sample):

The 110 ºC TLS under natural conditions is 102×10^3 counts/(mg×Gy). Post-annealing, the 110 ºC TLS rises dramatically to 328×10^3 counts/(mg×Gy), highlighting a 3-4-fold sensitisation effect.

PASMI-8 (Bright sample):

The 110 ºC TLS under natural conditions is 32×10^3 counts/(mg×Gy). After annealing, the 110 ºC TLS increases to 112×10^3 counts/(mg×Gy), indicating a 3-4-fold enhancement.

Annealing significantly enhances the 110 °C TLS for all samples, with the increase varying between three-fold and nearly 80-fold across different samples. The increase ranges from three-fold to 80-fold, with the dull sample (HELN) showing the highest proportional increase. Medium and bright samples (e.g., SR-25, MHD, and PASMI-8) show relatively smaller proportional increases (3-6 fold), likely because they are already partially sensitised under natural conditions. High-temperature annealing enhances luminescence sensitivity by modifying defect structures, suggesting that the natural thermal history of quartz significantly influences its luminescence sensitivity.

3.4.1 Effect of annealing on higher TL glow curve (200-450 °C)

TLAN is the TL glow curve up to 450 °C after preheating following laboratory annealing as described in section 3.3.2.

Fig. 3. 5, Fig. 3. 6 represents full TL glow curve (TLN1 and TLAN1), light-insensitive TL glow curve (TLN2, TLAN2) and light-sensitive TL glow curve (TLN1-TLN2, TLAN1-TLAN2) of samples HELN-2, SR-25, MHD and PASMI-8. The results are summarised below:

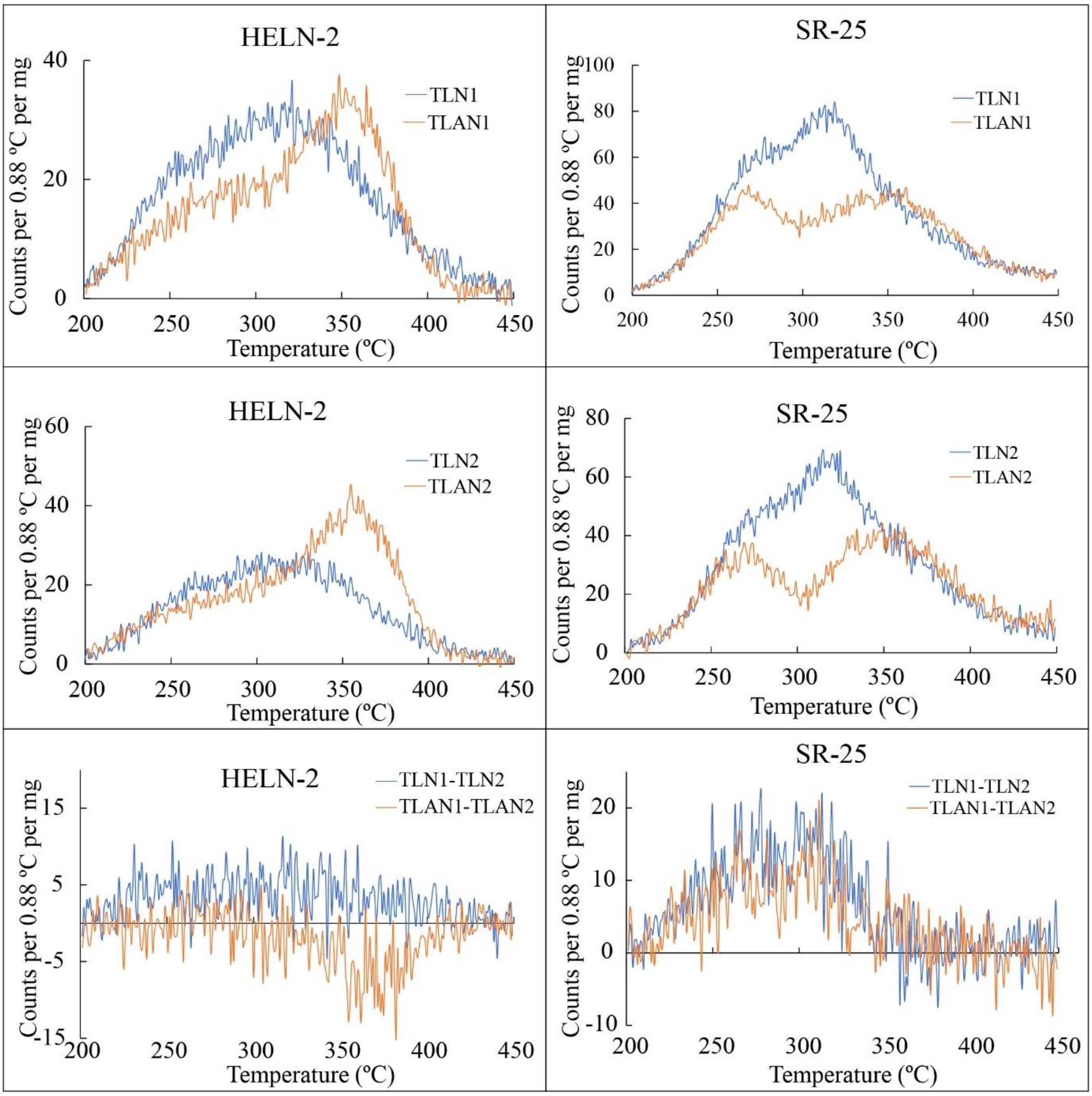

Fig. 3. 5: TL glow curves: (top) TLN1 and TLAN1, (middle) TLN2 and TLAN2, and (bottom) TLN1 - TLN2 and TLAN1 - TLAN2 for quartz samples HELN-2 and SR-25, respectively.

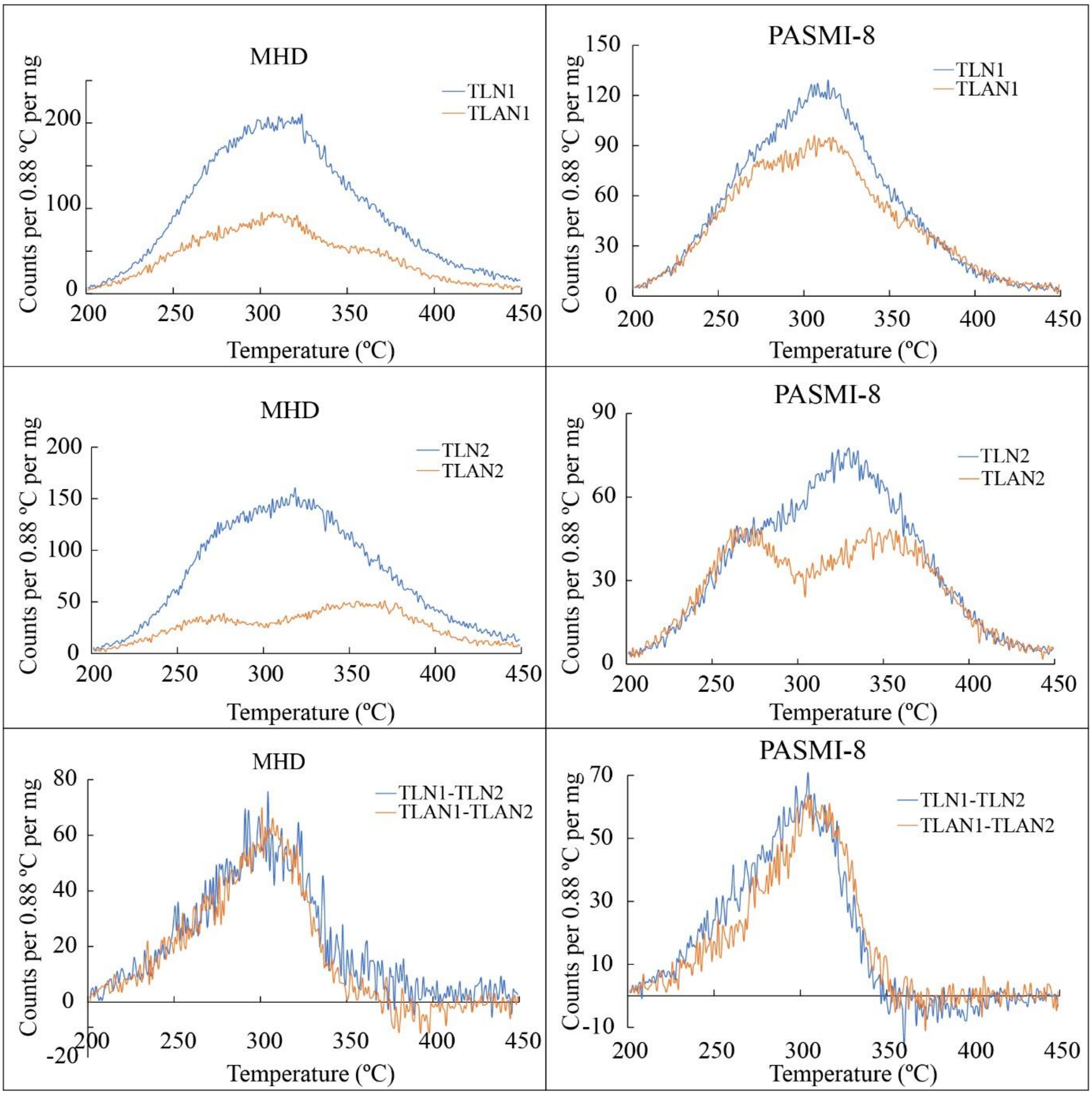

Fig. 3. 6: TL glow curves: (top) TLN1 and TLAN1, (middle) TLN2 and TLAN2, and (bottom) TLN1 - TLN2 and TLAN1 - TLAN2 for quartz samples MHD and PASMI-8, respectively.

Full TL glow curve (TLN1 and TLAN1)

- There is a decreasing trend in the full TL glow curve around 300 ºC due to annealing across all samples (Fig. 3. 5, Fig. 3. 6 top).

Light-insensitive TL glow curve (TLN2, TLAN2)

- There is a decreasing trend in the light-insensitive TL glow curve around 300 ºC due to annealing across all samples (Fig. 3. 5, Fig. 3. 6 middle). As a result, the broad TL glow curve separates into two distinct peak-shaped curves between 200-300 ºC and 300-450 ºC after annealing.

Light-sensitive TL glow curve (TLN1-TLN2, TLAN1-TLAN2)

- Annealing does not affect the light-sensitive TL glow curve's 200-450 ºC range (Fig. 3. 5, Fig. 3. 6 bottom).

Key Observations:

Annealing decreases the full TL glow curve and the light-insensitive TL glow curve, while the light-sensitive TL glow curve remains unaffected across all samples.

The higher TL peaks are believed to be related to the BSLS signal, and the light-sensitive portion of the TL glow curve would typically show an increasing trend after annealing. However, the fact that they remain the same in natural and annealing conditions raises questions about their direct correlation with the BSL signal.

3.4.2 Effect of annealing on BSLS

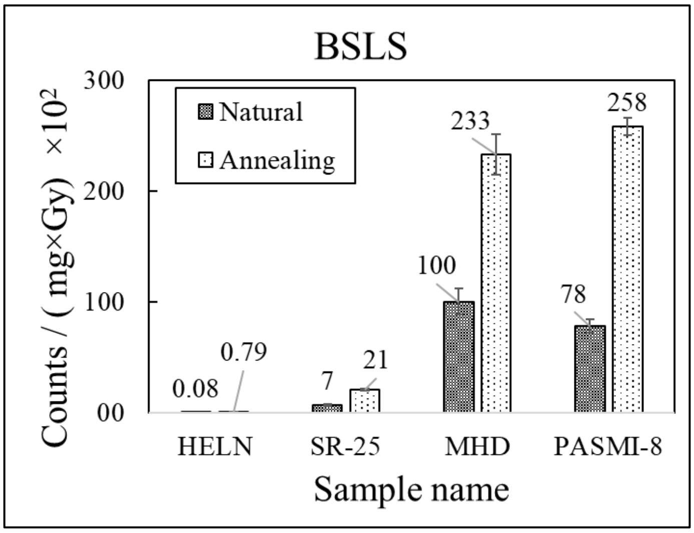

Fig. 3. 7: BSLS for quartz samples HELN, SR-25, MHD, and PASMI-8 under natural conditions and after annealing at 450 °C for 10 minutes.

Fig. 3. 7 presents the BSLS for four quartz samples—HELN, SR-25, MHD, and PASMI-8—under natural conditions and after annealing. The results are summarised as follows:

HELN (Dull sample):

The natural BSLS is 0.08×10^2 counts/(mg×Gy). After annealing, it increases significantly to 0.79×10^2 counts/(mg×Gy), demonstrating a nearly 10-fold enhancement.

SR-25 (Medium sample):

The natural BSLS is 7×10^2 counts/(mg×Gy). After annealing, it rises to 21×10^2 counts/(mg×Gy), indicating a 3-fold enhancement.

MHD (Bright sample):

The natural BSLS is 100×10^2 counts/(mg×Gy). After annealing, it increases to 233×10^2 counts/(mg×Gy), showing a 2.3-fold enhancement.

PASMI-8 (Bright sample):

he natural BSLS is 78×10^2 counts/(mg×Gy). After annealing, it increases to 258×10^2 counts/(mg×Gy), indicating a 3.3-fold enhancement.

The dull sample (HELN) exhibits the largest proportional increase in BSLS after annealing (~10-fold), whereas the medium sample (SR-25) and bright samples (MHD and PASMI-8) show increases ranging from 2 to 3-fold. Annealing significantly enhances BSLS in all samples, with the degree of enhancement decreasing as the natural sensitivity of the sample increases. This suggests that bright samples may already have a near-saturated sensitivity under natural conditions, limiting the proportional effect of annealing.

3.4.1 Effect of annealing on LM-BSL

Fig. 3. 8, Fig. 3. 9, Fig. 3. 10 and Fig. 3. 11 depict the LM-BSL of samples SR-1A (dull sample), SR-25 (medium sample), MHD (bright sample), and PASMI-8 (bright sample) under natural and after annealing conditions. The LM-BSL signals appear as a combination of multiple peaks, and after deconvolution, the components C1, C2, and C3 are identified as part of the LM-BSL signal (details provided in Chapter 2). These components define the PICS and initial trapped charge concentration of the peaks, as listed in Table 3. 7.

SR-1A (Dull Sample): The total LM-BSL signal increases by 6.88 times due to annealing. Component analysis shows a new component with PICS of 7.25×10^{-19} cm^2.

SR-25 (Medium Sample): Annealing enhances the total LM-BSL signal by 8.92 times. The component analysis shows no formation of new components, with the two existing ones persisting unchanged.

MHD (Bright Sample): Annealing enhances the total LM-BSL signal by 17.14 times. The component analysis reveals no introduction of additional components, with the existing two components remaining stable.

PASMI-8 (Bright Sample): The total LM-BSL signal increases by 13.13 times under annealing. The existing components remain unaffected, and no new components are detected.

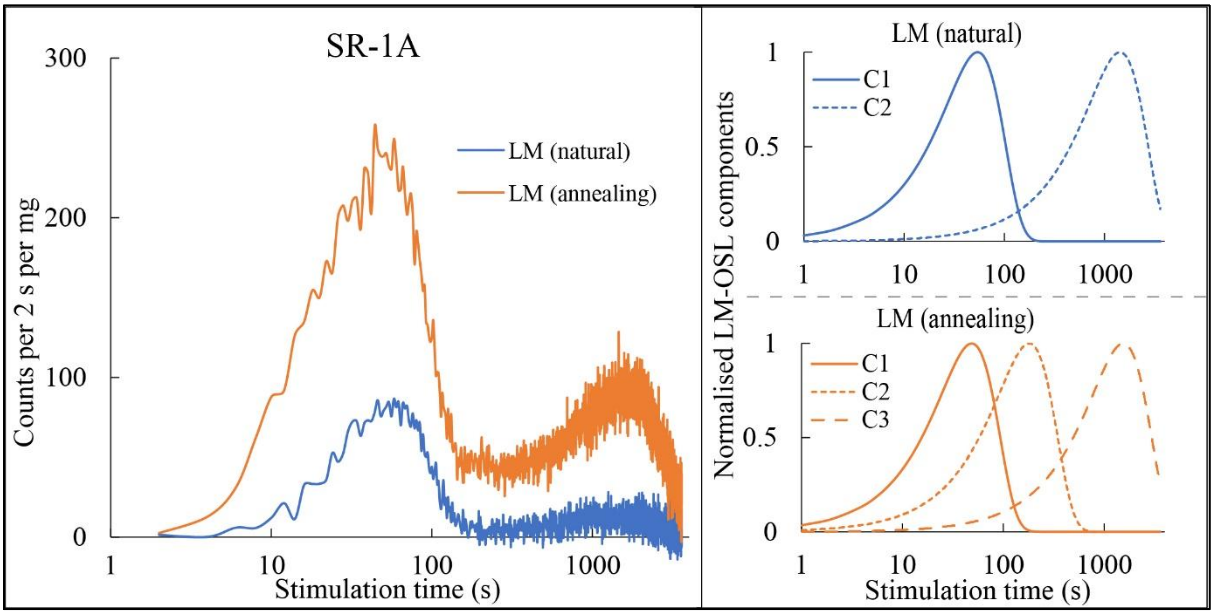

Fig. 3. 8: The left panel shows the LM-BSL of sample SR-1A (dull sample) under natural (blue) and annealed (orange) conditions. The right panels depict the deconvoluted, normalised LM-BSL components (C1, C2, and C3) for natural and annealed conditions.

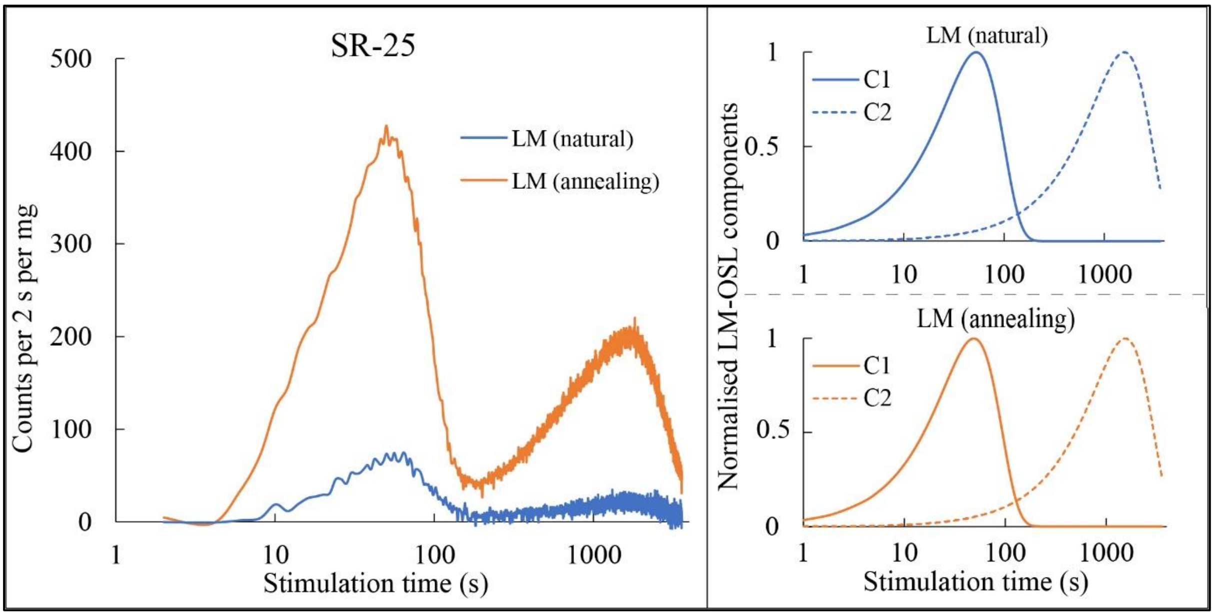

Fig. 3. 9: The left panel shows the LM-BSL of sample SR-25 (medium sample) under natural (blue) and annealed (orange) conditions. The right panels depict the deconvoluted, normalised LM-BSL components (C1 and C2) for natural and annealed conditions.

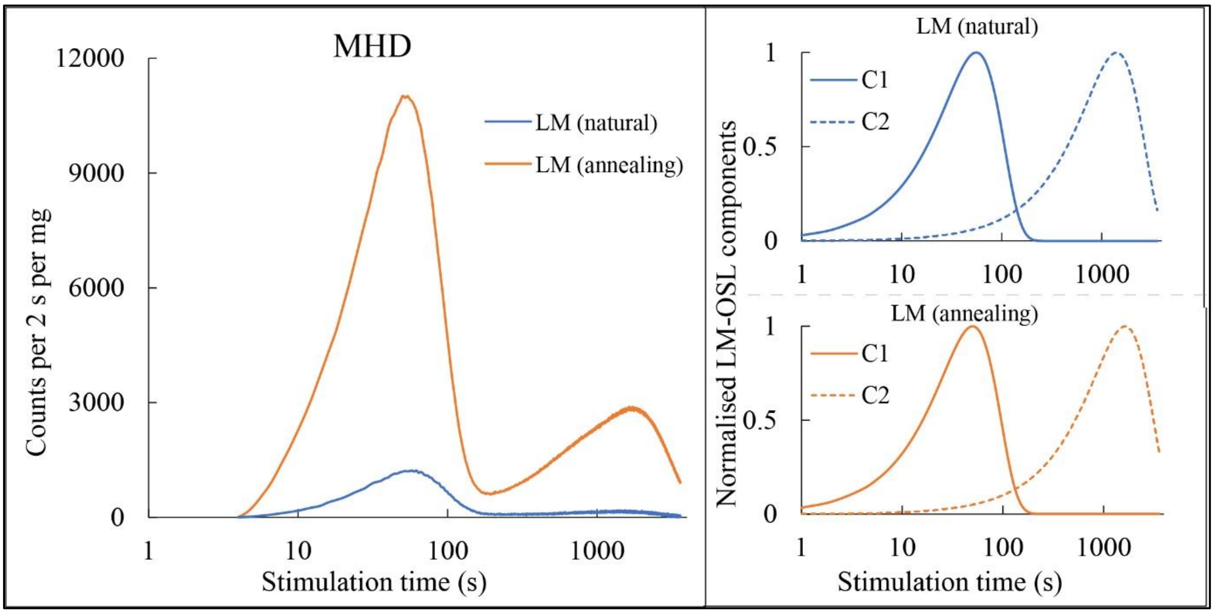

Fig. 3. 10: The left panel shows the LM-BSL of sample MHD (bright sample) under natural (blue) and annealed (orange) conditions. The right panels depict the deconvoluted, normalised LM-BSL components (C1 and C2) for natural and annealed conditions.

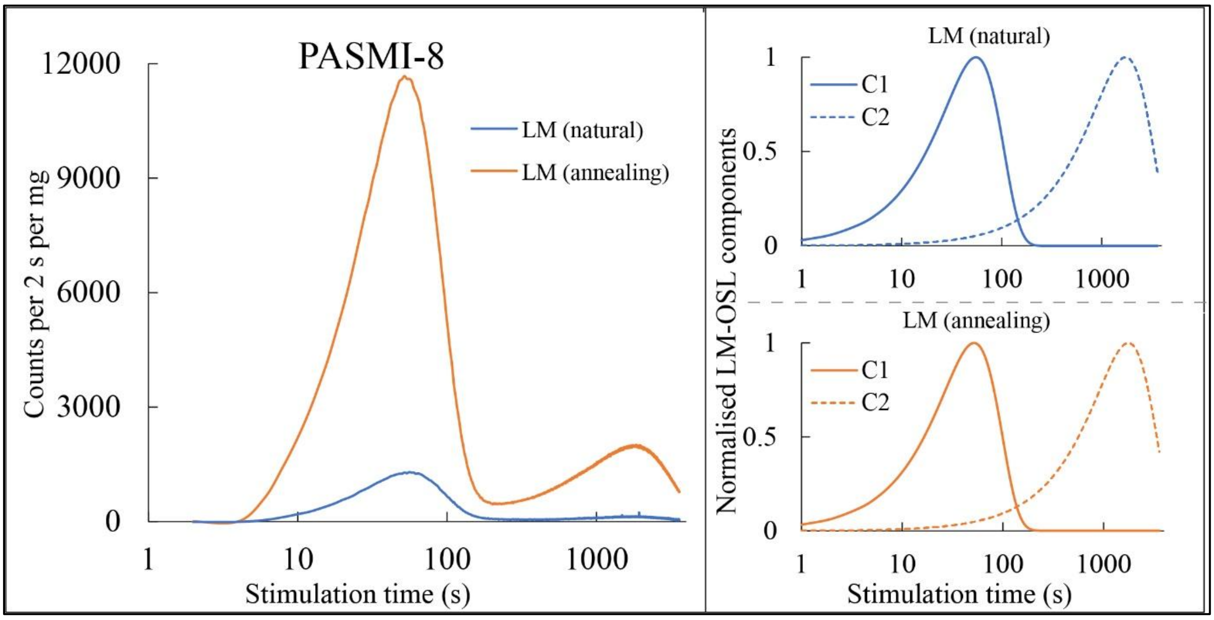

Fig. 3. 11: The left panel shows the LM-BSL of sample PASMI-8 (bright sample) under natural (blue) and annealed (orange) conditions. The right panels depict the deconvoluted, normalised LM-BSL components (C1 and C2) for natural and annealed conditions.

Table 3. 7: Initial trapped charge concentrations and PICS of quartz samples (SR-1A, SR-25, MHD, and PASMI-8) under natural and annealed conditions.

Sample name	Natural condition		Annealed condition	
	Initial trapped charge concentration	PICS (in cm^2)	Initial trapped charge concentration	PICS (in cm^2)
SR-1A (dull sample)	6.97×10^{3}	8.16×10^{-18}	1.82×10^{4}	1.01×10^{-17}
			7.33×10^{3}	7.25×10^{-19}
	2.95×10^{4}	1.18×10^{-20}	1.82×10^{4}	9.92×10^{-21}
SR-25 (medium sample)	5.56×10^{3}	8.57×10^{-18}	3.18×10^{4}	9.95×10^{-18}
	5.49×10^{4}	9.52×10^{-21}	5.07×10^{5}	9.85×10^{-21}
MHD (bright sample)	1.04×10^{5}	7.66×10^{-18}	8.55×10^{5}	9.45×10^{-18}
	3.65×10^{5}	1.20×10^{-20}	7.73×10^{6}	8.82×10^{-21}
PASMI-8 (bright sample)	1.10×10^{5}	7.80×10^{-18}	9.32×10^{5}	8.89×10^{-18}
	3.75×10^{5}	7.97×10^{-21}	5.65×10^{6}	7.63×10^{-21}

Annealing significantly increases the LM-BSL signals across quartz samples, with enhancements ranging from 6.88 times in the dull sample (SR-1A) to 17.14 times in the bright sample (MHD). The natural signal across all samples is dominated by two trap components (C1 and C2). However, annealing introduces a third component (C3) in the dull sample (SR-1A). The emergence of C3 post-annealing suggests the activation or creation of traps, likely due to annealing-induced structural changes in the quartz lattice. In contrast, the components remain the same after annealing for the medium sample (SR-25) and bright samples (MHD and PASMI-8).

3.4.2 Effect of annealing at different temperatures on BSLS

Annealing increases sensitivity significantly, so an experiment was conducted to investigate the sensitisation of BSLS as a function of annealing temperature using the protocol outlined in Table 3. 8. In step 1, samples were annealed at various temperatures (110 °C, 150 °C, 190 °C, 230 °C, 270 °C, 310 °C, 350 °C, 390 °C, 430 °C, 470 °C, and 510 °C) for 1 minutes in the Riso machine. In step 2, blue light stimulation at 125 °C was used to bleach the samples and remove residual luminescence signals. In step 3, a small beta dose of 6 Gy was applied to the samples, and in step 4, preheating was performed to eliminate unstable trapped electrons under room temperature conditions. In step 5, the BSLS is measured at 125 °C. Finally, the measurement process was repeated with various preheat temperatures (140 °C, 160 °C, 180 °C, and 200°C) to examine the independence of sensitisation from preheat temperature.

Table 3. 8: Protocol for annealing experiment.

Steps	Protocol	Remark
	Natural sample	Natural
1	Annealed at (110, 150, 190, 230, 270, 310, 350, 390, 430, 470& 510 °C) for 1 min	Different annealing temperature
2	BSL at 125 ºC	For bleaching residual signal
3	Dose (~ 6 Gy)	Irradiating sample
4	Preheat (PH)	Removing unstable traps at the laboratory time scale
5	BSL at 125 °C	BSLS signal
6	Go to step 3	To measure at different, preheat temperature

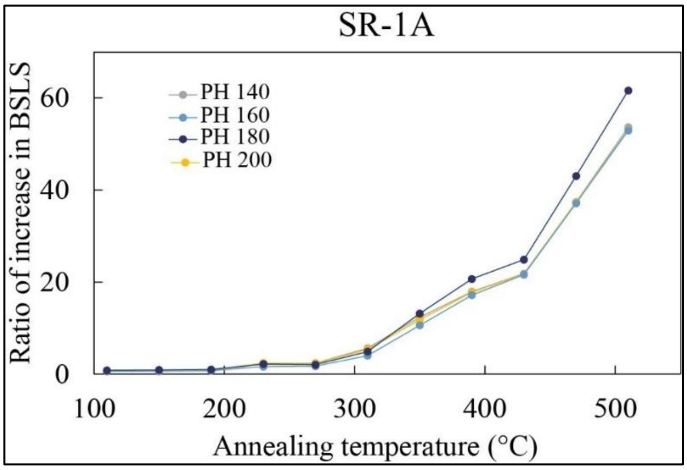

Fig. 3. 12: BSLS variation of quartz sample SR-1A at different annealing temperatures (100 °C to 500 °C) for preheat temperatures of 140 °C, 160 °C, 180 °C, and 200 °C.

Fig. 3. 12, Fig. 3. 13, Fig. 3. 14 and Fig. 3. 15 illustrate the variation in BSLS of quartz at different annealing temperatures for SR-1A (dull quartz), SR-25 (medium quartz), MHD (bright quartz), and PASMI-8 (bright quartz), respectively.

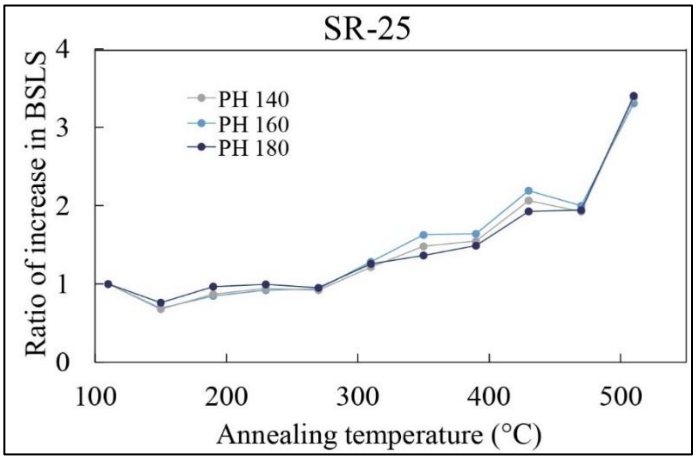

Fig. 3. 13: BSLS variation of quartz sample SR-25 at different annealing temperatures (100 °C to 500 °C) for preheat temperatures of 140 °C, 160 °C, and 180 °C.

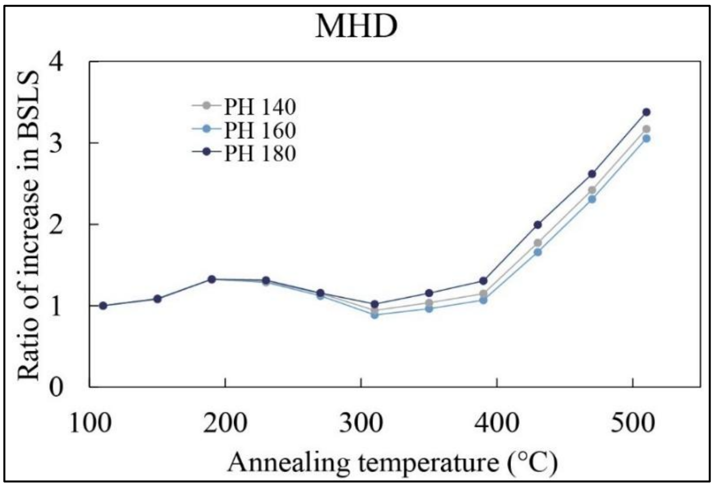

Fig. 3. 14: BSLS variation of quartz sample MHD at different annealing temperatures (100 °C to 500 °C) for preheat temperatures of 140 °C, 160 °C, and 180 °C.

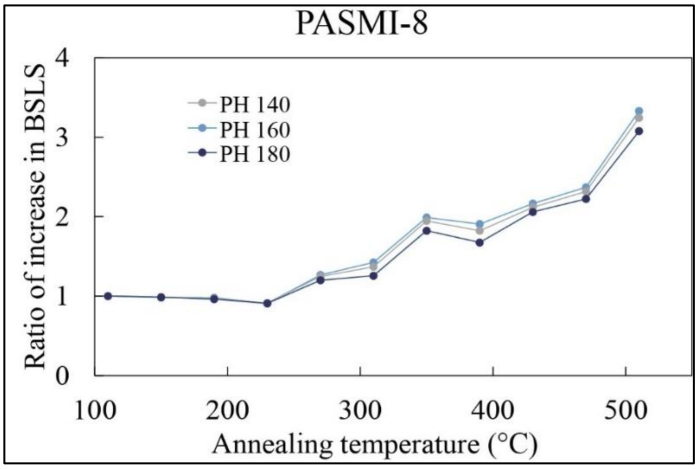

Fig. 3. 15: BSLS variation of quartz sample PASMI-8 at different annealing temperatures (100 °C to 500 °C) for preheat temperatures of 140 °C, 160 °C, and 180 °C.

- The sensitisation of SR-1A (dull sample, Fig. 3. 12) is significantly higher (~75-fold) compared to SR-25 (~4-fold, Fig. 3. 13), MHD (~3.7-fold, Fig. 3. 14), and PASMI-8 (~3-fold, Fig. 3. 15).
- The figures indicate three distinct regions: (Room Temperature – 270 °C), (270 °C – 430 °C), and (above 430 °C). Sharp increases in BSLS are observed around 270 °C and 430 °C, suggesting notable changes in the crystal lattice at these temperatures.
- The effects of annealing are much more pronounced in the dull sample (SR-1A), while medium (SR-25) and bright samples (MHD and PASMI-8) show less dramatic changes.
- The experiments conducted at different preheat temperatures confirm that sensitisation is independent of preheat temperature.

3.5 Effect of irradiation on luminescence characteristics of quartz

Irradiation is a significant natural factor that influences the luminescence characteristics of quartz sand. It involves the interaction of ionising high-energy radiation, such as alpha, beta, and gamma rays, emitted by naturally occurring radioisotopes. Major contributors include ^{238}U, ^{232}Th, ^{40}K, and others present in the soil across different regions of the Earth's crust, leading to significant spatial variations in natural dose rates (Guérin, 2013). This energy is deposited in matter through coulomb interactions for charged particles (alpha or beta radiation). Gamma radiation, being neutral, interacts by transferring energy to secondary charged particles and then coulomb interaction. Another source of radiation, cosmic rays, interact with the Earth's atmosphere and surface, with their dose contribution varying based on the longitude, latitude, altitude, and burial depth of the sample Prescott and Hutton (1988). However, cosmic dose rates typically contribute a small fraction of the total dose rate, often less than 10% in most cases. The natural dose rate received by quartz ranges from 0.5 - 4 Gy/ka (Duller, 2014).

Radiation can induce defects within quartz, which are generally classified into two categories: (1) atomic displacements from regular lattice positions by irradiation and (2) impurities modified by ionising radiation over time (Thompson, 2015). As a result, irradiation affects the luminescence characteristics. Rink (1994) noted that radiation damage within the quartz lattice strongly affects OSL characteristics. At high radiation doses, spectral emission shifts have been observed, attributed to changes in hole-trapping centres (Fasoli & Martini, 2016; Hunter et al., 2018; Mateus et al., 2020; Schmidt & Woda, 2019; Woda et al., 2002), along with variations in the trap depth of TL peaks (Mateus et al., 2020). These shifts suggest subtle alterations or creation in point defects, potentially modifying their roles in the luminescence process as recombination centres.

The present thesis uses a high radiation dose of 1000 Gy to ensure a significant impact on the quartz crystal while optimising machine time. The irradiation was performed using a ^{90}Sr/^{90}Y beta source, which emits electrons with a maximum energy of 2.27 MeV and a mean energy of approximately 600 keV (details provided in Chapter 2). The effects of this high dose were systematically studied on TL, CW-BSL, and LM-BSL signals.

3.5.1 Effect of irradiation on 110 ºC TLS

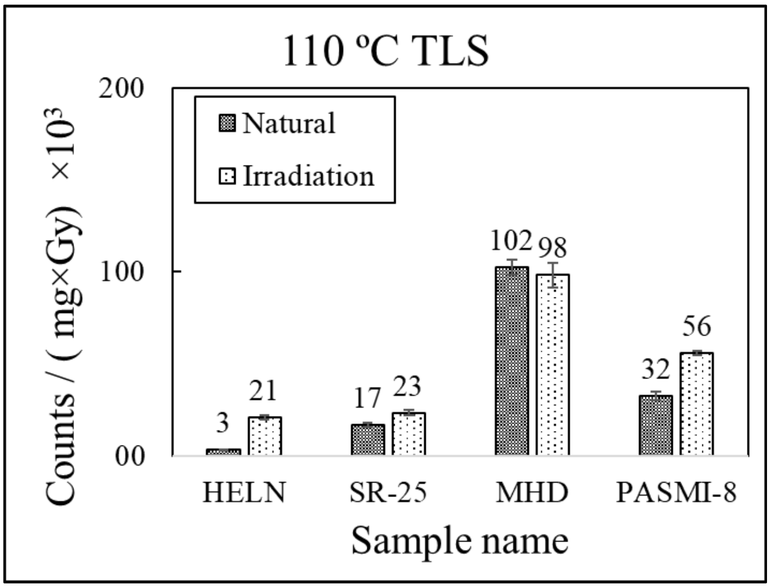

Fig. 3. 16: 110 ºC TLS for quartz samples HELN, SR-25, MHD, and PASMI-8 under natural conditions and after irradiation treatment.

Fig. 3. 16 illustrates the 110 ºC TLS for quartz samples under natural and irradiated conditions. The samples include HELN, SR-25, MHD, and PASMI-8. The results are summarised as follows:

HELN (Dull sample):

The 110 ºC TLS changes from 3×10^3 counts/(mg×Gy) to 21×10^3 counts/(mg×Gy) due to the effect of irradiation, indicating a 7-fold sensitisation.

SR-25 (Medium sample):

The 110 ºC TLS under natural conditions is 17×10^3 counts/(mg×Gy). After irradiation, the 110 ºC TLS increases to 23×10^3 counts/(mg×Gy), showing a ~1.35-fold enhancement.

MHD (Bright sample):

The 110 ºC TLS under natural conditions is 102×10^3 counts/(mg×Gy). Post-irradiation, the 110 ºC TLS changes to 98×10^3 counts/(mg×Gy), suggesting no significant sensitisation effect.

PASMI-8 (Bright sample):

The 110 ºC TLS changes from 32×10^3 counts/(mg×Gy) to 56×10^3 counts/(mg×Gy) due to the effect of irradiation, reflecting a ~1.75-fold enhancement.

Irradiation results in significant sensitisation for low-sensitivity quartz (HELN) with a 7-fold increase in 110 ºC TLS. Medium (SR-25) and bright (MHD and PASMI-8) samples show moderate enhancement (1.35–1.75-fold).

3.5.1 Effect of irradiation on higher TL glow curve (200-450 °C)

TLIR is the TL glow curve up to 450 °C after preheating following laboratory irradiation as described in section 3.3.2.

Fig. 3. 17 and Fig. 3. 18 represents the full TL glow curve (TLN1 and TLIR1), light-insensitive TL glow curve (TLN2, TLIR2) and light-sensitive TL glow curve (TLN1-TLN2, TLIR1-TLIR2) of samples HELN-2, SR-25, MHD and PASMI-8.

Results

Full TL glow curve (TLN1 and TLIR1)

1. After irradiation, A decreasing trend in the Full TL glow curves is observed in the dull sample (HELN) and medium sample (SR-25).

2. Conversely, an increasing trend, particularly in the 200–300 °C range, is observed in the bright samples (MHD and PASMI-8).

Light-insensitive TL glow curve (TLN2 and TLIR2)

1. Irradiation does not significantly affect the light-insensitive part (200–450 °C) in the dull sample (HELN) and medium sample (SR-25).

2. In bright samples (MHD and PASMI-8), there is an increase in the light-insensitive part due to high irradiation around 200-300 °C.

Light-sensitive TL peaks (TLN1-TLN2 and TLIR1-TLIR2)

1. A slight decrease in light-sensitive TL peaks is observed in the dull sample (HELN) and medium sample (SR-25).

2. In bright samples, no change is observed in MHD, whereas PASMI-8 shows an increase in the lower temperature range (200–300 °C).

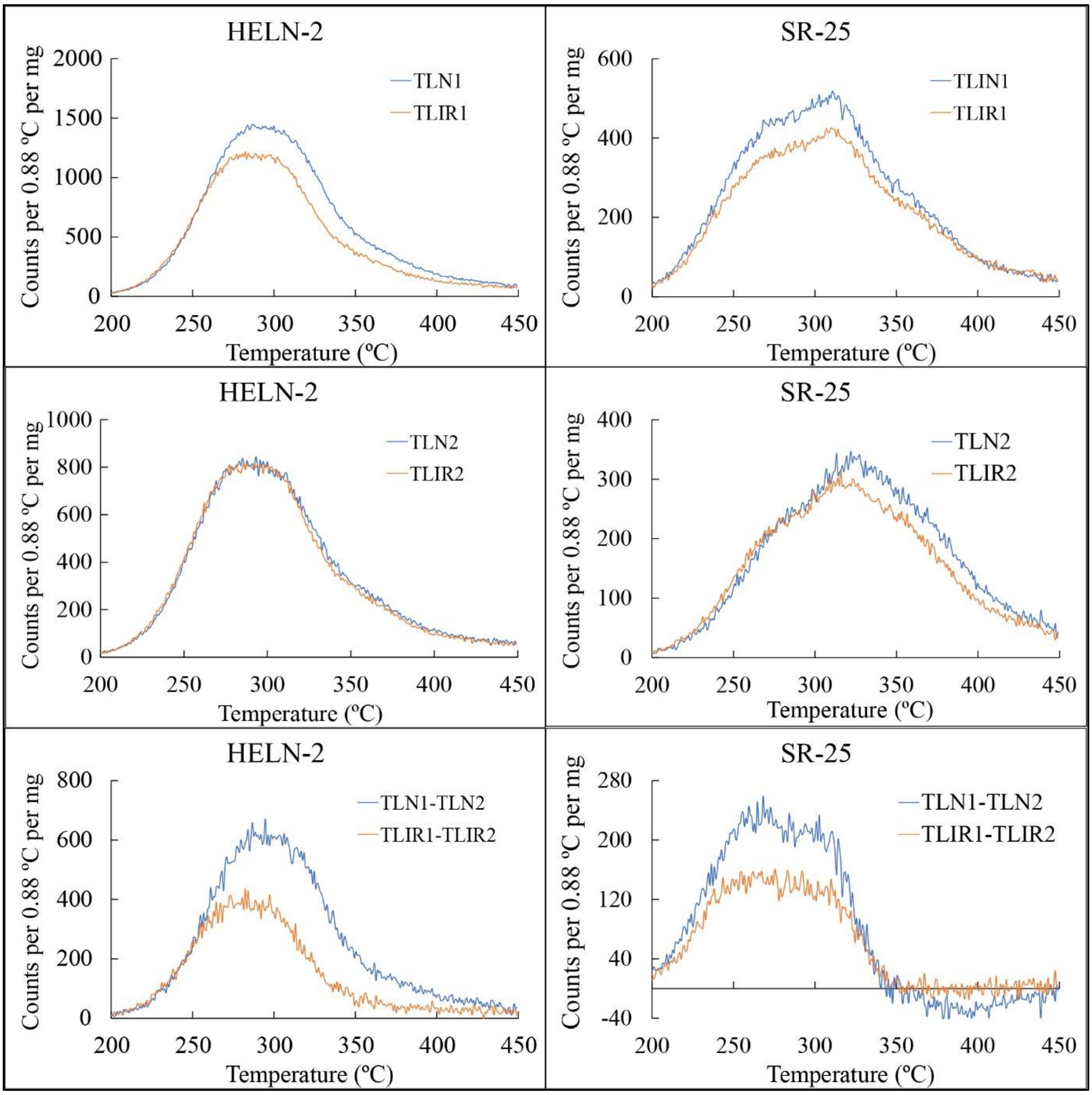

Fig. 3. 17: TL glow curves: (top) TLN1 and TLIR1, (middle) TLN2 and TLIR2, and (bottom) TLN1 - TLN2 and TLIR1 - TLIR2 for quartz samples HELN-2 and SR-25, respectively.

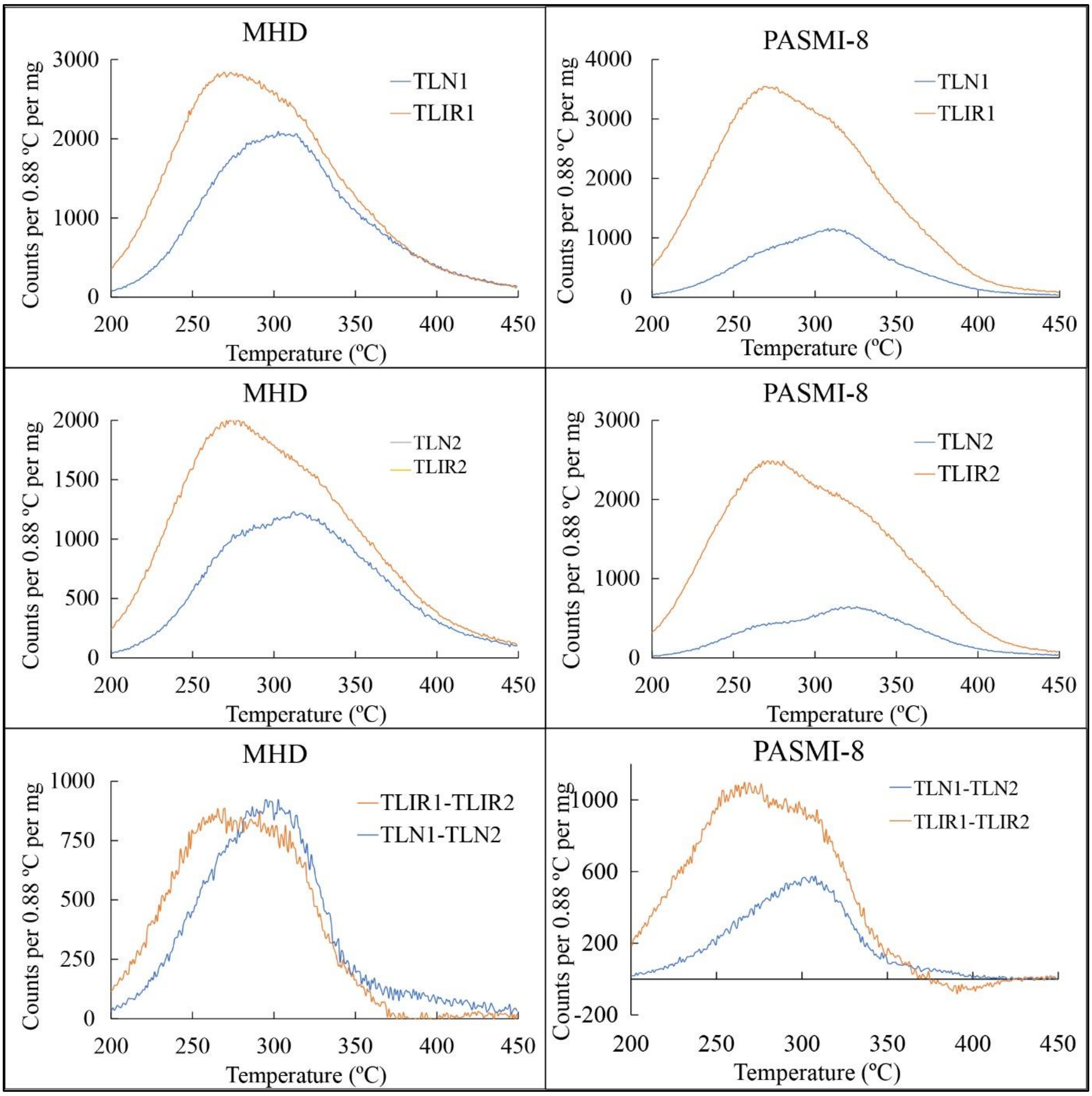

Fig. 3. 18: TL glow curves: (top) TLN1 and TLIR1, (middle) TLN2 and TLIR2, and (bottom) TLN1 - TLN2 and TLIR1 - TLIR2 for quartz samples MHD and PASMI-8, respectively.

Key Observations:

The effect of irradiation is most prominent in the 200–300 °C range. High irradiation does not significantly affect dull and medium samples (HELN and SR-25). Bright samples (MHD and PASMI-8) exhibit pronounced changes in the full TL glow curve and light-insensitive parts.

In the light-sensitive part, a decrease is observed in HELN and SR-25, while MHD shows no change and PASMI-8 exhibits an increase. Bright samples display distinct behaviour under irradiation.

Fig. 3. 19 represents the BSLS of four quartz samples—HELN, SR-25, MHD, and PASMI-8, under natural and irradiated conditions. The results are summarised as follows:

3.5.2 Effect of irradiation on BSLS

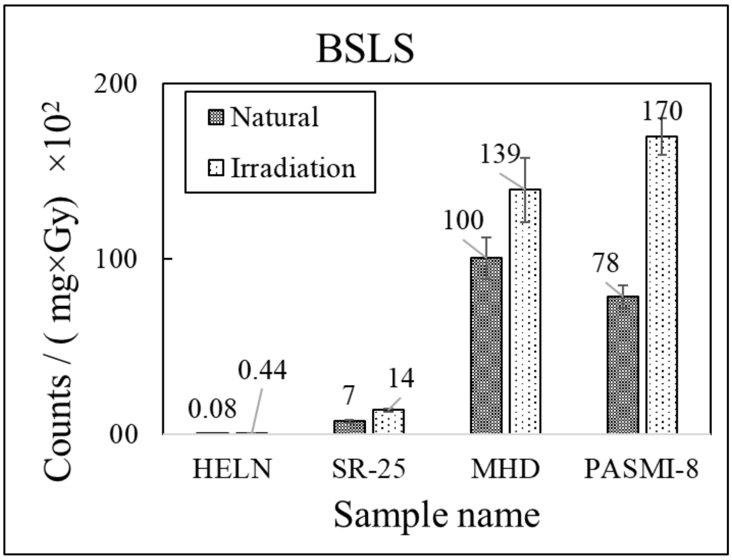

Fig. 3. 19: Blue light stimulated luminescence sensitivity (BSLS) for quartz samples HELN, SR-25, MHD, and PASMI-8 under natural conditions and after irradiation treatment.

HELN (Dull sample):

The natural BSLS is 0.08×10^2 counts/(mg×Gy). After irradiation, it increases significantly to 0.44×10^2 counts/(mg×Gy), showing a 5.5-fold enhancement.

SR-25 (Medium sample):

The BSLS under natural conditions is 7×10^2 counts/(mg×Gy). After irradiation, it rises to 14×10^2 counts/(mg×Gy), indicating a 2-fold increase.

MHD (Bright sample):

The natural BSLS is 100×10^2 counts/(mg×Gy). Post-irradiation, it increases to 139×10^2 counts/(mg×Gy), showing a 1.39-fold enhancement.

PASMI-8 (Bright sample):

The BSLS increases from 78×10^2 counts/(mg×Gy) under natural conditions to 170×10^2 counts/(mg×Gy) after irradiation, resulting in a 2.18-fold enhancement.

Irradiation significantly enhances the BSLS for all quartz samples, with dull samples (HELN) showing the highest proportional increase (5.5-fold). Medium and bright samples exhibit relatively smaller proportional enhancements (ranging from 1.39 to 2.18-fold). This suggests that samples with lower natural luminescence sensitivity are more responsive to irradiation than bright samples.

3.5.3 Effect of irradiation on LM-BSL

Fig. 3. 20, Fig. 3. 21, Fig. 3. 22 and Fig. 3. 23 present the LM-BSL responses of samples SR-1A (dull sample), SR-25 (medium sample), MHD (bright sample), and PASMI-8 (bright sample) under natural and irradiated conditions. The LM-BSL signals, composed of multiple peaks, were deconvoluted to identify distinct PICS and initial trapped charge concentrations. The corresponding PICS and charge concentrations for these peaks are detailed in Table 3. 9. The results are summarised below:

SR-1A (Dull Sample): There is an increase in total LM-OSL signal by 10.18 times due to irradiation. After irradiation, two middle components with PICS 1.81×10^{-18} cm^2 and 1.23×10^{-19} cm^2 appeared.

SR-25 (Medium Sample): There is an increase in total LM-OSL signal by 4.54 times due to irradiation. After irradiation, two middle components with PICS 1.16×10^{-18} cm^2 and 1.11×10^{-19} cm^2 appeared.

MHD (Bright Sample): There is an increase in total LM-OSL signal by 3.23 times due to irradiation. After irradiation, two middle components with PICS 2.27×10^{-19} cm^2 and 2.77×10^{-20} cm^2 appeared.

PASMI-8 (Bright Sample): There is an increase in total LM-OSL signal by 3.44 times due to irradiation. After irradiation, two middle components with PICS 5.46×10^{-19} cm^2 and 7.59×10^{-20} cm^2 appeared.

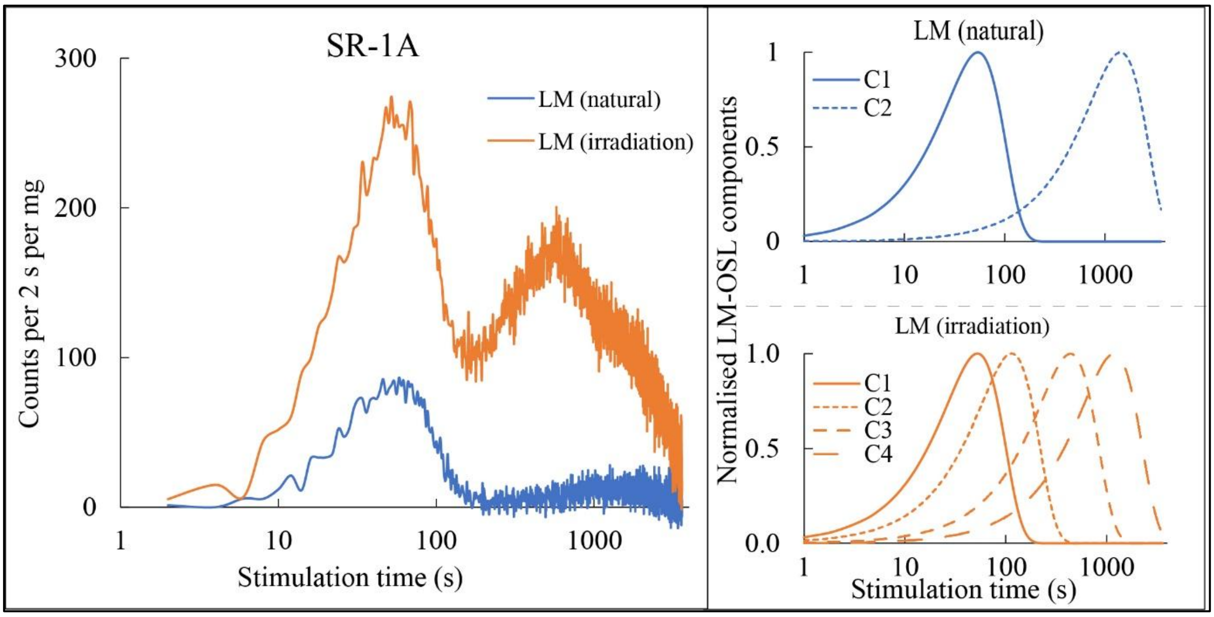

Fig. 3. 20: The left panel shows the LM-BSL of sample SR-1A (dull sample) under natural (blue) and irradiated (orange) conditions. The right panels depict the deconvoluted, normalised LM-BSL components (C1 and C2) for natural conditions and (C1, C2, C3, and C4) for irradiated conditions.

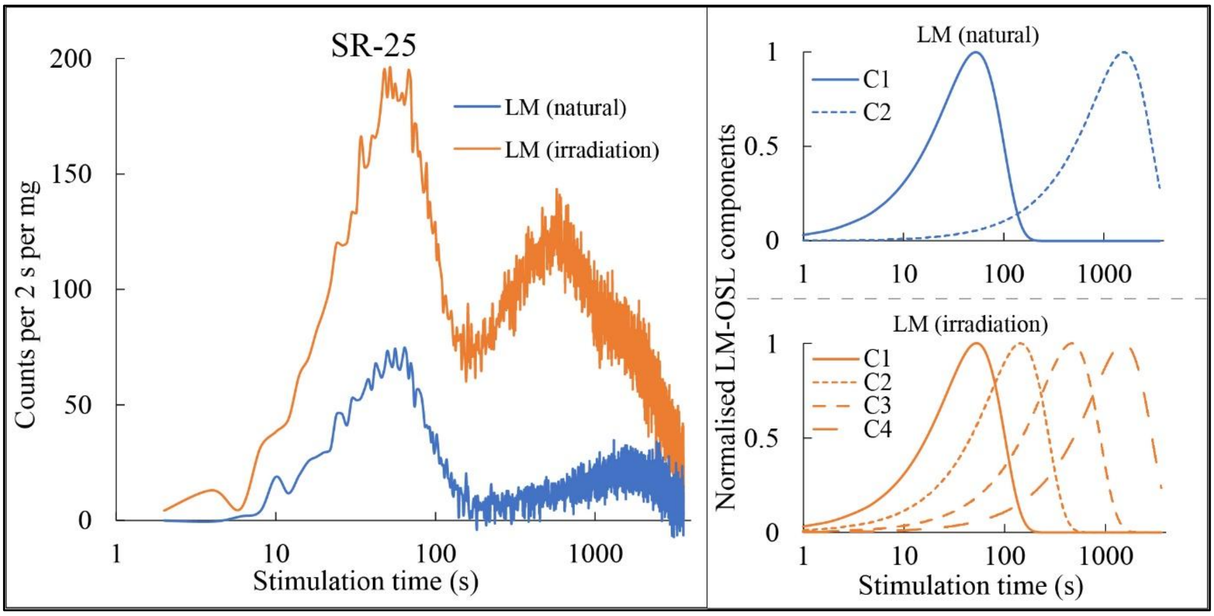

Fig. 3. 21: The left panel shows the LM-BSL of sample SR-25 (medium sample) under natural (blue) and irradiated (orange) conditions. The right panels depict the deconvoluted, normalised LM-BSL components (C1 and C2) for natural conditions and (C1, C2, C3, and C4) for irradiated conditions.

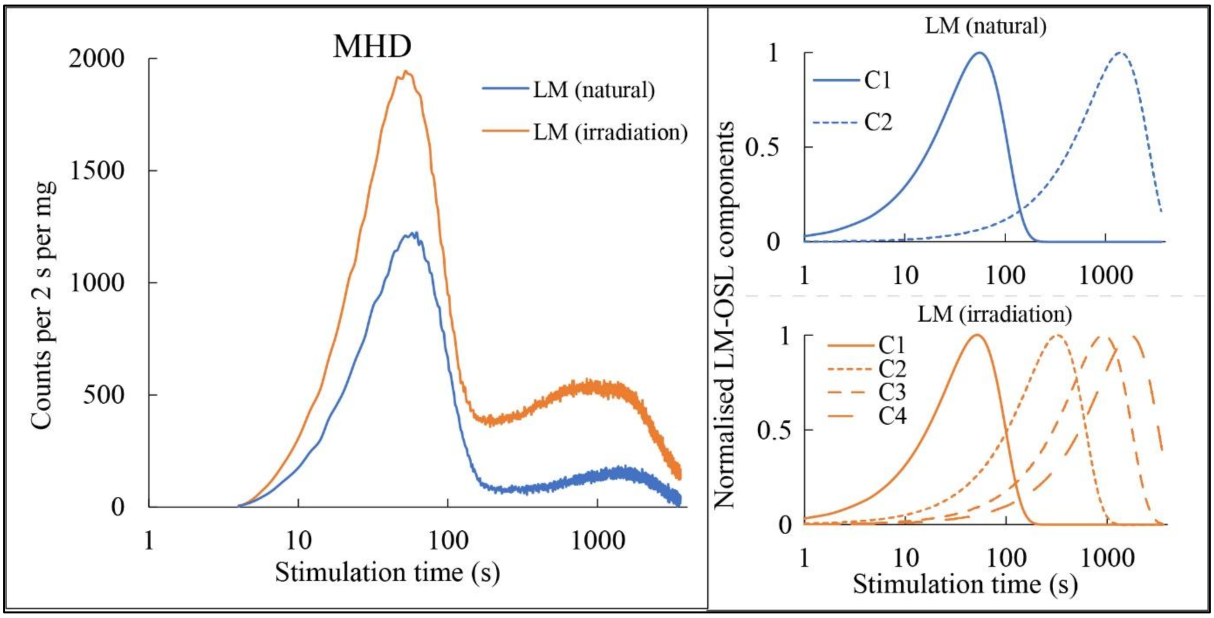

Fig. 3. 22: The left panel shows the LM-BSL of sample MHD (bright sample) under natural (blue) and irradiated (orange) conditions. The right panels depict the deconvoluted, normalised LM-BSL components (C1 and C2) for natural conditions and (C1, C2, C3, and C4) for irradiated conditions.

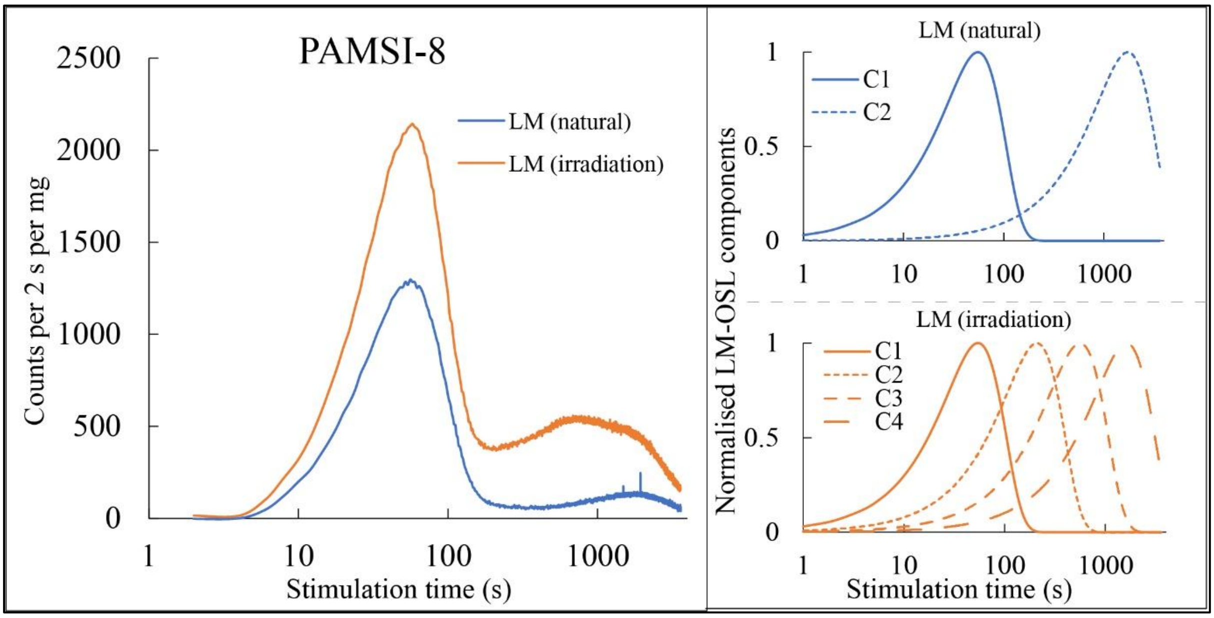

Fig. 3. 23: The left panel shows the LM-BSL of sample PASMI-8 (bright sample) under natural (blue) and irradiated (orange) conditions. The right panels depict the deconvoluted, normalised LM-BSL components (C1 and C2) for natural conditions and (C1, C2, C3, and C4) for irradiated conditions.

Table 3. 9: Initial trapped charge concentrations and PICS of quartz samples (SR-1A, SR-25, MHD, and PASMI-8) under natural and irradiated conditions.

Sample name	**Natural condition**		**Irradiated condition**	
	Initial trapped charge concentration	**PICS (in cm^2)**	**Initial trapped charge concentration**	**PICS (in cm^2)**
SR-1A (dull sample)	6.97×10^{3}	8.16×10^{-18}	1.89×10^{4}	8.65×10^{-18}
			1.38×10^{3}	1.81×10^{-18}
	2.95×10^{4}	1.18×10^{-20}	7.79×10^{4}	1.23×10^{-19}
			1.23×10^{5}	1.69×10^{-20}
SR-25 (medium sample)	5.56×10^{3}	8.57×10^{-18}	1.36×10^{4}	8.62×10^{-18}
			1.72×10^{3}	1.16×10^{-18}
	5.49×10^{4}	9.52×10^{-21}	6.20×10^{4}	1.11×10^{-19}
			1.90×10^{5}	1.04×10^{-20}
MHD (Bright sample)	1.04×10^{5}	7.66×10^{-18}	1.48×10^{5}	8.89×10^{-18}
			1.08×10^{5}	2.27×10^{-19}
	3.65×10^{5}	1.20×10^{-20}	3.66×10^{5}	2.77×10^{-20}
			9.69×10^{5}	8.30×10^{-21}
PASMI-8 (bright sample)	1.10×10^{5}	7.80×10^{-18}	1.70×10^{5}	8.05×10^{-18}
			3.60×10^{4}	5.46×10^{-19}
	3.75×10^{5}	7.97×10^{-21}	2.38×10^{5}	7.59×10^{-20}
			1.19×10^{6}	9.05×10^{-21}

Irradiation significantly sensitises the LM-OSL signals of quartz samples, with the enhancement ranging from 10.18 times in the dull sample (SR-1A) to 3.23–3.44 times in bright samples (MHD and PASMI-8). Additionally, irradiation introduces two middle components in the LM-OSL signals of all samples, characterised by distinct PICS. This provides a clear indication of defect creation or activation.

3.6 Effect of sunlight exposure on luminescence characteristics of quartz

Sunlight resets the luminescence signal in quartz. Sediments in nature experience a wide range of sunlight exposure conditions. Numerous studies found that the cycle of irradiation and bleaching causes sensitisation of the luminescence signal of quartz (Cao et al., 2022; Moayed et al., 2023; Moska & Murray, 2006; Pietsch et al., 2008; Soares et al., 2023). Studies by Li and Wintle (1992) have indicated that samples with a history of prolonged bleaching exhibit higher luminescence sensitivity, highlighting distinctions between aeolian and colluvial sediments. Based on sunlight exposure, Pietsch et al. (2008) suggest that the OSL sensitivity of quartz in these settings has the potential to provide information on fluvial transport processes.

The effects of sunlight exposure on the luminescence characteristics of quartz were investigated using samples with varying sensitivity: SR-1A (low sensitivity), SR-25 (medium sensitivity), MHD (high sensitivity), and PASMI-8 (high sensitivity). The samples were exposed to direct sunlight for approximately 260 hours during peak summer noon hours to ensure maximum solar exposure. The relationship between prolonged sunlight exposure and changes in luminescence behaviour was systematically examined.

3.6.1 Effect of sunlight on 110 ºC TLS

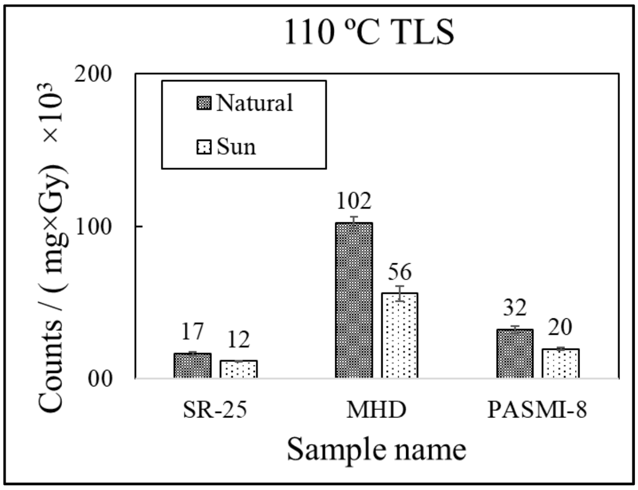

Fig. 3. 24: 110 ºC TLS for quartz samples SR-25, MHD, and PASMI-8 under natural conditions and after sunlight exposure.

Fig. 3. 24 illustrates the 110 ºC TLS for quartz samples under natural and sunlight-exposed conditions for samples SR-25, MHD, and PASMI-8. The results are summarised as follows:

SR-25 (Medium sample):

The 110 ºC TLS decreases from 17×10^3 counts/(mg×Gy) to 12×10^3 counts/(mg×Gy), which is 0.71 of the original value.

MHD (Bright sample):

The 110 ºC TLS decreases from 102×10^3 counts/(mg×Gy) to 56×10^3 counts/(mg×Gy), corresponding to a decrease to 0.55 of the natural 110 ºC TLS.

PASMI-8 (Bright sample):

The 110 ºC TLS drops from 32×10^3 counts/(mg×Gy) to 20×10^3 counts/(mg×Gy), which corresponds to 0.63 times the natural 110 ºC TLS.

Sunlight exposure consistently reduces 110 ºC TLS across all samples, with the largest decline observed in the brightest sample (MHD), reducing the sensitivity to 0.55 of its original level.

3.6.2 Effect of sunlight on higher TL glow curve (200-450 °C)

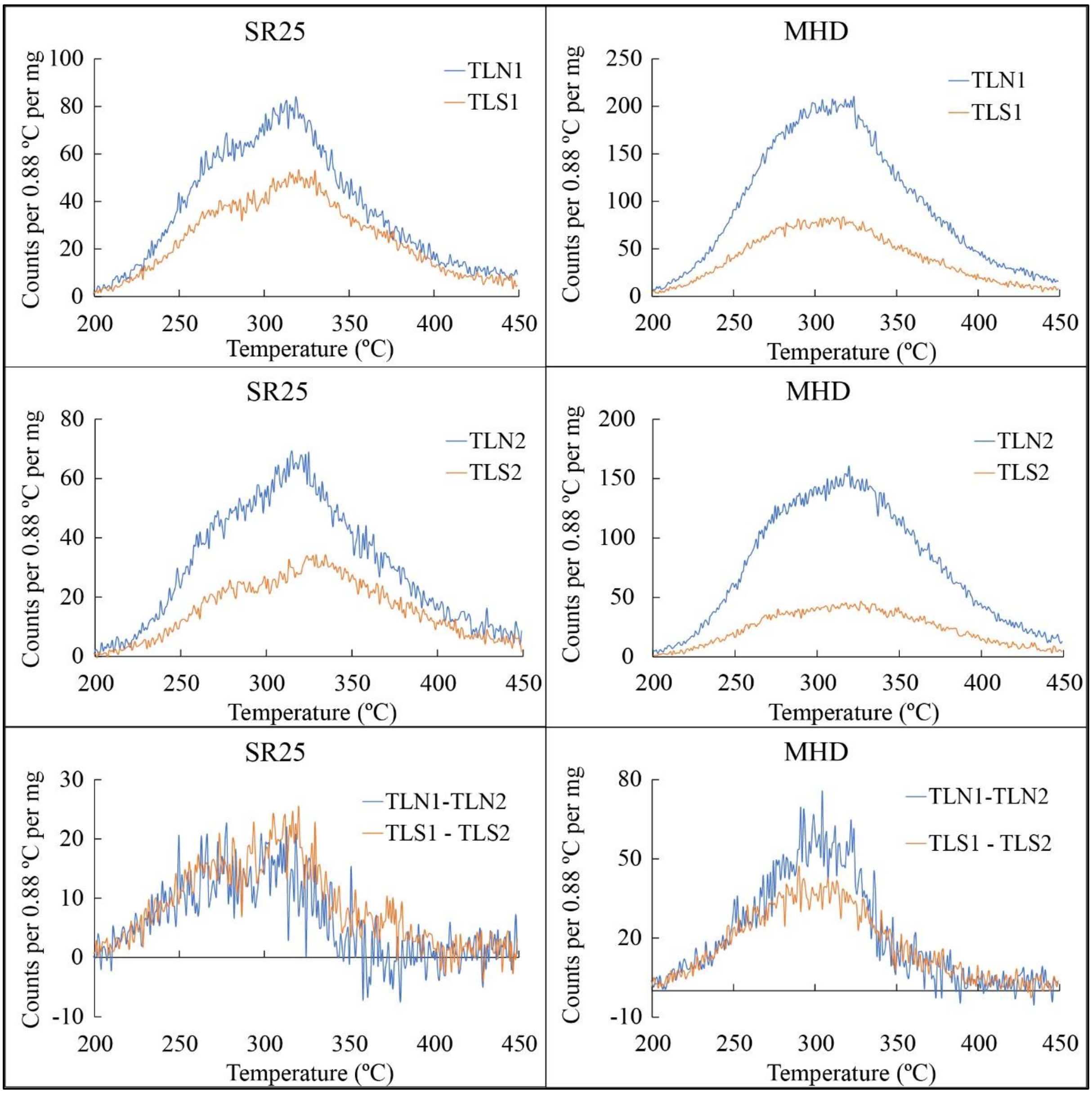

Fig. 3. 25: TL glow curves: (top) TLN1 and TLS1, (middle) TLN2 and TLS2, and (bottom) TLN1 - TLN2 and TLS1 - TLS2 for quartz samples SR25 and MHD, respectively.

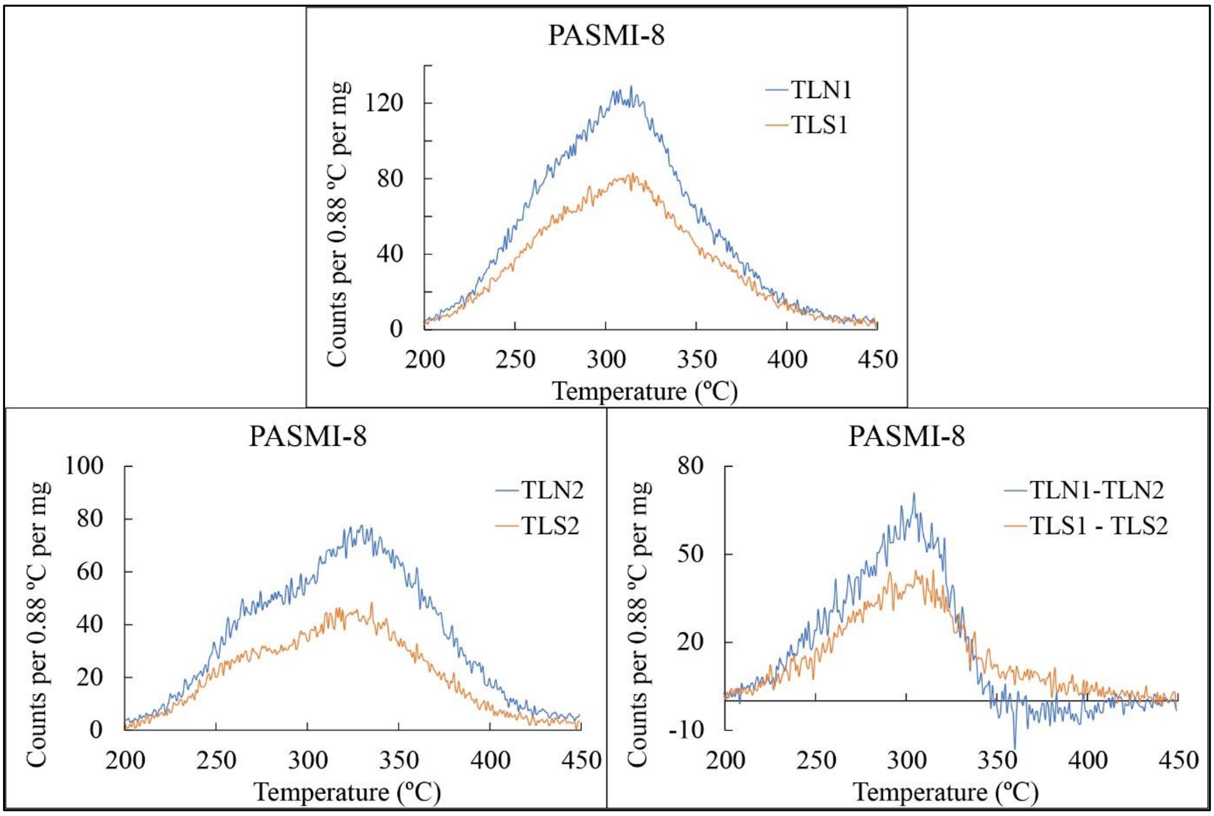

Fig. 3. 26: TL glow curves for quartz sample PASMI-8: (top) TLN1 and TLS1, (bottom-left) TLN2 and TLS2, and (bottom-right) TLN1 - TLN2 and TLS1 - TLS2.

TLS is the TL glow curve up to 450 °C after preheating following sun light exposure as described in section 3.3.2.

Fig. 3. 25 and Fig. 3. 26 represent the full TL glow curve (TLN1 and TLS1), light-insensitive TL glow curve (TLN2, TLS2) and light-sensitive TL glow curve (TLN1-TLN2, TLS1-TLS2) of samples SR-25, MHD and PASMI-8. Results are summarised below:

Full TL glow curve (TLN1 and TLS1)

1. There is a decrease in the full TL glow curve in all types of samples due to the effect of sunlight exposure.

Light-insensitive TL glow curve (TLN2, TLS2)

1. A consistent decrease in the light-insensitive TL glow curve is observed across the samples due to sunlight exposure.

Light-sensitive TL glow curve (TLN1-TLN2, TLS1-TLS2)

1. The light-sensitive part remains similar across all the samples, showing minimal impact from sunlight exposure.

Key Observations:

Sunlight exposure causes a general reduction in both the full TL glow curve and light-insensitive TL parts across all samples. However, the light-sensitive TL parts remain unaffected, indicating that the sunlight exposure primarily influences the trapped electron populations, contributing to the full TL glow curve and light-insensitive part while having negligible effects on the light-sensitive parts.

3.6.3 Effect of sunlight on BSLS

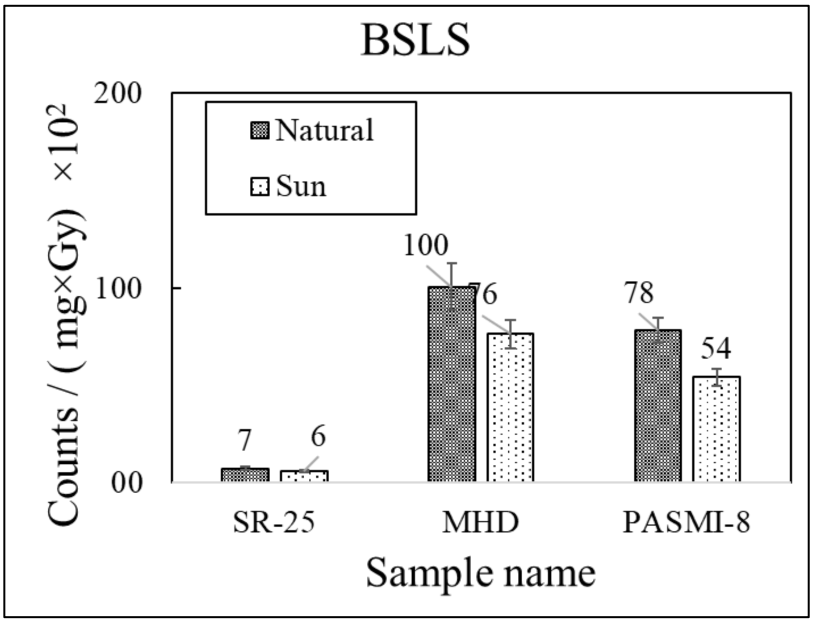

Fig. 3. 27: BSLS for quartz samples SR-25, MHD, and PASMI-8 under natural conditions and after sunlight exposure.

Fig. 3. 27 illustrates the BSLS for three quartz samples—SR-25, MHD, and PASMI-8, under natural and sunlight exposure conditions. The results are summarised as follows:

SR-25 (Medium sample):

The BSLS decreases slightly from 7×10^2 counts/(mg×Gy) under natural conditions to 6×10^2 counts/(mg×Gy), representing a reduction to 0.86 of the original value.

MHD (Bright sample):

The natural BSLS is 100×10^2 counts/(mg×Gy). After sunlight exposure, it reduces to 76×10^2 counts/(mg×Gy), 0.76 of the original value.

PASMI-8 (Bright sample):

The BSLS decreases from 78×10^2 counts/(mg×Gy) under natural conditions to 54×10^2 counts/(mg×Gy), indicating a reduction to 0.69 of the original value.

Sunlight exposure reduces BSLS for all quartz samples, with significant reduction observed in the bright samples (PASMI-8 and MHD), where the BSLS decreases to 0.69 and 0.76 of their natural values, respectively. Medium sensitivity samples (SR-25) show a smaller decrease (to 0.86 of the natural value). This indicates that sunlight exposure primarily diminishes the luminescence sensitivity of brighter quartz samples.

3.6.4 Effect of sunlight on LM-BSL

Fig. 3. 28, Fig. 3. 29, Fig. 3. 30 and Fig. 3. 31 present the LM-BSL responses of samples SR-1A (dull sample), SR-25 (medium sample), MHD (bright sample), and PASMI-8 (bright sample) under natural and sunlight-exposed conditions. The LM-BSL signals, composed of multiple peaks, were deconvoluted to reveal distinct PICS and initial trapped charge concentrations. The corresponding PICS and charge concentrations for these peaks are detailed in Table 3. 10. The results are summarised as follows:

SR-25 (Medium Sample): Sunlight exposure increases the total LM-BSL signal by 3.22 times. The component analysis shows no formation of new components, with the two existing ones persisting unchanged.

MHD (Bright Sample): A 1.52 times increase in the total LM-BSL signal is observed under sunlight exposure. The component analysis reveals the two components remain the same.

PASMI-8 (Bright Sample): The total LM-BSL signal increases by 1.27 times under sunlight exposure. The existing components remain the same due to the effect of sunlight exposure.

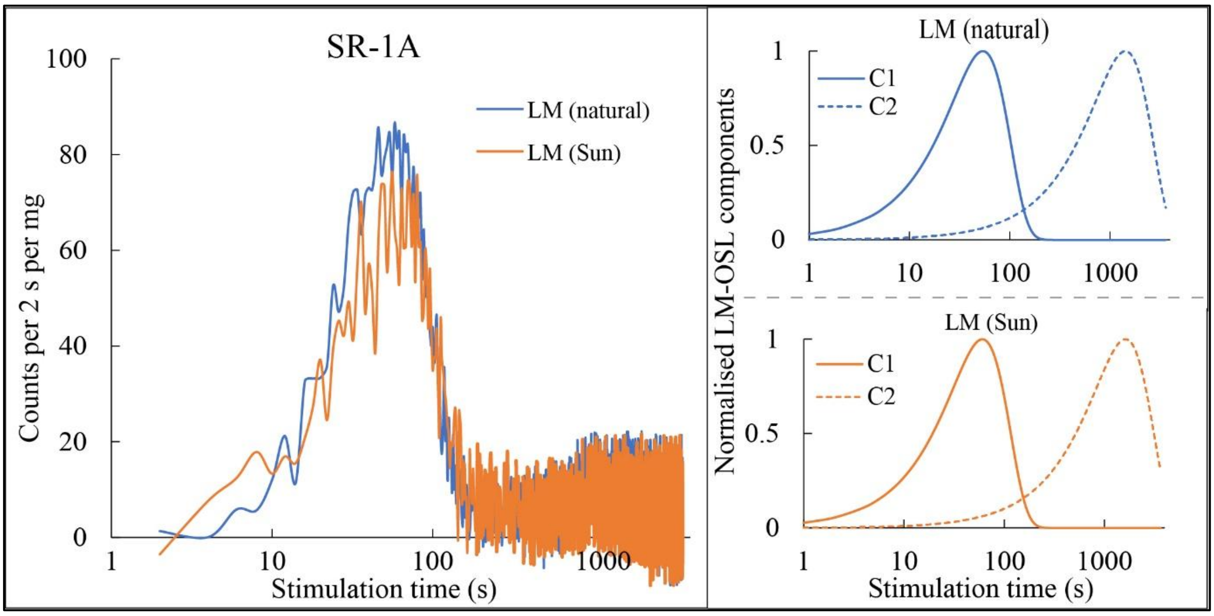

Fig. 3. 28: The left panel shows the LM-BSL of sample SR-1A (dull sample) under natural (blue) and UV-exposed (orange) conditions. The right panels depict the deconvoluted, normalised LM-BSL components (C1 and C2) for both natural and sunlight exposed conditions.

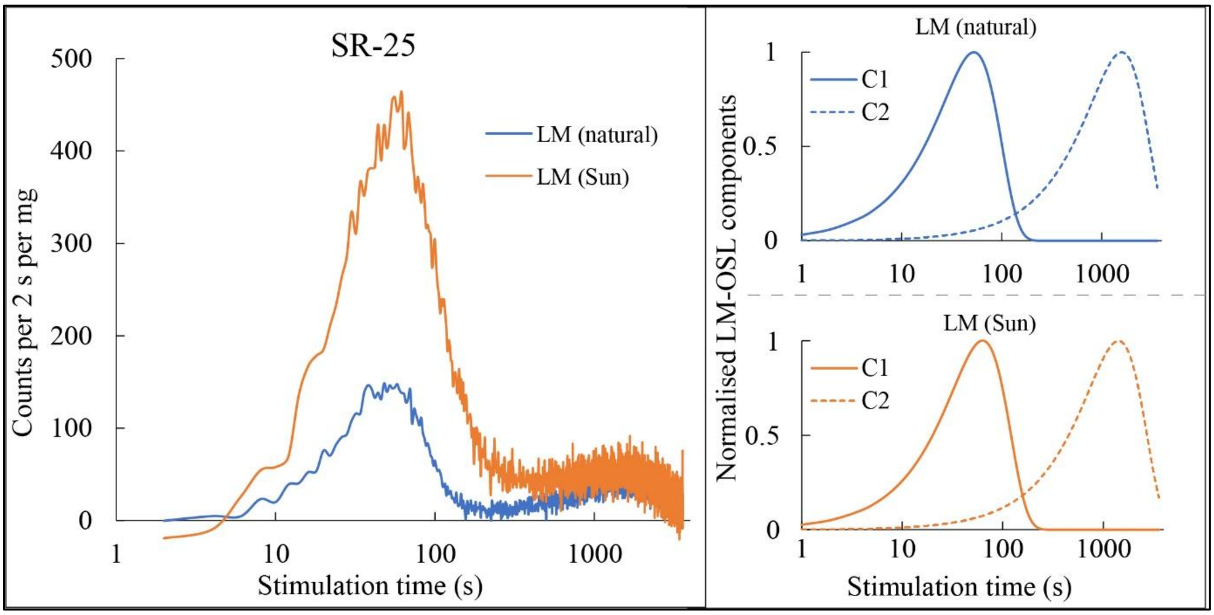

Fig. 3. 29: The left panel shows the LM-BSL of sample SR-25 (medium sample) under natural (blue) and sun-bleached (orange) conditions. The right panels depict the deconvoluted, normalised LM-BSL components (C1 and C2) for both natural and sunlight exposed conditions.

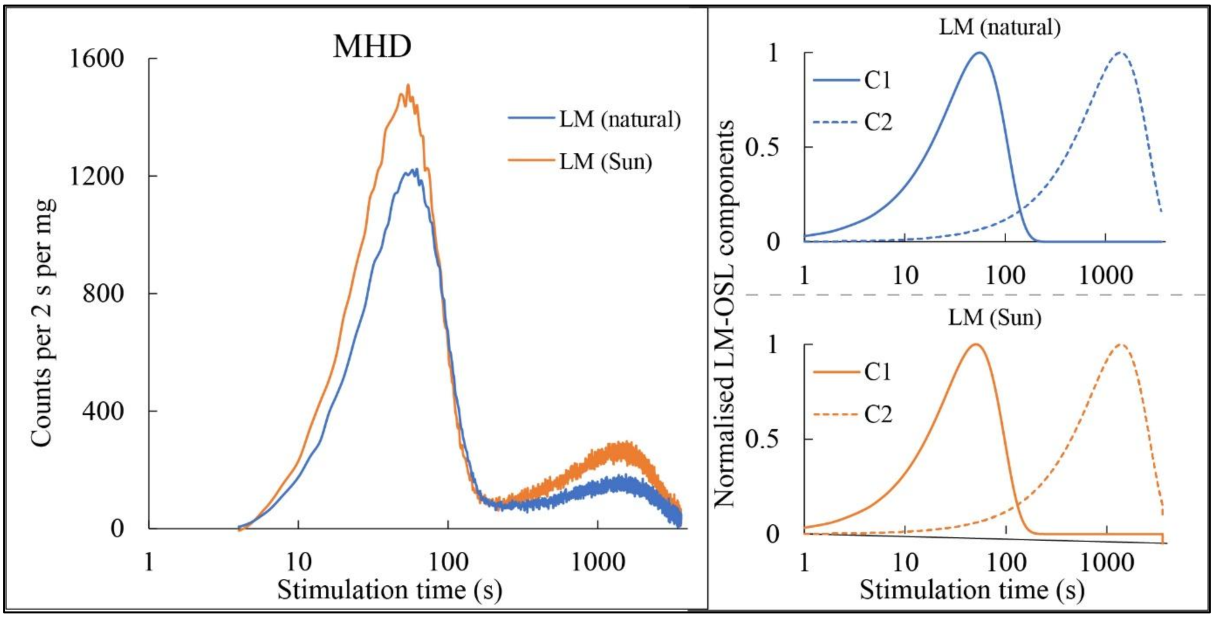

Fig. 3. 30: The left panel shows the LM-BSL of sample MHD (bright sample) under natural (blue) and sun-bleached (orange) conditions. The right panels depict the deconvoluted, normalised LM-BSL components (C1 and C2) for both natural and sunlight exposed conditions.

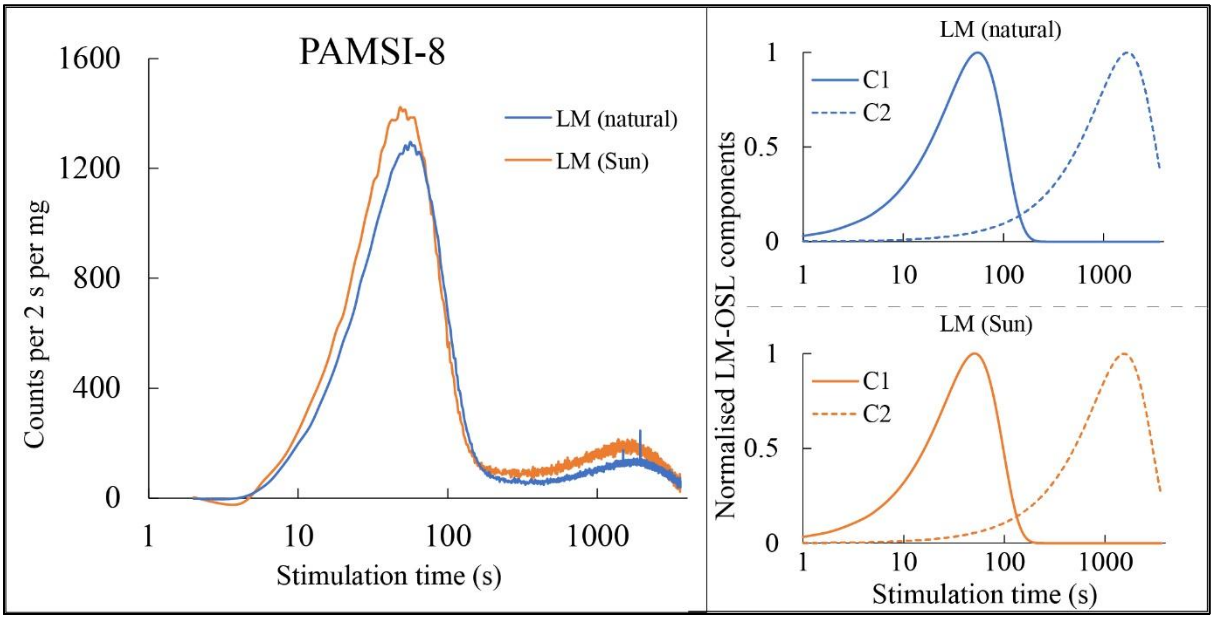

Fig. 3. 31: The left panel shows the LM-BSL of sample PASMI-8 (bright sample) under natural (blue) and sun-bleached (orange) conditions. The right panels depict the deconvoluted, normalised LM-BSL components (C1 and C2) for both natural and sunlight exposed conditions.

Table 3. 10: Initial trapped charge concentrations and PICS of quartz samples (SR-1A, SR-25, MHD, and PASMI-8) under natural and sunlight exposed conditions.

Sample name	Natural condition		Sunlight exposed condition	
	Initial trapped charge concentration	**PICS (in cm^2)**	**Initial trapped charge concentration**	**PICS (in cm^2)**
SR-1A (dull sample)	6.97×10^{3}	8.16×10^{-18}	6.42×10^{3}	6.50×10^{-18}
	2.95×10^{4}	1.18×10^{-20}	1.77×10^{4}	9.11×10^{-21}
SR-25 (medium sample)	5.56×10^{3}	8.57×10^{-18}	4.26×10^{4}	5.97×10^{-18}
	5.49×10^{4}	9.52×10^{-21}	1.36×10^{5}	1.18×10^{-20}
MHD (bright sample)	1.04×10^{5}	7.66×10^{-18}	1.15×10^{5}	9.32×10^{-18}
	3.65×10^{5}	1.20×10^{-20}	6.06×10^{5}	1.23×10^{-20}
PASMI-8 (bright sample)	1.10×10^{5}	7.80×10^{-18}	1.11×10^{5}	9.29×10^{-18}
	3.75×10^{5}	7.97×10^{-21}	4.81×10^{5}	9.98×10^{-21}

SR-1A (Dull Sample): The total LM-BSL signal decreases by 0.67 times under sunlight exposure. No new components emerge, and the two existing components remain constant.

Sunlight exposure exerts varying impacts on LM-BSL signals across quartz samples, causing a reduction in the dull sample (SR-1A) and enhancements ranging from 1.27 times in PASMI-8 to 3.22 times in SR-25. Crucially, component analysis consistently shows no emergence of new components.

3.7 Effect of UV exposure on luminescence characteristics of quartz

UV radiation, the higher-energy portion of the solar spectrum, can reach the Earth's surface and has the potential to affect the bonds within minerals. Williams et al. (2022) suggested UV exposure can sensitise OSL sensitivity as free E′1 centres may migrate through a hopping mechanism facilitated by solar UV exposure. These E′1 centres act as effective barriers, preventing holes from reaching luminescence centres. In this study, quartz samples (HELN-2, SR-25, MHD, and PASMI-8) were exposed to UV radiation at 265 nm for 60 hours using a low-pressure mercury vapour lamp. The effects of UV exposure on the luminescence characteristics of these diverse samples were systematically investigated.

3.7.1 Effect of UV exposure on 110 ºC TLS

Fig. 3. 32 illustrates the 110 ºC TLS for quartz samples under natural and UV-exposed conditions, measured in counts per unit dose (mg × Gy). The samples include HELN, SR-25, MHD, and PASMI-8. The results are summarised as follows:

HELN (Dull sample):

The 110 ºC TLS remains unchanged at 3×10^3 counts/(mg×Gy) under both natural and UV conditions, indicating no change due to UV exposure.

SR-25 (Medium sample):

The 110 ºC TLS decreases from 17×10^3 counts/(mg×Gy) to 11×10^3 counts/(mg×Gy), which is 0.65 of the original value.

MHD (Bright sample):

The 110 ºC TLS decreases from 102×10^3 counts/(mg×Gy) to 51×10^3 counts/(mg×Gy), corresponding to a decrease of 0.50 of natural 110 ºC TLS.

PASMI-8 (Bright sample):

The 110 ºC TLS decreases from 32×10^3 counts/(mg×Gy) to 25×10^3 counts/(mg×Gy), resulting in a decrease to 0.78 of the original value.

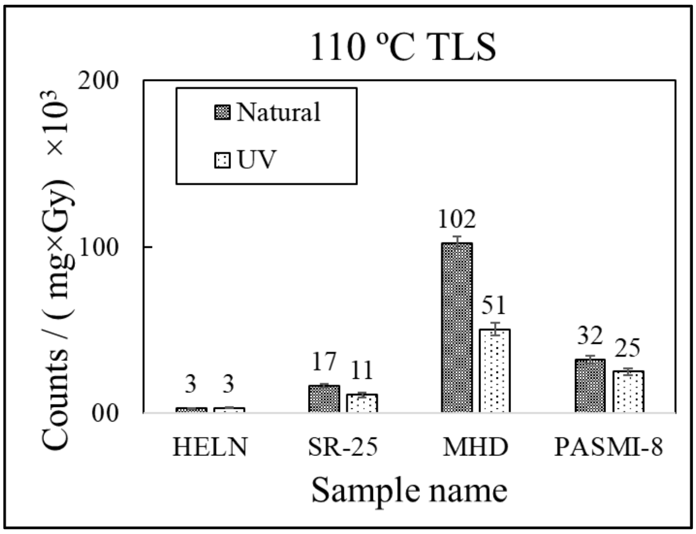

Fig. 3. 32: 110 ºC TLS for quartz samples HELN, SR-25, MHD, and PASMI-8 under natural conditions and after UV exposure.

UV exposure causes a reduction in 110 ºC TLS for medium (SR-25) and bright samples (MHD, PASMI-8), with the most significant decrease observed in the brightest sample (MHD), where the sensitivity reduces to 0.50 of its original value. Dull samples (HELN), however, remain unaffected by UV exposure.

3.7.2 Effect of UV exposure on higher TL glow curve (200-450 °C)

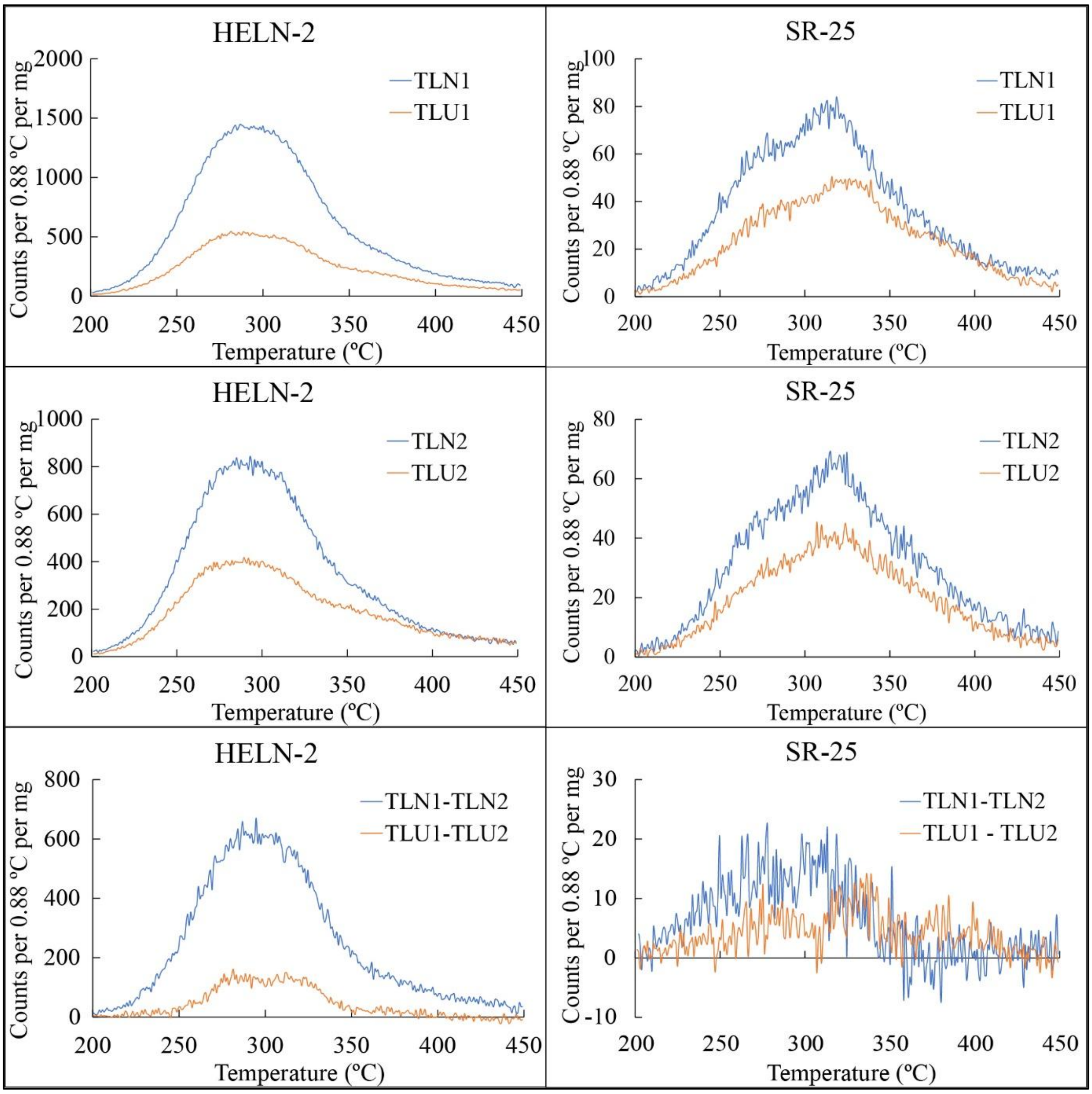

Fig. 3. 33: TL glow curves for quartz samples HELN-2 and SR-25: (top) TLN1 and TLU1, (middle) TLN2 and TLU2, and (bottom) TLN1 - TLN2 and TLU1 - TLU2.

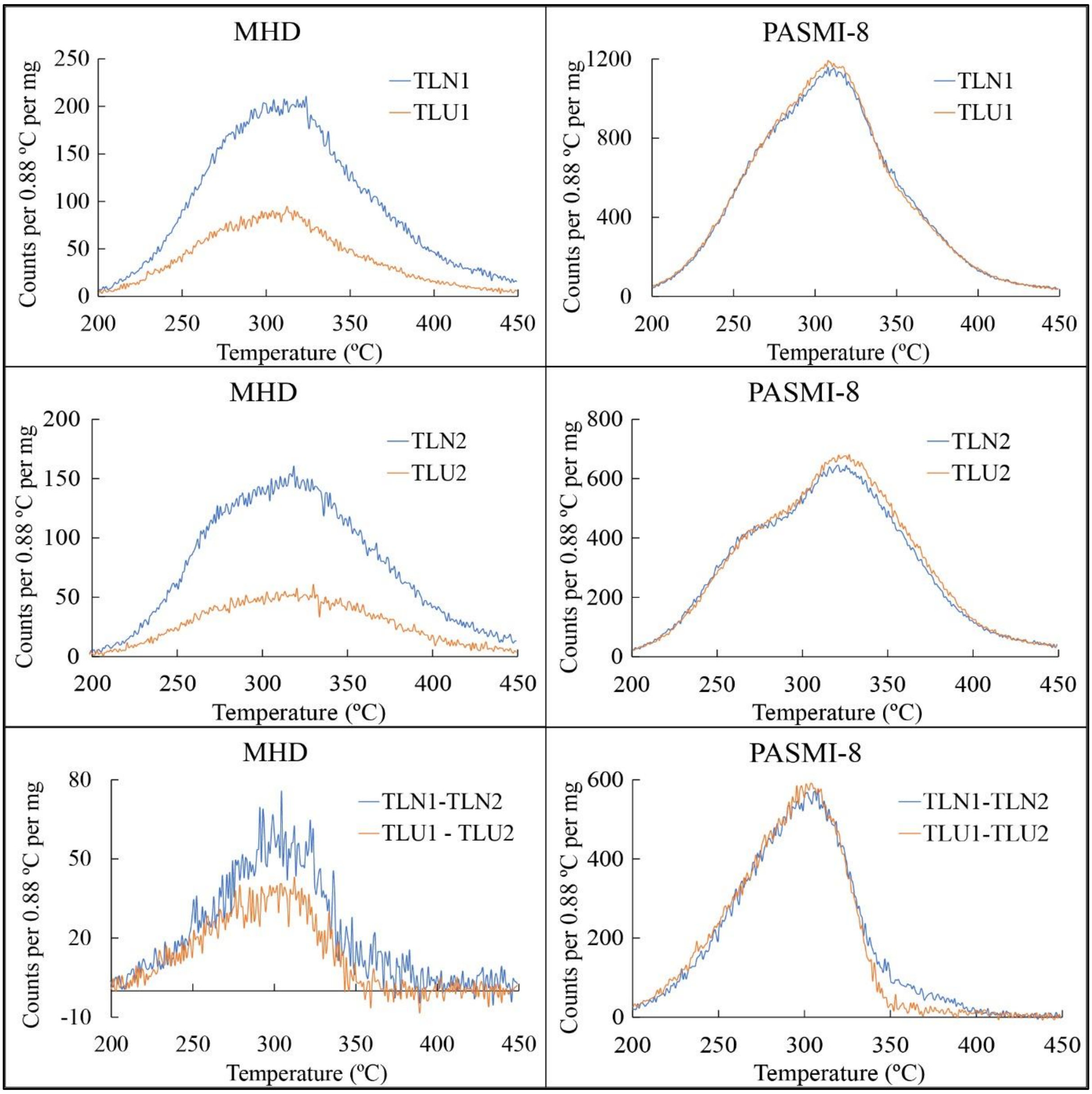

Fig. 3. 34: TL glow curves for quartz samples MHD and PASMI-8: (top) TLN1 and TLU1, (middle) TLN2 and TLU2, and (bottom) TLN1 - TLN2 and TLU1 - TLU2.

TLU is the TL glow curve up to 450 °C after preheating following UV exposure as described in section 3.3.2.

Fig. 3. 33 and Fig. 3. 34 represent the full TL glow curve (TLN1 and TLU1), light-insensitive TL glow curve (TLN2, TLU2) and light-sensitive TL glow curve (TLN1-TLN2, TLU1-TLU2) of samples HELN-2, SR-25, MHD and PASMI-8. The results are summarised below:

Full TL glow curve (TLN1 and TLU1)

1. UV exposure causes a slight decrease in the Full TL glow curves for samples HELN, SR-25, and MHD.

2. The PASMI-8 sample remains unaffected by UV exposure, showing no change in the Full TL glow curves.

Light-insensitive TL glow curve (TLN2, TLU2)

1. A slight decrease in the light-insensitive TL glow curve is observed across samples HELN, SR-25, and MHD after UV exposure.

2. The PASMI-8 sample shows no change in the light-insensitive TL glow curve under UV exposure.

Light-sensitive TL glow curve (TLN1-TLN2, TLU1-TLU2)

1. The light-sensitive part decreases in the dull sample (HELN) under UV exposure.

2. The medium sample (SR-25) and bright samples (MHD and PASMI-8) remain unchanged in their light-sensitive part of the TL.

Key Observations:

UV exposure leads to slight reductions in the full TL and light-insensitive TL glow curves for dull (HELN), medium (SR-25), and bright (MHD) samples, while PASMI-8 remains unaffected. The light-sensitive TL part decreases only in the dull sample (HELN), with the medium (SR-25) and bright samples (MHD and PASMI-8) remaining stable. Overall, the dull sample (HELN) is the most affected by UV exposure, whereas the bright sample PASMI-8 demonstrates resilience, showing no significant changes in any TL components.

3.7.3 Effect of UV exposure on BSLS

Fig. 3. 35 presents the BSLS for four quartz samples—HELN, SR-25, MHD, and PASMI-8—measured in counts per unit dose (mg × Gy) under natural and UV exposure conditions. The results are as follows:

HELN (Dull sample):

The BSLS decreases slightly from 0.08×10^2 counts/(mg×Gy) under natural conditions to 0.06×10^2 counts/(mg×Gy), indicating a reduction to 0.75 of the natural value.

SR-25 (Medium sample):

The BSLS decreases from 7×10^2 counts/(mg×Gy) to 6×10^2 counts/(mg×Gy) under UV exposure, representing a reduction to 0.86 of the natural value.

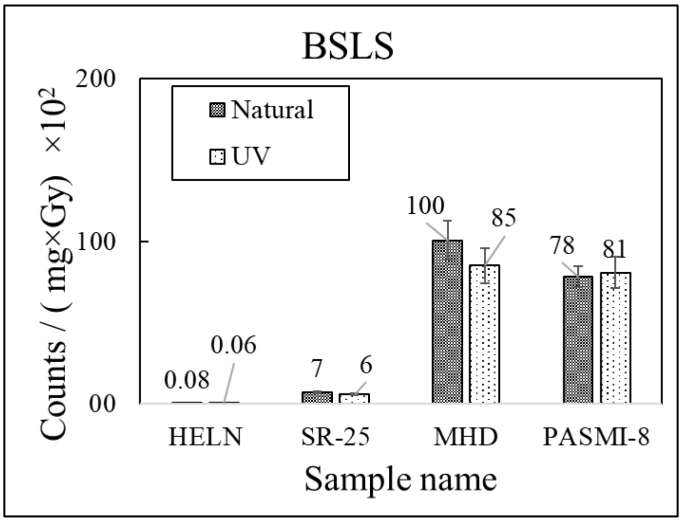

Fig. 3. 35: BSLS for quartz samples HELN, SR-25, MHD, and PASMI-8 under natural conditions and after UV exposure.

MHD (Bright sample):

The natural BSLS is 100×10^2 counts/(mg×Gy). After UV exposure, it decreases to 85×10^2 counts/(mg×Gy), which is 0.85 of the original value.

PASMI-8 (Bright sample):

The BSLS increases slightly from 78×10^2 counts/(mg×Gy) under natural conditions to 81×10^2 counts/(mg×Gy), indicating an enhancement to 1.04 of the natural value.

UV exposure shows an overall reduction in BSLS. Dull (HELN) and medium (SR-25) samples exhibit slight decreases, while the bright sample MHD experiences a moderate reduction. For PASMI-8, the BSLS remains within the error range, indicating minimal impact from UV exposure.

3.7.4 Effect of UV exposure on LM-BSL

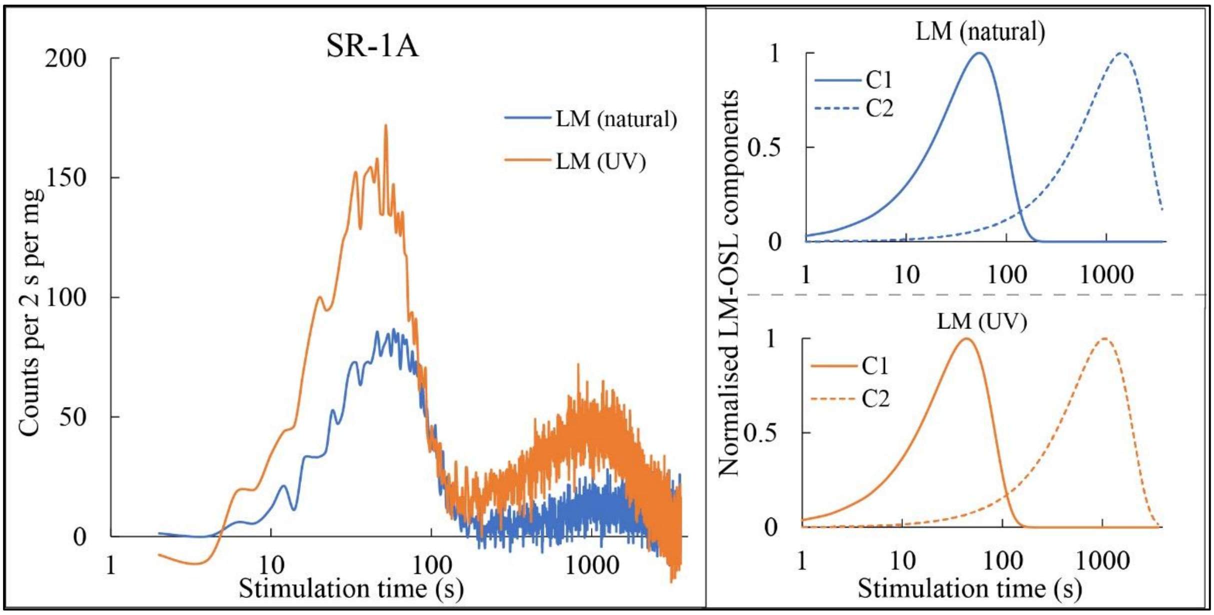

Fig. 3. 36: The left panel shows the LM-BSL of sample SR-1A (dull sample) under natural (blue) and UV-exposed (orange) conditions. The right panels depict the deconvoluted, normalised LM-BSL components (C1 and C2) for natural and UV-exposed conditions.

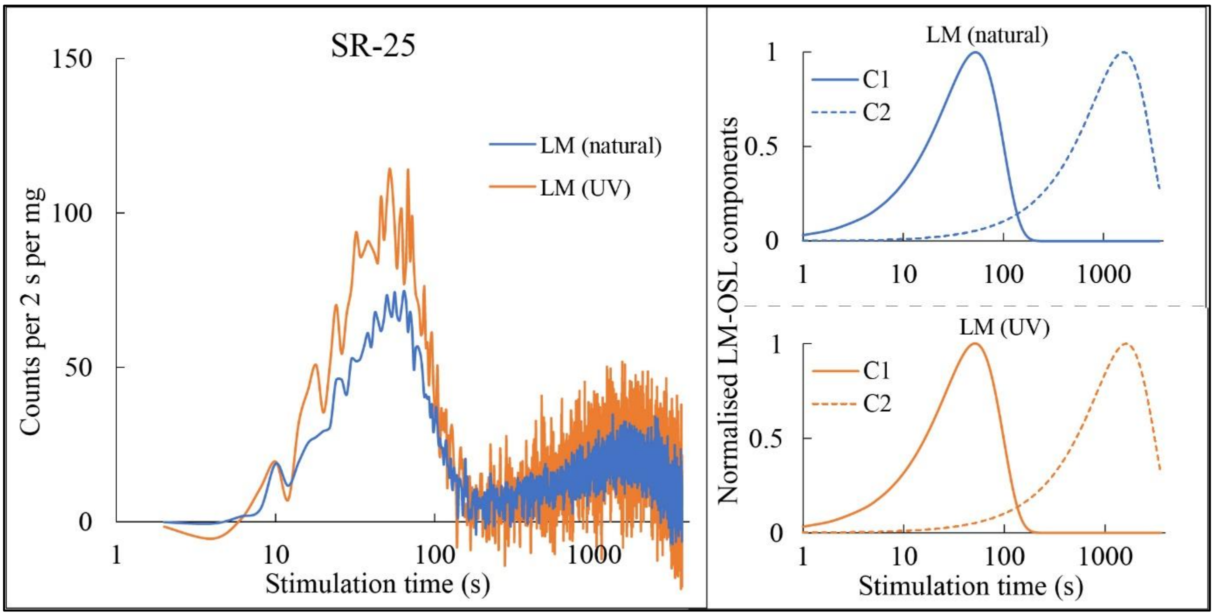

Fig. 3. 37: The left panel shows the LM-BSL of sample SR-25 (medium sample) under natural (blue) and UV-exposed (orange) conditions. The right panels depict the deconvoluted, normalised LM-BSL components (C1 and C2) for natural and UV-exposed conditions.

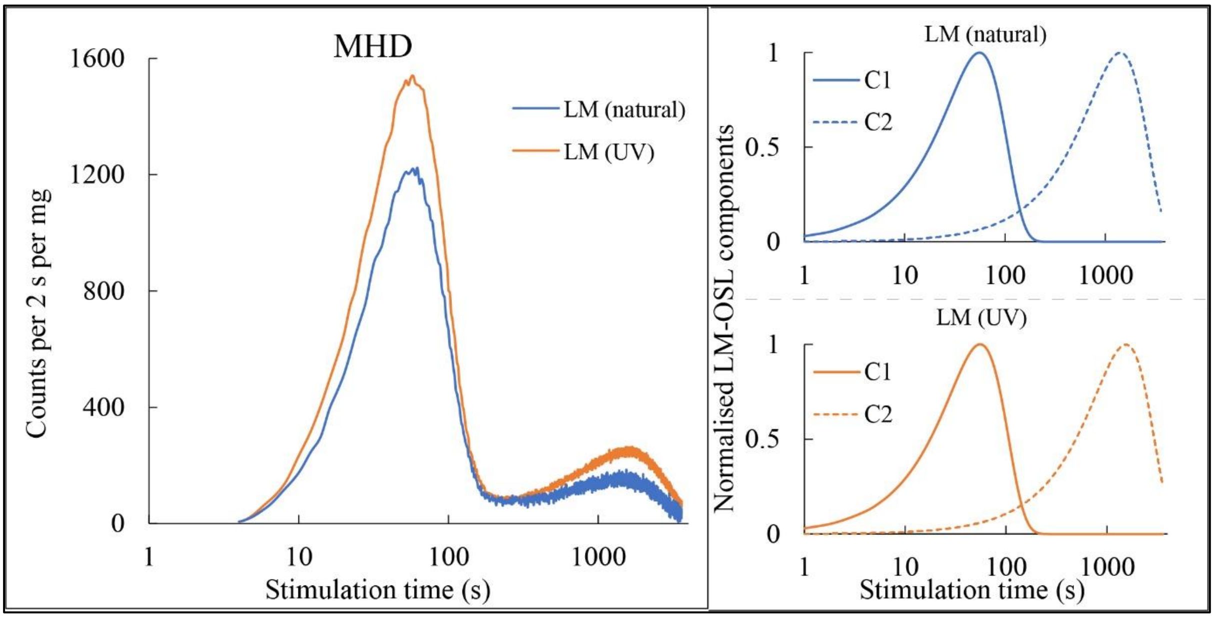

Fig. 3. 38: The left panel shows the LM-BSL of sample MHD (bright sample) under natural (blue) and UV-exposed (orange) conditions. The right panels depict the deconvoluted, normalised LM-BSL components (C1 and C2) for natural and UV-exposed conditions.

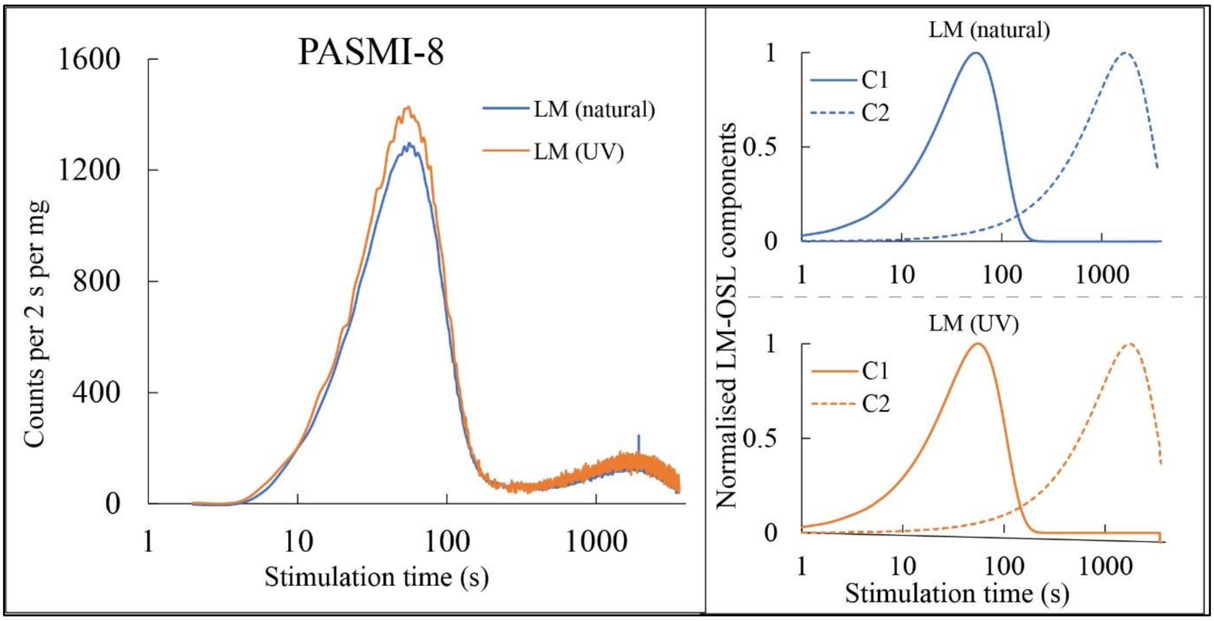

Fig. 3. 39: The left panel shows the LM-BSL of sample PASMI-8 (bright sample) under natural (blue) and UV-exposed (orange) conditions. The right panels depict the deconvoluted, normalised LM-BSL components (C1 and C2) for natural and UV-exposed conditions.

Table 3. 11: Initial trapped charge concentrations and PICS of quartz samples (SR-1A, SR-25, MHD, and PASMI-8) under natural and UV exposed conditions.

Sample name	**Natural condition**		**UV exposed condition**	
	Initial trapped charge concentration	**PICS (in cm ^{2})**	**Initial trapped charge concentration**	**PICS (in cm^{2})**
SR-1A (dull sample)	6.97×10^{3}	8.16×10^{-18}	1.02×10^{4}	1.23×10^{-17}
	2.95×10^{4}	1.18×10^{-20}	7.88×10^{4}	2.14×10^{-20}
SR-25 (medium sample)	5.56×10^{3}	8.57×10^{-18}	4.26×10^{4}	5.97×10^{-18}
	5.49×10^{4}	9.52×10^{-21}	1.36×10^{5}	1.18×10^{-20}
MHD (Bright sample)	1.04×10^{5}	7.66×10^{-18}	1.15×10^{5}	9.32×10^{-18}
	3.65×10^{5}	1.20×10^{-20}	6.06×10^{5}	1.23×10^{-20}
PASMI-8 (bright sample)	1.10×10^{5}	7.80×10^{-18}	1.11×10^{5}	9.29×10^{-18}
	3.75×10^{5}	7.97×10^{-21}	4.81×10^{5}	9.98×10^{-21}

Fig. 3. 36, Fig. 3. 37, Fig. 3. 38 and Fig. 3. 39 present the LM-BSL responses of samples SR-1A (dull sample), SR-25 (medium sample), MHD (bright sample), and PASMI-8 (bright sample) under natural and UV-exposed conditions. The LM-BSL signals were deconvoluted to identify distinct PICS and initial trapped charge concentrations. The corresponding PICS and charge concentrations for these LM-BSL peaks are detailed in Table 3. 11. The results are summarised as follows:

SR-1A (Dull Sample): The total LM-BSL signal increases by 2.56 times under UV exposure. No new components emerge, and the two existing components remain constant.

SR-25 (Medium Sample): UV exposure enhances the total LM-BSL signal by 1.21 times. The component analysis shows no formation of new components, with the two existing ones persisting unchanged.

MHD (Bright Sample): A 1.56 times increase in the total LM-BSL signal is observed under UV exposure. The component analysis reveals no introduction of additional components, with the existing two components remaining stable.

PASMI-8 (Bright Sample): The total LM-BSL signal increases by 1.16 times under UV exposure. The existing components remain unaffected, and no new components are detected.

UV exposure results in moderate enhancements in LM-BSL signals across all quartz samples, with increases ranging from 1.16 times in the bright sample (PASMI-8) to 2.56 times in the dull sample (SR-1A). The natural signal across all samples is dominated by two trap components (C1 and C2). UV exposure does not introduce new components, and the two existing components remain unchanged across the samples.

3.8 Discussion and conclusion

This chapter investigates the luminescence sensitivity changes in quartz due to potential natural factors mimicked in the laboratory, such as annealing, irradiation, sunlight exposure, and UV radiation. It explores the impact of these factors on various luminescence parameters, including thermoluminescence (TL) and linearly modulated blue stimulated luminescence (LM-BSL), using a set of quartz samples with varying sensitivities continuous wave blue stimulated luminescence (CW-BSL)

a. Effect of laboratory-treated factors on 110 ºC TLS

Annealing significantly enhances 110 ºC TLS, with dull sample (HELN) showing the highest proportional increase 80-fold while medium and bright samples exhibit smaller enhancements (3–6-fold). Irradiation also sensitises 110 ºC TLS, resulting in a 7-fold increase in the dull sample (HELN) and a 1–2-fold increase in medium and bright samples. In contrast, sunlight and UV exposure decrease 110 ºC TLS across all samples, with the bright sample (MHD) experiencing the most substantial reduction, up to 0.55 of its natural 110 ºC TLS.

b. Effect of laboratory-treated factors on higher TL glow curve (200-450 ºC)

In full TL glow curve:

Annealing shows a decreasing trend in the broad TL glow curve around 300 °C across all samples. Irradiation reduces the broad TL peak in dull and medium samples, while bright samples exhibit an increasing trend in the 200–300 °C range. Sunlight exposure leads to a consistent reduction in the Full TL glow curves across all samples. In contrast, UV exposure slightly reduces the Full TL glow curves across all samples except the PASMI-8 bright sample, which remains unaffected.

In the light-insensitive TL part:

There is a decreasing trend in the TL glow curve around 300 °C across all samples due to annealing. Irradiation does not significantly affect the peak in the dull and medium samples; however, in bright samples, an increase is observed around 200–300 °C peak. Sunlight exposure consistently reduces the TL glow curve across all samples. Under UV exposure, a decrease in the broad peak, except the bright sample (PASMI-8), remains unaffected.

In the light-sensitive TL part:

Annealing does not appear to affect the 200–450 °C range across all the samples. Irradiation shows A slight decrease in the light-sensitive TL glow curve observed in the dull and medium samples, whereas the bright sample MHD shows no change, and PASMI-8 exhibits an increase around 200–300 °C. Sunlight exposure also does not appear to affect the broad peak across all the samples as in the annealing case. In UV, the broad peak remains the same in all samples except the dull sample (HELN), which shows a slight decrease.

c. Effect of laboratory-treated factors on LM-BSL

Annealing significantly increases the LM-BSL signals across quartz samples, with enhancements ranging from 7 to 17 times. Similarly, irradiation sensitises the LM-OSL signals across all samples, with the enhancement factor ranging from 3-10 times. Sunlight exposure exerts varying impacts on LM-BSL signals across quartz samples, causing a minute reduction in the dull sample (SR-1A) and enhancements ranging from 1 to 3 times in other samples. UV exposure results in moderate enhancements in LM-BSL signals across all quartz samples, with increases ranging from 1 to 3 times.

The natural LM-BSL of all the samples shows two components. Annealing does not introduce any new component in all the samples except HELN, which shows a new component. Irradiation shows the creation or activation of two new components across all the samples. Sun and UV exposure, the components remain the same as in natural conditions.

d. Effect of laboratory-treated factors on BSLS

Annealing sensitises a maximum of 10-fold in dull samples, whereas others show an increase of 2-3 times. Similarly, irradiation showed an increase 7-fold in dull samples, while medium and bright samples increased by 1-2 times. Sunlight exposure decreases the natural value across all the samples by up to 0.69. UV exposure also reduces up to 0.75 times across all the samples except the bright sample PASMI-8, which remains the same.

The study demonstrates that luminescence sensitivity changes are dependent on the type of quartz sample and the influencing factor. Dull samples exhibit the most significant enhancements under annealing and irradiation, while medium and bright samples show moderate changes. Sunlight and UV exposure generally reduce luminescence sensitivity. Irradiation introduces two new component creations in all the samples. These findings underscore the importance of natural factors in controlling luminescence characteristics, with implications for sediment transport conditions.

e. Effect of annealing at different temperatures on BSLS

Annealing at various temperatures (110 °C, 150 °C, 190 °C, 230 °C, 270 °C, 310 °C, 350 °C, 390 °C, 430 °C, 470 °C, and 510 °C) for 10 minutes in the Riso machine reveals significant variation in BSLS sensitisation across quartz types. Dull quartz (SR-1A) shows the highest increase (~75-fold), followed by medium quartz (SR-25, ~4-fold) and bright quartz samples (MHD, ~3.7-fold; PASMI-8, ~3-fold). The data highlight three key temperature regions: room temperature to 280 °C, 300 °C to 450 °C, and above 450 °C, with sharp increases in BSLS around 280 °C and 450 °C, suggesting notable lattice changes. These findings emphasise the impact of annealing on the luminescence properties of quartz and lay the foundation for the investigations detailed in Chapter 4.

Chapter 4

4. Exploring luminescence variations in quartz and their relation to structural defects

4.1 Introduction

Luminescence is a phenomenon controlled by crystal defects, which depends on the magma composition and the thermodynamic conditions during the formation of the source rock (Preusser et al., 2009). Quartz minerals form in magma under hydrothermal conditions, resulting in the O-H bond being one of its notable defects. Chemical analyses of natural quartz samples from different origins have revealed a negative correlation between water content in the crystal lattice and OSL sensitivity, highlighting the critical role of water in influencing luminescence sensitivity (S. K. Sharma et al., 2017).

Using first-principles calculations, Rosa et al. (2005) investigated the interaction of water with α-quartz and examined the structural and thermodynamic properties of the resulting defects. Their study explored the geometry and stability of water-related defects, such as hydrogarnet defects ([4H] Si), Griggs defects, and interstitial water. These findings highlighted the role of water in altering the structural integrity of quartz and influencing its properties.

This study further explores the role of high-temperature annealing and water diffusion in influencing the luminescence sensitivity of quartz crystals. An instrument was designed and developed as a trial setup to diffuse water into quartz crystals at high temperatures under a water-saturated environment. Quartz samples were subjected to thermal and infrared (IR) studies to elucidate the relationship between structural and chemical changes in quartz and its luminescence sensitivity. Thermogravimetric analysis (TGA) was employed to evaluate thermal stability, while differential scanning calorimetry (DSC) (refer to Chapter 2) provided insights into heat exchange and chemical reactions during temperature ramping. Additionally, Fourier-transform infrared (FTIR) spectroscopy (refer to Chapter 2) was utilised to differentiate quartz samples with varying luminescence sensitivities based on their spectral properties. Spectroscopic analyses focused on O-H peak determination and crystallinity index calculations, which were found to correlate with the luminescence properties of quartz.

4.2 Effect of annealing at high temperature and water diffusion on quartz luminescence.

As discussed in Chapter 3, annealing significantly sensitises the luminescence of quartz, far more than irradiation and light exposure. This makes it a valuable tool for understanding the sensitisation process in quartz. To further explore this, an experiment was conducted on annealing quartz samples at high temperatures using a furnace to investigate their behaviour under extreme thermal conditions. Additionally, water diffusion inside the lattice at high temperatures was attempted to study its impact on luminescence in quartz.

The quartz samples used in this study are detailed in Table 4. 1. These samples were collected from the current channel of Bharathapuzha River, Kerala, India, with BP-CH and BP-PRL located approximately 132 km, 234 km downstream, respectively.

Table 4. 1: Details of BP-CH and BP-PRL quartz samples.

Sample Name	**Latitude (in degree)**	**Longitude (in degree)**	**Sample Type**	**Distance (km)**	**Elevation (m)**
BP-PRL	10.780208°	76.573531°	Sediment	132 km	3190
BP-CH	10.789464°	75.930147°	Sediment	234 km	2260

The quartz in each sample was divided into two parts and heated in a muffle furnace using alumina crucibles at different temperatures (220 °C, 400 °C, 550 °C, 700 °C, 800 °C, and 900 °C) for 30 minutes. One part was cooled at normal room temperature conditions while the other part was water quenched at the elevated temperature to facilitate water diffusion.

The 110 °C TLS and BSLS measurements were conducted following the protocol outlined in Table 4. 1. In step 1, the samples were bleached for 40 seconds, followed by irradiation with a small beta dose of 5 Gy in step 2. In step 3, the samples were preheated, and the 110 °C TLS was recorded. Finally, in step 4, the BSLS was measured at 125 °C. The method for calculating

110 °C TL and BSL intensity is described in Section 2.4.4. For comparative analysis, the recorded BSLS and 110 °C TLS values were normalised with respect to their natural values.

Table 4. 2: Measurement protocol for studying the effect of annealing temperature on the 110 °C TLS and BSLS of the quartz sample.

Steps	Protocol	Remark
	The natural or annealed sample	Sample
1	BSL 125 °C (40 s)	Bleaching
2	Beta dose (~5 Gy)	Irradiation
3	Preheat 220 °C	Record of 110 °C TLS
4	BSL 125 °C (40 s)	BSLS measurement

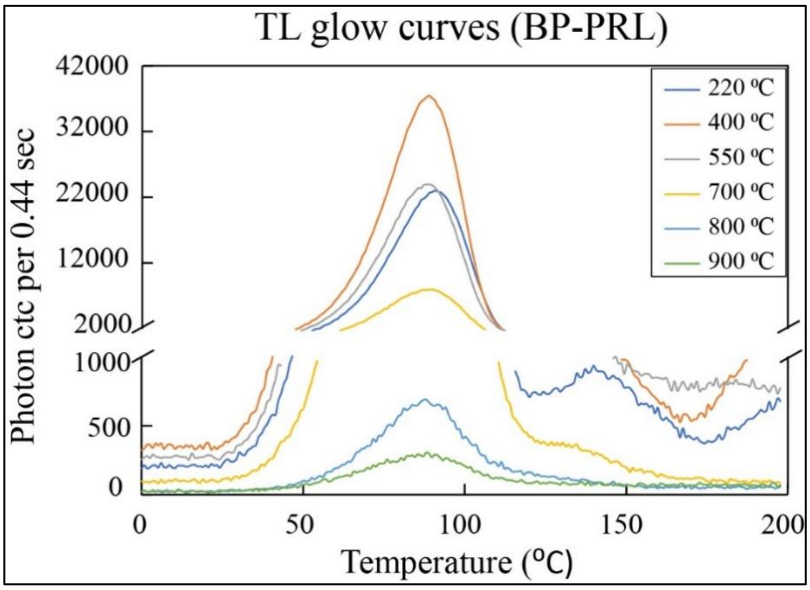

Fig. 4. 1: TL glow curve of quartz samples at different annealing temperatures.

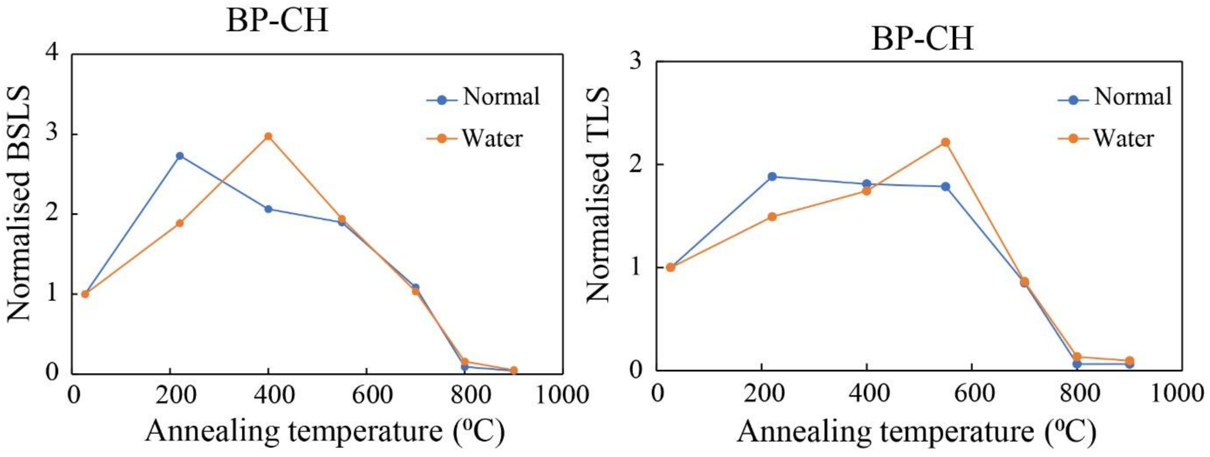

Fig. 4. 2: Normalised BSLS (left) and 110 °C TLS (right) for the quartz sample (BP-CH) at different annealing temperatures, with samples cooled under normal conditions and via water quenching.

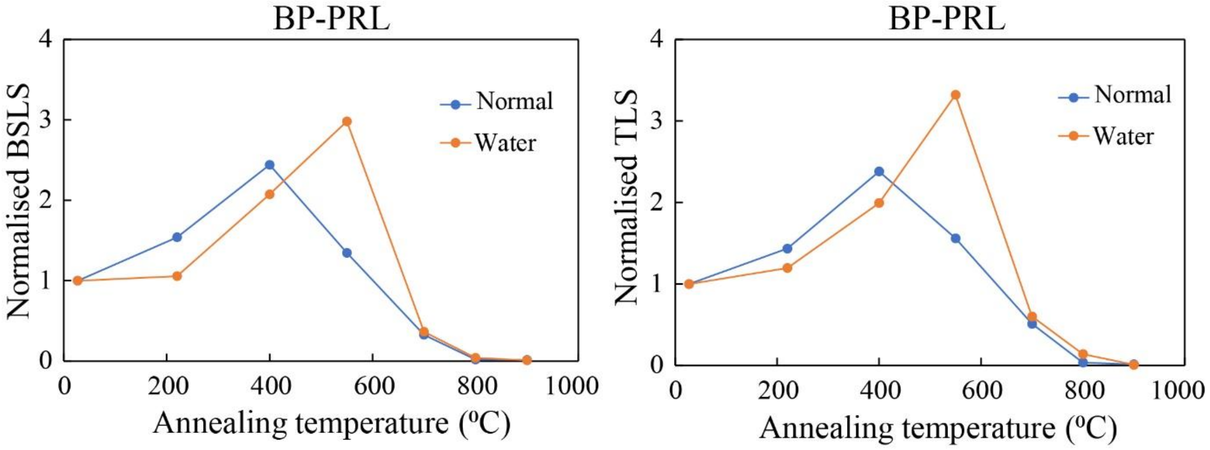

Fig. 4. 3: Normalised BSLS (left) and 110 °C TLS (right) for the quartz sample (BP-PRL) at different annealing temperatures, with samples cooled under normal conditions and via water quenching.

Fig. 4. 1 represents the TL glow curve for quartz samples annealed at different temperatures, highlighting the changes in the TL curve resulting from various thermal treatments.

Fig. 4. 2 and Fig. 4. 3 illustrate the effect of annealing temperature on normalised BSLS (left) and 110 °C TLS (right) for BP-CH and BP-PRL quartz samples under normal cooling and water quenching conditions. The normalised BSLS and 110 °C TLS values are presented to evaluate the luminescence sensitivity changes. The results are summarised as follows:

Normal cooling:

- BP-PRL Sample: The BSLS and 110 °C TLS increase with annealing temperature up to 400 °C. Beyond 400 °C, the sensitivity decreases, and samples annealed at 700 °C, 800 °C, and 900 °C exhibit 110 °C TLS and BSLS values below their natural levels.
- BP-CH Sample: The luminescence remains stable with values 2-3 times higher than the natural 110 °C TLS and BSLS for annealing temperatures of 220°C, 400°C, and 550°C.

However, at higher temperatures, the sensitivity decreases below its natural 110 °C TLS and BSLS.

Water quenching:

- In water-quenched quartz samples (BP-PRL and BP-CH), the sensitivity increases up to 550°C. Beyond this temperature, the sensitivity decreases sharply, falling below the natural values for samples annealed at higher temperatures. Water-quenched samples exhibit lower 110 °C TLS and BSLS than normally cooled samples up to 400 °C, followed by an increase at 550 °C.

This behaviour aligns with the well-established phase transition of quartz from alpha to beta quartz at 573°C, potentially leading to a significant decrease in sensitivity. The alpha-to-beta phase transition is a structural transformation involving lattice symmetry and bond length changes, possibly affecting the competition between radiative and non-radiative transition at the hole traps.

Sensitisation of annealed quartz at 700 and 900 °C:

The high-temperature annealed samples showed their 110 °C TLS and BSLS values below the natural levels. To investigate whether the sensitivity changes induced by annealing are permanent, the quartz samples were subjected to repeated sensitisation by heating at 450 °C for 20 minutes, following a protocol outlined in Table 4. 2, repeated for 10 cycles. Quartz samples annealed at 700 °C and 900 °C were selected for this experiment due to the observed decrease in sensitivity below natural BSLS and 110 °C TLS.

In step 1 of the protocol (Table 4. 3), the samples were bleached using BSL, followed by irradiation with a beta dose of 5 Gy. Subsequently, the samples were preheated to 220°C to record the 110 °C TLS, and the BSLS was measured in step 4. In step 5, the samples were annealed at 450°C for 20 minutes, after which the protocol returned to step 2 to repeat the cycle. The 110 °C TLS and BSLS values were normalised with respect to their natural levels and are presented in Fig. 4. 4.

Fig. 4. 4, quartz annealed at 700 °C shows a gradual recovery of its 110 °C TLS and BSLS sensitivity after 3 to 4 cycles of annealing, with each cycle performed at 450 °C for 20 minutes. Over the total of 10 cycles, the sensitivity increases to approximately twice its natural value. In contrast, quartz annealed at 900 °C demonstrates a slight increasing trend in luminescence sensitivity; however, it fails to achieve significant recovery relative to its natural value, with the normalised 110 °C TLS and BSLS consistently remaining below the natural levels throughout all 10 annealing cycles.

Table 4. 3: Protocol for testing the recovery of 110 °C TLS and BSLS through sensitisation of annealed quartz samples (700 °C and 900 °C).

Steps	Protocol	Remark
	Quartz sample	
1	BSL 125 °C (40 s)	Bleaching
2	Beta dose (~5 Gy)	Irradiation
3	Preheat 220 °C	Record of 110 °C TLS
4	BSL 125 °C (40 s)	Record of BSLS
5	Heating 450 °C (20 min)	Annealing
6	Go to step 2	

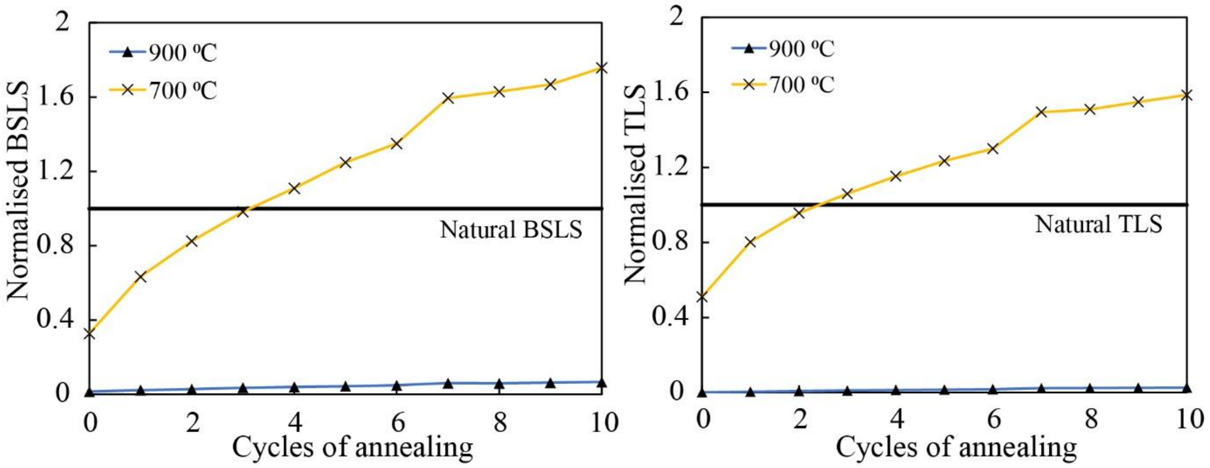

Fig. 4. 4: Sensitisation of BSLS (left) and 110 °C TLS (right) of annealed quartz samples (700 °C and 900 °C) over 10 cycles.

This recovery suggests that annealing enables defect rearrangement or lattice reorganisation within quartz, facilitating sensitivity restoration. In contrast, quartz annealed at 900 °C does not recover its luminescence sensitivity, as it might undergo a glass transition or irreversible structural changes at this higher temperature. This indicates that annealing at extreme temperatures causes permanent damage to the quartz lattice, preventing sensitivity recovery.

4.2.1 Trial instrumentation for water diffusion in quartz crystals

To enable controlled annealing and water diffusion in quartz crystals, the goal was to introduce water-related defects into the quartz lattice under high-temperature, water-saturated conditions. This required designing an experimental setup capable of simulating such an environment. A high-temperature, high-pressure apparatus was designed to achieve this, aiming to combine precise control over temperature and pressure.

The setup comprised an enclosed cylindrical body (Fig. 4. 5 left) made of SS316 stainless steel. The cylindrical design was engineered to endure pressures up to approximately 300 bar, creating a controlled environment for heating quartz samples in the presence of water. Heating was performed using a muffle furnace integrated with the system, as shown in Fig. 4. 5 (right).

Fig. 4. 5: Cylindrical body for heating quartz in a water-saturated environment (left) and heating in the furnace (right).

Fig. 4. 6: Deteriorated forms of the high-temperature instrument.

Despite the promising design and expert guidance, maintaining high pressure within the apparatus proved to be a significant challenge. Multiple attempts were made to optimise the system, but issues such as material degradation and pressure loss persisted during the experiments. The high-temperature instrument showed signs of deterioration after repeated trials, as depicted in Fig. 4. 6. These limitations highlighted the challenges of achieving stable high-pressure conditions for water diffusion in quartz and underscored the need for further refinement in experimental design to successfully introduce water-related defects into quartz crystals in a controlled manner.

4.3 Thermal studies

Since annealing significantly influences the luminescence behaviour of quartz, thermal studies offer valuable insights into the associated structural and chemical changes occurring with temperature. Techniques such as thermogravimetric analysis (TGA) and differential scanning calorimetry (DSC) provide essential information on material responses during controlled temperature ramping, allowing correlations with changes in luminescence sensitivity. For this study, three quartz samples with different luminescence sensitivities were selected: HELN (low sensitivity), SR-25 (medium sensitivity), and PASMI-8 (high sensitivity), as described in Chapter 3.

4.3.1 Thermogravimetric analysis (TGA)

Thermogravimetric analysis (TGA) is used to study the thermal stability of materials by measuring mass loss as a function of temperature.

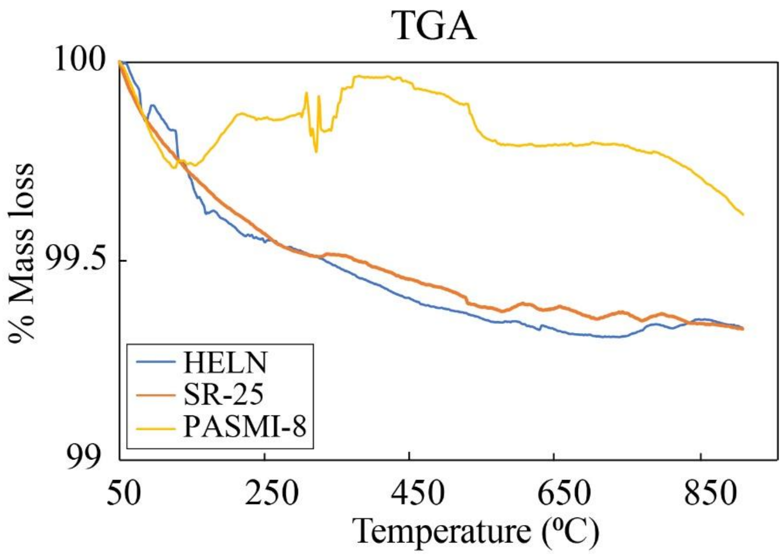

Fig. 4. 7: TGA analysis showing mass loss as a function of temperature for HELN, SR-25, and PASMI-8 quartz samples.

The TGA results (Fig. 4. 7) indicate a noticeable mass loss in the HELN (dull) and SR-25 (medium) quartz samples, while the PASMI-8 (bright) quartz sample shows negligible mass loss. This suggests that structural water-related defects, such as silanol groups or water inclusion, may be converted to water vapour during heating, resulting in mass loss, as described by the reaction in equation 4.1 (Bambauer et al., 1969).

$$2\ \equiv\text{Si–OH} \rightarrow\ \equiv\text{Si–O–Si}\equiv + H_2O \tag{4.1}$$

4.3.2 Differential scanning calorimetry (DSC)

Differential scanning calorimetry (DSC) analysis facilitates heat exchange of the material as a function of temperature.

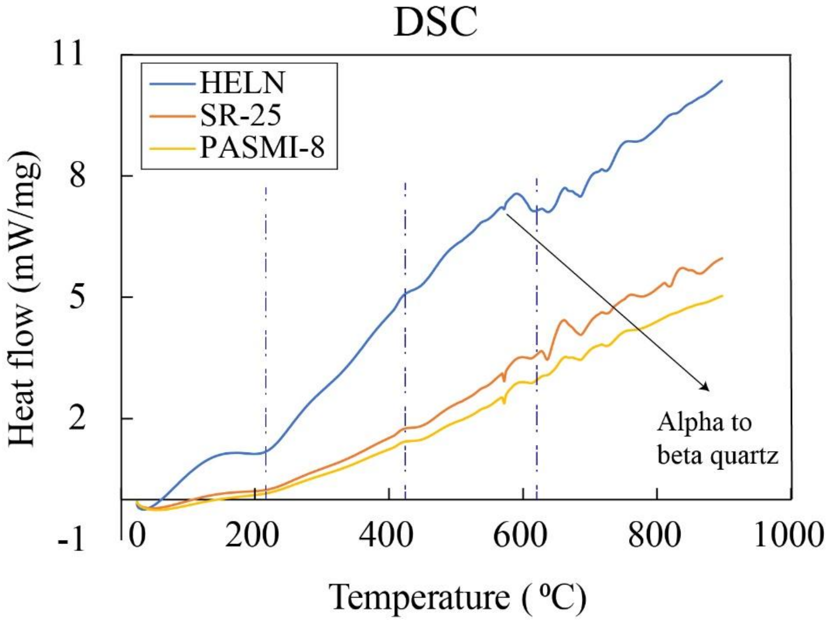

Fig. 4. 8: DSC analysis showing heat flow as a function of temperature for HELN, SR-25, and PASMI-8 quartz samples, highlighting the alpha-to-beta quartz phase transition.

The DSC analysis (Fig. 4. 8) reveals three distinct thermal regions: up to 200 °C, 200–420 °C, and beyond 600°C, suggesting chemical reactions or phase changes in the quartz samples. The phase transition between alpha and beta quartz is observed as a narrow endothermic peak at 573 °C. Additionally, the DSC data highlights changes in crystal properties around 200 °C, 420 °C, and 620 °C, marking critical thermal events. These thermal regions align with the luminescence changes observed during heating, as discussed for quartz samples in Chapter 3 (Fig. 3. 12 to Fig. 3. 15). These findings emphasise the strong correlation between the thermal behaviour of quartz and its luminescence properties, highlighting the critical role of structural changes in determining sensitivity.

4.4 IR spectroscopy

Infrared (IR) spectroscopy provides insights into molecular vibrations, serving as a tool to identify structural and chemical properties of materials. Fourier transform infrared (FTIR) spectra were recorded in the range of 1200 to 400 cm^{-1} (Fig. 4. 9), and peaks corresponding to O–H vibrations and crystallinity were analysed for three quartz types: HELN (low sensitivity), SR-25 (medium sensitivity), and PASMI-8 (high sensitivity) (Table 4. 3). Details of these samples are provided in Chapter 3.

Peak related to O-H vibration:

The range 3000–3600 cm^{-1} encompasses the fundamental OH- vibrations Since water content influences the luminescence sensitivity of quartz crystals (Gaweł et al., 2021; S. K. Sharma et al., 2017; Stalder, 2021). FTIR was utilised to quantify water speciation in quartz samples of varying sensitivity, enabling the exploration and correlation between luminescence sensitivity and water content.

Crystallinity index:

The infrared spectra of quartz in the 1200–400 cm^{-1} region display characteristic vibrational bands associated with the SiO_4 tetrahedral framework (Gadsden, 1975). Notably, the 695 cm^{-1} band, attributed to symmetrical bending vibrations arising from octahedral site symmetry, is strongly linked to the degree of crystallinity in quartz (Saikia, 2014). In contrast, the 778 cm^{-1} band, associated with tetrahedral–tetrahedral ion vibrations, remains relatively unaffected by variations in pressure and temperature, making it a stable internal reference. The absence of the 695 cm^{-1} band in amorphous silica reflects the lack of long-range structural order, as previously reported by Hlavay et al. (1978). These spectral features thus serve as reliable indicators of quartz crystallinity and growth characteristics.

To evaluate the purity and structural relationships in quartz, the crystallinity index (CI) is calculated as the ratio of peak intensities at 778 cm^{-1} and 695 cm^{-1}, using the baseline method (Razva et al., 2014; Saikia, 2014). The crystallinity index (CI) is inversely proportional to crystallinity: a lower CI indicates well-crystallised quartz, while a higher CI signifies poorly crystallised quartz (Ramasamy & Suresh, 2009). Crystallinity reflects the proportion of crystalline material within a mixture of crystalline and non-crystalline phases.

Table 4. 3 represents the characteristics of quartz samples (HELN, SR-25, and PASMI-8), including their integrated OH absorbance and crystallinity index (CI).

- O–H vibration peak: HELN (dull sample) exhibits the highest OH absorbance area in the 3600–3000 cm^{-1} region, around 1.03 a.u., followed by SR-25 (medium luminescence) with 0.77 a.u., and PASMI-8 (bright sample) showing the lowest value of 0.31 a.u.. This decreasing trend in OH content correlates with increasing luminescence sensitivity, consistent with the findings of S. K. Sharma et al. (2017).
- Crystallinity index (CI): HELN, associated with dull luminescence, shows higher crystallinity, indicated by a lower CI value of 1.13. SR-25 exhibits a CI of 2.00, reflecting lower crystallinity. For PASMI-8, the characteristic quartz peaks are indistinct, making the crystallinity index not applicable.

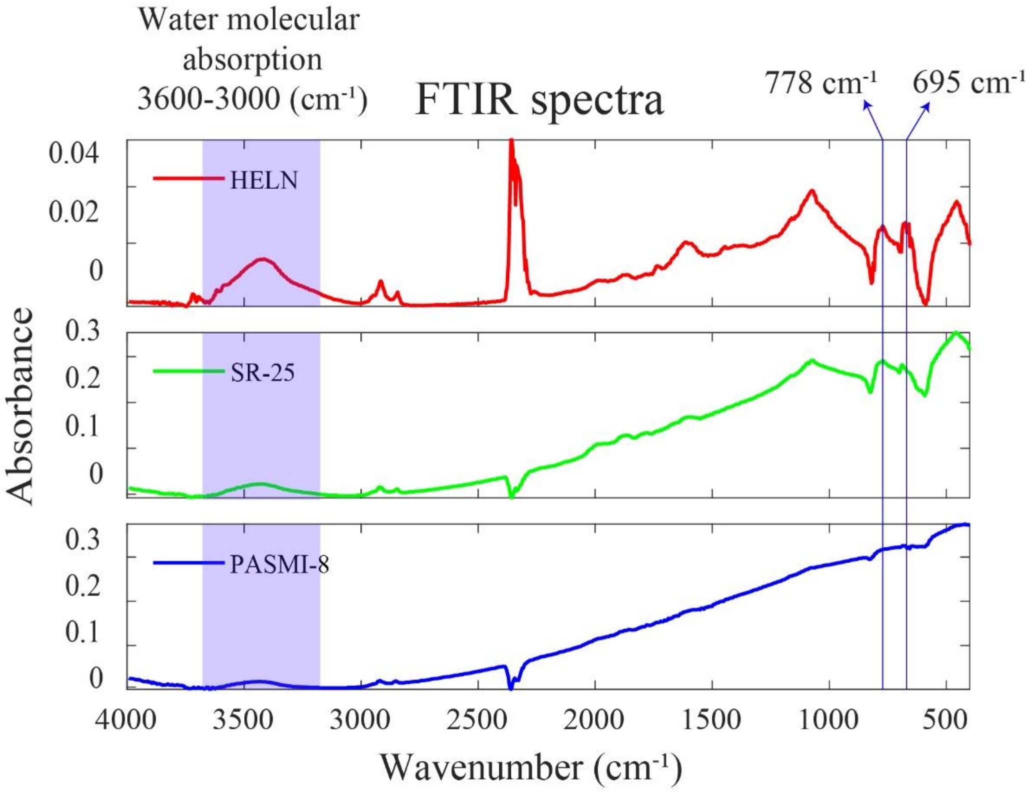

Fig. 4. 9: FTIR spectra of quartz samples HELN (dull), SR-25 (medium), and PASMI-8 (bright). The shaded region (3600–3000 cm^{-1}) highlights the O-H vibrational range associated with water molecular absorption. Peaks at 778 cm^{-1} and 695 cm^{-1} correspond to crystallinity.

Table 4. 4: Characteristics of quartz samples (HELN, SR-25, and PASMI-8), including their source, luminescence type, BSLS, O-H absorbance, and crystallinity index.

Sample name	**Source**	**Luminescence type**	**BSLS (Photon counts / (Gy × mg))**	**O-H absorbance area (in a.u.)**	**Crystallinity index (in a.u.)**
HELN	Quartzite rock	Dull	7 ± 1	1.03	1.13
SR-25	Sediment	Medium	759 ± 82	0.77	2.00
PASMI-8	Sediment	Bright	10324 ± 1293	0.31	NA

4.5 Summary and conclusion

a. High-temperature annealing and diffusion of water

Both normally cooled and water-quenched quartz exhibit an increase in 110 °C TLS and BSLS beyond their natural values at annealing temperatures of 220 °C, 400 °C, and 550 °C. However, for samples annealed at 700 °C, 800 °C, and 900 °C, the sensitivity values decrease below their natural levels. This aligns with the alpha-to-beta quartz phase transition at 573 °C, where structural changes in lattice symmetry and bond lengths likely impact the competition between radiative and non-radiative transitions at hole traps. Water-quenched samples exhibit lower 110 °C TLS and BSLS than normally cooled samples up to 400 °C, followed by an increase at 550 °C; the reasons remain unclear.

Quartz annealed at 700 °C regained natural sensitivity after 4 cycles of heating at 450 °C and doubled after 10 cycles, suggesting defect rearrangement or lattice reorganisation. However, quartz annealed at 900 °C showed no recovery, likely due to irreversible structural changes or a glass transition, indicating permanent lattice damage at extreme temperatures.

The results revealed that the phase transition significantly affects quartz luminescence, likely due to structural rearrangements within the lattice, highlighting the critical role of annealing and structural changes in shaping luminescence behaviour.

b. Thermal analysis

Thermogravimetric Analysis (TGA) revealed noticeable mass loss in dull and medium quartz samples, while bright quartz exhibited minimal mass loss. This suggests that structural water-related defects, such as silanol groups, may be converted to water vapour during heating (Bambauer et al., 1969).

The DSC analysis reveals three distinct thermal regions: up to 200 °C, 200–420 °C, and beyond 600 °C, suggesting chemical reactions or phase changes in the quartz samples highlight changes in crystal properties around 200 °C, 420 °C, and 620 °C. These thermal regions align with the luminescence changes observed during heating, as discussed for quartz samples in Chapter 3 (Fig. 3. 12 to Fig. 3. 15). These findings emphasise the strong correlation between the thermal behaviour of quartz and its luminescence properties, highlighting the critical role of structural changes in determining sensitivity.

c. FTIR analysis

In the FTIR analysis, it is observed that dull quartz exhibits significantly higher absorbance in the O-H vibrational range, whereas bright quartz shows comparatively lower absorbance. These results are consistent with the findings of S. K. Sharma et al. (2017) and suggest the potential role of O-H groups acting as luminescence quenchers. This observation is further supported by TGA results, which indicate a mass loss likely corresponding to the release of water associated with these O-H groups.

The crystallinity index study reveals dull quartz has higher crystallinity and lower luminescence, while bright quartz shows the opposite. This suggests either transportation-induced amorphisation or increased impurities reduce crystallinity and enhance luminescence.

Chapter 5

5. Luminescence: a proxy for earth surface studies

5.1 Introduction

Provenance studies provide crucial insights into the **sources and pathways of sediment transport**, offering information about geological, environmental, and climatic factors that influence sediment deposition. They play an essential role in understanding landscape evolution and assessing natural sediment budgets.

In the past decade, the **luminescence sensitivity of quartz grains** has emerged as a valuable proxy in provenance analysis by preserving information about sediment transport and depositional environments. As a result, luminescence sensitivity can be used to trace sediment provenance. This chapter investigates **variations in luminescence sensitivity across river basins** to better understand luminescence signal variations, distinguish sediment sources, and quantify sediment mixing at different confluences. Additionally, it examines whether the transport environment impacts the luminescence sensitivity of quartz.

This chapter aims to evaluate the potential of luminescence sensitivity in quartz as an indicator of sediment provenance, specifically addressing the following objectives:

1. Variation in luminescence sensitivity between source rocks, weathered rocks, and sediments.
2. The influence of transport distance on luminescence sensitivity in fluvial system (Sabarmati River and Yamuna River).
3. Quantification of sediment contributions from various tributaries and hill slopes, including the Beas confluence, Nubra-Shyok confluence, Sabarmati case, and artificially mixed samples.
4. The effect of aeolian input on the luminescence sensitivity of river channel sediments in semi-arid region rivers (the case of Sabarmati River)
5. Single-grain quartz luminescence sensitivity analysis and the effect of grain shape (roundness and sphericity) on luminescence sensitivity.

5.2 Sabarmati River

Provenance studies help delineate sediment sources, fluxes, and dispersal patterns through space and time. Parameters such as grain-size distribution, mineralogical composition, heavy mineral assemblages and isotope systematics are commonly used to infer source lithologies, sediment production rates, and transport trajectories (Dey et al., 2023; Duan et al., 2023; Niu et al., 2022; Xu et al., 2022; Weltje & von Eynatten, 2004). These inferences are then interpreted in the context of tectonic and climatic forcings (Bernard & Sinclair, 2022; Sharman et al., 2019). While isotope analyses and heavy mineral studies have been widely applied in provenance research, they only reflect the composition and metamorphic history of the parent rocks (Basu et al., 1990; Morton, 1985; Weltje & von Eynatten, 2004). Usage of isotope couples like Sr-Nd is efficient for understanding comparative fluxes from binary sources (Dey et al., 2023), but for multimodal sources, it falls short.

In recent years, the use of luminescence sensitivity (LS), defined as the luminescence intensity (photons s^{-1}) normalised by sample mass and absorbed radiation dose, has been explored for sediment provenance studies (e.g. Bartyik et al., 2021; Del Rio et al., 2021; Goswami et al., 2024; Hou et al., 2024, 2025; Mineli et al., 2021; Nascimento et al., 2015; Nian et al., 2018; Parida et al., 2025; Sawakuchi et al., 2012, 2014, 2018). LS depends on the physical and chemical environments of the magma and its cooling rate during the crystallisation (Hashimoto et al., 1994, 1997). These conditions determine the incorporation of trace elements and creation of lattice defects that eventually participate in the luminescence process (Correcher et al., 2009; Gotte and Ramseyer, 2012; Krbetschek et al., 1997; Mikhailik et al., 2011; Singh et al., 2015; Trukhin, 2019). Post-crystallisation changes in the virgin LS occurs due to irradiation from natural radioactivity over geological times, changes in stress fields and faulting, daylight exposure during rock weathering and transport, and thermal history that could comprise geothermal gradients, heating due to forest fires and lava flows (Cao et al., 2021; Jeong & Choi, 2012; Nelson et al., 2022; Fitzsimmons, 2011; Mateus et al., 2020; Odom and Rink, 1989; Pietsch et al., 2008; Parida et al., 2025; Schilles et al., 2001; Zhang et al., 2022). These events, together and individually, provide energy to induce changes in lattice configurations, defect creation, inter-defect charge transfer, and thence modify LS (Caicedo et al., 2022; Han et al., 2000; Li, 2002; Poolton et al., 2000; Zimmerman, 1971). LS of quartz varies over 10 orders of magnitude, and have been related to the concentration of OH radicals in quartz lattice (S. K. Sharma et al., 2017; Stadler et al., 2019, 2025).

Gray et al. (2019) reviewed recent developments in the application of luminescence sensitivity (LS) for provenance studies. Besides LS, the use of other luminescence parameters such as saturation dose, de-trapping rates, and the relative amplitudes of components in linearly modulated blue-stimulated luminescence (LM-BSL) for sediment provenance has also been explored (Gong et al., 2014, 2015; Gray et al., 2019; Tsukamoto et al., 2011). LS has also been used to estimate sediment fluxes (Goswami et al., 2024; Parida et al., 2025), and its relationship with the denudation rate has been explored (Del Rio et al., 2021; Parida et al., 2025; Sawakuchi et al., 2018). Lü and Sun (2011) examined variations of LS with grain size, and studies by Moska and Murray (2006), Pietsch et al. (2008) and others have documented increases in LS due to repeated cycles of burial and daylight exposure.

Building on this context, spatial variations in luminescence sensitivity (LS) of quartz along a ~160 km transect of the upper Sabarmati River basin, from its origin in the Aravalli Range to the Dharoi dam, were investigated (Fig. 5. 1). Sediment dispersal in the upper Sabarmati basin is complex due to multi-modality in sediment flux from numerous tributaries, sediments wind transported from gullied river terraces and paleodunes from downstream direction and anthropogenic activities such as agriculture and riverbed mining (Sonam et al., 2021). These complexities prompted us to document the spatial patterns of LS along the river to examine the relative amplitude of the processes mentioned above and understand their impact on sediment provenance studies.

5.2.1 Geological and geomorphological settings

The Sabarmati River drains the mid-Archean to Cenozoic rocks of the Proterozoic Aravalli Delhi fold belt. It flows southwest for ~400 km before ending its journey in the Gulf of Khambhat (Fig. 5. 1). The folded mountain chain is tectonically inactive and undergoes climate-induced denudation. The maximum elevation in the Sabarmati Basin is about 1200 m above msl, and the topographic relief is moderate. Pediments with thin layers of soil on the surface are present at the base of mountains. Rill and gully erosion are dominant among the surface erosion processes. Fig. 5. 2 provides a geological map of the study area. Associated supergroups and rock types are listed in Table 5. 1. Major rock types in the catchments are quartzites, phyllites, gneisses and schists (Table 5. 1, Fig. 5. 2; SOI, 1972; Dasgupta et al., 2000; Fareeduddin, 2020; Tandon et al., 1997).

This River basin covers an area of 21,674 km^2, with annual precipitation ranging between 500–1000 mm and potential evapotranspiration between ~1600–2000 mm (Gibling & Tandon, 1997; Thokchom et al., 2017; Sonam et al., 2021; Rastogi & Sarin, 2005; GOI, 2014). Most rainfall occurs during the monsoon months (June–September), with 30–40 rainy days per year, resulting in a regional annual water deficit of ~800–1000 mm. Wind speeds range from 20–38 km/h and occasionally exceed Bagnold's threshold for wind transport of fine to medium sand (Allchin & Goudie, 1971; Juyal et al., 2003).

Upstream of Dharoi dam, the river passes through narrow, confined valleys and in the midstream, it transitions into broad intermontane valleys before entering the plains. The river channel has a pool–riffle sequence, typical of gravel-bed systems, and its longitudinal connectivity is frequently disrupted during low-flow stages (Sonam et al., 2021). Only during the monsoon season, the hydrologic and sediment connectivity is established along the river, barring disruptions due to minor dams and reservoirs.

In the mid-downstream part of the basin, the stratigraphy of the Sabarmati basin comprises a four-fold subdivision of fluvial and aeolian deposits (Tandon et al., 1997). The sequence begins with NE–SW trending semi-arid alluvial fans, overlain by a heterolithic unit indicative of phases of high-energy episodic flooding and aeolian reworking (Juyal et al., 2000, 2003; Srivastava et al., 2001; Gibling & Tandon, 1997; Jain and Tandon, 2003; Tandon et al., 1997). Fluvial sands, mud deposits, and aeolian sediments overlie this and suggest varied, climate-controlled depositional environments with phases of incision and aggradation (Tandon et al., 1997). Luminescence dating places the age of this succession to be >300 ka (Tandon et al., 1997).

Sabarmati is a gravel-bed river till Dharoi dam, beyond which it changes to a sand-bed river (Sonam et al., 2021). Most of the fine-grained, sand-sized sediment load is derived from the weathering of Aravalli bedrock in the catchment during its long antiquity and also through remobilisation of transiently stored sediments by gully erosion of fluvial terraces. In the lower reach, gully erosion of banks and aeolian deposits supply sand to the river. They mix with sediments from upstream at local scales and traverse downstream. Some of these sands are recycled and transported upstream by the winds.

Sample detail:

LS of forty-five samples (Table 5. 2) from (a) rocks and boulders in the river catchment, (b) sediments of the trunk channel, (c) tributaries, viz., Wakal, Mansi, Pamri, Sei, and smaller rivulets, (for locations, see Fig. 5. 1), (d) a weathered rock horizon, and (e) dune sands from paleodune-fields (Juyal et al., 2003), were measured. Sediment samples were collected underwater, and at places where the channel was dry, the upper 5-10 cm of surface material was removed prior to sampling. Sediments were sieved onsite for < 1000 µm grain fractions and sealed in opaque black bags for further processing in the laboratory. Table 5. 3 collates rock samples collected from different locations in the basin.

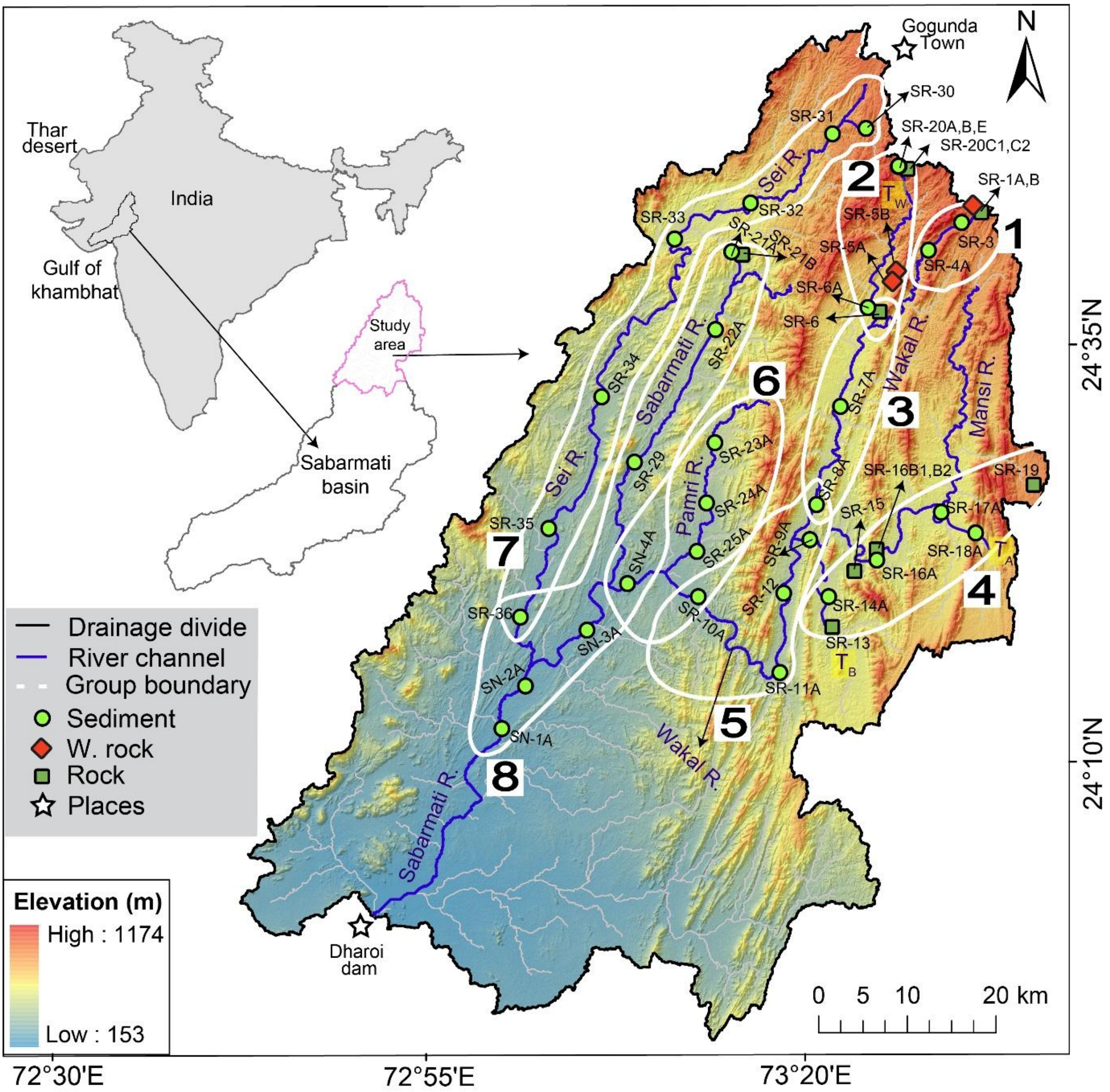

Fig. 5. 1: Map showing Sabarmati River and its tributaries in the upper catchment. Sample locations are marked along rivers and grouped based on the tributary confluences (Table 5. 8) to understand luminescence sensitivity variations as a function of downstream distance.

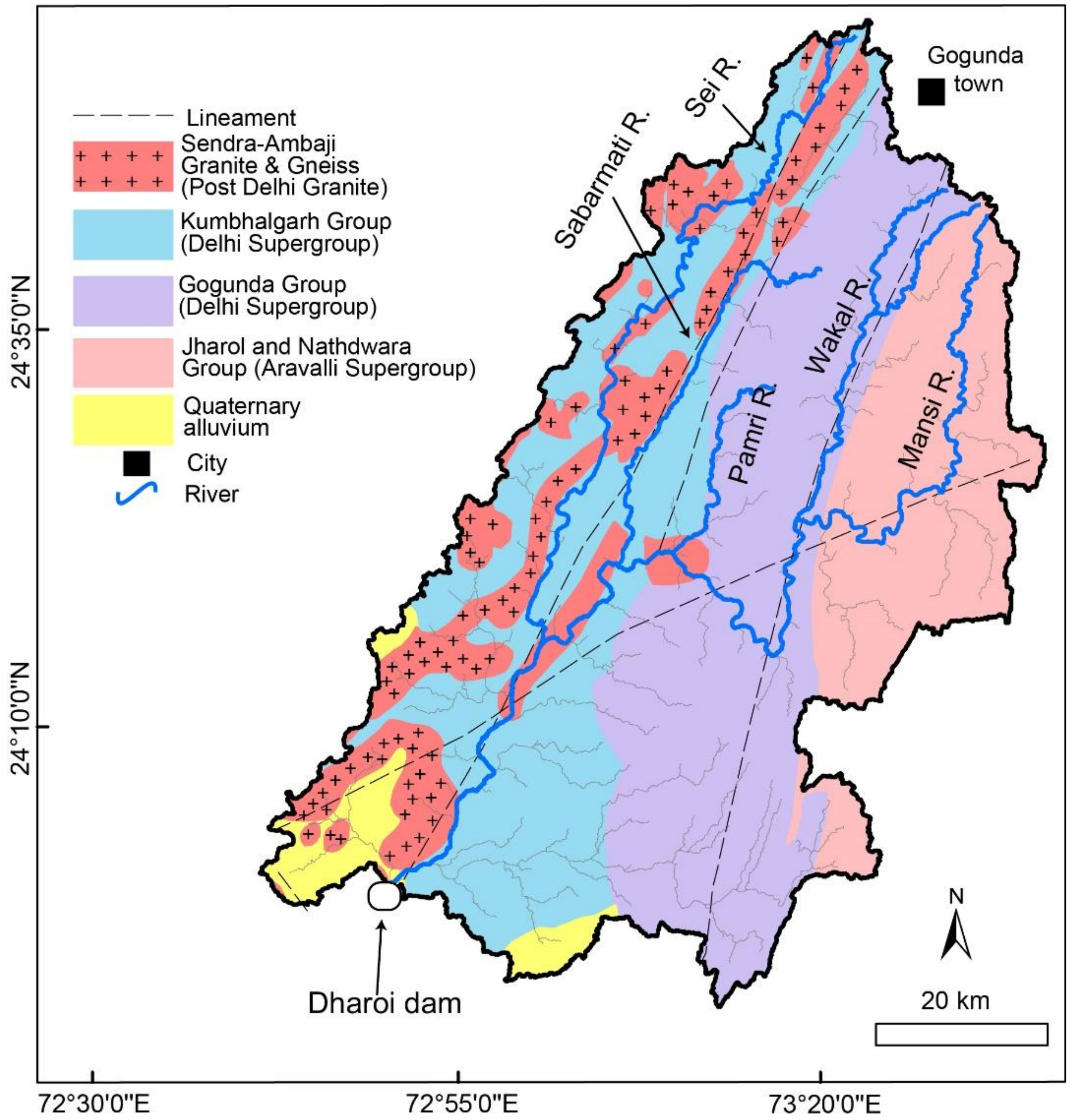

Fig. 5. 2: Geological map of the upper Sabarmati River basin showing major lithological units, tributaries, and lineaments.

Table 5. 1: General geological rock types in the upper Sabarmati River basin (source: GSI 2011).

Age	**Supergroup/Group**	**Group/ intrusive**	**General rock types**
Quaternary to Recent		Alluvium and Colluvium	Undifferentiated alluvial and fluvial sediments- Unconsolidated sand, silt, clay, pebble and gravel beds
Paleoproterozoic to Mesoproterozoic		Sendra-Ambaji Granite & Gneiss	Granitoids rich in quartz, plagioclase, K-feldspars, with variable proportions of Biotite and hornblende
	Delhi Supergroup rocks (1100-550 Ma)	Kumbhalgarh Group	Calcareous and argillaceous metasedimentary rocks
		Gogunda/Alwar Group	Arenaceous sequence of quartzite and interbedded schist and metabasic rocks
Paleoproterozoic	Aravalli Supergroup rocks (3500-1800 Ma)	Jharol/Nathdwara Group	Phyllite, chlorite schist, garnetiferous mica schist, quartzite, grit and conglomerate, bands of mafic-ultramafic. A suite of rocks, sometimes intercalated with quartzite bands
* Sendra-Ambaji granite is an intrusive rock.			

Table 5. 2: Sabarmati River sample details.

Sample Name	**Latitude (in degree)**	**Longitude (in degree)**	**Sample Type**	**Distance (km)**	**Elevation (m)**
'SR-1A'	24.7233833	73.5080000	W. rock	0	838
'SR-1B'	24.7233833	73.5080000	Rock	0	838
'SR-20C1'	24.7687667	73.4221000	Rock	0	863
'SR-20C2'	24.7687667	73.4221000	Rock	0	863
'SR-5A'	24.63716667	73.40886667	Rock	21	643
'SR-5B'	24.6371667	73.4088667	W. rock	21	643
'SR-6'	24.6307500	73.3951833	Rock	22	600
'SR-21B'	24.6799833	73.2374333	Rock	0	518
'SR-19'	24.4500810	73.5836280	Rock	0	844

Table 5. 2(continued): Sabarmati River sample details.

Sample Name	Latitude (in degree)	Longitude (in degree)	Sample Type	Distance (km)	Elevation (m)
'SR-16B1'	24.3700167	73.4026167	Rock	64	506
'SR-16B2'	24.3700167	73.4026167	Rock	64	506
'SR-15'	24.3659333	73.3801833	Rock	66	556
'SR-13'	24.3108820	73.3349950	Rock	16	554
'SR-20A'	24.7687667	73.4221000	Sediment	0	863
'SR-20B'	24.7683500	73.4212833	Sediment	0	861
'SR-21A'	24.6799833	73.2374333	Sediment	0	518
'SR-3'	24.7123500	73.4929833	Sediment	2	785
'SR-4A'	24.6837833	73.4558333	Sediment	11	721
'SR-6A'	24.6307500	73.3951833	Sediment	22	600
'SR-7A'	24.5248167	73.3601333	Sediment	38	532
'SR-8A'	24.4255000	73.3352167	Sediment	52	472
'SR-9A'	24.3892000	73.3231000	Sediment	78	449
'SR-12'	24.3353333	73.3001500	Sediment	88	421
'SR-11A'	24.2550833	73.2966833	Sediment	99	388
'SR-10A'	24.3309500	73.2054500	Sediment	117	323
'SR-18A'	24.3985667	73.5117333	Sediment	12	586
'SR-17A'	24.4191000	73.4734500	Sediment	18	543
'SR-16A'	24.3700167	73.4026167	Sediment	64	506
'SR-14A'	24.3324000	73.3496333	Sediment	20	494
'SR-23'	24.4866666	73.2216666	Sediment	16	446
'SR-24'	24.4257667	73.2132833	Sediment	24	391
'SR-25'	24.3766667	73.2034333	Sediment	32	344
'SN-4A'	24.3430333	73.1268000	Sediment	127	290
'SR-22A'	24.6012000	73.2206833	Sediment	23	434
'SN-3A'	24.2955000	73.0827667	Sediment	139	258
'SN-2A'	24.2380500	73.0157333	Sediment	151	231
'SN-1A'	24.1948667	72.9901333	Sediment	157	223
'SR-29'	24.4714000	73.1417000	Sediment	40	353
'SR-30'	24.7753000	73.3961000	Sediment	0	830
'SR-31'	24.8069000	73.3506000	Sediment	7	663
'SR-32'	24.7342000	73.2669000	Sediment	22	562
'SR-33'	24.7019000	73.1836000	Sediment	34	503
'SR-34'	24.5297000	73.0989000	Sediment	65	368
'SR-35'	24.3969000	73.0389000	Sediment	83	308
'SR-36'	24.2897000	73.0069000	Sediment	96	270

Table 5. 3: Dominant lithology of the area for each collected sample.

Collected rock / W. rock sample	Collected sediment sample	Dominant rock types of the area
SR-1A (Weathered Quartzite), -1B (Gneiss), -20C1 (Granite), 20C2 (Quartzite)	SR-3, -4A, -20A, -20B	Quartzite, Biotite schist
SR-5A (Phyllite soil), -5B (Weathered Phyllite), -6 (Quartzite)	SR-6A	Calc gneiss, Calc schist
	SR-7A, -8A, -9A, -11A, -12	Phyllite, Quartzite
	SR-10A, -30, -34	Biotite Schist, calc schist
SR-13 (Phyllite)	SR-14A	Biotite Schist, Quartzite
SR-15 (Granite), -16B1 (Quartzite), -16B2(Mica schist)	SR-16A	Quartzite, Mica schist
SR-19 (Quartzite)	SR-17A, -18A	Phyllite, Schist, Mica schist
SR-21B (Phyllite)	SR-21A, -22A, -29, -31, -32, -33, -35, -36, SN-1A, -2A, -3A, -4A	Calc Gneiss, Granite
	SR-23, -24, -25	Marble, Granite

5.2.2 Sample processing and measurements

The sediment and rock samples were processed following the methodology outlined in Chapter 2, section 0, and analysed using the Riso TL/OSL instrument, as detailed in section 2.3. Extracted quartz grains were tested for feldspar contamination using infrared-stimulated luminescence (IRSL; Hütt et al., 1988; Smith et al., 1990). A monolayer of extracted quartz grains, 5 mm in diameter, was mounted on stainless steel discs with Silkospray™ for TLS/BSLS measurements.

Table 5. 4(a & b) lists the measurement protocols used to measure luminescence for single aliquot and single-grain quartz. The 110 °C TL and BSL sensitivities (TLS and BSLS) were measured using the protocol (a) in Table 5. 4. Quartz aliquots were first bleached using blue stimulation at 125 °C for 80 s to remove natural luminescence, followed by irradiation with a 6 Gy test dose. TL was then recorded up to 220 °C. As the conventional 110 °C glow peak appeared at ~90 °C for these samples, photon counts between 60 °C and 110 °C were integrated to calculate TL intensity. BSL was subsequently measured at 125 °C for 40 s. BSL intensity in the first 0.16 seconds was not used to avoid any ultrafast signal (Jain et al., 2003). Photon counts in the interval 0.16 - 0.8 seconds and the final 8 seconds were used as signal and background, respectively. Comparison of photon counts with and without the first channel

suggested that the medium and slow components of quartz do not affect any of inferences (Fig. 5. 3). TL and BSL intensity after weight and beta dose normalisation provided TLS or BSLS. Typically, 6-10 aliquots were measured, and their average LS with the corresponding standard error was used. As each aliquot comprises 1000-1500 grains, the average LS for each sample was based on an average luminescence yield of ~10,000 grains. For simplicity of discussion, 100 photon counts/ mg/ Gy is designated as 1 Unit.

For single-grain measurements (protocol (b) in Table 5. 4), the discs were first preheated, and the natural GSL was recorded. This was followed by a 24 Gy beta dose and a second preheat step, after which the GSL was recorded at 125 °C (step 5). The GSL signal was integrated over the interval 0-0.16 s, and the average count from the final 0.76 s of the stimulation was taken as the background. Following each GSL measurement, the grains were re-irradiated, and their IRSL was used to identify occasional feldspar or feldspar-bearing grains. Data from such grains were not used in the analysis. Grains with GSL < 20 counts were classified as non-luminescent, while those with GSL > 1000 counts were designated as super-bright grains. Typically, 800–1000 grains were measured per sample, and their GSL were used for comparison, with the realisation that variations in grain size affect both mass and absorbed dose and would introduce intrinsic scatter. However, since lower mass implies smaller grain size and proportionally lower absorbed dose, it was considered that the net effects of variability in grain size would not be substantive. Though caution is warranted at present, it was reasonably assumed that the measurement of a large number of grains would provide a reasonably representative account of sample behaviour. The single-grain data were used primarily to understand general trends in luminescence response.

Laboratory experiments were conducted using the protocol outlined in Table 5. 5 to simulate natural sensitisation of TLS during sediment transport. Part (a) describes the sensitisation cycles applied to quartz aliquots, involving blue LED bleaching, beta irradiation, TL measurement at 161 °C to remove the photo-transferred thermoluminescence (PTTL), followed by a 3 Gy beta dose and TLS measurement at 110 °C. This cycle was repeated ten times to assess sensitisation trends. Part (b) outlines the corresponding protocol for single-grain quartz measurements. It includes preheating, initial measurement of the natural signal (SG-GSL), artificial irradiation, and subsequent sensitivity measurement. This cycle was repeated 25 times to evaluate the sensitisation behaviour of individual grains.

The following experiments were carried out:

- TLS and BSLS measurements of quartz from rocks, sediments, and dune sands (Table 5. 4a);
- TLS measurement and estimation of notional age weathered horizons on a phyllite rock surface (Table 5. 4a);
- TLS measurement under cycles of dose-bleach sensitisation (Table 5. 5);
- GSL measurements on single-grains from rocks and sediments (Table 5. 4b);
- SG-GSL measurement under cycles of dose-bleach sensitisation (Table 5. 5b).

Table 5. 4(a): 110°C TLS and BSLS measurement protocol. (b): Single-grain GSLS measurement.

(a)

Steps	**Treatment**	**Remarks**
1	BSL at 125 ºC, 80 sec	Bleaching the natural signal
2	Beta dose (~6 Gy)	Giving artificial irradiation
3	TL (2 ºC/sec from room temp to 220 ºC)	Measurement of 110 ºC TL intensity
4	BSL at 125 ºC, 40 sec	Measurement of BSL intensity

(b)

Steps	**Treatment**	**Remarks**
1	TL (2 ºC/sec from room temp to 200 ºC)	Preheating
2	SG-GSL at 125 ºC, 2 sec	Natural GSL of grain
3	Beta dose (~24 Gy)	Giving artificial irradiation
4	TL (2 ºC/sec from room temp to 200 ºC)	Preheating
5	SG-GSL at 125 ºC, 2 sec	**Measurement of GSLS**
6	SG-IRSL at 50 ºC, 1 sec	Feldspar identification

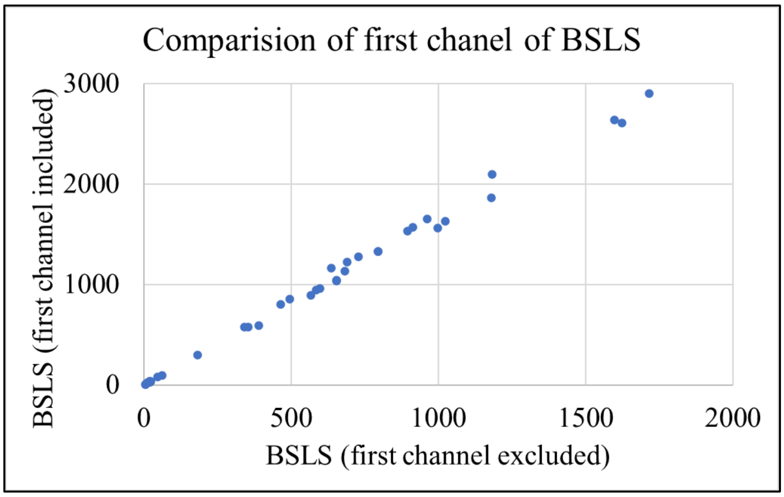

Fig. 5. 3: Comparison of photon counts of BSLS signal with and without the first channel of quartz samples.

Table 5. 5(a): Protocol for the cycle of bleaching and dose for quartz aliquot. (b): Protocol for the cycle of bleaching and dose for quartz single grain

(a)

Steps	**Treatment**	**Remarks**
1	BSL for 1 Hour (at RT, 125ºC)	Bleaching event
2	Beta (0, 5 and 40 Gy)	deposition event
3	BSL for 1 Hour (at RT, 125ºC)	Bleaching event
4	TL 161 ºC	Removing the PTTL signal
5	Beta 3 Gy	Irradiation dose
6	TL 201 ºC	**Measurement of 110 ºC TLS**
7	Go to step 1	

(b)

Steps	**Treatment**	**Remarks**
1	TL (2 ºC/sec from room temp to 200 ºC)	Preheating
2	SG-GSL at 125 125 ºC, 2 sec	Natural GSL of grain
3	Beta dose (~24 Gy)	Giving artificial irradiation
4	TL (2 ºC/sec from room temp to 200 ºC)	Preheating
5	SG-GSL at 125 ºC, 2 sec	**Measurement of GSLS**
6	Go to step 3	

5.2.3 Results

Inter-comparison of TLS and BSLS signals:

The TLS and BSLS of quartz from all the samples were compared, and these had a correlation coefficient (R2) of 0.77 (Fig. 5. 4), suggesting that broadly their results can be used interchangeably. The same premise was used for SG-GSLS. In subsequent analyses, TLS was used, primarily due to its higher photon output. Standard error in TLS for aliquot measurements ranged from ± 4-13% for sediments and ± 5-30% for rocks and weathered rocks. For dose-normalised SG-GSLS measurements, only the photon counting errors (typically < 20%) were used. Fig. 5. 5 provides a schematic documentation of the variation of TLS of the quartz sample along the R. Sabarmati (Sabarmati River) course.

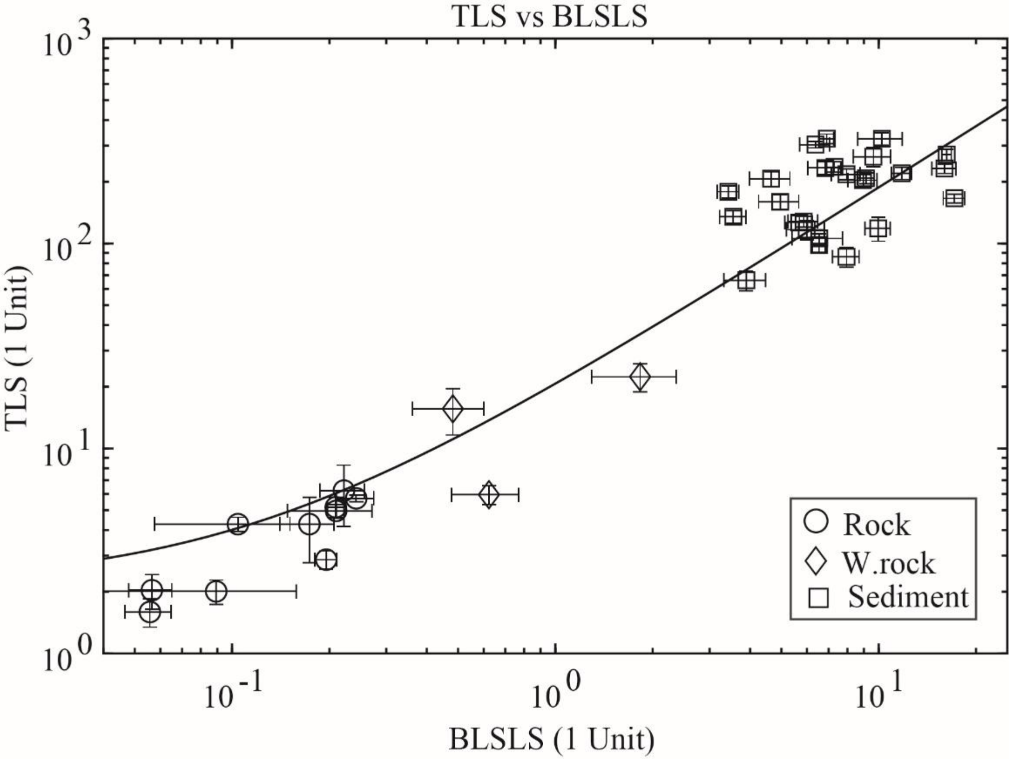

Fig. 5. 4: Correlation between 110 °C TLS and BSLS of samples collected from the Sabarmati River basin. These are correlated with a linear fit of R^2=0.77.

TLS of quartz from rocks and weathered rocks:

TLS of quartz from Quartzites, phyllites and their weathered components is tabulated in Table 5. 6. Generally, the TLS of quartz from weathered rocks was higher compared to that of the parent rocks. In the case of soil horizons, the TLS of the weathered zone (SR-5A) and underlying semi-weathered consolidated phyllite rock (SR-5B) was 22.4 and 5.9 Units at a depth of ~35 cm (Fig. 5. 5; Fig. 5. 8(a, b)), respectively. Double SAR palaeodoses of SR-5A and -5B (Jain and Singhvi, 2001; Murray and Wintle, 2000) were 48±4 Gy and 81±15 Gy (Table 5. 7), respectively, suggestive of their notional ages of 16±1 and 27±5 ka (assuming a dose rate of 3Gy/ka based on the average radioactivity of the Sabarmati basin values reported by Juyal et al. (2003)). This age offset for rock surfaced under weathering could either be due to pedoturbation (Bateman et al. 2003; Wilkinson & Humphreys, 2005) or through traces of wind-transported higher TLS grains.

Table 5. 6: TLS of rock samples (Sabarmati River).

Sample name	Rock	TLS (Units)
SR-19	Quartzite	2.0 ± 0.3
SR-16B1	Quartzite	6.2 ± 2.1
SR-20C2	Quartzite	5.0 ± 0.4
SR-6	Quartzite cobbles	2.0 ± 0.4
SR-1A	Weathered Quartzite	15.6 ± 4.0
SR-21B	Phyllite	5.7 ± 0.2
SR-13	Phyllite	1.6 ± 0.3
SR-5B	Less weathered Phyllite	5.9 ± 0.6
SR-5A	Highly weathered Phyllite	22.4 ± 3.5
SR-15	Granite	4.3 ± 0.3
SR-20C1	Granite	4.3 ± 1.5
SR-1B	Gneiss	2.9 ± 0.3
SR-16B2	Mica-schist	5.2 ± 0.6

Table 5. 7: Summary of equivalent dose (De) data of samples SR-5A and SR-5B.

Sample name	No of aliquot	De (Gy) Central age	Optical age (Ka)	OD (%)	% of saturated aliquot
SR-5A	24	48 ± 4	16 ± 1	32 ± 2	23
SR-5B	24	81 ± 15	27 ± 5	46 ± 5	71

TLS of quartz from sediments:

Continuity of sediment transport in the Sabarmati River is modulated by multiple tributary inputs, rugged hilly terrain, and local-scale anthropogenic activities. Therefore, to simplify an understanding of the variation of TLS along the river trajectory, the basin was subdivided into seven groups. This sub-division was based on major tributary confluences and physiographic features (Fig. 5. 1; Table 5. 8). Group-wise TLS data, along with downstream distance, elevation, and confluence details, is summarised in Table 5. 9. These results are discussed below.

Table 5. 8: Samples names and geological area of each group details.

Groups	**Sample names**	**Geological area**
Group 1	SR-1A (Weathered Quartzite), SR-1B (Gneiss), SR-3, SR-4.	Uppermost region of the Wakal River. These three samples are situated in the upper catchment and are best suited to examine downstream variations in LS and part of the same tributary.
Group 2	SR-20E, A, B, SR20C1 (Granite), SR20C2 (Quartzite), SR-6A, SR-6 (Quartzite), SR-5A (Phyllite soil), -5B (Weathered Phyllite),	A small tributary, 'T_X' of the Wakal River. SR-5A represents a weathered soil of a parent consolidated metamorphic phyllite sample (SR-5B).
Group 3	SR-4, SR-6A, SR-7A and SR-8A.	It covers the confluence of the small tributary 'T_X' in the Wakal River.
Group 4	SR-18A, -17A, -16A, SR16B1 (Quartzite), SR16B2 (Mica schist), SR15 (Granite), SR-19 (Quartzite), SR-9A, SR-14A and SR-13 (Phyllite).	Sediment dynamics of Mansi River, a small tributary 'T_A' and its confluence with a small tributary ' T_B'.
Group 5	SR-8A, SR-9A, SR-12, SR-11A and SR-10A.	Confluence of the Mansi River and Wakal River.
Group 6	SR-23, SR-24, SR-25, SR-10A and SN4A.	It covers the sediments of the Pamri River and its confluence with the Wakal River.
Group 7	SR-30, -31, -32, -33, -34, and SR-35	It covers the sediments of the Sei River
Group 8	SR-21A, -21B (Phyllite), -22A, -29, SR-36, SN-4A, -3A, -2A and -1A.	Sediments of Sabarmati River and its confluence with the Wakal and Sei River.

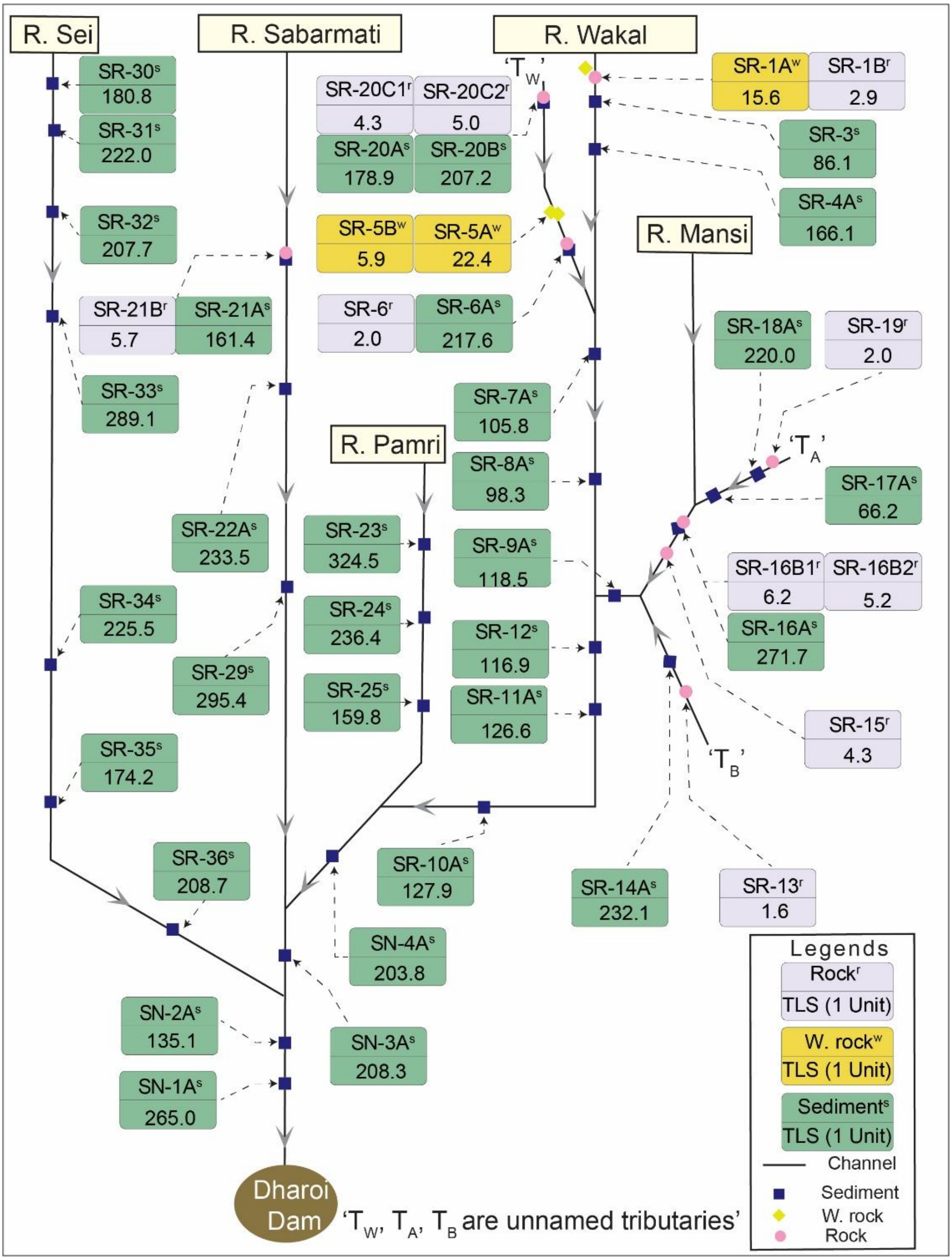

Fig. 5. 5: Schematic diagram of the Sabarmati River Basin. ^{r}, ^{w} *&* ^{s} *denote rock, weathered rock and sediment samples, respectively. 110 ºC TLS are presented in 1 Unit (100 photon counts /mg/Gy).*

Table 5. 9: TLS (Units) of the samples are presented with distance (km) from the source and elevation (m) in groups. The trunk river is highlighted in pink, confluences are marked in blue, and rocks and weathered rocks (W. rock) are denoted by '★', ‘ ’ respectively.

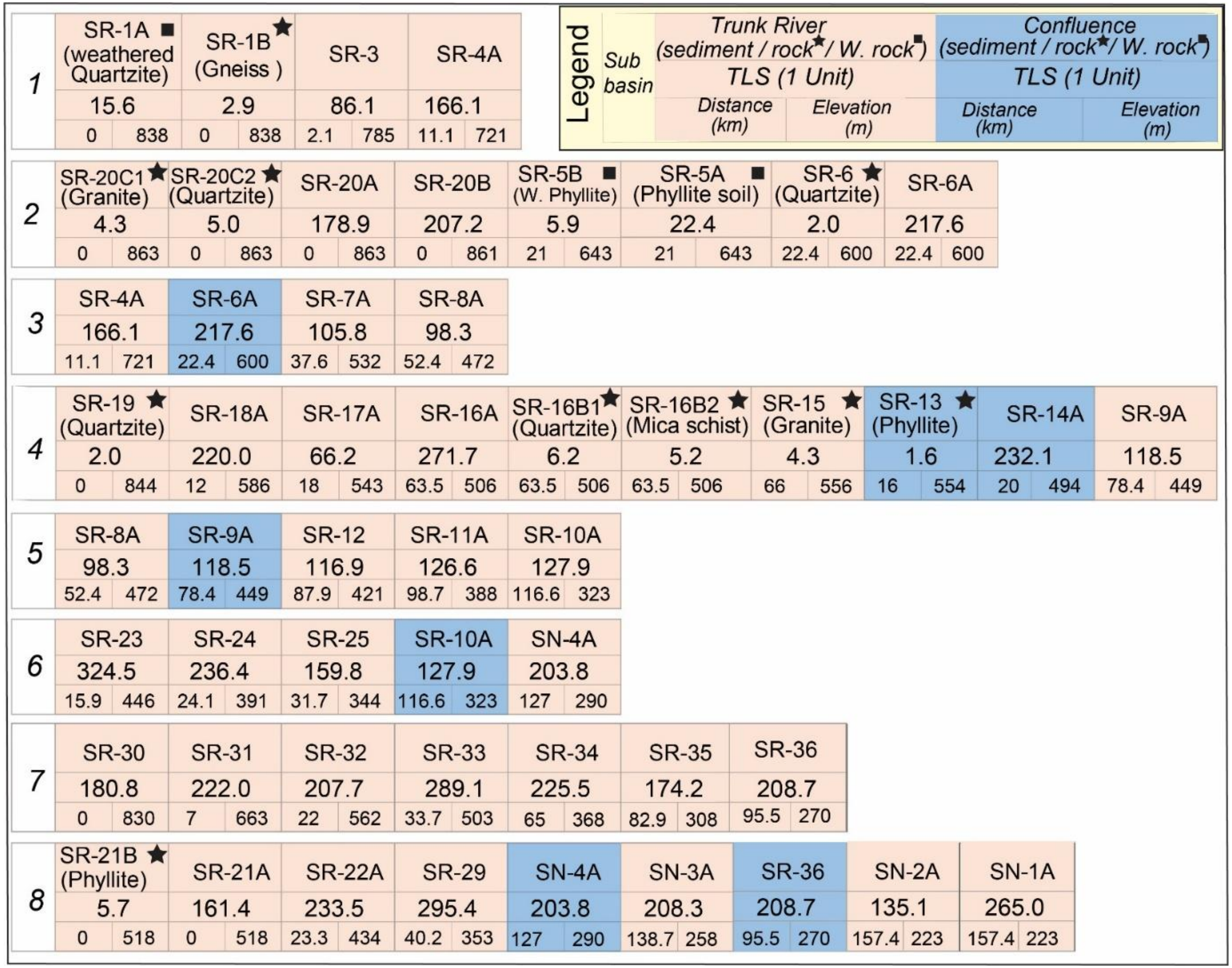

Legend

Sub basin	Trunk River (sediment / rock★/ W. rock■) TLS (1 Unit)		Confluence (sediment / rock★/ W. rock■) TLS (1 Unit)	
	Distance (km)	Elevation (m)	Distance (km)	Elevation (m)

Sub basin	Sample	TLS	Distance (km)	Elevation (m)
1	SR-1A ■ (weathered Quartzite)	15.6	0	838
	SR-1B ★ (Gneiss)	2.9	0	838
	SR-3	86.1	2.1	785
	SR-4A	166.1	11.1	721
2	SR-20C1 ★ (Granite)	4.3	0	863
	SR-20C2 ★ (Quartzite)	5.0	0	863
	SR-20A	178.9	0	863
	SR-20B	207.2	0	861
	SR-5B ■ (W. Phyllite)	5.9	21	643
	SR-5A ■ (Phyllite soil)	22.4	21	643
	SR-6 ★ (Quartzite)	2.0	22.4	600
	SR-6A	217.6	22.4	600
3	SR-4A	166.1	11.1	721
	SR-6A	217.6	22.4	600
	SR-7A	105.8	37.6	532
	SR-8A	98.3	52.4	472
4	SR-19 ★ (Quartzite)	2.0	0	844
	SR-18A	220.0	12	586
	SR-17A	66.2	18	543
	SR-16A	271.7	63.5	506
	SR-16B1 ★ (Quartzite)	6.2	63.5	506
	SR-16B2 ★ (Mica schist)	5.2	63.5	506
	SR-15 ★ (Granite)	4.3	66	556
	SR-13 ★ (Phyllite)	1.6	16	554
	SR-14A	232.1	20	494
	SR-9A	118.5	78.4	449
5	SR-8A	98.3	52.4	472
	SR-9A	118.5	78.4	449
	SR-12	116.9	87.9	421
	SR-11A	126.6	98.7	388
	SR-10A	127.9	116.6	323
6	SR-23	324.5	15.9	446
	SR-24	236.4	24.1	391
	SR-25	159.8	31.7	344
	SR-10A	127.9	116.6	323
	SN-4A	203.8	127	290
7	SR-30	180.8	0	830
	SR-31	222.0	7	663
	SR-32	207.7	22	562
	SR-33	289.1	33.7	503
	SR-34	225.5	65	368
	SR-35	174.2	82.9	308
	SR-36	208.7	95.5	270
8	SR-21B ★ (Phyllite)	5.7	0	518
	SR-21A	161.4	0	518
	SR-22A	233.5	23.3	434
	SR-29	295.4	40.2	353
	SN-4A	203.8	127	290
	SN-3A	208.3	138.7	258
	SR-36	208.7	95.5	270
	SN-2A	135.1	157.4	223
	SN-1A	265.0	157.4	223

Group-1: This group covers a 22 km stretch from the source of the Wakal River to its confluence with a tributary 'T$_W$' (Fig. 5. 1). TLS of weathered quartzite (SR-1A) and gneiss (SR-1B) were 15.5 Units and 2.9 Units, respectively. TLS of sediments SR-3 and SR-4A in the river channel at 2 and 11 km from SR-1A were 86.1 and 166.1 Units (Table 5. 9; Fig. 5. 6 a, b).

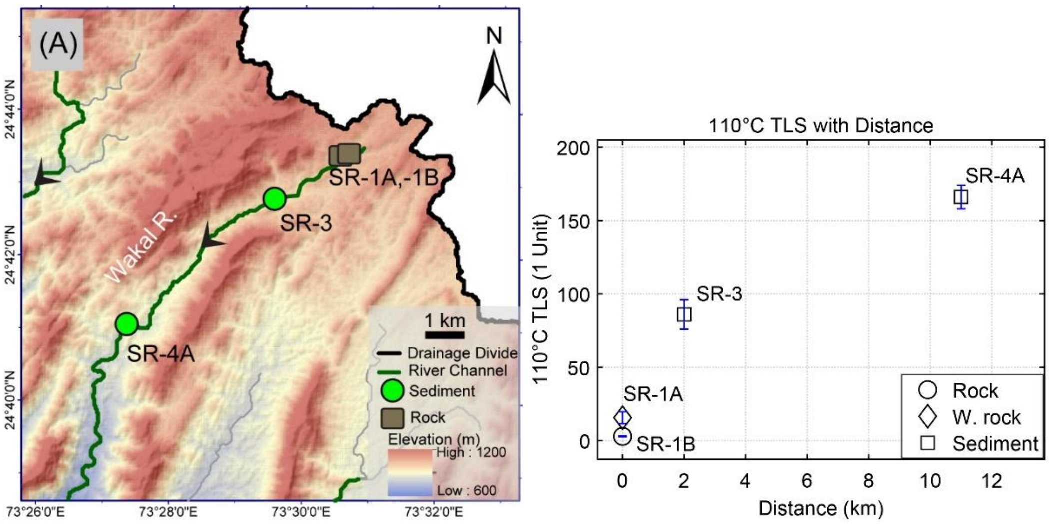

Fig. 5. 6: (a) Spatial map and (b) 110 ºC TLS of samples with distance for group 1.

Group-2: This group of samples is from 24 km section of tributary 'TW' of the Wakal River (Fig. 5. 1; Fig. 5. 7a). Three rock samples along this segment, viz.: SR-20C1 (granite), SR-20C2 (quartzite) and SR-6 (quartzite cobbles), had TLS of 4.3, 5.0 and 2.0 Units, respectively. Sediments SR-20A (from gully), SR-20B (from active channel), and SR-6A (~23 km downstream) gave TLS of 178.9, 207.2, and 217.6 Units, respectively (Table 5. 9; Fig. 5. 7a, b).

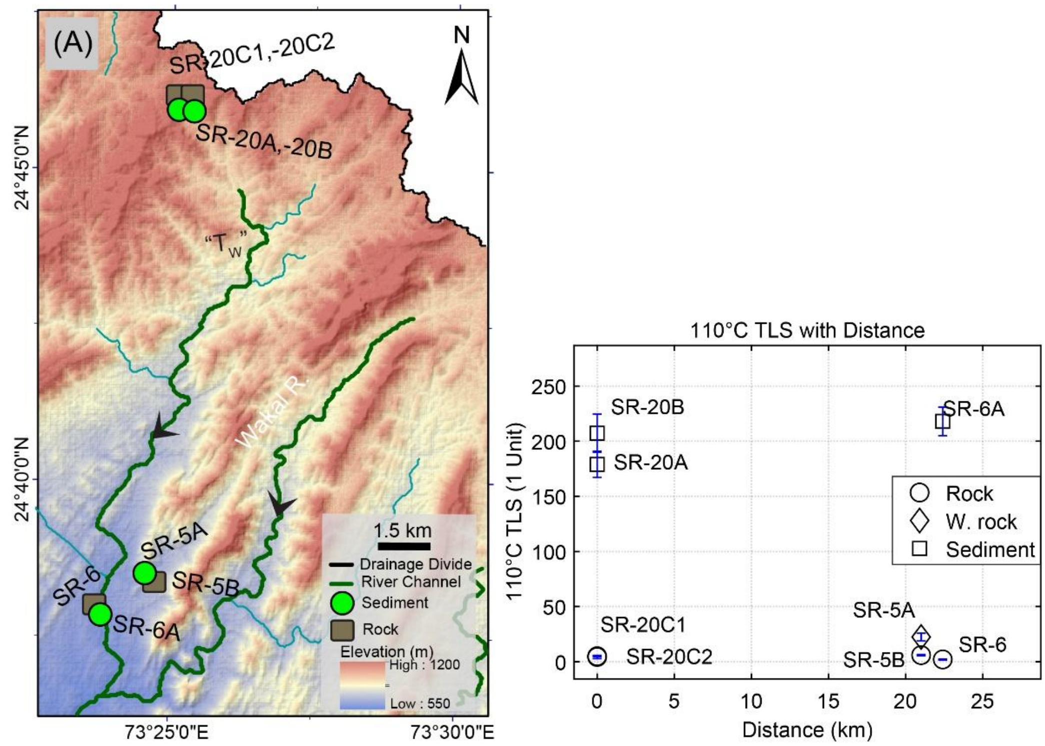

Fig. 5. 7: (a) Spatial map and (b) 110 ºC TLS of samples with distance for group 2.

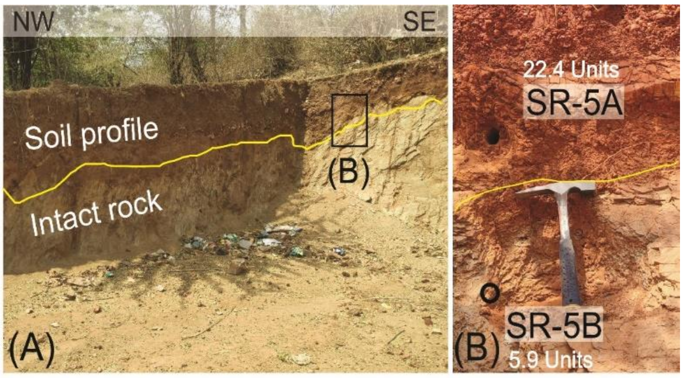

Fig. 5. 8: Field pictures show a weathered zone soil profile SR-5A (soil) with intact semi-weathered consolidated rock SR-5B (Phyllite) along the Sabarmati River bank with 110 °C TLS of 22.4 and 5.9 Units, respectively.

Group-3: This group comprises the confluence of the tributary 'T_W' (SR-6A) with Wakal River (SR-4A and 7A, pre- and post-confluence samples), and their corresponding TLS were 217.6, 166.1 and 105.8 Units. TLS of sediment samples SR-8A (15 km downstream of SR-7A) was 98.3 Units (Table 5. 9; Fig. 5. 1; Fig. 5. 9(a, b)).

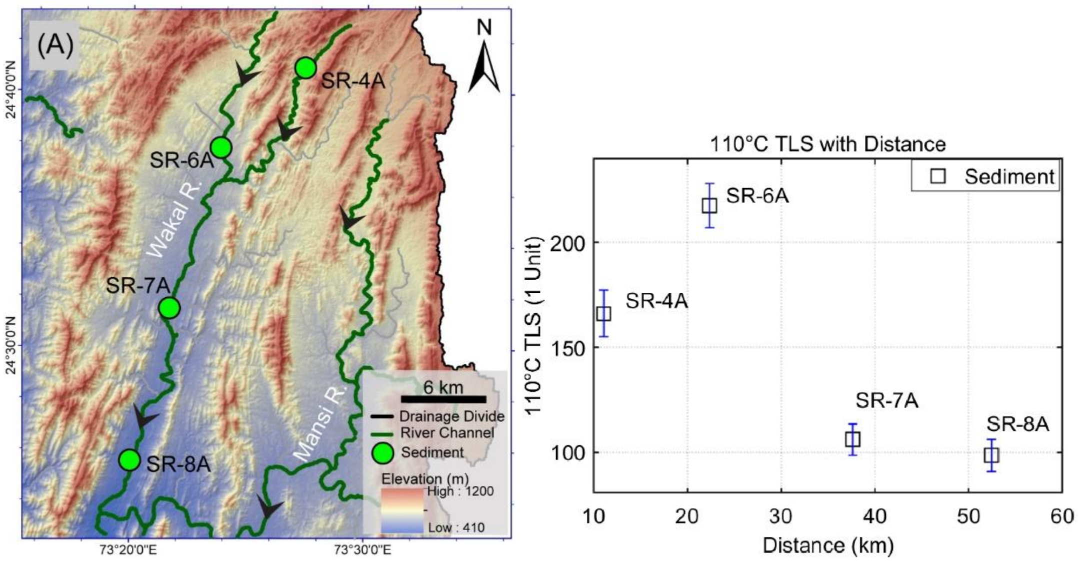

Fig. 5. 9: (a) Spatial map and (b) 110 ºC TLS of samples with distance for group 3.

Group-4: In this region, R. Mansi traverses through hilly terrain with local check dams and two tributaries, T_A and T_B (Fig. 5. 1; Fig. 5. 10a, b). The rock samples SR-19 (quartzite), -15 (granite), -16B1 (quartzite), -16B2 (mica schist), and -13 (phyllite) had TLS of 2.0, 4.3, 6.2, 5.2 and 1.6 Units, respectively. Along the tributary TA, sediment samples SR-18A and -17A, 10 km downstream, yielded a TLS of 220.0 and 66.2 Units. Sediment from tributary TB (SR-14A) and that of Mansi River bed (SR-16A and SR-9A, pre- and post-confluence) had a TLS of 232.1, 271.7 and 118.5 Units, respectively (Table 5. 9; Fig. 5. 10 a, b).

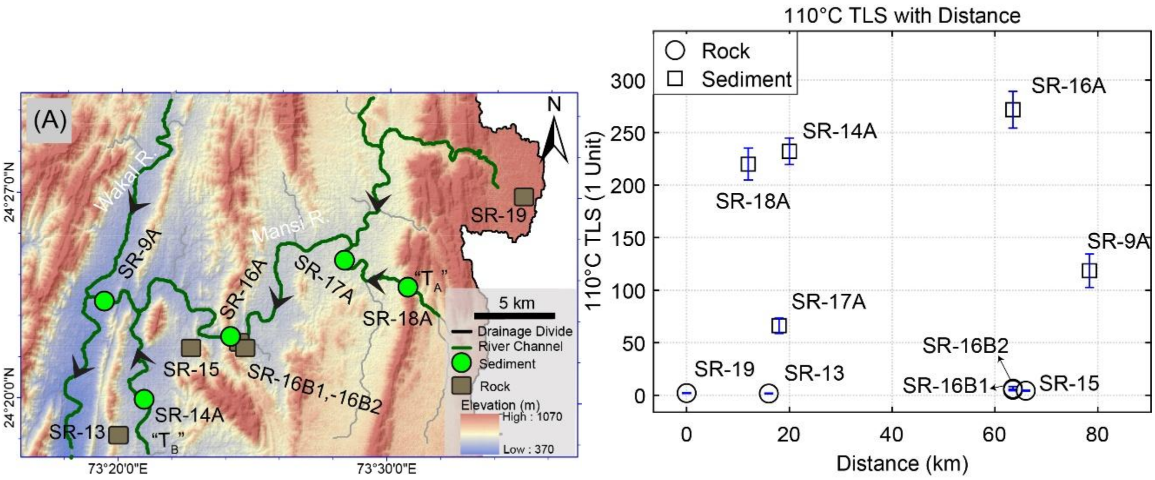

Fig. 5. 10: (a) Spatial map and (b) 110 ºC TLS of samples with distance for group 4.

Group-5: This group has the confluence of R. Mansi and R. Wakal (Fig. 5. 1; Fig. 5. 11 a). Sediment SR-8A from the Wakal River bed had a TLS of 98.3 Units, and that from the Mansi River (SR-9A) had a TLS of 118.5 Units. Sediments SR-12, SR-11, and SR-10, at post-confluence distances of 8 km, 17 km, and 35 km, had TLS of 116.9, 126.6 and 127.9 Units, respectively (Table 5. 9; Fig. 5. 11 a, b).

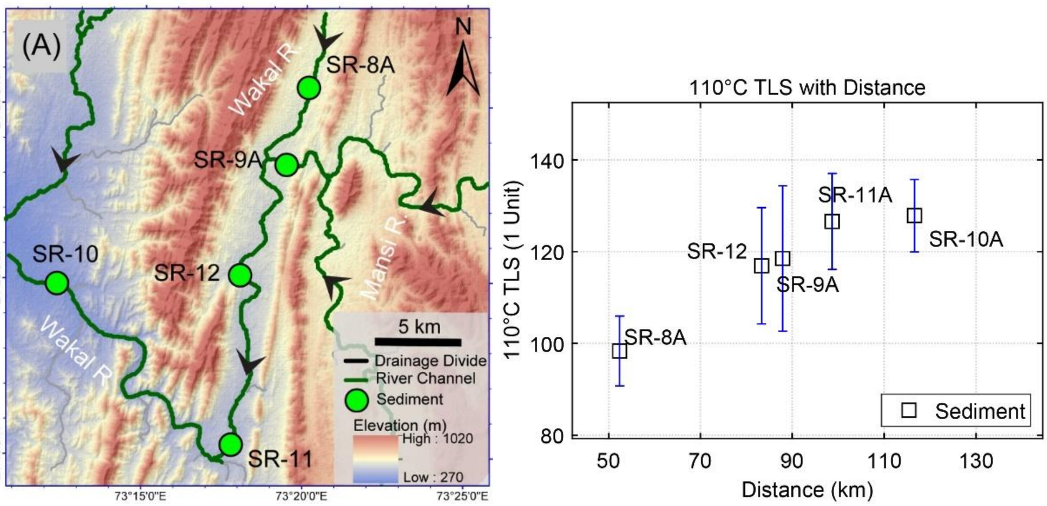

Fig. 5. 11: (a) Spatial map and (b) 110 ºC TLS of samples with distance for group 5.

Group-6: This group (Fig. 5. 1; Fig. 5. 12 a) comprises sediments from hilly terrain where the R. Pamri meets R. Wakal. Sediments SR-23, SR-24, and SR-25 at 15 km, 25 km, and 30 km downstream in the Pamri River had a TLS of 324.5, 236.4, and 159.8 Units, respectively (Table 5. 9; Fig. 5. 12 b). Pre- and post-confluence samples SR-10A (pre) and SN-4A (post) in the Wakal River had a TLS of 127.9 Units and 203.8 Units.

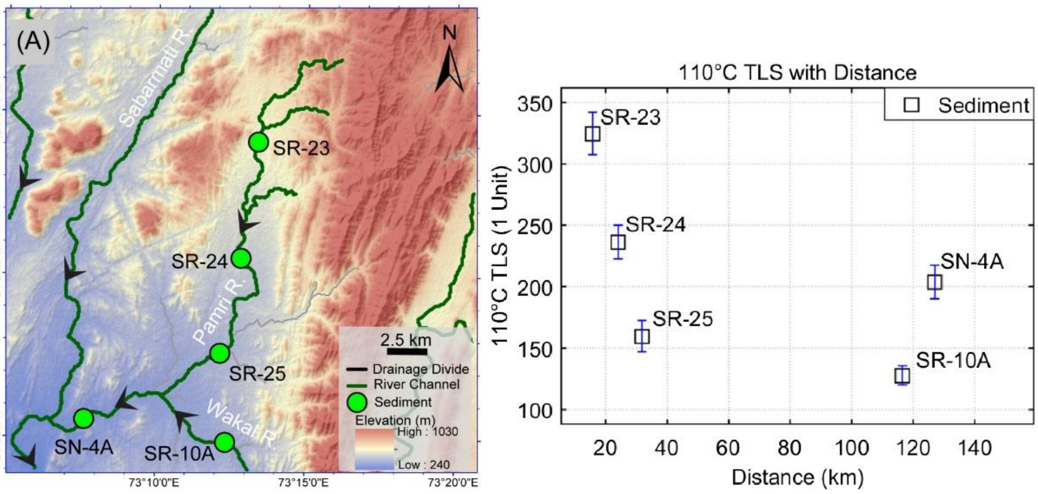

Fig. 5. 12: (a) Spatial map and (b) 110 ºC TLS of samples with distance for group 6.

Group-7: This group comprises sediments from the Sei River (Fig. 5. 1; Fig. 5. 13 a). Samples SR-30, -31, -32, -33, -34, -35, and SR-36, collected at distances of 0, 7, 22, 33.7, 65, and 82 km, exhibit TLS of 180.8, 222.0, 207.7, 289.1, 225.5, 174.2, and 208.7 units, respectively (Table 5. 9; Fig. 5. 13 b).

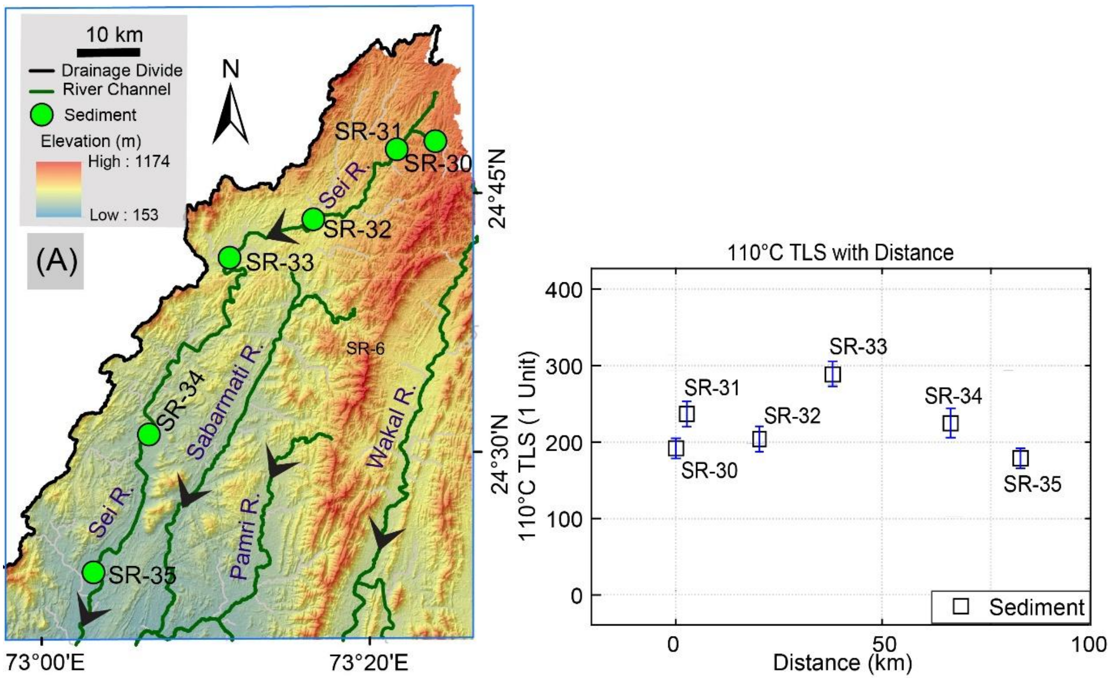

Fig. 5. 13: (a) Spatial map and (b) 110 ºC TLS of samples with distance for group 7.

Group-8: Here, R. Wakal and R. Sei merge with R. Sabarmati (Fig. 5. 1; Fig. 5. 14 a). A phyllite rock (SR-21B) had a TLS of 5.7 Units. Six sediment samples (SR-21A, -22A, -29A, SN-4A, SR-36, SN-3A, -2A and 1A) showed TLS of 161.4, 233.5, 295.4, 203.8, 208.3, 208.7, 135.1 and 265 Units, respectively (Table 5. 9; Fig. 5. 14 b).

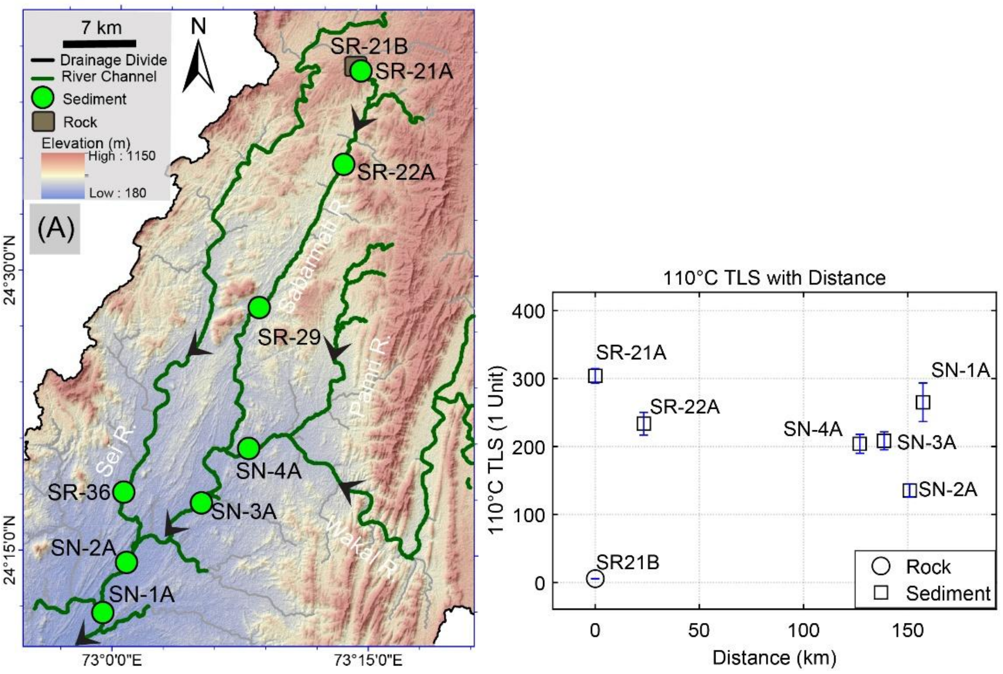

Fig. 5. 14: (a) Spatial map and (b) 110 ºC TLS of samples with distance for group 8.

A synoptic summary of results is as follows,

a. TLS of rock samples, viz., granites, phyllites, schists, and quartzites, range between 1.6 and 6.2 Units. TLS values of ≤10 Units are hereafter referred to as "low TLS".
b. TLS of a semi-weathered rock and overlying weathered horizon were 5.9 and 22.4 Units, respectively.
c. Sediment TLS ranged between 66 and 325 Units. The average sediment TLS is about 45 times of average rock TLS.

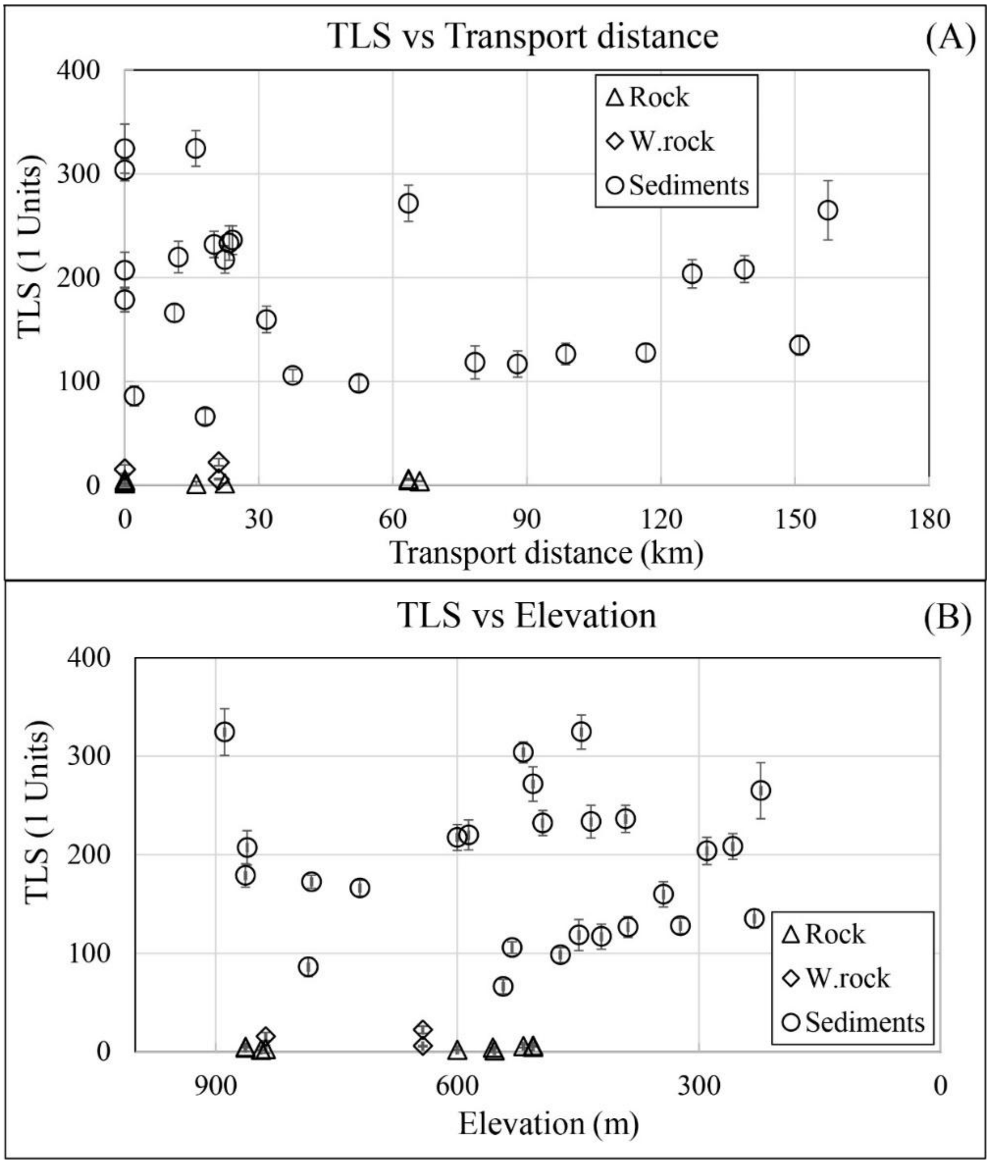

Fig. 5. 15: Variation of 110 °C TLS for all collected sediments and rocks with transport distance (a) and elevation (b). Note the absence of a systematic trend with either transport distance or elevation, indicating that other factors contribute to 110 °C TLS.

Plots of TLS versus transport distance (Fig. 5. 15A) and elevation (Fig. 5. 15B), intended to assess the influence of hillslope processes, did not exhibit a clear trend, and the presence of high-TLS grains near the river's source suggests contributions from additional sources besides locally derived sediments. Paleodunes are widespread in the basin and are extensively gullied. Given the semi-arid to arid climate and high wind drift potential, it is plausible that sands from these dunes get transported upstream by winds. Accordingly, TLS of quartz from dune sediments and coastal sands near the river's terminus were analysed.

TLS of dunes and aeolianites:

Paleodunes in the region reach heights up to 50 m and comprise reworked alluvium. Like the adjacent river terraces, these dunes are extensively gullied and contribute sediment to the river system (Allchin et al., 1978; Juyal et al., 2003; Merh & Chamyal, 1997; Singhvi & Kar, 2004; Tandon et al., 1997). Anthropogenic activities also accentuate gullying processes (Sonam et al., 2021). TLS of dune sands in the vicinity of the river was measured using the protocol in Table 5. 4 a, and the TLS values ranged between 54.9 and 404.1 Units (Table 5. 10).

Table 5. 10: 110 °C TLS of aeolian deposits (sample ref: Juyal et al., 2003)

Sample code	**Location**	**Latitude**	**Longitude**	**110 °C TLS (Units)**
TR-249	Dharoi I	24°00.68' N	72°48.07' E	244 ± 11
TR-252	Dharoi I	24°00.68' N	72°48.07' E	116 ± 9
TR-255	Dharoi I	24°00.68' N	72°48.07' E	90 ± 3
TR-256	Dharoi I	24°00.68' N	72°48.07' E	55 ± 3
TR-258	Dharoi II	24°00.68' N	72°48.07' E	94 ± 3
TR-257	Dharoi II	24°00.68' N	72°48.07' E	80 ± 4
TR-243	Akhaj	23°26.62' N	72°28.38' E	151 ± 4
TR-244	Akhaj	23°26.62' N	72°28.38' E	278 ± 15
TR-233	Tajpura I	22°26.89' N	72°28.33' E	261 ± 9
TR-232	Tajpura I	22°26.89' N	72°28.33' E	404 ± 23
TR-260b	Tajpura II	22°26.89' N	72°28.33' E	224 ± 3
TR-242	Dabka	22°15.00' N	72°57.29' E	196 ± 12

The other possible source of sediment is the shelf of the Gulf of Khambhat. During periods of low sea level, an additional 200–300 km of shelf area was exposed (Juyal et al., 2006; Saha et al., 2016), making it available for denudation by winds (Table 5. 10). As the wind direction is favourable and competent, it is likely that some of these grains were transported several hundred km inland and, in this process, would have experienced sufficient burial and bleaching cycles to sensitise the quartz. Thermoluminescence sensitivity (TLS) measurements from two aeolianite deposits, dated to 43 ka and 4 ka (K. Sharma et al., 2017), yielded values of 168.8 and 338.8 Units, respectively.

Single-grains GSL analysis:

Green light stimulated luminescence from single-grains of a granite (SR-20C1), a river sediment (SR-21A), and a palaeodune sample (TR-232) was measured and compared, based on the premise that GSL of individual grains can be meaningfully compared on a per grain per unit dose basis. Approximately 800–1200 grains were measured for each sample using protocol in Table 5. 4 b. The results are summarised in Fig. 5. 16, and the following observations can be made:

a. Each rock type has occasional (< 0.5 %) super-bright grains that account for > 80 % of the total light sum for an aliquot.
b. Up to ~97% of grains from the rocks and 60-80% in river sediments did not yield luminescence, nor did they respond to the sensitisation cycle.
c. Dune sands had a higher proportion of brighter grains, and the GSL of fluvial sediments was between those of palaeodune sands and source rocks.

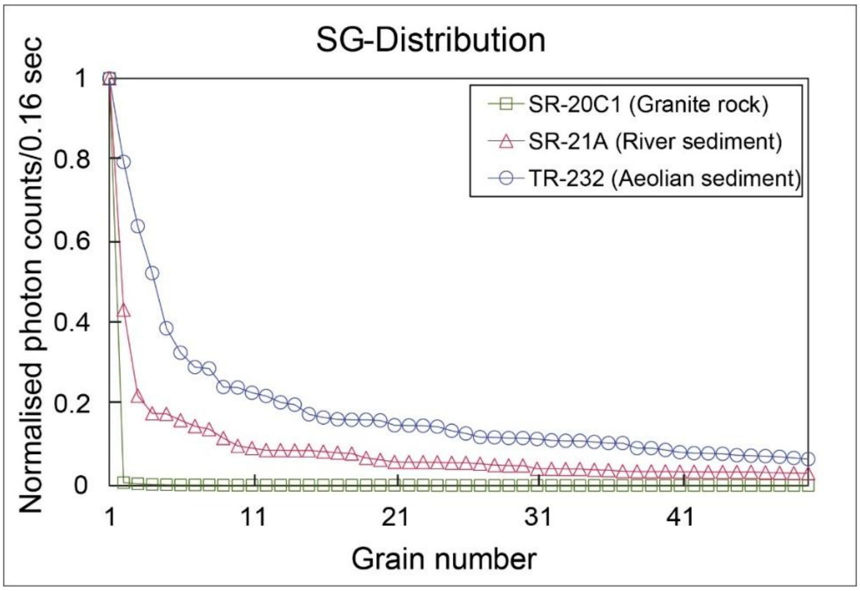

Fig. 5. 16: Green light stimulated luminescence signals (top 50 single grains out of 1000 measured) from (A) granite rock (SR-20C1), (B) fluvial sediment (SR-21A) from the Sabarmati basin, and (C) aeolian sand (TR-232) from Tajpura, arranged in decreasing order.

Laboratory sensitisation experiments:

To investigate the differences in TLS between rocks and sediments, laboratory experiments to simulate sediment transport (via daylight exposure) and burial (via irradiation) cycles were conducted on quartz from a quartzite SR-19. The protocol for this is outlined in Table 5. 5 a. We examined three scenarios: continuous transport, temporary residence at point bars followed by reworking, and repeated burial and reworking.

a. cycles of transport without any intervening storage (cycles of daylight-induced bleaching without irradiation, i.e. no beta dose),
b. cycles of transport with short-duration (~1-1.5 ka) burial en route (that led to quartz accruing a beta dose of 5 Gy at an assumed dose rate of ~3Gy/ka) and,
c. cycles of transport with longer burial en route (10-15 ka, i.e. a beta dose of ~40 Gy at an assumed dose rate of 3 Gy/ka).

Across all these scenarios, TLS exhibited an increase of up to 1.3 to 2 times after twenty cycles of irradiation and simulated daylight bleaching. The rate of increase in TLS diminished with increasing cycles (Fig. 5. 17).

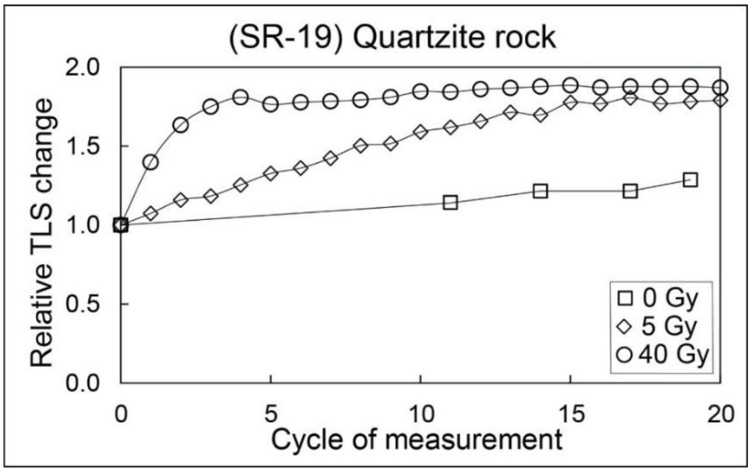

Fig. 5. 17: Relative 110 °C TLS change in rock sample SR-19 (Quartzite) due to cycles of irradiation and bleaching in the laboratory for three scenarios with irradiation doses 0, 5 and 40Gy. Each cycle has 2 hours of bleaching (Table 5. 5a).

A similar set of irradiations (40 Gy) and blue LED bleach (2 hours) cycles was performed on quartz aliquots from SR-8A (river sediment), SR-1A (weathered quartzite rock), and SR-19 (quartzite rock) protocol in Table 5. 5a and the results are shown in Fig. 5. 18. Where, the quartz sediment (SR-8A), weathered rock (SR-1A) and rock (SR-19) showed an increase in TLS by 1.8, 1.6 and 1.2 times, respectively. The TLS after a few cycles is consistent with the saturation pattern observed in Fig. 5. 18. It is important to note that these sensitisation data are based on single aliquots, and the differences between Fig. 5. 17 and Fig. 5. 18 likely reflect disc-to-disc variability. Ideally, multiple discs would have been measured to improve statistical reliability; however, only a limited number could be analysed due to practical constraints. The results should therefore be considered indicative of a general trend.

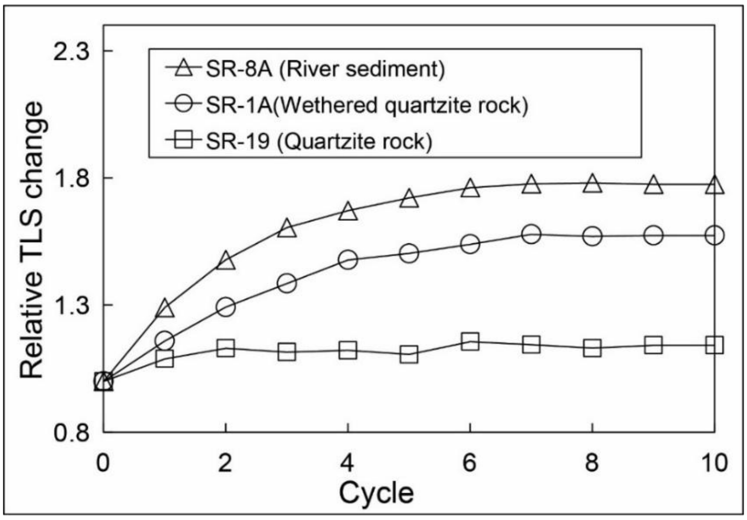

Fig. 5. 18: Relative 110 °C TLS change with sensitisation cycles for three samples: SR-8A (river sediment), SR-1A (weathered quartzite rock), and SR-19 (quartzite rock). Each cycle has 2 hours of bleaching (Protocol in Table 5. 5a).

In addition to the sensitisation of quartz aliquots, 1200 individual grains from a quartzite rock SR-19 were subjected to 25 sensitisation cycles involving irradiation (~24 Gy) and bleaching, following the protocol outlined in Table 5. 5b. The results are shown in Fig. 5. 19. The GSLS of each grain was normalised to its initial value and fitted to a linear trend (Fig. 5. 19, left), and the slope distribution is shown in Fig. 5. 19 (right). Approximately 97% of the grains did not exhibit any measurable luminescence. Among the luminescent grains, slope values ranged from -0.08 to 0.26, suggestive of no change and up to ~ 25% increase per cycle in the sensitivity of luminescent grains.

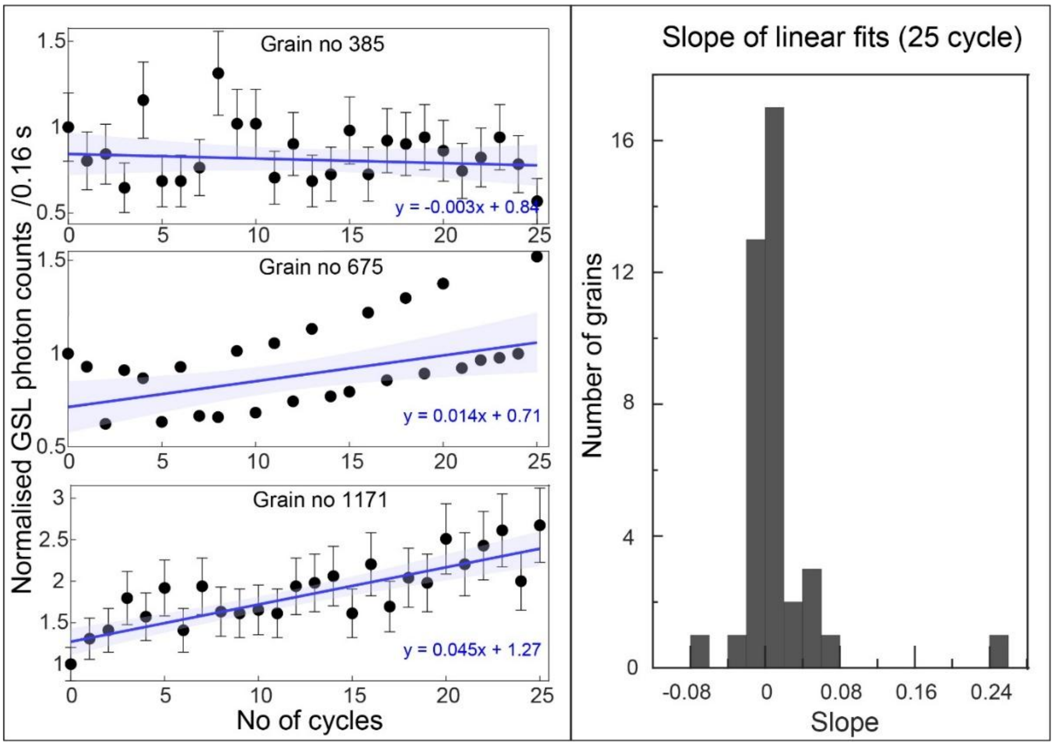

Fig. 5. 19: Variation in GSL photon counts with sensitisation cycles for three individual quartz grains from SR-19 (quartzite rock) (left) (Protocol in Table 5. 5b). Distribution of GSL enhancement of grains (right).

5.2.4 Discussion

Sediment transport in the Sabarmati River basin, with its numerous tributaries, hilly terrain and other geomorphic processes, is complex. The TLS of rocks ranged between 1.6 and 6.2 Units, weathered rock between 5.9 and 22.4 Units, sediments between 66.2 and 324.5 Units, palaeodune sands between 54.9 and 404.1 Units, and aeolianites between 168.8 and 338.8 Units (Fig. 5. 5; Table 5. 9; Table 5. 10). TLS values of sediments did not show a clear trend with transport distance or elevation; instead, TLS versus distance and elevation plots resembled a scatter plot (Fig. 5. 15). A significant scatter in TLS, near the origin of the river, suggested that additional sources beyond local bedrock contribute to sediment composition. This possibility was examined further. Generally, lower TLS observed along the river course is likely due to low TLS quartz derived from gully erosion and hillslope processes. Steep terrain, with sparse vegetation, facilitates rapid downslope transport that offers limited daylight exposure of rock-derived quartz without possibilities of intermediate storage, leading to low TLS under such circumstances. However, the presence of scattered high TLS values along the river suggests incorporation of small amounts of highly sensitised grains from pre-eminently rock-derived sediment.

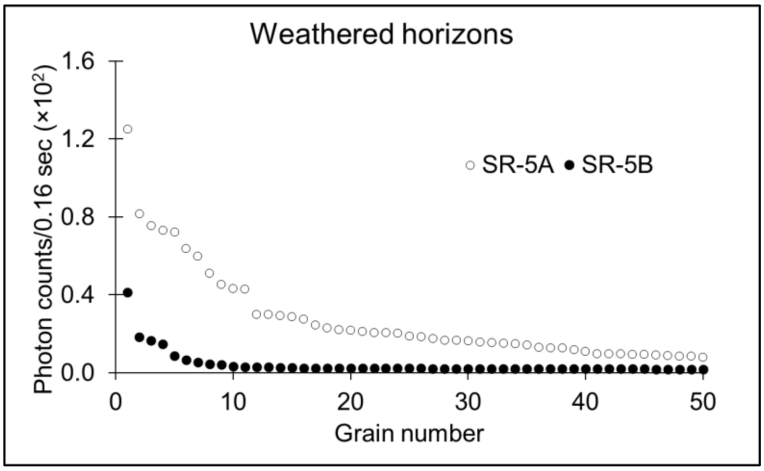

Fig. 5. 20: Green-stimulated luminescence signals from the top 50 single grains (out of 1000 measured) for (1) the weathered sample (SR-5A) and (2) its semi-weathered parent (SR-5B), both derived from weathered horizons on rock surfaces.

The soil horizons contained a higher number of luminescent grains (Fig. 5. 20) compared to rocks, likely due to repeated pedoturbation cycles, as well as a greater proportion of super-bright grains. The stability of the weathered surface may have allowed sufficient time for aeolian input. Further evidence comes from the comparison of two stratigraphically adjacent samples: the proportion of aliquots that failed to yield palaeodoses due to luminescence saturation was 23% in the weathered near-surface sample and 71% in the weakly weathered rock (Table 5. 7). Ideally, dose distributions from ancient rocks should exhibit saturated or equilibrium signals. In addition, the overdispersion (OD) of palaeodoses from twenty-four 5 mm aliquots was 32% and 46% in the weathered and weakly weathered samples, respectively. The difference of ~11 ka between the notional OSL ages of two differently weathered horizons estimates the TLS rate increase from 5.9 to 22.4 Units. The observed low ages, high OD, and a high proportion of saturated aliquots suggest the combined influence of pedoturbation and/or contamination by aeolian grains deposited at the surface and then moved below (Wilkinson & Humphreys, 2005; Bateman et al., 2003). In this semi-arid to arid region with sparse vegetation cover, pedoturbation is likely to progress slowly, making an external wind-transported sediment input a more plausible mechanism that modulates TLS along the river course. Under such conditions, the spatial randomness of observed TLS in the river sediment is also easy to comprehend.

Sensitisation experiments simulating deposition and erosion cycles (Fig. 5. 17; Fig. 5. 18) indicate a maximum TLS increase of 2–5 times, consistent with earlier reports (Parida et al., 2025; Pietsch et al., 2008; Cao et al., 2017; Zhang et al., 2022). This increase is insufficient to account for the 45-fold difference in TLS between host rock and river sediment. In the sensitisation experiment (Fig. 5. 17), simple extrapolations suggest that achieving such enhancement would require over 800 transport cycles with 0 Gy of burial per cycle. Even under an intermediate scenario involving 5 Gy burial per cycle, approximately 600 cycles would be needed to reach a 45-fold increase in TLS (Fig. 5. 17). These ballpark estimates imply that hundreds of thousands to over a million years of repeated reworking of alluvium would only explain the observed TLS levels of quartz grains.

The foregoing suggests that, irrespective of the multiplicity of geomorphic processes, the observed TLS of the river and the high sensitivity of dune-derived quartz would require a long recycling time. The answer possibly lies in the fact that Sabarmati alluvium was and is being derived through the denudation of the Aravalli Ranges. These supplied sediments to fill the Sabarmati Graben of Paleogene or older age, which were reworked through gullying and aeolian processes (Sonam et al., 2021; Narula et al., 2000; Valdiya, 2016; Valdiya and Sanwal, 2017). Thus, the Sabarmati Graben, with a history extending beyond the Palaeocene, provided sufficient time for sediments to undergo multiple cycles of recycling and sensitisation. This needs to be followed for further refinements, and a few suggestions for future studies that emerge from these studies are presented below.

While the mixing of high TLS dune sands could explain the spatial distribution of TLS in the Sabarmati River, the physical mechanism responsible for such high TLS values remains unclear and warrants further investigation. Sensitisation experiments are, to an extent, instructive. In Fig. 5. 17 and Fig. 5. 18, we notice that laboratory experiments do not provide an increase in sensitivity beyond ~1.8 times in 10-20 cycles. Similarly, single-grain data (Fig. 5. 19) shows that in 25 cycles, the brighter grains get sensitised 2-3 times, which is far too low for bedrock TLS to reach the observed sediment TLS. Fig. 5. 18 indicates that, on a laboratory timescale, the sensitisation process slows progressively for all grain types, including rocks, weathered rocks, and sediments. Thus, the only way the TLS of sediment gets higher is through a process that enables the creation and retention of trap centres in the quartz lattice through recycling. While a long residence time, as alluded to above, is a possibility, it will be of interest to identify and quantify such a process to explain higher TLS of sediment grains. This would also explain the presence of a higher proportion of brighter grains in sediments compared to rocks (Fig. 5. 16).

New insights that emerge from single-grain data are: in the first case, approximately 97% of grains from rocks exhibited no luminescence, and 60–80% in river sediments showed no detectable luminescence and did not respond to sensitisation cycles. As much as luminescence grains are used for provenance, we suggest that non-luminescent grains could also serve as a proxy for sediment source, and this aspect needs to be explored. It will also be of interest to understand the reason that quenches the luminescence of such quartz grains. Second, end-member mixing calculations using the highest TLS among seven aeolian quartz samples suggest that ~50 ± 30% of bright aeolian quartz mixed with average rock-derived quartz is required to reproduce the TLS variation observed in river sediments. The large variability arises due to location dependent mixing and a large range of TLS values.

A third possibility arises from the work of Parida et al. (2025), who linked the thermoluminescence sensitivity (TLS) of quartz grains to source rock denudation rates derived by Lupker et al. (2012). A comparison between their sediment TLS values and ours suggests that the Aravalli region has a denudation rate of approximately 10 mm/ka or lower. Such a slow denudation rate permits time for some of the grains to be sensitised to observed sediment TLS levels (Parida et al., 2025; Sawakuchi et al., 2018). These estimates accord with sediment flux studies in the nearby Mahi and Banas basins (Guha & Jain, 2020; Jain, Personal communication) with similar lithology and climate, suggestive of a denudation rate of ~8-10mm/ka. ^{10}Be-derived average denudation rate in the Luni basin in a similar climate and lithology range is around 5 mm/ka (Kaushal, Personal communication). Once calibrated, quartz TLS measurements could serve as a practical tool for estimating basin-scale denudation rates.

5.3 Yamuna River

5.3.1 Geological and geomorphological settings

The Yamuna River is a major tributary of the Ganga River, originating from the Yamunotri Glacier near the Banderpoonch peaks in the higher Himalayas at an elevation of approximately 6,387 meters. It travels a distance of about 1,370 km through the states of Uttarakhand, Himachal Pradesh, Haryana, Delhi, Uttar Pradesh, Rajasthan, and Madhya Pradesh, finally joining the Ganga at Allahabad (now known as Prayagraj).

Upon entering the Indo-Gangetic plains near Dak Pathar, the Yamuna transitions from a narrow, high-energy mountainous channel into a wider, meandering floodplain. The catchment area of the Yamuna lies across the Himalayas in the north, the Peninsular Plateau in the south, and the Indo-Gangetic Plain in between (Sinha et al., 2009; Yadav et al., 2023).

The river's discharge, heavily influenced by the monsoon, reaches its peak during the monsoon months (July to September) and significantly reduces outside this period, which affects sediment transport and deposition patterns. The region experiences mean annual daytime temperatures ranging from 30 to 35 °C, with maximum temperatures reaching approximately 40 °C in summer and minimum temperatures around 18 °C in winter.

As the river progresses through its middle course, it is characterised by extensive floodplains where it deposits alluvial sediments. This stretch is highly meandering, forming broad loops and bends as it loses energy.

5.3.1 Sample details and preparation

Samples were collected along a transect from Paonta Sahib in the Himalayan foothills to Delhi, covering the Yamuna's transition from a confined mountain river to a broad floodplain system (Fig. 5. 21). Table 5. 11 provides details on each sampling site, including latitude, longitude, sample type, transport distance from the origin, and elevation. This range of locations enables an analysis of how luminescence sensitivity varies with transport distance and depositional environment.

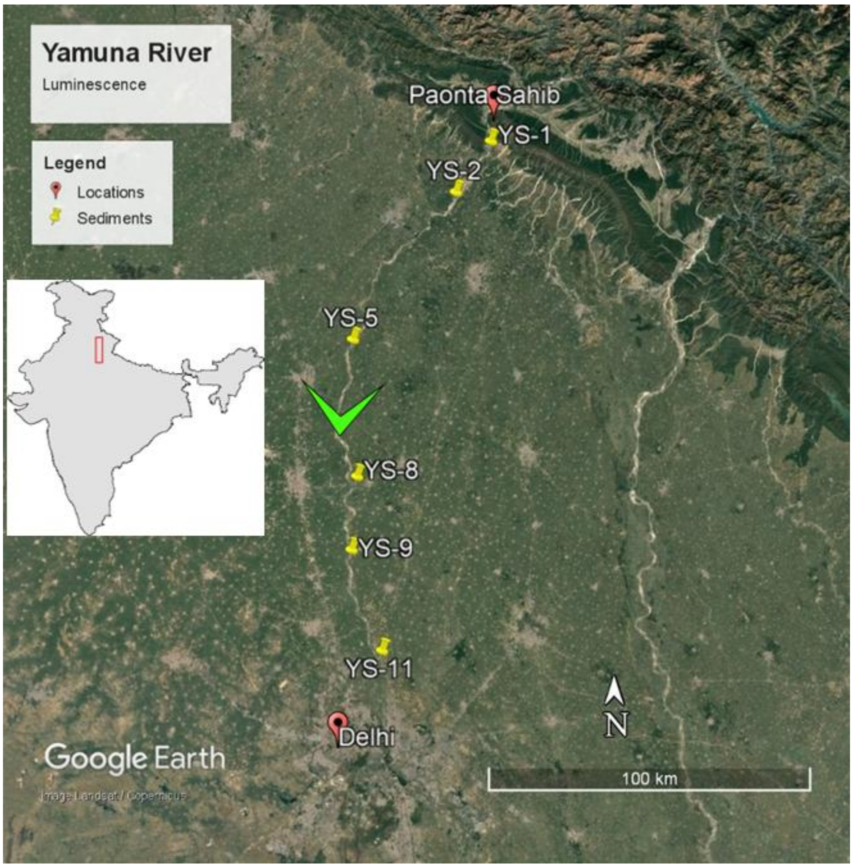

Fig. 5. 21: Map showing the sampling locations along the Yamuna River from Paonta Sahib to Delhi. The inset highlights the study region within India.

Table 5. 11: Sample details of Yamuna Basin.

Sample Name	**Latitude (in degrees minutes and seconds)**	**Longitude (in degrees, minutes, and seconds)**	**Type**	**Distance (km)**	**Elevation (m)**
YS1	30°18'43.60"N	77°34'59.80"E	Sediment	0	350
YS2	30°10'17.70"N	77°28'14.30"E	Sediment	20	302
YS5	29°45'47.80"N	77° 8'29.20"E	Sediment	86	268
YS8	29°22'59.60"N	77° 9'17.60"E	Sediment	133	250
YS9	29°10'45.40"N	77° 8'12.70"E	Sediment	161	243
YS11	28°53'52.90"N	77°13'59.90"E	Sediment	197	234

In alignment with protocols for the Sabarmati River, Yamuna River samples were collected from riverbed deposits, with wet sieving performed on-site to retain sediment grains in the 90–150 µm range (Fig. 5. 22).

Fig. 5. 22: Wet sieving of the sediments (Yamuna River)

Sample YS-1 was designated as the starting point, with distances measured from this location (0 km). The sample details are provided in the accompanying Table 5. 11.

Approximately 8 to 10 aliquots of each sample were used for TLS and BSLS measurements. To maintain consistency in the discussion, 1 photon count per milligram per Gray is designated as 1 Unit in the analysis of the Yamuna River samples. It should be noted that this unit differs from the Sabarmati River case, where 100 photon counts per milligram per Gy were defined as 1 Unit (measured using the Risø TL/OSL DA-15 system). Measurements for the Yamuna River samples were carried out using the Risø TL/OSL DA-20 system.

5.3.2 Results and discussion

As shown in Fig. 5. 23(A), BSLS values increase with distance from the source, peaking around 50 km downstream before reaching a stable plateau. This trend suggests that the early stages of sediment transport are critical for sensitisation, while further downstream movement has limited additional impact on BSLS. In contrast, Fig. 5. 23 (B) shows a slight decrease in 110 °C TLS values, from approximately 600 units near the source to around 550 units downstream. In this case, the sensitivity of the samples remains constant with increasing transport distance. This stability likely reflects rapid sediment transport in a high-energy fluvial system. As the Yamuna River, originates in the Himalayas and maintains continuous flow throughout the year. The consistently short residence time may limit the extent of sensitisation, suggesting that transport rate plays a critical role in controlling the evolution of quartz luminescence sensitivity.

Future work could expand this analysis to other river systems to validate these findings and explore factors influencing 110 °C TLS and BSLS responses to transport.

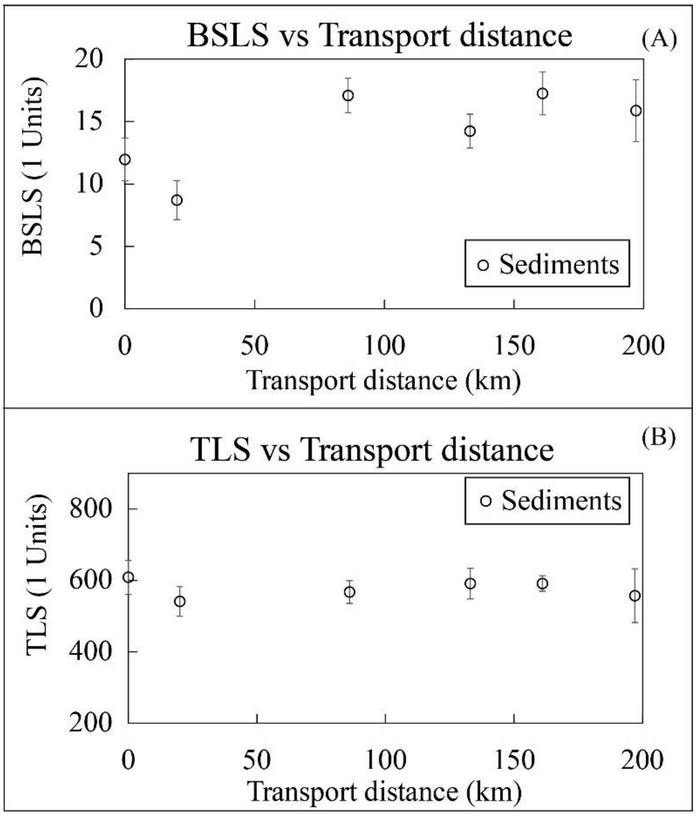

Fig. 5. 23: Variation of (A) 110 °C TLS and (B) BSLS for sediments with transport distance.

5.4 Sediment provenance quantification

To understand the contributions of different sediment sources within the river system, sediment provenance was quantified using luminescence sensitivity as a proxy. Provenance quantification provides insights into sediment dynamics and the relative influence of distinct source regions, as well as the tectonic and climatic conditions influencing the area. The luminescence sensitivity of quartz grains depends upon impurities present in source rocks and the activation of luminescence-related impurities during transport, thus mimicking the signatures of parent lithology (Rink et al., 1994; Preusser et al., 2006; Sawakuchi et al., 2011; Chauhan and Singhvi, 2019).

5.4.1 Methodology

Assuming the conservation of luminescence parameters in sediment mixing and applying mass conservation principles, sediment contributions can be quantified. In natural settings, sediments from multiple sources combine in specific proportions. Considering a two-source model, where sediments from sources A and B mix at location C (Fig. 5. 24), the mixing fractions from each source are denoted as X and Y, respectively. Given that luminescence has distinct measurable parameters, such as multiple thermoluminescence (TL) peaks and optically stimulated luminescence (OSL) components, it is possible to determine these fractions if the number of unique luminescence parameters is equal to or greater than the number of sources.

For a two-source system, the fractions X and Y can be calculated by solving the following set of linear equations:

$$mX + nY = p \tag{5.1}$$
$$X + Y = 1 \tag{5.2}$$

Where m, n, and p represent the luminescence properties of source A, source B, and the mixed sediment 'C' at the confluence, respectively.

Notably, several luminescence characteristics, such as TL peak intensities and OSL components, can serve as independent parameters, providing internal consistency checks for estimating source proportions. Solving equations (5.1) and (5.2) yields the following expressions (5.3 and 5.4) for X and Y:

$$X = \frac{p - n}{m - n} \tag{5.3}$$
$$Y = \frac{p - m}{n - m} \tag{5.4}$$

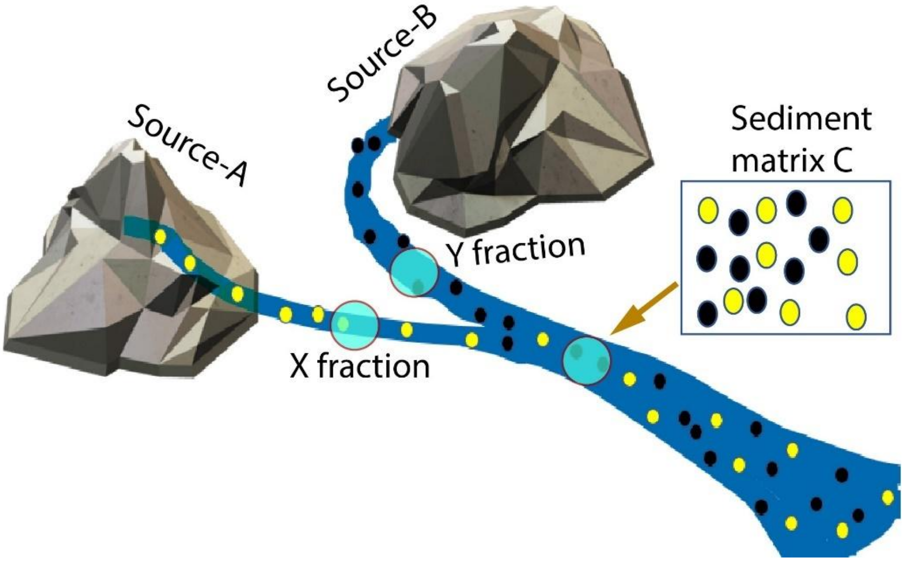

Fig. 5. 24: A schematic diagram of provenance from two sources, A and B, providing the sediment fraction x and y. Sediment collected at a later point of the river (C) to use luminescence as a proxy to evaluate the values x and y.

5.4.2 Measurement and protocol

Quartz grains were processed using standard separation techniques outlined in previous sections. The samples were mounted on stainless steel discs and initially measured for IRSL signals to detect any feldspar contamination. Each aliquot was weighed and dose-normalised to ensure sensitivity accuracy.

BSLS Measurement

For the measurement of **Blue-Stimulated Luminescence Sensitivity (BSLS)**, the aliquots were first bleached with blue stimulation for 80 seconds at 125 °C to erase residual natural luminescence signals (Table 5. 12). The aliquots were then irradiated with a small laboratory dose (~15 Gy) and preheated to 220 °C. An IRSL measurement was conducted to remove any luminescence signal associated with feldspar contamination, after which BSL was measured at 70 % power at the designated sample location using a UV detection window (U-340). The aliquots were then annealed at 450 °C for 10 minutes, and the measurement process was repeated from step 2 to capture the BSL signal after annealing. For each sample, 5–10 aliquots were measured, and an average BSL value was calculated. All signals were weighed and dose-normalised to get the sensitivity.

TLS Measurement

For the **Thermoluminescence Sensitivity (TLS)** measurement (Table 5. 13), a full TL glow curve was recorded with background subtraction using a detection filter (a U-340 filter (330 ± 50 nm) for UV detection or a blue filter pack (440 ± 40 nm) or an open window filter (330–770 nm)). The aliquots were then annealed at 450 °C for 10 minutes. After the aliquots are given the same irradiation dose, they are measured again for the TL glow curve with the respective detection window. 5–10 aliquots were measured for each sample, and an average integral TL value was calculated. All signals were weighed and dose-normalised to get the sensitivity.

Laboratory experiments were conducted by mixing sediment samples from two known provenances in specific proportions, and the source fractions were then estimated using the proposed equations (5.3 and 5.4). In a second set of experiments, natural samples with unknown source mixtures were analysed, enabling accurate determination of their source fractions. Additional details of these cases are provided below.

Table 5. 12: Sequence of procedures used to measure BLS sensitivity of quartz.

Steps	**Treatment**	**Remarks**
1	BSL at 125 ºC, 80 sec	Bleaching the natural signal
2	Beta dose (~15 Gy)	Giving artificial irradiation
3	TL (2 ºC/sec from room temp to 220 ºC)	
4	IRSL at 50 ºC, 100 sec (Optical Power 70%)	Removing possible feldspar contamination signal
5	BSL at 125 ºC, 40 sec (Optical Power 70%)	Measurement of BSL intensity
6	Anneal at 450 ºC for 10 min	Sensitisation by annealing
7	Repeat (2 onwards)	For measurement after sensitisation

Table 5. 13: Sequence of procedures used to measure TL sensitivity of quartz.

Steps	**Treatment**	**Remarks**
1	Beta Dose (~15 Gy)	Giving artificial irradiation
2	TL 450 ºC with background subtraction	Recording TL signal
3	Anneal at 450 ºC for 10 min	Annealing
4	Beta Dose (~15 Gy)	Giving artificial irradiation
5	TL 450 ºC with background subtraction	Record post-anneal TL signal

5.4.3 Controlled experiment:

Controlled experiments were conducted to test the feasibility of the mixing hypothesis and to identify the luminescence characteristics suitable for the successful recovery of known laboratory mixed fractions. Controlled mixtures were prepared using samples from the main trunk river and its upstream tributary near the confluence. This approach allowed for the evaluation of the methodology's effectiveness in intra-basin studies and provided an external verification of the technique's validity.

In this study, samples **SMRS-20** and **TRT-60** were combined in a known proportion, with 70% SMRS-20 and 30% TRT-60, to create the **MIX** sample. Luminescence techniques were then used to calculate the contributions of each source in this mixture. Their glow curves are presented in (Fig. 5. 25).

Result and discussion

Fig. 5. 25 shows the full TL glow curve of the TRT, SMRS and mix samples. The luminescence signal is measured, and after normalising, the fraction of SMRS in the mixed sample is listed in Table 5. 14.

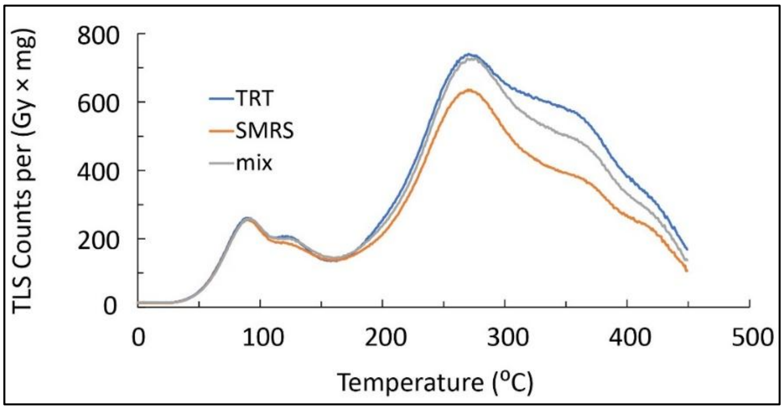

Fig. 5. 25: TLS glow curve of the artificially mixed samples.

Table 5. 14: % contribution of SMRS of the artificially mixed sample using luminescence parameters.

Sl no	**Luminescence parameter**	**Integrated Channel / Temperature (°C)**	**Detection window In nm**	**SMRS-20 Sensitivity**	**MIX Sensitivity**	**TRT-60 Sensitivity**	**% from SMRS**
1	95 °C TL	75-105 °C	330 ± 50	227	235	249	66
2	130 °C TL	118-140 °C	330 ± 50	171	177	199	77
3	Annealed 310 °C TL	250-350 °C	330 ± 50	95	109	144	71
4	200 °C TL	175-220 °C	330 -770	661	778	938	58
6	Annealed BSLS	Signal: (2–6); Background: (201–250)	330 ± 50	487	639	1105	75

The "% from SMRS" column in Table 5. 14 shows the contribution of SMRS in the MIX sample for each luminescence parameter. The results indicate that luminescence signals specifically, 95 °C TL, 130 °C TL, annealed 310 °C TL, 200 °C TL, and annealed BSLS, serve as reliable indicators of SMRS content, with contributions 68±9%, closely aligning with the expected 70% mixing ratio. The variation in contribution values across different luminescence parameters demonstrates the potential of using multiple luminescence characteristics to validate sediment source contributions in two-body mixing scenarios, supporting the applicability of this technique in natural settings.

5.4.4 Sediment budgeting in the Nubra Shyok confluence:

The Nubra and Shyok Rivers converge in the high-altitude region of the Ladakh Himalayas, forming a unique geomorphological setting influenced by rugged topography and glacial activity. Nubra River contributes sediments to Shyok River (Fig. 5. 26). The TRT-60 sample from the Nubra River and the SMRS-20 sample from the Shyok River converge, creating a mixed sample, CHAL-50, at the confluence (Fig. 5. 26). Sediment budgeting was performed using luminescence sensitivity measurements to determine the proportion of material contributed by the Nubra River to the Shyok River.

The thermoluminescence (TL) glow curves of TRT-60, SMRS-20, and CHAL-50 were recorded (Fig. 5. 27), revealing multiple TL peaks associated with various trap groups. The TL peak before and after annealing and BSLS are recorded. The contributions from different TL peaks and the blue-stimulated luminescence (BSLS) signal are summarised in

Table 5. 15.

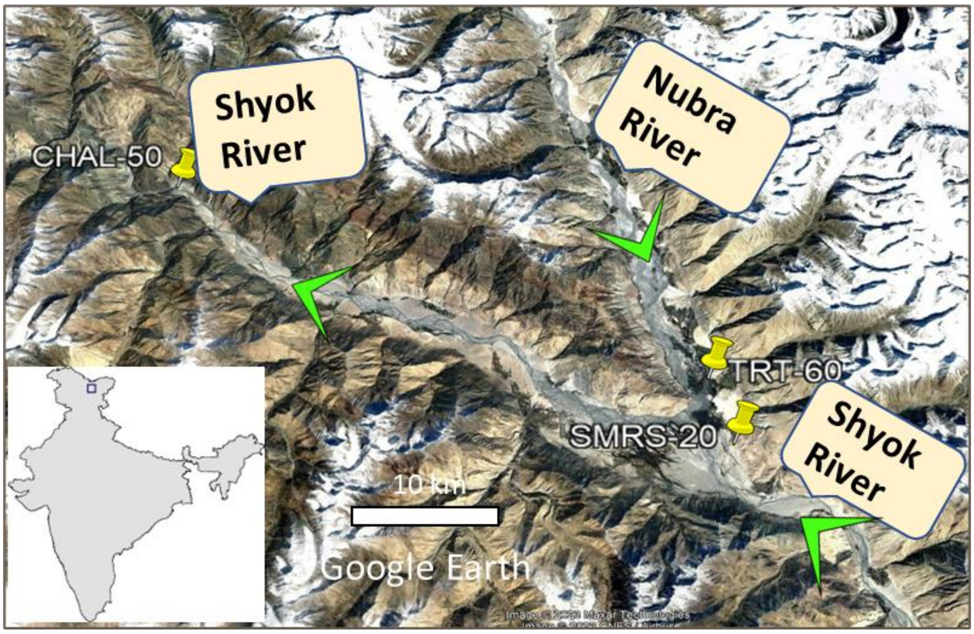

Fig. 5. 26: Map depicting the sampling locations (CHAL-50, SMRS-20, and TRT-60) along the Shyok River and Nubra River in the study area. The inset highlights the study region within India.

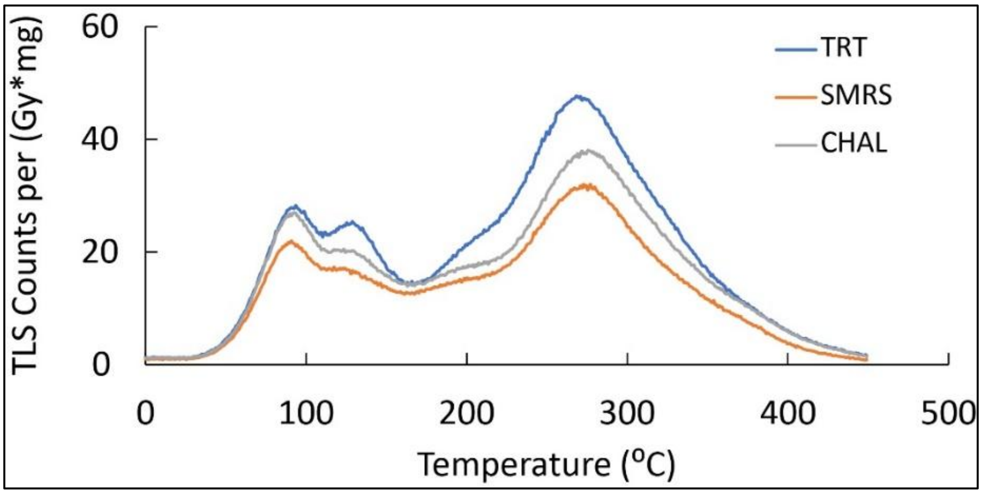

Fig. 5. 27: TLS glow curve of the samples from Nubra and Shyok confluence.

Table 5. 15: % contribution of SMRS of Nubra River after confluence using different luminescence parameters.

Sl no	**Luminescence parameter**	**Integrated Channel / Temperature (°C)**	**Detection window In nm**	**TRT-60 Sensitivity**	**CHAL-50 Sensitivity**	**SMRS-20 Sensitivity**	**% from Nubra River (TRT-60)**
1	95 TL	75-105 °C	330 -770	93226	122259	128913	19
2	95 TL	75-105 °C	330 ± 50	885	838	823	24
3	Annealed BSLS	Signal: (2–6); Background: (201–250)	330 ± 50	1934	1046	764	24
4	95 TL	75-105 °C	440 ± 40	39353	54768	59302	23
5	375 TL	350-390 °C	330 -770	1989	1470	1350	19

Result and Discussion:

The results indicate a consistent contribution from the Nubra River across multiple parameters, with percentages ranging from 19% to 24%, depending on the specific luminescence parameter analysed (

Table 5. 15). The variation in contributions across different luminescence parameters provides insights into the mixing dynamics and source contributions at the Nubra-Shyok confluence. While individual luminescence peaks vary slightly, the average contribution from the Nubra River remains around 24%, confirming a significant, but not dominant, influence of Nubra sediments in the mixed sediment load at present time. This analysis highlights the effectiveness of using multiple luminescence characteristics, such as TL peaks and BSLS, to cross-validate sediment source contributions.

5.4.5 Sediment budgeting in the Beas confluence:

A sediment budgeting study was conducted at the confluence of the Beas River and a small tributary near Solang in Himachal Pradesh. Near Solang, the river valley is steep and narrow, shaped by intense erosional processes. In this region, sediments from the tributary (sample B06) mix with those from the Beas River, creating a combined sediment load downstream. Samples B07 and B08 represent sediment before and after the confluence, respectively (Fig. 5. 28). The study aimed to quantify the sediment contribution from the tributary to the Beas River using thermoluminescence (TL) and optically stimulated luminescence (OSL) measurements.

Thermoluminescence glow curves for the three samples (B06, B07, and B08) were recorded and analysed (Fig. 5. 29). Luminescence parameters were measured in the visible window, and sediment budgeting was calculated by integrating and normalising the TL and OSL signals. The results are presented in Table 5. 16.

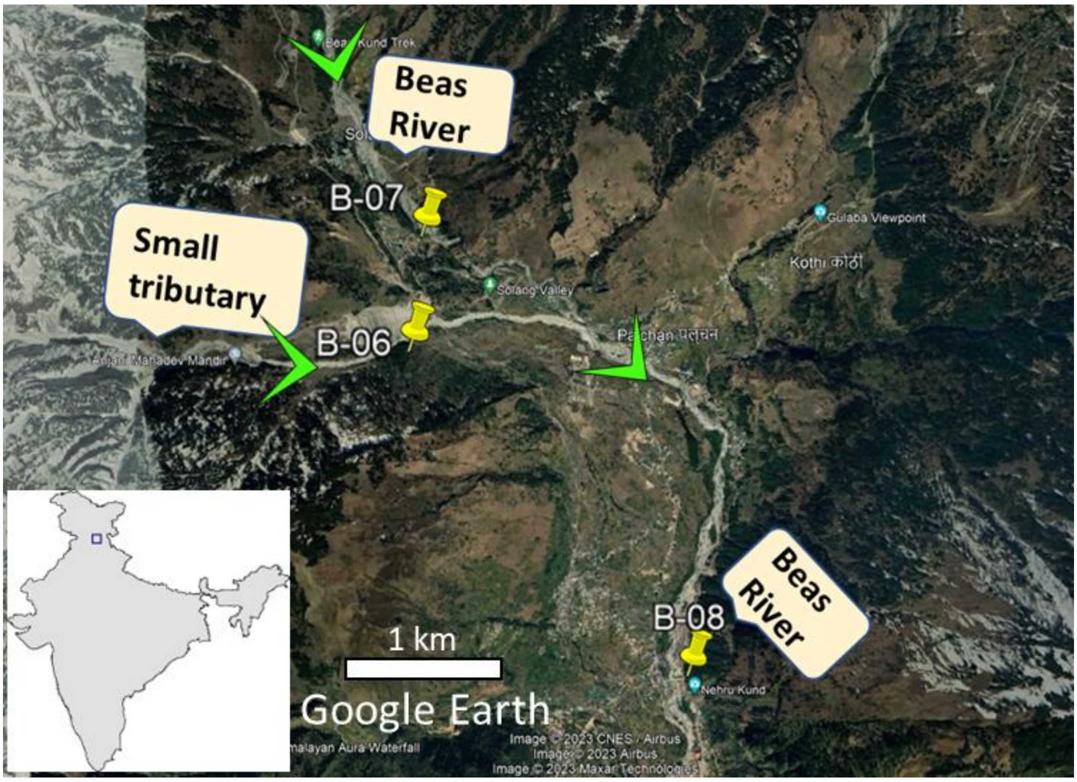

Fig. 5. 28: Map illustrating the sampling locations (B-06, B-07, and B-08) along the Beas River and its small tributary in the study area. The inset shows the study region within India.

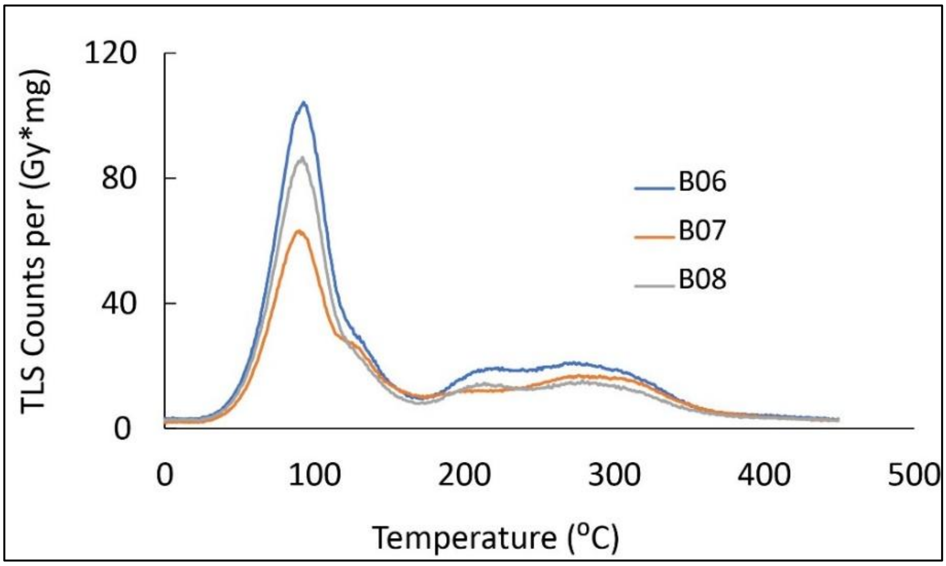

Fig. 5. 29: TLS glow curve of the samples from Beas.

Table 5. 16: % contribution of sediments B-06 to Beas River is derived using luminescence parameters.

Sl no	**Luminescence parameter**	**Integrated Channel / Temperature (°C)**	**Detection window (in nm)**	**B-06 sensitivity**	**B-07 sensitivity**	**B-08 sensitivity**	**% from (B-06) River**
1	90 °C TL	78-103 °C	330 ± 50	1465	891	1214	56
2	205 °C TL	190-220 °C	330 ± 50	291	199	221	24
3	Annealed 90 °C TL	78-103 °C	330 ± 50	153663	109009	123807	33
4	Annealed 135 °C TL	130-145 °C	330 -770	348	258	283	28

Results and discussion:

The results indicate that the tributary contributes significantly to the Beas River's sediment load, with contributions varying from 24% to 36% depending (

Table 5. 16) on the luminescence parameter (205 °C TL, annealed 90 °C TL, annealed 135 °C TL and BSLS). The average contribution of the tributary (B-06) to the sediment load at the confluence is approximately 30%, calculated by averaging the contributions from the different luminescence parameters.

However, the higher contributions observed in the 90 °C TL (56%) and annealed BSLS (108%) parameters suggest a deviation from the anticipated two-source mixing model. This discrepancy may be attributed to additional sediment input from fresh erosion in the area, as the region near the confluence is prone to erosion. Freshly eroded material from nearby hill slopes likely influences specific luminescence signals, particularly those with higher values, complicating the sediment budget and reflecting an influx beyond the simple two-body mixing condition.

5.4.6 Wakal River confluence

The Wakal River confluence, located near Biroti in Rajasthan, India, is a region where the Mansi River joins the Wakal River. This area is characterised by mountainous valleys with steep slopes and intense erosion from the surrounding hills, which contribute significantly to the river's sediment load. To determine the sediment budget at the Wakal-Mansi confluence (Fig. 5. 30), samples were collected from the Wakal River before the confluence (SR-8A), the Mansi River (SR-9A), and downstream of the confluence (SR-12). Luminescence sensitivity measurements were conducted for each sample, and the contribution from the Mansi River (SR-9A) was estimated using multiple luminescence parameters. The TL glow curves for these samples are shown in Fig. 5. 31, and the results are summarised in Table 5. 17.

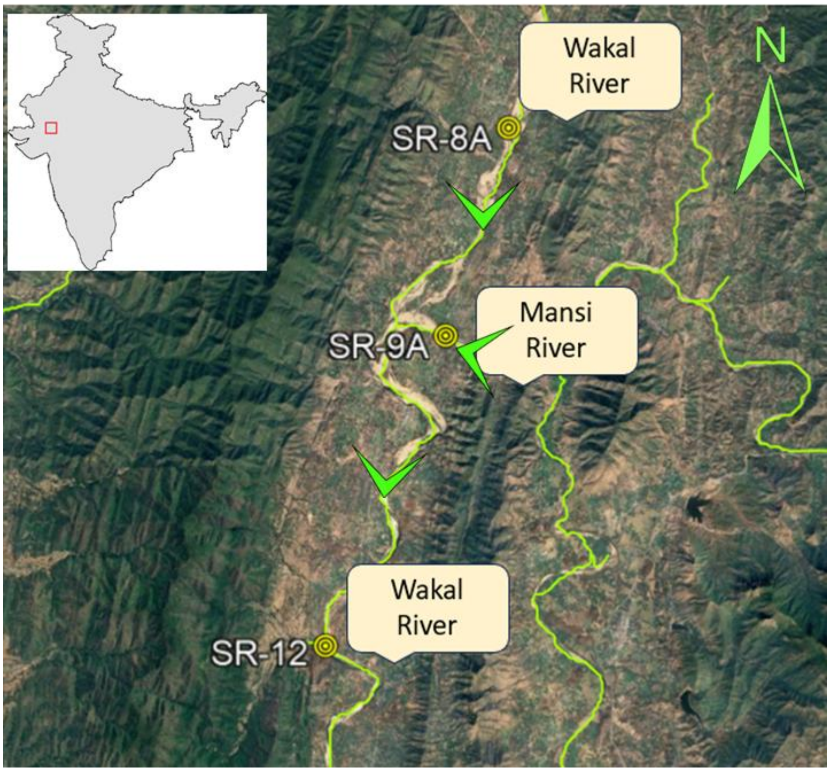

Fig. 5. 30: Map showing the sampling locations (SR-8A, SR-9A, and SR-12) along the Wakal River and Mansi River in the study area. The inset highlights the study region within India.

Table 5. 17 presents sensitivity values for SR-8A, SR-9A, and SR-12 across several luminescence parameters, showing the calculated contribution of Mansi River sediments in the post-confluence sample (SR-12). The results indicate a varied contribution from the Mansi River, with some unexpected values potentially due to additional sediment sources from nearby hill slopes.

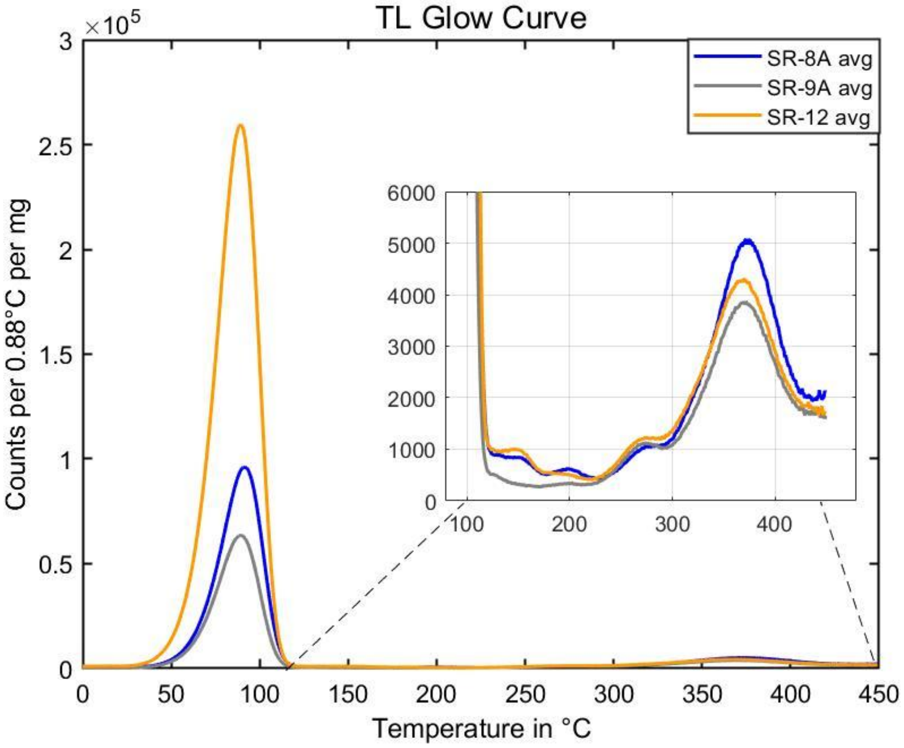

Fig. 5. 31: TL glow curve of the samples from Sabarmati River. (Inset is showing the zoomed figure of higher TL peaks)

Results and Discussion:

<u>BSLS (330 ± 50 nm):</u> This parameter shows a negative contribution of -16% from the Mansi River, suggesting interference from additional sediment sources, likely from hill slope erosion, impacting the luminescence signal.

<u>Annealed 375 °C TL (330–770 nm):</u> This parameter reflects a significant contribution of 62% from the Mansi River.

<u>Annealed 205 °C TL (330–770 nm) and 205 °C TL (330–770 nm):</u> These parameters show contributions of 33% and 31%, respectively, from the Mansi River, providing more moderate but consistent estimates.

Table 5. 17: % contribution of sediments of Mansi River (SR-8) to Wakal River is derived using luminescence parameters.

Sl no	**Luminescence parameter**	**Integrated Channel / Temperature (⁰C)**	**Detection window (in nm)**	**SR-8A Sensitivity**	**SR-9A Sensitivity**	**SR-12 Sensitivity**	**% from (SR-9) Mansi River**
1	BSLS	Signal: (2–6); Background: (201–250)	330 ± 50	654	997	599	-16
2	Annealed 375 ⁰C TL	345-400 ⁰C	330 -770	285726	219677	244576	62
3	Annealed 205 ⁰C TL	185-222 ⁰C	330 -770	23547	13633	20319	33
4	205 ⁰C TL	185-222 ⁰C	330 -770	23991	18677	22360	31

The average contribution of the Mansi River to the post-confluence sediment load, based on most of the luminescence parameters, is approximately 32%, excluding the anomalous negative value observed in the BSLS parameter and annealed 375 ⁰C TL parameter. The broad range of contributions, from -16% to 62%, indicates variability in the luminescence response, likely due to interference from freshly eroded sediments entering the river from the surrounding hill slopes.

In the subsequent analysis, efforts are made to estimate the probable hill slope contribution by examining specific luminescence parameter ranges that are characteristic of recently eroded hill slope sediments. These findings highlight the complex dynamics of sediment mixing in areas with active erosion and underscore the importance of using multiple luminescence characteristics to obtain accurate sediment provenance data in such environments.

5.4.7 Finding unknown % contribution of sediment using three body mixing

A three-body mixing model was applied to assess the probable contribution of hill slope sediments to the Wakal River confluence. This model considers the unique luminescence parameters of hill slope sediments, which are generally lower in sensitivity compared to sediments collected at the confluence from the main rivers. Including the hill slope component allows for a more accurate interpretation of discrepancies observed in the luminescence data from the Wakal Mansi confluence system.

The model assumes that the luminescence signal from hill slope material should be well-distinguishable from noise, ensuring minimal error. Three luminescence parameters were used to estimate hill slope contributions: BSLS, annealed 375 °C TL and annealed 205 °C TL.

The sensitivity of luminescence parameters for SR-8, SR-9, and SR-12 are represented in (Table 5. 17). The value of luminescence parameters BSLS, annealed 375 °C TL, annealed 205 °C TL and 205 °C TL are taken as a, b, c and d, respectively.

Results and discussion:

The following equations where consider x_1, x_2 and x_3 as the contribution fractions from SR-8A, SR-9A and hill slope sediments, respectively. These equations aim to determine the percentage contribution from hill slope sediments along with their probable luminescence parameters.

$$x_1 + x_2 + x_3 = 1 \tag{5.5}$$

$$654\, x_1 + 996\, x_2 + a\, x_3 = 599 \tag{5.6}$$

$$285726\, x_1 + 219677\, x_2 + b\, x_3 = 244576 \tag{5.7}$$

$$23547\, x_1 + 13633\, x_2 + c\, x_3 = 20319 \tag{5.8}$$

$$23991\, x_1 + 18677\, x_2 + d\, x_3 = 22360 \tag{5.9}$$

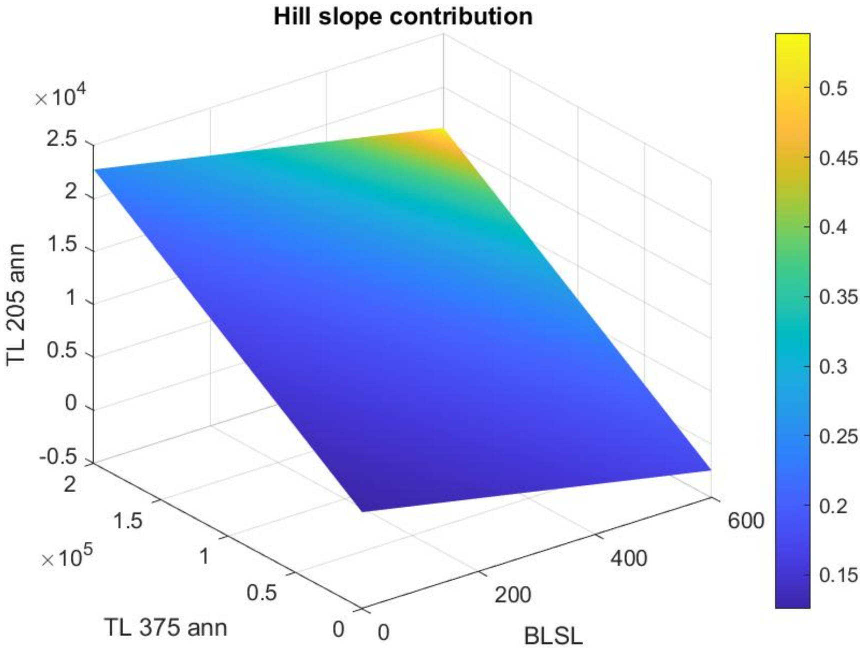

Fig. 5. 32: 3D surface plot shows the probable value of Luminescence parameters of Hill slope sediment, and colour bar map tells the corresponding hill slope contribution.

The probable percentage contribution from hill slope can be determined by solving equations 5.5, 5.6, 5.7, and 5.8. A three-dimensional surface plot in Fig. 5. 32 presents the estimated luminescence parameter values for hill slope sediments, with a colour bar indicating the associated percentage contribution. Based on this model, and through iterative solutions of the equations, the hill slope contribution to the Wakal River sediment load is estimated to reach up to 54 percent, assuming the luminescence parameters fall within the following bounds:

1. BSL < 600 Counts / (Gy × mg)
2. Annealed 375 °C TL < 219000 Counts / (Gy × mg)
3. And annealed 205 °C TL < 13000 Counts / (Gy × mg)

These upper bounds of luminescence of hill-slope sediment are chosen so that it should have lower luminescence sensitivity compared to river sediments. The contribution estimates indicate that a substantial portion of the sediment in the Wakal River at the confluence may originate from hill slope erosion, particularly in this high-erosion, mountainous terrain.

The results of this study suggest that laboratory-controlled experiments can help identify suitable luminescence parameters for sediment budgeting in specific sample mixtures. Therefore, it is recommended to perform control experiments using known mixed fractions to understand the luminescence behaviour of the samples, which can guide parameter selection for subsequent analyses. Moreover, employing multiple luminescence parameters and averaging the values derived from these different characteristics can improve reliability. However, caution is advised in contexts with significant human disturbance, where the applicability of this approach may be limited.

5.5 Relationship between grain shape and luminescence sensitivity

Grain shape, often indicative of sediment maturity, provides insights into the sediment's transport history. During transport, grains may undergo size reduction due to abrasion, leading to rounding of sharp edges and corners. The degree of roundness, therefore, can serve as an indicator of how long a sediment grain has been in the transportation cycle. It is well known that fluvial transport sensitizes the luminescence of quartz (Pietsch et al., 2008). This establishes a hypothesis that quartz grain shape may have a relation with its luminescence.

Parameters such as sphericity and roundness are valuable for differentiating sedimentary environments (Patro & Sahu, 1974; Resentini et al., 2018). Typically, well-rounded grains indicate long-distance travel, while angular grains are generally derived from nearby sources.

5.5.1 Sphericity and roundness

- **Sphericity** measures how closely the shape of a grain resembles a sphere, independent of its size (Fig 5.28). High sphericity generally indicates more advanced weathering and transport. Here, the width-to-length ratio sphericity (SWL) is calculated by taking the ratio of the width (d2) to the length (d1) of the particle.

$$SWL = \frac{d2}{d1}$$

- **Roundness** measures the sharpness of a grain's edges and corners, which typically smooth out with prolonged transport (Fig 5.28). Roundness was originally defined by Wadell (1935) as the ratio of the average radius of curvature at the particle's corners (Ri) to the radius of the maximum inscribed circle (Ci):

$$R = \frac{\text{Average radius of curvature of corners}}{\text{The radius of the maximum inscribed circle}}$$

Both sphericity and roundness were calculated in this study using two-dimensional projections of the grains. Grain shape characteristics were determined through microscopic imaging and processed using MATLAB code to quantify sphericity and roundness.

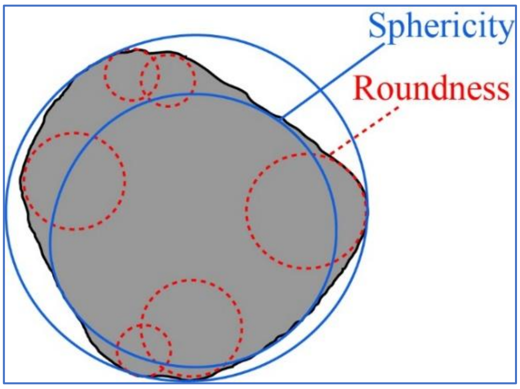

Fig. 5. 33: Schematic illustration of sphericity and roundness of a particle.

Sample: The quartz sample SR-23 from the Sabarmati River basin was analysed for single-grain luminescence, with grain shapes quantified using microscopic images and processing techniques. Two-dimensional projections of the grains were adjusted to grayscale to improve the accuracy of shape analysis.

Grain shape analysis

High-resolution images of the quartz grains were obtained using a microscope and converted to grayscale (Fig. 5. 33). The images are adjusted to ensure clear contrast, allowing for accurate detection of grain boundaries. Using the MATLAB program by Zheng., 2014, the images are converted to binary by setting a threshold and isolating the grains from the background. This binary format enables the extraction of the grains' outlines. Sphericity was determined by analysing the grain's outline relative to an ideal circular shape. This measurement involved calculating the perimeter and area ratios to quantify deviations from circularity, thereby indicating the degree of sphericity. The roundness is computed by measuring the sharpness of the edges and corners. This is achieved by fitting circles to the corners of each grain's outline and determining the average radius of curvature at these points relative to the grain's maximum inscribed circle (Fig. 5. 34).

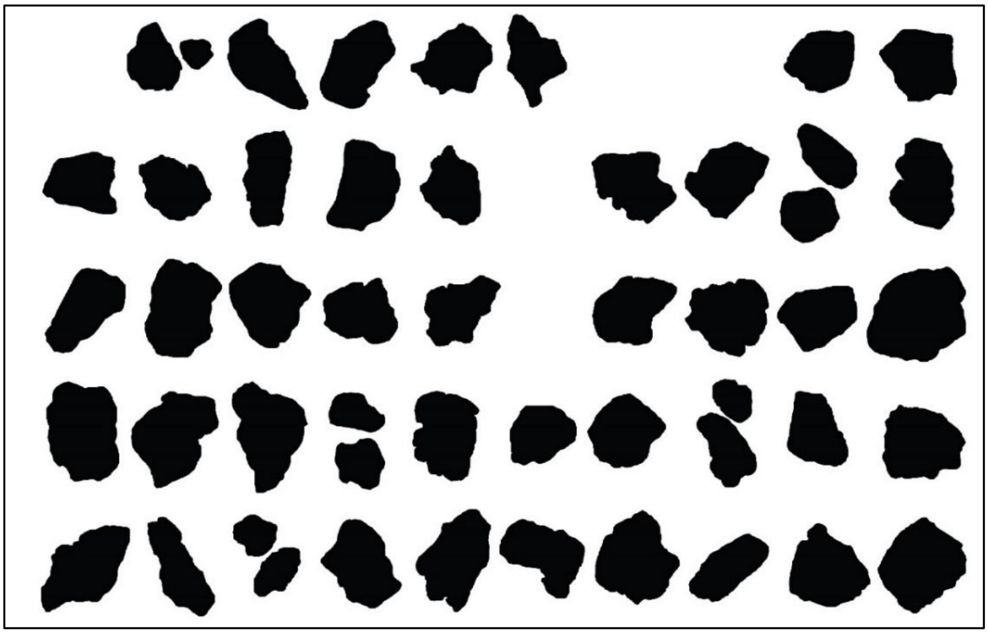

Fig. 5. 34: Two-dimensional projections of the grains, adjusted for grayscale and converted to binary format for shape analysis.

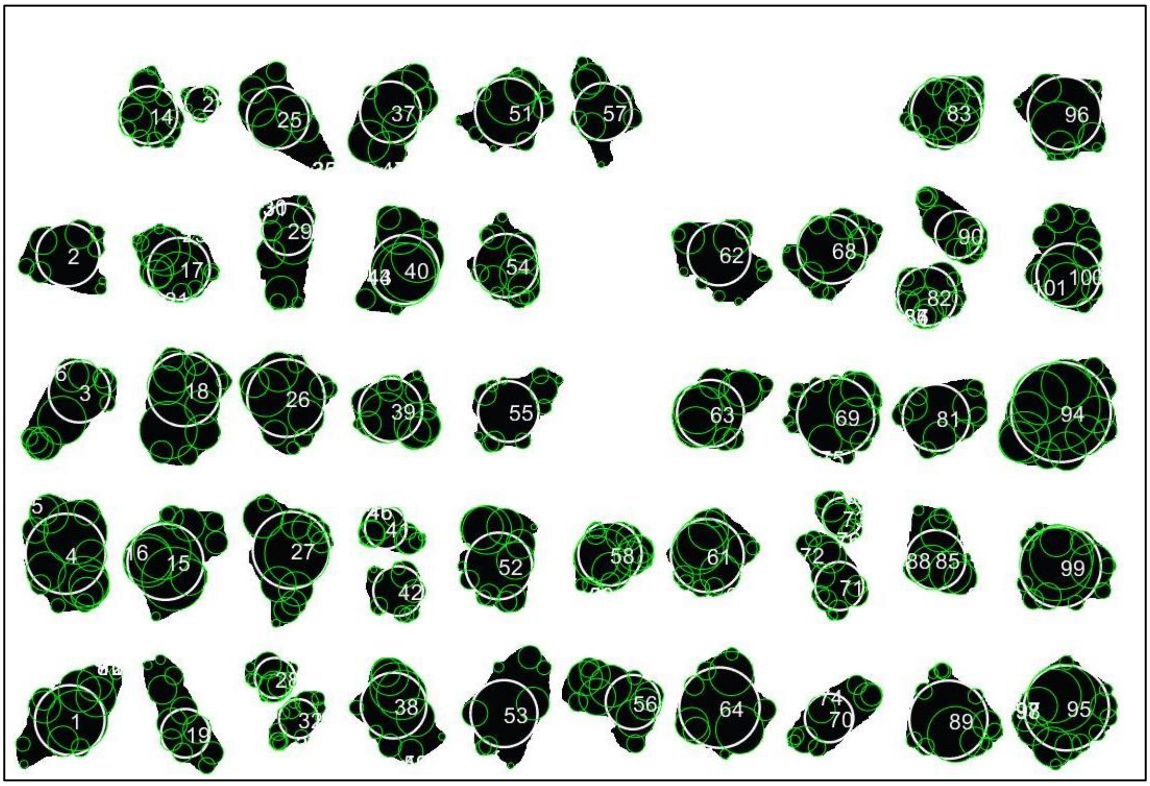

Fig. 5. 35: Curvature of grain corners identified by fitting green circles; the radius of the maximum inscribed circle is indicated by the white circle.

5.5.2 Single grain luminescence measurement

Single-grain luminescence measurements were conducted on 100 grains of sample SR-21A (Sabarmati River sediment), using the Riso DA-15 instrument equipped with a green laser for optical stimulation (refer to Chapter 2).

Initially, the natural luminescence of the grains was removed through bleaching followed by preheating. Single-grain OSL measurements were then performed (Table 5. 18). The single-grain disc was subsequently irradiated with a 24 Gy dose, preheated at 200 °C, and measured again for OSL. This procedure enables a direct comparison between luminescence sensitivity and grain shape characteristics.

Table 5. 18: Protocol for measurement of single grain signal.

Steps	Treatment	Remarks
1	TL 200 °C	Preheat
2	SG OSL	Bleaching of natural dose
4	Dose 24 Gy	Irradiating grains
5	TL 200 °C	Preheat
6	SG OSL	Signal measurement

Result and discussion

Fig. 5. 36A displays the relationship between roundness and single-grain (SG) luminescence signal intensity. The data shows considerable scatter, with no clear trend or consistent increase in luminescence sensitivity as roundness increases. This lack of correlation suggests that factors such as intrinsic mineral properties or microstructural defects may have a stronger influence on luminescence sensitivity than grain roundness.

Similarly, Fig. 5. 36B illustrates the relationship between sphericity and SG signal intensity, and, like the roundness data, it shows no discernible trend. The absence of correlation here implies that sphericity, representing the overall shape of the grain, does not significantly impact the luminescence response.

Overall, the lack of a clear relationship between grain shape (both roundness and sphericity) and luminescence sensitivity suggests that shape parameters are not primary determinants of luminescence behaviour in these quartz grains. Instead, this finding points to the potential importance of other factors, such as crystal lattice defects, mineral impurities, or surface microstructures, in controlling luminescence sensitivity.

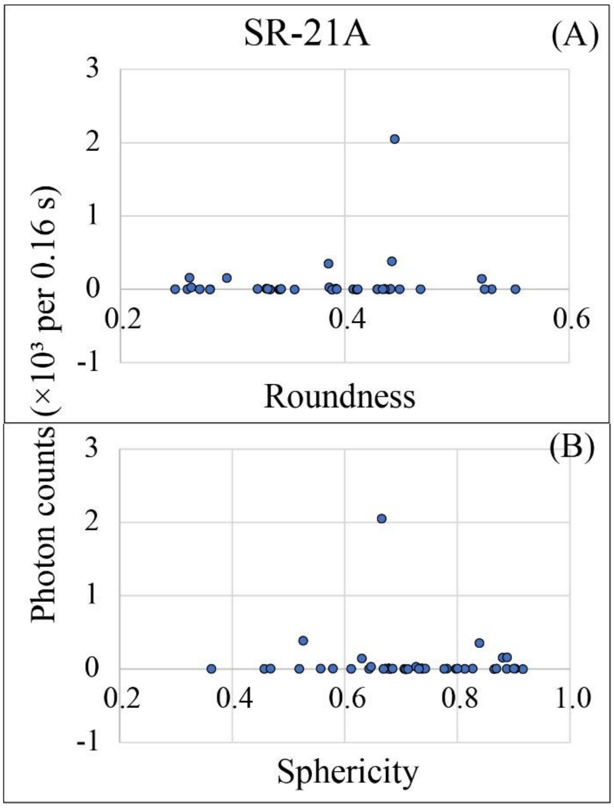

Fig. 5. 36: Single grain luminescence signal vs (A) roundness and (B) Sphericity.

5.6 Conclusion

The study has provided critical insights into the potential of luminescence sensitivity as a proxy for sediment provenance and transport history. The main conclusions from each section are:

Rock vs sediment luminescence sensitivity:

The 110 °C TLS and BSLS show a broad co-variation trend across the Sabarmati basin. Rock samples exhibit TLS values ranging from 1.6 to 6.2 Units. Weathered rock samples range from 5.9 to 15.6 Units, while sediments show a significantly higher TLS range from 66 to 325 Units. This wide range highlights how rock type and weathering processes affect luminescence sensitivity, with sediment samples showing the highest TLS values due to transport and possible aeolian influence.

Influence of transport distance on luminescence sensitivity:

Transport distance alone does not linearly influence luminescence sensitivity (110 °C TLS and BSLS), as demonstrated in the Sabarmati and Yamuna River analyses. Instead, in the Sabarmati River case, contributions from aeolian, hillslope sediment, and confluence effects are significant.

Laboratory sensitisation studies and field 110 °C TLS values imply that fluvial transport over tens of thousands of years could lead to the observed levels of 110 °C TLS sensitisation.

A significant disparity was seen between the TLS of bedrock and river-transported sediments, with the latter being up to 45 times more sensitive. Achieving high TLS values of sediments beginning from the rock would require prolonged recycling of bedrock-derived quartz over million-year timescales. Laboratory sensitisation experiments yielded only a 2–3-fold increase, indicating that a time-dependent relaxation mechanism in the trap centre may facilitate continuous sensitisation in natural settings. The underlying mechanism of this process needs elucidation for its use in estimating time scales of landscape evolution.

TLS for denudation rate:

TLS values suggest denudation rates of 10mm/ka, which accords with estimates from nearby basins (Guha & Jain, 2020; V. Jain personal communication) and is slightly lower than Western Ghat basins, which are undergoing a stronger climatic forcing.

Sediment provenance quantification at confluences:

By applying multi-parameter luminescence measurements, the study effectively quantified sediment contributions from different tributaries and hill slopes at confluences, such as the Nubra-Shyok and Wakal River junctions. At the Sabarmati River confluence, the use of two-body mixing methods for sediment budgeting is complicated by unknown variables, such as varying sediment contributions from tributaries and hill slopes. A three-body mixing model was developed to account for additional hill slope inputs, providing plausible ranges for luminescence parameters indicative of fresh hill slope contributions. This combined approach offered detailed sediment budgeting insights and revealed complex dynamics in high-erosion regions, where hill slope sediments significantly impact the overall sediment load alongside the primary tributary sources.

Impact of grain shape on luminescence sensitivity:

While initial hypotheses suggested that sphericity and roundness could influence luminescence sensitivity, no clear trends were observed. This suggests that macroscopic grain shape does not significantly impact luminescence response, and factors such as mineralogical properties or microstructural defects are likely more critical.

Use non-luminescent grain:

Single-grain analysis indicates that in rock samples, ~< 0.5% of grains are super-bright and contribute nearly > 80% of the total luminescence signal. This highlights the need for detailed luminescence and isotopic characterisation to evaluate their potential in provenance and dating studies (Chauhan & Singhvi, 2019; Yoshida et al., 2000). These also show the presence of non-luminescent grains unaffected by blue-bleach cycles. These grains merit further investigation using isotope systematics, and, akin to their luminescence counterparts, these can potentially be used as a proxy for provenance.

Implications for provenance studies:

The findings support the application of luminescence sensitivity as a tool for provenance studies, particularly in multi-source river basins with active erosion and aeolian inputs. The data highlight that luminescence sensitivity can effectively reflect sediment source contributions, but results should be interpreted with an understanding of environmental and geological complexities. In case of Sabarmati multiplicity of sediment sources makes the Sabarmati a complex system. The present study provides a caveat for using TLS for provenance in fluvial systems influenced by aeolian activity.

Overall, this chapter advances the application of luminescence sensitivity as a reliable tool in sediment provenance analysis, offering a refined methodology to quantify and understand sediment sources in complex fluvial systems. The findings lay a foundation for further studies, especially in dynamic sedimentary environments influenced by multiple erosion and transport factors.

Chapter 6

6. Summary and future outlook

6.1 Summary: present understanding

The thesis examines the potential of quartz luminescence as a tool for sediment tracing in natural systems, aiming to establish a physics-based understanding of luminescence sensitivity. This understanding forms the basis for developing reliable methodologies applicable across diverse contexts. It addresses the fundamental question of how natural processes influence the luminescence properties of quartz grains and investigates the relationship between luminescence sensitivity and quartz crystal domains. Furthermore, the study evaluates the applicability of quartz luminescence in natural environments, with a focus on variations in luminescence sensitivity within fluvial systems, its role in sediment budgeting, and its relationship with grain shape. The objectives of the thesis are:

1. *Investigate natural factors affecting the luminescence characteristics of quartz during its antiquity in nature.*
2. *Role of structural defects of quartz crystal in its luminescence properties*
3. *Implications for earth surface studies*

A summary of the results present in the thesis is given below:

Natural factors affecting the quartz luminescence

This study aims to identify luminescence parameters relevant to provenance studies and to infer the natural conditions experienced by quartz crystals. It has that quartz luminescence sensitisation occurs during its transport and is influenced by sedimentary history and the source lithology of quartz (Fitzsimmons, 2011). In some cases, repeated deposition and reworking enhance the luminescence sensitivity of quartz (Pietsch et al., 2008). To simulate natural transportation processes, quartz samples with dull, medium, and high luminescence sensitivities were subjected to laboratory treatments, including annealing, high-dose irradiation, prolonged solar exposure, and UV exposure. The effects of these treatments were evaluated by systematically recording changes in luminescence parameters, which are linked to modifications in the traps or defects within the crystal structure.

Annealing significantly enhances 110 ºC TLS, with the dull sample showing the highest proportional increase 80-fold, while medium and bright samples exhibit smaller enhancements (3–6-fold). Irradiation also sensitises 110 ºC TLS, resulting in a 7-fold increase in the dull sample and a 1–2-fold increase in medium and bright samples. In contrast, sunlight and UV exposure decrease 110 ºC TLS across all samples, with the bright sample experiencing the substantial reduction, up to 0.55 of its natural 110 ºC TLS. A similar trend is followed by the BSLS of quartz.

In case of higher TL peak, 1. The full TL glow curve shows varying responses to treatments. Annealing causes a decreasing trend in broad TL peaks around 300 °C across all samples. Irradiation reduces peaks in dull and medium samples but increases them in bright samples in the 200–300 °C range. Sunlight and UV exposure consistently reduce TL peaks. The full TL glow curve is separated as a light-sensitive and light-insensitive part by bleaching the sample during measurement. The light-insensitive part is generally reduced by annealing, sunlight, and UV exposure. Irradiation has minimal impact on dull and medium samples but increases the 200–300 °C region in bright samples. Light-sensitive parts show minimal changes under sunlight and UV exposure. Annealing does not significantly affect the 200–450 °C range, while irradiation causes a slight decrease in dull and medium samples but increases the bright sample's 200–300 °C range.

The natural LM-BSL of all samples shows two components. Annealing activates a new defect group, the dull component. Irradiation activates two new defect groups in all samples. Sunlight and UV exposure do not alter the components, which remain as in natural conditions. The total LM-BSL signals increase in all samples after treatment, with enhancements of 7–17 times from annealing, 3–10 times from irradiation, and 1–3 times from sunlight and UV exposure.

The study highlights how luminescence parameters change during transport pathways from source to sink. Luminescence signals like BSLS and 110 °C TLS follow similar trends under natural factors, while other components behave uniquely, potentially recording distinct conditions they face. Any extreme thermal event can make a significant change compared to irradiation and sunlight exposure.

Exploring luminescence variations in quartz and their relation to structural defects

This study explores the factors influencing the luminescence sensitivity of quartz crystals, focusing on the effects of annealing, water diffusion, and structural changes. The key findings are summarised below:

High-temperature annealing at 220 °C, 400 °C, and 550 °C enhances the 110 °C TLS and BSLS signals, while temperatures above 700 °C–900 °C led to a decrease in sensitivity beyond natural levels. This decline is attributed to structural changes during the alpha-to-beta quartz phase transition at 573 °C. Sensitivity partially recovers after repeated heating at 450 °C, but not for samples annealed at 900 °C, indicating permanent lattice damage.

In high-temperature annealing, the quartz at 220 °C, 400 °C, and 550 °C enhances 110 °C TLS and BSLS, but sensitivity decreases beyond natural levels at 700 °C–900 °C due to structural changes during the alpha-to-beta quartz phase transition at 573 °C. Sensitivity partially recovers after repeated heating at 450 °C but not for samples annealed at 900 °C, indicating permanent lattice damage. These findings highlight the role of structural rearrangements in luminescence behaviour. Normal cooling and water quenching exhibit only minor differences up to 550 °C, though the underlying reason remains unclear. Conducting high-pressure and high-temperature (HPHT) experiments could provide better insights into this phenomenon.

Thermogravimetric Analysis (TGA) revealed noticeable mass loss in dull and medium quartz samples, while bright quartz exhibited minimal mass loss. This suggests that structural water-related defects, such as silanol groups, may be converted to water vapour during heating (Bambauer et al., 1969). The DSC analysis reveals three distinct thermal regions: up to 200 °C, 200–420 °C, and beyond 600 °C, which may reflect chemical reactions or phase changes in the samples. These thermal regions align with the luminescence changes observed during heating, highlighting the critical role of structural changes in determining sensitivity.

In the FTIR analysis, it is observed that dull quartz exhibits significantly higher absorbance in the O-H vibrational range, whereas bright quartz shows comparatively lower absorbance. These results are consistent with the findings of S. K. Sharma et al. (2017) and suggest the potential role of O-H groups acting as luminescence quenchers. This observation is further supported by TGA results, which indicate a mass loss likely corresponding to the release of water associated with these O-H groups. The crystallinity index study reveals dull quartz has higher crystallinity and lower luminescence, while bright quartz shows the opposite. This suggests either transportation-induced amorphisation or increased impurities reduce crystallinity and enhance luminescence.

Understanding these factors provides valuable insights into the mechanisms underlying luminescence behaviour, with implications for luminescence changes in natural environments and the processes driving these variations. Overall, the chapter provides insights into the interplay of thermal processes, water content, and crystal structure in determining quartz's luminescence behaviour.

Luminescence: a proxy for earth surface studies

As discussed in Chapter 3, natural factors influence the luminescence of quartz, particularly the 110 °C TLS and BSLS signals. These variations are linked to structural defects explored in Chapter 4. Building on this understanding, this chapter applies these insights to natural systems, focusing on the key aspects below:

Sediment budgeting at river confluence:

Sediment budgeting at confluences was achieved using multiple luminescence parameter measurements (205 °C TL, annealed 90 °C TL, annealed 135 °C TL, and BSLS). For artificially mixed samples, the measured contributions closely matched applied proportions, validating the approach for natural systems. At the Nubra-Shyok confluence, present-day contributions from the Nubra River were estimated at 19% to 24%. In the Beas River system, a tributary contributed 24% to 36% of sediment load. A three-body mixing model effectively quantified additional hill slope contributions in the Wakal River system, with unknown luminescence parameters indicating a maximum input of approximately 54%.

Variation of luminescence along the river:

The study also focuses on the Sabarmati River, with its seasonal flow and semi-arid setting, and part of the Yamuna River, offering insights into fluvial sediment transport across a broad floodplain, assessing the impact of transport distance and exploring the effect of aeolian input in semi-arid rivers in the luminescence properties of quartz. These results of the Sabarmati River showed a broad co-variation between 110 °C TLS and BSLS. Rock samples exhibit 110 °C TLS values ranging from 1.6 to 6.2 units, weathered rock samples range from 5.9 to 15.6 units, and sediment samples show significantly higher 110 °C TLS values ranging from 66 to 325 units. OSL analysis suggests a 3.8-fold sensitisation over the 18 Gy equivalent dose difference, implying the effect of pedoturbation on quartz's luminescence sensitivity. Recycling experiments involving dose and bleaching cycles suggest that sediment 110 °C TLS evolved from rock 110 °C TLS over a timescale of more than a million years. The analysis concludes that transport distance alone does not influence luminescence sensitivity (110 °C TLS and BSLS) in the Sabarmati River. Instead, aeolian input, hillslope contributions, and confluence effects significantly impact luminescence sensitivity.

In case of Yamuna River along the floodplain shows no increasing trend in luminescence sensitivity across a transport distance of 200 km, likely due to the rapid transport of quartz grains in this system.

Quartz luminescence and its grain shape

Although initial hypotheses suggested that sphericity and roundness could influence luminescence sensitivity, no clear trends were observed, implying that intrinsic mineral properties may be more significant. Overall, luminescence sensitivity proves to be a valuable tool for provenance studies, provided that interpretations consider environmental and geological complexities, offering a solid foundation for future research in dynamic sedimentary systems.

6.2 Future outlook

1. Multispectral analysis of the effects of natural factors on quartz luminescence

Chapter 3 of this thesis primarily focused on the U-340 window. However, the luminescence spectrum depends on the type of luminescence centres present in quartz. To gain a comprehensive understanding of how natural factors—such as thermal treatments, bleaching, and irradiation—affect luminescence, future work will need to use different spectral windows. These will probe distinct luminescence centres and enhance our understanding of the various processes involved.

2. Effect of pedogenesis on quartz luminescence for different type of rocks

There is a significant gap in luminescence sensitivity between quartz in rock and in river sediments, with weathering of rocks serving as an intermediate stage. For instance, in a weathered phyllite rock and the soil formed on it (Chapter 5), both 110 °C TLS and BSLS values were observed to increase. While all rocks initially exhibit similar 110 °C TLS values, their subsequent sensitisation may differ under natural conditions. Future studies will need to investigate how different rock types and their weathering processes affect quartz luminescence. This will be crucial for applying luminescence as a tool in sediment transport and budgeting studies.

3. HPHT experiments for controlled diffusion of defects in quartz

Since defects in the crystal structure are the key element influencing quartz luminescence, future work will involve conducting HPHT experiments to control the diffusion of these defects. This will be crucial for gaining a fundamental understanding of luminescence changes and represents an important direction for future research.

4. Combining ESR with luminescence

Electron Spin Resonance (ESR) serves as a powerful tool to identify paramagnetic defects in quartz. Future studies should integrate ESR with luminescence measurements to provide deeper insights into the defects present within the lattice, offering promising prospects for understanding luminescence behaviour.

5. Quartz single-grain luminescence studies

Quartz aliquot measurements average signals from approximately 2,000 grains, yet fewer than 10% (Jacobs et al., 2003) typically contribute measurable luminescence. The reasons for this variability are not well characterised. Future work will involve investigating single-grain luminescence to provide a more detailed and comprehensive understanding of its applications in provenance studies. Single-grain optically stimulated luminescence (OSL) analysis will offer enhanced resolution for sediment provenance studies, particularly in systems with significant grain-to-grain variability in luminescence sensitivity. Unlike multi-grain analyses, which can mask subtle variability (Dave et al., 2024), the single-grain approach will help resolve sensitisation effects, metamorphic histories, and sediment transport pathways.

Bibliography

Agbeshie, A. A., Abugre, S., Atta-Darkwa, T., & Awuah, R. (2022). A review of the effects of forest fire on soil properties. Journal of Forestry Research, 33(5), 1419–1441. https://doi.org/10.1007/s11676-022-01475-4

Aitken, M. J. (1985). Thermoluminescence Dating. Academic Press.

Allchin, B., & Goudie, A. (1971). Dunes, Aridity and Early Man in Gujarat, western India. Man, 6(2), 248. https://doi.org/10.2307/2798265

Allchin, B., Goudie, A. S., & Hegde, K. (1978). The prehistory and palaeogeography of the Great Indian Desert. Academic Press.

Bailey, R.M., Smith, B.W., & Rhodes, E.J. (1997). Partial bleaching and the decay form characteristics of quartz OSL. Radiation Measurements, 27(2), 123–136. https://doi.org/10.1016/s1350-4487(96)00157-6

Bambauer, H. U., Brunner, G. O., & Laves, F. (1969). Light scattering of heat-treated quartz in relation to hydrogen-containing defects. American Mineralogist, 54, 718–724.

Bartyik, T., Magyar, G., Filyó, D., Tóth, O., Blanka-Végi, V., Kiss, T., Marković, S., Persoiu, I., Gavrilov, M., Mezősi, G., Sipos, G. (2021). Spatial differences in the luminescence sensitivity of quartz extracted from Carpathian Basin fluvial sediments. Quaternary Geochronology 64. https://doi.org/10.1016/j.quageo.2021.101166

Basu, A. R., Sharma, M., & DeCelles, P. G. (1990). Nd, Sr-isotopic provenance and trace element geochemistry of Amazonian foreland basin fluvial sands, Bolivia and Peru: implications for ensialic Andean orogeny. Earth and Planetary Science Letters, 100(1–3), 1–17. https://doi.org/10.1016/0012-821x(90)90172-t

Bateman, M. D., Frederick, C. D., Jaiswal, M. K., & Singhvi, A. K. (2003). Investigations into the potential effects of pedoturbation on luminescence dating. Quaternary Science Reviews, 22(10–13), 1169–1176. https://doi.org/10.1016/S0277-3791(03)00019-2

Bernard, T., & Sinclair, H. D. (2022). Accelerated sediment delivery to continental margins during post-orogenic rebound of mountain ranges. Basin Research, 35(2), 642–661. https://doi.org/10.1111/bre.12727

Bock, B., Bahlburg, H., Wörner, G., & Zimmermann, U. (2000). Tracing Crustal Evolution in the Southern Central Andes from Late Precambrian to Permian with Geochemical and Nd and Pb Isotope Data. The Journal of Geology, 108(5), 515–535. https://doi.org/10.1086/314422

Bohm, J. (1995). Realstruktur von Kristallen. E. Schweizerbart'sche Verlagsbuchhandlung.

Bulur, E. (1996). An alternative technique for optically stimulated luminescence (OSL) experiment. Radiation Measurements, 26(5), 701–709. https://doi.org/10.1016/s1350-4487(97)82884-3

Bøtter-Jensen, L. (1997). Luminescence techniques: instrumentation and methods. Radiation Measurements, 27(5–6), 749–768. https://doi.org/10.1016/s1350-4487(97)00206-0

Bøtter-Jensen, L., McKeever, S., & Wintle, A. (2003). Optically stimulated luminescence dosimetry. Elsevier.

Cao, Z., Jiang, Y., Xu, J., Zhao, J., & Zhao, C. (2022). Luminescence sensitivity of quartz from rocks under in situ chemical weathering conditions. Frontiers in Earth Science, 10. https://doi.org/10.3389/feart.2022.940212

Chandel, H. N., Patel, A. D., Vaghela, H. R., & Ubale, G. P. (2006). An effective and reusable sampling pipe for luminescence dating. Ancient TL, 24(1), 21–22.

Chauhan, N. (2013). Luminescence Dating: Basic Approach to Geochronology. Defect and Diffusion Forum/Diffusion and Defect Data, Solid State Data. Part a, Defect and Diffusion Forum, 347, 111–137. https://doi.org/10.4028/www.scientific.net/ddf.347.111

Chauhan, N., & Singhvi, A. (2019). Changes in the optically stimulated luminescence (OSL) sensitivity of single grains of quartz during the measurement of natural OSL: Implications for the reliability of optical ages. Quaternary Geochronology, 53, 101004. https://doi.org/10.1016/j.quageo.2019.101004

Chicco, J. M., Mandrone, G., & Vacha, D. (2023). Effects of wildfire on soils: Field studies and modelling on induced underground temperature variations. Frontiers in Earth Science, 11. https://doi.org/10.3389/feart.2023.1307569

Choi, J. H., Duller, G. A. T., & Wintle, A. G. (2006). Analysis of quartz LM-OSL curves. Ancient TL, 24(1), 9–20. https://doi.org/10.26034/la.atl.2006.390

Correcher, V., Garcia-Guinea, J., Bustillo, M. A., & Garcia, R. (2009). Study of the thermoluminescence emission of a natural α-cristobalite†. Radiation Effects and Defects in Solids, 164(1), 59–67. https://doi.org/10.1080/10420150802270995

Dasgupta, S., Narula, P. L., Acharyya, S. K., & Banerjee, J. (2000). Seismotectonic atlas of India and its environs. In Geological Survey of India eBooks. http://ci.nii.ac.jp/ncid/BA77799673.

Del Río, I., Sawakuchi, A. O., Góes, A. M., Hollanda, M. H. B. M., Furukawa, L. Y., Porat, N., Jain, M., Mineli, T. D., & De Assis Negri, F. (2021). Luminescence signals of quartz and feldspar as new methods for stratigraphic discrimination and provenance analysis of siliciclastic successions: The case of the Parnaíba Basin (Brazil) of West Gondwana. Basin Research, 33(6), 2938–2959. https://doi.org/10.1111/bre.12590

Dey, S., Chauhan, N., Mahala, M. K., Chakravarti, P., Vashistha, A., Jain, V., & Ray, J. S. (2022). Dominant role of deglaciation in Late Pleistocene–Early Holocene sediment aggradation in the Upper Chenab valley, NW Himalaya. Quaternary Research, 113, 122–133. https://doi.org/10.1017/qua.2022.57

DTU Nutech. (2016). Guide to "The Risø Single Grain Laser OSL system". Technical University of Denmark, Roskilde.

DTU Physics. (2021). Guide to the Risø TL/OSL reader. Technical University of Denmark.

Duan, Z., Li, C., Guo, Y., Ng, N. C. W., Yang, S., Bui, V. V., Nguyen, D. V., Duan, X., Yin, P., Tran, T. T. T., Le, D. N., Nguyen, T. H. H., & Dang, H. N. (2023). Sr-Nd isotopic fingerprints of Red River sediments and its implication for provenance discrimination in the South China Sea. Marine Geology, 457, 106997. https://doi.org/10.1016/j.margeo.2023.106997

Duller, G. A. T. (2014). Luminescence dating. In Springer eBooks (pp. 1–21). https://doi.org/10.1007/978-94-007-6326-5_125-1

Dunkl, I., Di Giulio, A., & Kuhlemann, J. (2001). Combination of Single-Grain Fission-Track chronology and morphological analysis of detrital zircon crystals in provenance studies: Sources of the Macigno Formation (Apennines, Italy). Journal of Sedimentary Research, 71(4), 516–525. https://doi.org/10.1306/102900710516

Fareeduddin, N., Pant, N., Gupta, S., Chakraborty, P., Sensarma, S., Jain, A., Prasad, G., Srivastava, P., Rajan, S., & Tiwari, V. M. (2020). The geodynamic evolution of the Indian Subcontinent- an introduction. Episodes, 43(1), 7–18. https://doi.org/10.18814/epiiugs/2020/020001

Fasoli, M., & Martini, M. (2016). The composite nature of the thermoluminescence UV emission of quartz. Journal of Luminescence, 173, 120–126. https://doi.org/10.1016/j.jlumin.2015.12.049

Feigl, F. J., Fowler, W., & Yip, K. L. (1974). Oxygen vacancy model for the E1′ center in SiO2. Solid State Communications, 14(3), 225–229. https://doi.org/10.1016/0038-1098(74)90840-0

Fitzsimmons, K. (2011). An assessment of the luminescence sensitivity of Australian quartz with respect to sediment history. Geochronometria, 38(3), 199–208. https://doi.org/10.2478/s13386-011-0030-9

Fleming, S. J. (1979). Thermoluminescence techniques in archaeology. Clarendon Press, London.

Fowler, W. B., Rudra, J. K., Edwards, A. H., & Feigl, F. J. (1988). Theory of Oxygen-Vacancy defects in silicon dioxide. In Springer eBooks (pp. 107–112). https://doi.org/10.1007/978-1-4613-1031-0_12

Franklin, A. (1997). On the interaction between the rapidly and slowly bleaching peaks in the TL glow curves of quartz. Journal of Luminescence, 75(1), 71–76. https://doi.org/10.1016/s0022-2313(97)00099-9

Franklin, A., Prescott, J., & Scholefield, R. (1995). The mechanism of thermoluminescence in an Australian sedimentary quartz. Journal of Luminescence, 63(5–6), 317–326. https://doi.org/10.1016/0022-2313(94)00068-n

Furetta, C. (2003). Handbook of Thermoluminescence. https://doi.org/10.1142/5167

Gadsden, J. A. (1975). Infrared spectra of minerals and related inorganic compounds. https://ci.nii.ac.jp/ncid/BA07281841

Garver, J. I., Royce, P. R., & Smick, T. A. (1996). Chromium and Nickel in Shale of the Taconic Foreland: A Case Study for the Provenance of Fine-Grained Sediments with an Ultramafic Source. Journal of Sedimentary Research, Vol. 66. https://doi.org/10.1306/d42682c5-2b26-11d7-8648000102c1865d

Gaweł, B. A., Ulvensøen, A., Łukaszuk, K., Muggerud, A. M. F., & Erbe, A. (2021). In situ high temperature spectroscopic study of liquid inclusions and hydroxyl groups in high purity natural quartz. Minerals Engineering, 174, 107238. https://doi.org/10.1016/j.mineng.2021.107238

Gibling, M. R., & Tandon, S. K. (1997). Erosional marks on consolidated banks and slump blocks in the Rupen River, north-west India. Sedimentology, 44(2), 339–348. https://doi.org/10.1111/j.1365-3091.1997.tb01528.x

Goldstein, S., O'Nions, R., & Hamilton, P. (1984). A Sm-Nd isotopic study of atmospheric dusts and particulates from major river systems. Earth and Planetary Science Letters, 70(2), 221–236. https://doi.org/10.1016/0012-821x(84)90007-4

Gong, Z., Sun, J., Lü, T., & Tian, Z. (2014). Investigating the optically stimulated luminescence dose saturation behavior for quartz grains from dune sands in China. Quaternary Geochronology, 22, 137–143. https://doi.org/10.1016/j.quageo.2014.01.003

Gong, Z., Sun, J., & Lü, T. (2015). Investigating the components of the optically stimulated luminescence signals of quartz grains from sand dunes in China. Quaternary Geochronology, 29, 48–57. https://doi.org/10.1016/j.quageo.2015.06.004

Goswami, K., Panda, S. K., Alappat, L., & Chauhan, N. (2023). Luminescence for sedimentary provenance quantification in river basins: A methodological advancement. Quaternary Geochronology, 79, 101488. https://doi.org/10.1016/j.quageo.2023.101488

Götte, T., & Ramseyer, K. (2012). Trace element characteristics, luminescence properties and real structure of quartz. In Springer geology (pp. 265–285). https://doi.org/10.1007/978-3-642-22161-3_12

Götze, J., & Zimmerle, W. (2000). Quartz and silica as guide to provenance in sediments and - sedimentary rocks. In Schweizerbart eBooks. http://ci.nii.ac.jp/ncid/BA56545280

Götze, J., Pan, Y., & Müller, A. (2021). Mineralogy and mineral chemistry of quartz: A review. Mineralogical Magazine, 85(5), 639–664. https://doi.org/10.1180/mgm.2021.72

Götze, J., Plötze, M., & Habermann, D. (2001). Origin, spectral characteristics and practical applications of the cathodoluminescence (CL) of quartz - a review. Mineralogy and Petrology, 71(3–4), 225–250. https://doi.org/10.1007/s007100170040

Götze, J. (2009). Chemistry, textures and physical properties of quartz — geological interpretation and technical application. Mineralogical Magazine, 73(4), 645–671. https://doi.org/10.1180/minmag.2009.073.4.645

Gray, H. J., Jain, M., Sawakuchi, A. O., Mahan, S. A., & Tucker, G. E. (2019). Luminescence as a sediment tracer and provenance tool. Reviews of Geophysics, 57(3), 987–1017. https://doi.org/10.1029/2019rg000646

Güler, E., Uğur, G., Uğur, Ş., & Güler, M. (2020). A theoretical study for the band gap energies of the most common silica polymorphs. Chinese Journal of Physics, 65, 472–480. https://doi.org/10.1016/j.cjph.2020.03.014

Guralnik, B., Ankjærgaard, C., Jain, M., Murray, A., Müller, A., Wälle, M., Lowick, S., Preusser, F., Rhodes, E., Wu, T., Mathew, G., & Herman, F. (2015). OSL-thermochronometry using bedrock quartz: A note of caution. Quaternary Geochronology, 25, 37–48. https://doi.org/10.1016/j.quageo.2014.09.001

Han, Z., Li, S., & Tso, M. W. (2000). Effects of annealing on TL sensitivity of granitic quartz. Radiation Measurements, 32(3), 227–231. https://doi.org/10.1016/s1350-4487(99)00270-x

Hashimoto, T., Hayashi, Y., Koyanagi, A., Yokosaka, K., & Kimura, K. (1986a). Red and blue colouration of thermoluminescence from natural quartz sands. International Journal of Radiation Applications and Instrumentation Part D Nuclear Tracks and Radiation Measurements, 11(4–5), 229–235. https://doi.org/10.1016/1359-0189(86)90039-7

Hashimoto, T., Koyanagi, A., Yokosaka, K., Hayashi, Y., & Sotobayashi, T. (1986b). Thermoluminescence color images from quartzs of beach sands. GEOCHEMICAL JOURNAL, 20(3), 111–118. https://doi.org/10.2343/geochemj.20.111

Hashimoto, T., Yokosaka, K., Habuki, H., & Hayashi, Y. (1989). Provenance search of dune sands using thermoluminescence colour images (TLCIs) from quartz grains. International Journal of Radiation Applications and Instrumentation Part D Nuclear Tracks and Radiation Measurements, 16(1), 3–10. https://doi.org/10.1016/1359-0189(89)90003-4

Hlavay, J., Jonas, K., Elek, S., & Inczedy, J. (1978). Characterisation of the particle size and the crystallinity of certain minerals by IR spectrophotometry and other instrumental methods—II. Investigations on quartz and feldspar. Clays and Clay Minerals, 26(2), 139–143. https://doi.org/10.1346/ccmn.1978.0260209

Hou, C., Jin, J., Ling, Z., Wei, J., & Xu, D. (2023). Spatio-temporal variation in quartz luminescence sensitivity in the coastal area of China. CATENA, 234, 107585. https://doi.org/10.1016/j.catena.2023.107585

Hou, C., Jin, J., Ma, M., Liu, G., Ling, Z., Wei, J., & Xu, D. (2025). Temporal variation of luminescence sensitivity and environmental changes during the mid–late Holocene recorded in estuarine coastal deposits from South China. CATENA, 255, 109022. https://doi.org/10.1016/j.catena.2025.109022

Hubert, N. J. F. (1962). A Zircon-Tourmaline-Rutile Maturity Index and the Interdependence of the Composition of Heavy Mineral Assemblages with the Gross Composition and Texture of Sandstones. Journal of Sedimentary Research, Vol. 32. https://doi.org/10.1306/74d70ce5-2b21-11d7-8648000102c1865d

Hunter, P., Spooner, N., & Smith, B. (2018). Thermoluminescence emission from quartz at 480 nm as a high-dose radiation marker. Radiation Measurements, 120, 143–147. https://doi.org/10.1016/j.radmeas.2018.04.001

Huntley, D. J., Godfrey-Smith, D. I., & Thewalt, M. L. W. (1985). Optical dating of sediments. Nature, 313(5998), 105–107. https://doi.org/10.1038/313105a0

Hütt, G., Jaek, I., & Tchonka, J. (1988). Optical dating: K-feldspars optical response stimulation spectra. Quaternary Science Reviews, 7(3–4), 381–385. https://doi.org/10.1016/0277-3791(88)90033-9

Ichikawa, Y. (1965). Dating of ancient ceramics by thermoluminescence. Bulletin of the Institute of Chemical Research, Kyoto University, 43, 1–6.

Jain, M., Murray, A., & Bøtter-Jensen, L. (2003). Characterisation of blue-light stimulated luminescence components in different quartz samples: implications for dose measurement. Radiation Measurements, 37(4–5), 441–449. https://doi.org/10.1016/s1350-4487(03)00052-0

Jain, S. K., Nayak, P. C., Singh, Y., & Chandniha, S. K. (2017). Trends in rainfall and peak flows for some river basins in India. Current Science, 112(8), 1712–1726. https://doi.org/10.18520/cs/v112/i08/1712-1726

Jain, V., Wasson, R., McCulloch, M., Kaushal, R. K., & Singhvi, A. K. (2022). Controls on sediment provenance in the Baghmati river catchment, Central Himalaya, India. Journal of Earth System Science, 131(1). https://doi.org/10.1007/s12040-021-01759-z

Jeong, G. Y., & Choi, J. (2012). Variations in quartz OSL components with lithology, weathering and transportation. Quaternary Geochronology, 10, 320–326. https://doi.org/10.1016/j.quageo.2012.02.023

Judd, E. J., Tierney, J. E., Lunt, D. J., Montañez, I. P., Huber, B. T., Wing, S. L., & Valdes, P. J. (2024). A 485-million-year history of Earth's surface temperature. Science, 385(6715). https://doi.org/10.1126/science.adk3705

Jung, R., Mommsen, H., & Pacciarelli, M. (2015b). From west to west: Determining production regions of Mycenaean pottery of Punta di Zambrone (Calabria, Italy). Journal of Archaeological Science Reports, 3, 455–463.

Jung, R., Mommsen, H., & Pacciarelli, M. (2015b). From west to west: Determining production regions of Mycenaean pottery of Punta di Zambrone (Calabria, Italy). Journal of Archaeological Science Reports, 3, 455–463. https://doi.org/10.1016/j.jasrep.2015.07.004

Juyal, N., Chamyal, L.S., Bhandari, S., Bhushan, R., Singhvi, A.K. (2006). Continental record of the southwest monsoon during the last 130 ka: evidence from the southern margin of the Thar Desert, India. Quaternary Science Reviews 25, 2632–2650. https://doi.org/10.1016/j.quascirev.2005.07.020

Juyal, N., Kar, A., Rajaguru, S.N., & Singhvi, A. K. (2003). Luminescence chronology of aeolian deposition during the Late Quaternary on the southern margin of Thar Desert, India. Quaternary International, 104(1), 87–98. https://doi.org/10.1016/s1040-6182(02)00137-4

Kirsh, Y. (1992). Kinetic analysis of thermoluminescence. Physica Status Solidi (A), 129(1), 15–48. https://doi.org/10.1002/pssa.2211290102

Kitis, G., Gomez-Ros, J. M., & Tuyn, J. W. N. (1998). Thermoluminescence glow-curve deconvolution functions for first, second and general orders of kinetics. Journal of Physics D Applied Physics, 31(19), 2636–2641. https://doi.org/10.1088/0022-3727/31/19/037

Kitis, G., & Pagonis, V. (2008). Computerised curve deconvolution analysis for LM-OSL. Radiation Measurements, 43(2–6), 737–741. https://doi.org/10.1016/j.radmeas.2007.12.055

Krbetschek, M.R., Götze, J., Dietrich, A., Trautmann, T. (1997). Spectral information from minerals relevant for luminescence dating. Radiation Measurements 27, 695–748. https://doi.org/10.1016/S1350-4487(97)00223-0

Kreutzer, S. (2024). fit_LMCurve(): Nonlinear least squares fit for LM-OSL curves (Version 0.3.4). In S. Kreutzer, C. Burow, M. Dietze, M. C. Fuchs, C. Schmidt, M. Fischer, J. Friedrich, N. Mercier, A. Philippe, S. Riedesel, M. Autzen, D. Mittelstrass, H. J. Gray, J. Galharret, & M. Colombo (Eds.), Luminescence: Comprehensive luminescence dating data analysis (R package version 0.9.26).

Kreutzer, S., (2023). fit_CWCurve(): Non-linear Least Squares Fit for CW-OSL curves -beta version-. Function version 0.5.2. In: Kreutzer, S., Burow, C., Dietze, M., Fuchs, M.C., Schmidt, C., Fischer, M., Friedrich, J., Mercier, N., Philippe, A., Riedesel, S., Autzen, M., Mittelstrass, D., Gray, H.J., Galharret, J., 2023. Luminescence: Comprehensive Luminescence Dating Data Analysis. R package version 0.9.21. https://CRAN.R-project.org/package=Luminescence

Kreutzer, S., (2023). fit_CWCurve(): Non-linear Least Squares Fit for CW-OSL curves -beta version-. Function version 0.5.2. In: Kreutzer, S., Burow, C., Dietze, M., Fuchs, M.C., Schmidt, C., Fischer, M., Friedrich, J., Mercier, N., Philippe, A., Riedesel, S., Autzen, M., Mittelstrass, D., Gray, H.J., Galharret, J., 2023. Luminescence: Comprehensive Luminescence Dating Data Analysis. R package version 0.9.21.

Kuenzer, C., Zhang, J., Jing, L., Huadong, G., & Dech, S. (2013). Thermal infrared remote sensing of surface and underground coal fires. In Remote sensing and digital image processing (pp. 429–451). https://doi.org/10.1007/978-94-007-6639-6_21

Kuhn, R., Trautmann, T., Singhvi, A., Krbetschek, Wagner, G., & Stolz, W. (2000). A study of thermoluminescence emission spectra and optical stimulation spectra of quartz from different provenances. Radiation Measurements, 32(5–6), 653–657. https://doi.org/10.1016/s1350-4487(00)00090-1

Kuhns, C., Larsen, N. A., & McKeever, S. (2000). Characteristics of LM-OSL from several different types of quartz. Radiation Measurements, 32(5–6), 413–418. https://doi.org/10.1016/s1350-4487(00)00065-2

Lave, C. A. (1970). The demand for urban mass transportation. The Review of Economics and Statistics, 52(3), 320. https://doi.org/10.2307/1926301

Levy, P. W. (1974). Physical principles of thermoluminescence and recent developments in its measurement.

Li, S., & Wintle, A. (1992). Luminescence sensitivity change due to bleaching of sediments. International Journal of Radiation Applications and Instrumentation Part D Nuclear Tracks and Radiation Measurements, 20(4), 567–573. https://doi.org/10.1016/1359-0189(92)90006-h

Li, S. (2002). Luminescence sensitivity changes of quartz by bleaching, annealing and UV exposure. Radiation Effects and Defects in Solids, 157(3), 357–364. https://doi.org/10.1080/10420150212998

Liu, L., Yang, S., Liu, X., Li, P., Wang, H., & Zhou, J. (2022). Variation of luminescence sensitivity of quartz grains from loess in eastern Tibetan Plateau and its provenance significance. Frontiers in Earth Science, 10. https://doi.org/10.3389/feart.2022.939638

Lü, T., Sun, J. (2011). Luminescence sensitivities of quartz grains from eolian deposits in northern China and their implications for provenance. Quaternary Research 76, 181–189. https://doi.org/10.1016/j.yqres.2011.06.015

Marfunin, A. S. (1979). Spectroscopy, luminescence and radiation centers in Minerals. In Springer eBooks. https://doi.org/10.1007/978-3-642-67112-8

Mateus, F. D. C., Asfora, V. K., Guzzo, P. L., & Barros, V. S. (2020). Investigation of the spectrally resolved TL signals of natural quartz single crystals sensitised by high-dose gamma radiation and moderate heat treatments. Nuclear Instruments and Methods in Physics Research Section B: Beam Interactions With Materials and Atoms, 486, 37–47. https://doi.org/10.1016/j.nimb.2020.11.001

McKeever, S. W. S. (1985). Thermoluminescence of solids. https://doi.org/10.1017/cbo9780511564994

Merh, S. S., & Chamyal, L. (1997). The Quaternary geology of Gujarat alluvial plains. Proceedings of the Indian National Science Academy, 63, 1–98.

Mikhailik, V.B., Di Stefano, P.C.F., Henry, S., Kraus, H., Lynch, A., Tsybulskyi, V., Verdier, M.A. (2011). Studies of concentration dependences in the luminescence of Ti-doped Al2O3. Journal of Applied Physics 109. https://doi.org/10.1063/1.3552943

Mineli, T.D., Sawakuchi, A.O., Guralnik, B., Lambert, R., Jain, M., Pupim, F.N., Rio, I. del, Guedes, C.C.F., Nogueira, L. (2021). Variation of luminescence sensitivity, characteristic dose and trap parameters of quartz from rocks and sediments. Radiation Measurements 144, 106583. https://doi.org/10.1016/j.radmeas.2021.106583

Mo, P. (2020). Internal rolling method for particle shape evaluation and reconstruction. PLoS ONE, 15(11), e0242162. https://doi.org/10.1371/journal.pone.0242162

Moayed, N. K., Fattahi, M., Autzen, M., Haghshenas, E., Tajik, V., Shoaie, Z., Bailey, M., Sohbati, R., & Murray, A. (2023). The sensitisation of quartz extracted from andesite. Radiation Measurements, 170, 107048. https://doi.org/10.1016/j.radmeas.2023.107048

Morton, A.C. (1985). Heavy Minerals in Provenance Studies in Zuffa, G.G. ed., provenance of arenites. D. Reidel publishing Company 148, 249–277.

Morton, A., Mundy, D., & Bingham, G. (2012). High-frequency fluctuations in heavy mineral assemblages from Upper Jurassic sandstones of the Piper Formation, UK North Sea: Relationships with sea-level change and floodplain residence. In Geological Society of America eBooks. https://doi.org/10.1130/2012.2487(10

Moska, P., & Murray, A. (2006). Stability of the quartz fast-component in insensitive samples. Radiation Measurements, 41(7–8), 878–885. https://doi.org/10.1016/j.radmeas.2006.06.005

Murray, A., & Wintle, A. (2000). Luminescence dating of quartz using an improved single-aliquot regenerative-dose protocol. Radiation Measurements, 32(1), 57–73. https://doi.org/10.1016/S1350-4487(99)00253-X

Nascimento, D.R.D., Sawakuchi, A.O., Guedes, C.C.F., Giannini, P.C.F., Grohmann, C.H., Ferreira, M.P. (2015). Provenance of sands from the confluence of the Amazon and Madeira rivers based on detrital heavy minerals and luminescence of quartz and feldspar. Sedimentary Geology 316, 1–12. https://doi.org/10.1016/j.sedgeo.2014.11.002

Nian, X., Zhang, W., Qiu, F., Qin, J., Wang, Z., Sun, Q., Chen, J., Chen, Z., Liu, N. (2018). Luminescence characteristics of quartz from Holocene delta deposits of the Yangtze River and their provenance implications. Quaternary Geochronology 49, 131–137. https://doi.org/10.1016/j.quageo.2018.04.010

Niu, B., Liu, B., Zhang, X., Liu, F., Zhou, Q., Chen, Q., Qu, J., & Liu, B. (2022). Evaluation of five different sediment fingerprinting approaches for estimating sediment source contributions in an arid region. Geoderma, 427, 116131. https://doi.org/10.1016/j.geoderma.2022.116131

NOAA’s National Weather Service. (n.d.). How hot is lightning? https://www.weather.gov/safety/lightning-temperature

Odom, A. L., & Rink, W. J. (1989). Natural accumulation of Schottky–Frenkel defects: Implications for a quartz geochronometer. Geology, 17(1), 55. https://doi.org/10.1130/0091-7613(1988)017

Papanicolaou, A. N., Elhakeem, M., Krallis, G., Prakash, S., & Edinger, J. (2007). Sediment Transport Modeling Review—Current and Future Developments. Journal of Hydraulic Engineering, 134(1), 1–14. https://doi.org/10.1061/(asce)0733-9429(2008)134:1(1

Parida, S., Kaushal, R., Chauhan, N., & Singhvi, A. (2025). Changes in thermoluminescence sensitivity of 110°C glow peak of quartz grains from sediments of River Ganga: Observation and implications. Earth and Planetary Science Letters, 656, 119267. https://doi.org/10.1016/j.epsl.2025.119267

Paterson, M. S. (1986). The thermodynamics of water in quartz. Physics and Chemistry of Minerals, 13(4), 245–255. https://doi.org/10.1007/bf00308276

Patro, B. C., & Sahu, B. K. (1974). Factor analysis of sphericity and roundness data of clastic quartz grains: Environmental significance. Sedimentary Geology, 11(1), 59–78. https://doi.org/10.1016/0037-0738(74)90005-0

Peng, J., Dong, Z., & Han, F. (2016). tgcd: An R package for analysing thermoluminescence glow curves. SoftwareX, 5, 112–120. https://doi.org/10.1016/j.softx.2016.06.001

Pietsch, T.J., Olley, J.M., Nanson, G.C. (2008). Fluvial transport as a natural luminescence sensitiser of quartz. Quaternary Geochronology 3, 365–376. https://doi.org/10.1016/j.quageo.2007.12.005

Pinkerton, H., James, M., & Jones, A. (2002). Surface temperature measurements of active lava flows on Kilauea volcano, Hawai′i. Journal of Volcanology and Geothermal Research, 113(1–2), 159–176. https://doi.org/10.1016/s0377-0273(01)00257-8

Poolton, N. R. J., Smith, G. M., Riedi, P. C., Bulur, E., Bøtter-Jensen, L., Murray, A. S., & Adrian, M. (2000). Luminescence sensitivity changes in natural quartz induced by high-temperature annealing: A high frequency EPR and OSL study. Journal of Physics D Applied Physics, 33(8), 1007–1017. https://doi.org/10.1088/0022-3727/33/8/318

Porat, N. (2006). Use of magnetic separation for purifying quartz for luminescence dating. Ancient TL, 24(2): 33–36.

Prescott, J., & Hutton, J. (1988). Cosmic ray and gamma ray dosimetry for TL and ESR. International Journal of Radiation Applications and Instrumentation Part D: Nuclear Tracks and Radiation Measurements, 14(1–2), 223–227. https://doi.org/10.1016/1359-0189(88)90069-6

Preusser, F., Chithambo, M. L., Götte, T., Martini, M., Ramseyer, K., Sendezera, E. J., Susino, G. J., & Wintle, A. G. (2009). Quartz as a natural luminescence dosimeter. Earth-Science Reviews, 97(1–4), 184–214. https://doi.org/10.1016/j.earscirev.2009.09.006

Ramasamy, V., & Suresh, G. (2009). Mineral characterisation and crystalline nature of quartz in Ponnaiyar River sediments, Tamilnadu, India. American-Eurasian Journal of Sustainable Agriculture, 4(2), 103–107. https://www.idosi.org/aejsr/4(2)09/11.pdf

Randall, J. T., & Wilkins, M. H. F. (1945). Phosphorescence and electron traps II. The interpretation of long-period phosphorescence. Proceedings of the Royal Society of London a Mathematical and Physical Sciences, 184(999), 390–407. https://doi.org/10.1098/rspa.1945.0025

Rastogi, N., & Sarin, M. (2005). Chemical characteristics of individual rain events from a semi-arid region in India: Three-year study. Atmospheric Environment, 39(18), 3313–3323. https://doi.org/10.1016/j.atmosenv.2005.01.053

Razva, O., Anufrienkova, A., Korovkin, M., Ananieva, L., & Abramova, R. (2014). Calculation of quartzite crystallinity index by infrared absorption spectrum. IOP Conference Series: Earth and Environmental Science, 21, 012006. https://doi.org/10.1088/1755-1315/21/1/012006

Resentini, A., AndÒ, S., & Garzanti, E. (2018b). Quantifying roundness of detrital minerals by image analysis: sediment transport, shape effects, and provenance implications. Journal of Sedimentary Research, 88(2), 276–289.

Rink, W., Rendell, H., Marseglia, E., Luff, B., & Townsend, P. (1993). Thermoluminescence spectra of igneous quartz and hydrothermal vein quartz. Physics and Chemistry of Minerals, 20(5). https://doi.org/10.1007/bf00215106

Rosa, A. L., El-Barbary, A. A., Heggie, M. I., & Briddon, P. R. (2005). Structural and thermodynamic properties of water-related defects in α-quartz. Physics and Chemistry of Minerals, 32(5–6), 323–331. https://doi.org/10.1007/s00269-005-0005-6

Saha, S., Burley, S. D., Banerjee, S., Ghosh, A., & Saraswati, P. K. (2016). The morphology and evolution of tidal sand bodies in the macrotidal Gulf of Khambhat, western India. Marine and Petroleum Geology, 77, 714–730. https://doi.org/10.1016/j.marpetgeo.2016.03.028

Saikia, B. J. (2014). Spectroscopic estimation of geometrical structure elucidation in natural SiO_2 crystal. Journal of Materials Physics and Chemistry, 2(2), 28–33. https://doi.org/10.12691/jmpc-2-2-3

Sawakuchi, A.O., Blair, M.W., DeWitt, R., Faleiros, F.M., Hyppolito, T., Guedes, C.C.F. (2011). Thermal history versus sedimentary history: OSL sensitivity of quartz grains extracted from rocks and sediments. Quaternary Geochronology 6, 261–272. https://doi.org/10.1016/j.quageo.2010.11.002

Sawakuchi, A. O., Rodrigues, F. C. G., Mineli, T. D., Mendes, V. R., Melo, D. B., Chiessi, C. M., & Giannini, P. C. F. (2020). Optically stimulated luminescence sensitivity of quartz for provenance analysis. Methods and Protocols, 3(1), 6. https://doi.org/10.3390/mps3010006

Sawakuchi, A. O., Guedes, C. C. F., DeWitt, R., Giannini, P. C. F., Blair, M. W., Nascimento, D. R., & Faleiros, F. M. (2012). Quartz OSL sensitivity as a proxy for storm activity on the southern Brazilian coast during the Late Holocene. Quaternary Geochronology, 13, 92–102. https://doi.org/10.1016/j.quageo.2012.07.002

Sawakuchi, A.O., Jain, M., Mineli, T.D., Nogueira, L., Bertassoli, D.J., Häggi, C., Sawakuchi, H.O., Pupim, F.N., Grohmann, C.H., Chiessi, C.M., Zabel, M., Mulitza, S., Mazoca, C.E.M., Cunha, D.F. (2018). Luminescence of quartz and feldspar fingerprints provenance and correlates with the source area denudation in the Amazon River basin. Earth and Planetary Science Letters 492, 152–162. https://doi.org/10.1016/j.epsl.2018.04.006

Sawakuchi, A., Blair, M., DeWitt, R., Faleiros, F., Hyppolito, T., & Guedes, C. (2010). Thermal history versus sedimentary history: OSL sensitivity of quartz grains extracted from rocks and sediments. Quaternary Geochronology, 6(2), 261–272.

Schilles, T., Poolton, N. R. J., Bulur, E., Bøtter-Jensen, L., Murray, A. S., Smith, G. M., Riedi, P. C., & Wagner, G. A. (2001). A multi-spectroscopic study of luminescence sensitivity changes in natural quartz induced by high-temperature annealing. Journal of Physics D: Applied Physics, 34(5), 722–731. https://doi.org/10.1088/0022-3727/34/5/310

Schmidt, C., & Woda, C. (2019). Quartz thermoluminescence spectra in the high-dose range. Physics and Chemistry of Minerals, 46(9), 861–875. https://doi.org/10.1007/s00269-019-01046-w

Seyedolali, A., Krinsley, D. H., Boggs, S., O'Hara, P. F., Dypvik, H., & Goles, G. G. (1997). Provenance interpretation of quartz by scanning electron microscope–cathodoluminescence fabric analysis. Geology, 25(9), 787. https://doi.org/10.1130/0091-7613(1997)025

Sharma, K., Bhatt, N., Shukla, A. D., Cheong, D., & Singhvi, A. K. (2017). Optical dating of late Quaternary carbonate sequences of Saurashtra, western India. Quaternary Research, 87(1), 133–150. https://doi.org/10.1017/qua.2016.12

Sharma, S. K., Chawla, S., Sastry, M.D., Gaonkar, M., Mane, S., Balaram, V., Singhvi, A. K. (2017). Understanding the reasons for variations in luminescence sensitivity of natural quartz using spectroscopic and chemical studies. Proceedings of the Indian National Science Academy 83, 645–653. https://doi.org/10.16943/ptinsa/2017/49024

Sharman, G. R., Sylvester, Z., & Covault, J. A. (2019). Conversion of tectonic and climatic forcings into records of sediment supply and provenance. Scientific Reports, 9(1). https://doi.org/10.1038/s41598-019-39754-6

Singarayer, J., & Bailey, R. (2003). Further investigations of the quartz optically stimulated luminescence components using linear modulation. Radiation Measurements, 37(4–5), 451–458. https://doi.org/10.1016/s1350-4487(03)00062-3

Singh, N., Singh, V., Watanabe, S., Chubaci, J.F.D., Rao, T.K.G., Gao, H., Mardina, P. (2016). Studies of defects and optical properties of CaAl12O19:Ho3+ phosphor material. Journal of Alloys and Compounds 663, 235–242. https://doi.org/10.1016/j.jallcom.2015.12.049

Singhvi, A.K., Kar, A. (2004). The aeolian sedimentation record of the Thar desert. Proceedings of the Indian Academy of Sciences, Earth and Planetary Sciences 113, 371–401. https://doi.org/10.1007/BF02716733

Sinha, R., Kettanah, Y., Gibling, M. R., Tandon, S. K., Jain, M., Bhattacharjee, P. S., Dasgupta, A. S., & Ghazanfari, P. (2009). Craton-derived alluvium as a major sediment source in the Himalayan Foreland Basin of India. Geological Society of America Bulletin, 121(11–12), 1596–1610. https://doi.org/10.1130/b26431.1

Skuja, L. (2000). OPTICAL PROPERTIES OF DEFECTS IN SILICA. In Springer eBooks (pp. 73–116). https://doi.org/10.1007/978-94-010-0944-7_3

Smith, B.W., & Rhodes, E.J. (1994). Charge movements in quartz and their relevance to optical dating. Radiation Measurements, 23(2–3), 329–333. https://doi.org/10.1016/1350-4487(94)90060-4

Smith, B. W., Rhodes, E. J., Stokes, S., Spooner, N. A., & Aitken, M. J. (1990). Optical Dating of Sediments: Initial Quartz Results From Oxford. Archaeometry 32, 19–31. https://doi.org/10.1111/j.1475-4754.1990.tb01078.x

Soares, B. R., Mateus, F. D. C., Asfora, V. K., & Guzzo, P. L. (2023). Investigating the OSL components and the sensitivity changes in a natural quartz crystal showing an intense post-sensitisation TL signal. Radiation Effects and Defects in Solids, 178(9–10), 1081–1096. https://doi.org/10.1080/10420150.2023.2211196

SOI (1972). Survey of India. Geological Quadrangle Maps, Bangalore.

Sonam, N., Jain, V., Fryirs, K., & Brierley, G. (2021). Geomorphic characterization of a seasonal river network in semi-arid western India using the River Styles Framework. Journal of Asian Earth Sciences X, 7, 100077. https://doi.org/10.1016/j.jaesx.2021.100077

Souza, P. E., Pupim, F. N., Mazoca, C. E., Del Río, I., Mineli, T. D., Rodrigues, F. C., Porat, N., Hartmann, G. A., & Sawakuchi, A. O. (2023). Quartz OSL sensitivity from dating data for provenance analysis of Pleistocene and Holocene fluvial sediments from lowland Amazonia. Quaternary Geochronology, 74, 101422. https://doi.org/10.1016/j.quageo.2023.101422

Spooner, N. (1994). On the optical dating signal from quartz. Radiation Measurements, 23(2–3), 593–600. https://doi.org/10.1016/1350-4487(94)90105-8

Stalder, R. (2021). OH point defects in quartz – a review. European Journal of Mineralogy, 33(2), 145–163. https://doi.org/10.5194/ejm-33-145-2021

Syvitski, J. P. M., VöRöSmarty, C. J., Kettner, A. J., & Green, P. (2005). Impact of humans on the flux of terrestrial sediment to the global Coastal Ocean. Science, 308(5720), 376–380. https://doi.org/10.1126/science.1109454

Tandon, S., Sareen, B., Rao, M., & Singhvi, A. (1997). Aggradation history and luminescence chronology of Late Quaternary semi-arid sequences of the Sabarmati basin, Gujarat, Western India. Palaeogeography, Palaeoclimatology, Palaeoecology, 128(1–4), 339–357. https://doi.org/10.1016/s0031-0182(96)00035-1

Thokchom, S., Bhattacharya, F., Prasad, A. D., Dogra, N., & Rastogi, B. (2017). Paleoenvironmental implications and drainage adjustment in the middle reaches of the Sabarmati River, Gujarat: Implications towards hydrological variability. Quaternary International, 454, 1–14. https://doi.org/10.1016/j.quaint.2017.07.026

Thompson, J. W. (2015). Radiation defect. In Encyclopedia of Earth Sciences Series (p. 657). https://doi.org/10.1007/978-94-007-6304-3_53

Timms, N. E., Erickson, T. M., Zanetti, M. R., Pearce, M. A., Cayron, C., Cavosie, A. J., Reddy, S. M., Wittmann, A., & Carpenter, P. K. (2017). Cubic zirconia in >2370 °C impact melt records Earth's hottest crust. Earth and Planetary Science Letters, 477, 52–58. https://doi.org/10.1016/j.epsl.2017.08.012

Tobin, R. C., & Schwarzer, D. (2013). Effects of sandstone provenance on reservoir quality preservation in the deep subsurface: experimental modelling of deep-water sand in the Gulf of Mexico. Geological Society London Special Publications, 386(1), 27–47. https://doi.org/10.1144/sp386.17

Trukhin, A.N. (2019). Luminescence of natural α-quartz crystal with aluminium, alkali and noble ions impurities. Journal of Luminescence, 214, 116602. https://doi.org/10.1016/j.jlumin.2019.116602

Tsukamoto, S., Nagashima, K., Murray, A., & Tada, R. (2010). Variations in OSL components from quartz from Japan sea sediments and the possibility of reconstructing provenance. Quaternary International, 234(1–2), 182–189. https://doi.org/10.1016/j.quaint.2010.09.003

Tsukamoto, S., Nagashima, K., Murray, A.S., Tada, R. (2011). Variations in OSL components from quartz from Japan sea sediments and the possibility of reconstructing provenance. Quaternary International 234, 182–189. https://doi.org/10.1016/j.quaint.2010.09.003

Tucker, G. E., & Hancock, G. R. (2010). Modelling landscape evolution. Earth Surface Processes and Landforms, 35(1), 28–50. https://doi.org/10.1002/esp.1952

Valdiya, K. S. (2016). Tertiary basins: Along coasts and offshore. In The Making of India. Springer, Cham, 675–706.

Valdiya, K. S., & Sanwal, J. (2017). Sabarmati Plain and Saurashtra–Kachchh terranes. In Developments in Earth Surface Processes (Vol. 22, pp. 207–221). Elsevier.

Vella, E., Messina, F., Cannas, M., & Boscaino, R. (2011). Unraveling exciton dynamics in amorphous silicon dioxide: Interpretation of the optical features from 8 to 11 eV. Physical Review B, 83(17). https://doi.org/10.1103/physrevb.83.174201

Von Eynatten, H., & Wijbrans, J. R. (2003). Precise tracing of exhumation and provenance using40Ar/39Ar geochronology of detrital white mica: the example of the Central Alps.

Geological Society London Special Publications, 208(1), 289–305. https://doi.org/10.1144/gsl.sp.2003.208.01.14

Van Rijn, L. C. (1993). Principles of sediment transport in rivers, estuaries and coastal seas. http://ci.nii.ac.jp/ncid/BA28467043

Wadell, H. (1935). Volume, shape, and roundness of quartz particles. The Journal of Geology, 43(3), 250–280. https://doi.org/10.1086/624298

Wark, D. A., & Watson, E. B. (2006). TitaniQ: a titanium-in-quartz geothermometer. Contributions to Mineralogy and Petrology, 152(6), 743–754. https://doi.org/10.1007/s00410-006-0132-1

Weltje, G. J., & von Eynatten, H. (2004). Quantitative provenance analysis of sediments: review and outlook. Sedimentary Geology, 171(1–4), 1–11. https://doi.org/10.1016/j.sedgeo.2004.05.007

Wilkinson, M.T., Humphreys, G.S. (2005). Exploring pedogenesis via nuclide-based soil production rates and OSL-based bioturbation rates. Australian Journal of Soil Research 43, 767–779. https://doi.org/10.1071/SR04158

Williams, O. M., Smith, B. W., & Spooner, N. A. (2022). A role for oxygen vacancies in quartz luminescence. Radiation Measurements, 154, 106774. https://doi.org/10.1016/j.radmeas.2022.106774

Woda, C., Schilles, T., Rieser, U., Mangini, A., & Wagner, G. A. (2002). Point defects and the blue emission in fired quartz at high doses: A Comparative Luminescence and EPR study. Radiation Protection Dosimetry, 100(1), 261–264. https://doi.org/10.1093/oxfordjournals.rpd.a005862

World Temperature Records - current results. (n.d.-b). https://www.currentresults.com/Weather-Extremes/index.php

Wotton, B. M., Gould, J. S., McCaw, W. L., Cheney, N. P., & Taylor, S. W. (2011). Flame temperature and residence time of fires in dry eucalypt forest. International Journal of Wildland Fire, 21(3), 270. https://doi.org/10.1071/wf10127

Xu, Z., Belmont, P., Brahney, J., & Gellis, A. C. (2022). Sediment source fingerprinting as an aid to large-scale landscape conservation and restoration: A review for the Mississippi River Basin. Journal of Environmental Management, 324, 116260. https://doi.org/10.1016/j.jenvman.2022.116260

Yadav, A., Boothroyd, R. J., Smith, G. H. S., & Sen, S. (2023). Morphological adjustments of the Yamuna River in the Himalayan foothills in response to natural and anthropogenic stresses. Hydrological Processes, 37(7). https://doi.org/10.1002/hyp.14934

Yoshida, H., Roberts, R., Olley, J., Laslett, G., & Galbraith, R. (2000). Extending the age range of optical dating using single “supergrains” of quartz. Radiation Measurements, 32(5–6), 439–446. https://doi.org/10.1016/S1350-4487(99)00287-5

Zhang, J., Li, S.H., Sun, J., Tongyan, L., Zhou, X., Hao, Q. (2022). Quartz luminescence sensitivity variation in the Chinese loess deposits: the potential role of wildfires. Journal of Quaternary Science 38, 49–60. https://doi.org/10.1002/jqs.3462

Zheng, J., & Hryciw, R. D. (2015). Traditional soil particle sphericity, roundness and surface roughness by computational geometry. Géotechnique, 65(6), 494–506. https://doi.org/10.1680/geot.14.p.192

Zimmerman, J. (1971). The radiation-induced increase of the 100°C thermoluminescence sensitivity of fired quartz. Journal of Physics C: Solid State Physics, 4(18), 3265–3276. https://doi.org/10.1088/0022-3719/4/18/032

Zular, A., Sawakuchi, A. O., Guedes, C. C., & Giannini, P. C. (2015). Attaining provenance proxies from OSL and TL sensitivities: Coupling with grain size and heavy minerals data from southern Brazilian coastal sediments. Radiation Measurements, 81, 39–45. https://doi.org/10.1016/j.radmeas.2015.04.010

List of Publications

Published in peer-reviewed journals:

1. Kartika Goswami [a], Santunu Kumar Panda [a], Linto Alappat [b], Naveen Chauhan [a, *] (2023) Luminescence for sedimentary provenance quantification in river basins: A methodological advancement. ‘Quaternary Geochronology’, Volume 79, 101488, (https://doi.org/10.1016/j.quageo.2023.101488)

Under review (provide title(s)):

1. Documenting Variations in Luminescence Sensitivity of Quartz in a River Basin at the Desert Margin: The Case of River Sabarmati. (Panda, S. K. [1,2], Kaushal, R.K. [1], Parida, S. [1], Chauhan, N. [1], Singhvi, A.K. [1]) (Submitted in ‘Earth Surface Processes and Landforms’, Manuscript number: ESP-24-0319)
2. Rapid Late Pleistocene frontal fault growth and Sutlej drainage reorganization in the western Himalaya Kordt, Jonas (1); Dey, Saptarshi (2); Bookhagen, Bodo (3); Rugel, George (4); Lachner Johannes (4); Vivo-Vilches, Carlos (5); Panda, Santunu Kumar (2); Chauhan, Naveen (2); Thiede, Rasmus (1)

In preparation (provide title(s)):

1. Potential natural processes and their effect on luminescence properties of quartz (Panda, S. K. [1,2], Chauhan, N. [1])

Presentations in Conferences/ Workshops

- International e-conference ‘Luminescence and ESR dating (LED-2021).; Spatial variations in luminescence sensitivity of quartz extracted from source rocks and fluvial sediments of the Sabarmati River basin, Western India: Implications for provenance studies.; Online; (13th to 17th September, 2021).
- National e-conference ‘National Conference on Luminescence and its applications (NCLA-2021)’; “Luminescence Sensitivity of Quartz as a Fingerprint for Provenance Analysis: Case Study on Sabarmati River Basin, Western India”.; Online; (22nd to 28th February 2021).
- Work shop on ‘Luminescence dating and applications. (ALD 2023); Exploring potential luminescence sensitizer of quartz. ;(IISER Kolkata); (1st to 3rd February, 2023, Online).
- 7th International Conference on Luminescence and is Application (ICLA 2023); Understanding the change in sensitivity of quartz by annealing and diffusion of water at high temperature.; CSIR IICT Hyderabad; (3rd to 6th July, 2023)